

THE DYNAMICS OF SATELLITE GALAXIES

by

Dennis Fabian Zaritsky

A Dissertation Submitted to the Faculty of the
DEPARTMENT OF ASTRONOMY
In Partial Fulfillment of the Requirements
For the Degree of
DOCTOR OF PHILOSOPHY
In the Graduate College
THE UNIVERSITY OF ARIZONA

1 9 9 1

INFORMATION TO USERS

This manuscript has been reproduced from the microfilm master. UMI films the text directly from the original or copy submitted. Thus, some thesis and dissertation copies are in typewriter face, while others may be from any type of computer printer.

The quality of this reproduction is dependent upon the quality of the copy submitted. Broken or indistinct print, colored or poor quality illustrations and photographs, print bleedthrough, substandard margins, and improper alignment can adversely affect reproduction.

In the unlikely event that the author did not send UMI a complete manuscript and there are missing pages, these will be noted. Also, if unauthorized copyright material had to be removed, a note will indicate the deletion.

Oversize materials (e.g., maps, drawings, charts) are reproduced by sectioning the original, beginning at the upper left-hand corner and continuing from left to right in equal sections with small overlaps. Each original is also photographed in one exposure and is included in reduced form at the back of the book.

Photographs included in the original manuscript have been reproduced xerographically in this copy. Higher quality 6" x 9" black and white photographic prints are available for any photographs or illustrations appearing in this copy for an additional charge. Contact UMI directly to order.

U·M·I

University Microfilms International
A Bell & Howell Information Company
300 North Zeeb Road, Ann Arbor, MI 48106-1346 USA
313/761-4700 800/521-0600

Order Number 9208037

The dynamics of satellite galaxies

Zaritsky, Dennis Fabian, Ph.D.

The University of Arizona, 1991

U·M·I

**300 N. Zeeb Rd.
Ann Arbor, MI 48106**

THE DYNAMICS OF SATELLITE GALAXIES

by

Dennis Fabian Zaritsky

A Dissertation Submitted to the Faculty of the
DEPARTMENT OF ASTRONOMY
In Partial Fulfillment of the Requirements
For the Degree of
DOCTOR OF PHILOSOPHY
In the Graduate College
THE UNIVERSITY OF ARIZONA


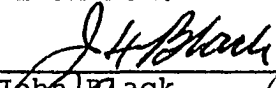
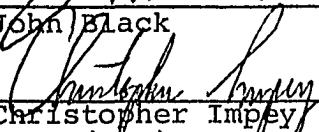
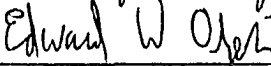
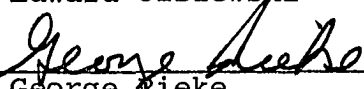
1 9 9 1

THE UNIVERSITY OF ARIZONA
GRADUATE COLLEGE

2


As members of the Final Examination Committee, we certify that we have read
the dissertation prepared by Dennis Fabian Zaritsky
entitled THE DYNAMICS OF SATELLITE GALAXIES

and recommend that it be accepted as fulfilling the dissertation requirement
for the Degree of Doctor of Philosophy.

	<u>9/9/91</u>
Simon D.M. White	Date
	<u>9/9/91</u>
John Black	Date
	<u>9/9/91</u>
Christopher Impey	Date
	<u>9/9/91</u>
Edward Olszewski	Date
	<u>9/9/91</u>
George Rieke	Date

Final approval and acceptance of this dissertation is contingent upon the
candidate's submission of the final copy of the dissertation to the Graduate
College.

I hereby certify that I have read this dissertation prepared under my
direction and recommend that it be accepted as fulfilling the dissertation
requirement.

	<u>9/9/91</u>
Dissertation Director Simon D.M. White	Date

STATEMENT BY AUTHOR

This dissertation has been submitted in partial fulfillment of requirements for an advanced degree at The University of Arizona and is deposited in the University Library to be made available to borrowers under the rules of the Library.

Brief quotations from this dissertation are allowable without special permission, provided that accurate acknowledgment of source is made. Requests for permission for extended quotation from or reproduction of this manuscript in whole or in part may be granted by the head of the major department or the Dean of the Graduate College when in his or her judgement the proposed use of the material is in the interest of scholarship. In all other instances, however, permission must be obtained from the author.

SIGNED: De Zeeb

ACKNOWLEDGEMENTS

Thanks to K.-Y. Lo, N. Scoville, and E. Shaya, who helped a novice undergraduate through two different “summer” research programs and introduced me to “real astronomy”.

I also gratefully acknowledge financial assistance from the NSF (Graduate Fellowship and Simon’s grants), from the State of Arizona (a TA and the Minority Graduate Student Travel Fund), from P. Strittmatter and Steward Obs. (publication support for my more independent ventures) and from CTIO (travel support).

Most relevant regarding the work presented here are my thanks to Simon White for providing the ideas and letting me try them out (and then finding my mistakes). Astronomy, by its nature, is a fairly inexact, exact science. From Simon I’ve learned that this fact should not dissuade one from careful and thorough work.

Thanks to my other collaborators on this project: C. Frenk, S. Lorrimer, and R. Smith. Who knows how many satellites we would have if they had had any clear weather at all? Also thanks also to those who provided comments on earlier versions of this manuscript: J. Black, J. Charlton, C. Frenk, C. Impey, E. Olszewski, and G. Rieke.

I also greatly appreciated the freedom I had to try other projects (one of which even turned out to be incorporated into Chapter 2). Special thanks to my various collaborators on that and other projects: M. Aaronson (who I had originally ...a long long time ago, thought was going to be my thesis advisor), R. Elston, S. Grossman, J. Hill, J. Huchra, R. Kennicutt, J. Lowenthal, E. Olszewski, R. Peterson, H.-W. Rix, and R. Schommer. Special thanks to R. Elston for demonstrating that being *just* a graduate student shouldn’t impose any limitations. Also special thanks to J. Hill, whose MX spectrometer and the imitations it inspired, have been the workhorse of most of my observational work. Thanks EdO for all the help, anecdotes, and otherwise useful information¹. Thanks to H.-W. Rix, who provided many stimulating conversations and who kindly escorted me to several Cambridge pubs and Indian restaurants. Thanks also to all the other past and present graduate students, especially M. Cornell, R. Cutri, M. Dinniman, D. Foss, B. Januzzi, D. Kelly, K. Katris, B. Latter, M. Lesser, and R. Saffer and for making Steward Obs. a nicer place to spend the majority of my waking hours. In addition, thanks to J. Liebert and R. Kennicutt for being two of the good guys.

Finally, I thank my parents for ... everything. This manuscript is dedicated to them with all my love.

¹Extra-special thanks go to Julia Olszewski for turning EdO into a marshmallow.

Table of Contents

LIST OF ILLUSTRATIONS	8
LIST OF TABLES	11
ABSTRACT	13
CHAPTER 1 : Review and Preview. I	15
1.1 Introduction	15
1.2 Dark Matter and Satellite Galaxies	16
1.3 Dark Matter in Galactic Halos	18
1.3.1 Rotation Curves	18
1.3.2 Binary Galaxies	20
1.3.3 Theoretical Prejudices	26
1.4 Satellite Galaxies	27
1.4.1 Observational Studies of Satellite Galaxies	27
1.4.2 Theoretical Studies of Satellite Galaxies	28
1.5 Summary	30
CHAPTER 2 : The Mass of the Galaxy	31
2.1 Introduction	31

2.2	Observations	32
2.3	Results and Discussion	38
2.3.1	Statistical Analysis	40
2.3.2	Timing Arguments	49
2.3.3	An Unbound Leo I ?	55
2.4	Timing Arguments for the Local Group	57
2.4.1	The Models	58
2.4.2	Discussion	60
2.5	Conclusions	65
CHAPTER 3 : Spiral Galaxies and Satellite Dynamics: Data . . .		68
3.1	Introduction	68
3.2	The Data	69
3.2.1	The Selection of Primary Galaxies	69
3.2.2	The Search for Satellites	75
3.3	A Look at the Data	101
3.3.1	Asymmetric Velocity Distribution	101
3.3.2	Identifying Interlopers	113
3.3.3	The Number of Satellites	115
3.3.4	The Radial Distribution of Satellites	119
3.3.5	The 2-Dimensional Distribution of Satellites	121
3.3.6	The Characteristics of the Satellites	123
3.3.7	The Angular Momentum of Primaries and Satellites	131
3.4	Summary	133

CHAPTER 4 : Spiral Galaxies and Satellite Dynamics : Analysis	135
4.1 Introduction	135
4.2 Random Phase Models	138
4.2.1 Point-Mass Random-Phase Models	139
4.2.2 Extended-Mass Random-Phase Models	152
4.3 Secondary Infall Models	158
4.3.1 "Analytic" Solution	160
4.3.2 Numerical Solution	168
4.3.3 Scaling Properties	187
4.3.4 Comparing Models and Data	193
4.3.5 Additional Complications	214
4.4 Summary	219
CHAPTER 5 : Review and Preview. II	222
5.1 Summary of Results	222
5.1.1 Satellite Galaxies	222
5.1.2 Galactic Halos	224
5.2 The Future for Studies of Satellite Galaxies	229
5.3 Conclusion	232
REFERENCES	234

List of Illustrations

1.1	Comparison of Data from Previous Studies	21
2.1	Comparison of He-Ne-Ar and Etalon Calibration Spectra	35
2.2	Point Mass Model Results	45
2.3	Isothermal Sphere Model Results	46
2.4	Observed vs. Theoretical Distributions	47
3.1	Absolute Magnitude Histogram for Primary Galaxies with Satellites	70
3.2	Histogram of Recessional Velocities for Primaries with Satellites . .	73
3.3	Histogram of Magnitude Differences Between Primaries and Satellites	76
3.4	H I Velocity Uncertainties	78
3.5	Argus Sky Subtraction	83
3.6	Representative ARGUS Satellite Spectra	84
3.7	MMT Velocity Error Distribution	88
3.8	r_p vs. $ \Delta v $	90
3.9	Primary Galaxy Position Angle Error Distribution	91
3.10	Blue Magnitude Error Distribution	92
3.11	Semi-Major Axis Error Distribution	94
3.12	Velocity Difference Histogram for Satellite Sample	102
3.13	Minimum P/T of Background vs. Background Fraction	112

3.14 Possible Interlopers in the $r_p - \Delta v $ Plane	115
3.15 Distributions of Satellites per Primary for Various Subsamples	117
3.16 Number of Satellites vs. Primary Rotation Curve Amplitude	119
3.17 Distribution of Projected Separations	120
3.18 Position Angle Difference Scatterplot	122
3.19 Surface Brightness vs. Projected Separation	124
3.20 Hubble Type vs. Projected Separation	125
3.21 Comparison of Absorption and Emission Line Systems	127
3.22 Satellite Luminosity Function	128
3.23 Semi-Major Axis vs. Projected Separation	130
3.24 Prograde and Retrograde Orbits	132
4.1 Keplerian Simulations vs. Observations	145
4.2 Keplerian Simulations: 2-D KS Probe Through Parameter Space	148
4.3 Keplerian Simulations: 2-D KS Probe Through Parameter Space	149
4.4 Distribution of Point Particles for a Secondary Infall Model	171
4.5 Mass Profiles vs. Orbital Eccentricity	175
4.6 Satellite Search Volume	177
4.7 Distribution of Satellites in True Distances	180
4.8 Mass Profiles of Secondary Infall Models: Relaxed Core	185
4.9 Mass Profiles of Secondary Infall Models: Dependence on α	186
4.10 On Rescaling the Models	190
4.11 $ \Delta v $ vs. Rotation Curve Amplitude	191
4.12 KS Results from Modified Secondary Infall Models: $\gamma = 1.6$	203

4.13 KS Results from Modified Secondary Infall Models: $\gamma = 1.8$	204
4.14 KS Results from Modified Secondary Infall Models: $\gamma = 2.0$	205
4.15 KS Results from Modified Secondary Infall Models: v_c Dependence	206
4.16 Mass Profiles from Secondary Infall Models: Within 500 kpc	211
4.17 Mass Profiles from Secondary Infall Models: Beyond 500 kpc	212
5.1 Future Constraints on Ω_0 and e ?	231

List of Tables

1.1	Results from Binary Galaxy Studies	22
2.1	Measured Heliocentric Velocities for Standard Stars	36
2.2	Measured Heliocentric Velocities for Program Stars	39
2.3	Velocities and Distances of Remote Satellites of the Milky Way . . .	41
2.4	Results of Statistical Analysis	43
2.5	Timing Argument Models	52
2.6	Parameters of Remote Local Group Members	59
2.7	Local Group Timing Model Results	61
3.1	Satellites Identified With MX and ARGUS	85
3.2	Data for Primary and Satellite Galaxies	95
3.3	Primaries Without Known Satellites	101
3.4	Observed P/T Values	103
3.5	Simulated Interloper P/T Values	109
3.6	Prograde and Retrograde Satellites	133
4.1	Point Mass Model Parameters and Results	142
4.2	Description of Satellite Samples	150
4.3	Estimates of Total Mass Using Bahcall-Tremaine Mass Estimator .	151

4.4	Extended Mass Model Parameters and Results	155
4.5	Correlation Coefficients for Satellite Samples	156
4.6	Results Using White <i>et al.</i> 's Models	157
4.7	Modified Secondary Infall Model Results : Sample 0	199
4.8	Modified Secondary Infall Model Results : Sample 1	200
4.9	Modified Secondary Infall Model Results : Sample 2	202
4.10	Halo Parameters for Secondary Infall Models	209

ABSTRACT

We use the positions and velocities of satellites of our galaxy and of other spiral galaxies to determine the radial mass profile of dark matter halos.

We combine our measurement of the velocities of five remote Galactic satellites with published observations of the other Galactic satellites to obtain a complete sample of test particles. We then apply statistical techniques and timing arguments to deduce that the mass of the Galaxy is $\gtrsim 1.3 \times 10^{12} M_{\odot}$ for standard assumptions and that the halo extends beyond 100 kpc Galactocentric distance. We confirm our result by examining the dynamics of other Local Group galaxies.

Subsequently, we expand our study to include nearby ($1000 \text{ km s}^{-1} < v_R < 7000 \text{ km s}^{-1}$) Sb-Sc type galaxies. We use multiaperture spectrometers to conduct a survey for satellite galaxies and are able to double the sample of known satellite galaxies (satellites are defined to be at least eight times fainter than the primary) of isolated unbarred late-type spirals. The homogeneity of the primaries allows us to combine observations of satellites of various primaries and analyze the dynamical properties of the ensemble. The characteristics of this satellite sample (number, radial and azimuthal distribution, luminosity function, orbital characteristics, and contamination) are discussed.

Finally, new models of the dynamics of satellite galaxies are developed that include the effects of the cosmological evolution of the halos and do not presume that halos are virialized. These models are used to constrain the mass distribution in which the satellite galaxies orbit. We conclude that only model halos with more than $10^{12} M_{\odot}$ within a galactocentric radius of 200 kpc are acceptable (90% confidence limit) for orbits of eccentricity < 0.9 . The preferred models (60% confidence limit) are of halos with more than $1.6 \times 10^{12} M_{\odot}$ within 200 kpc. Halos that formed in a universe with $\Omega = 1$ also fall within the preferred range and have $\sim 3 \times 10^{12} M_{\odot}$

within 200 kpc. In addition, we infer that the satellites' orbital eccentricities are typically less than 0.9. These results, in conjunction with the results obtained for the halo of our galaxy, constitute convincing evidence for the existence of large (> 200 kpc) and massive ($> 10^{12} M_{\odot}$, $M/L > 80$) dark matter halos around isolated unbarred late-type spiral galaxies.

Chapter 1

Review and Preview. I

1.1 Introduction

The dark matter problem is arguably the most important issue in contemporary astronomy. Zwicky (1933) was the first to notice a discrepancy between the apparent mass of luminous material in the Coma galaxy cluster and that inferred from the dynamics of member galaxies. Since that work, similar discrepancies have been observed in a variety of astronomical environments. To resolve the discrepancy, one may postulate that non-luminous material of unknown composition is present, referred to broadly as dark matter, or that Newton's law of gravity inaccurately describes the force between widely-separated masses. Because a proper understanding of mass and gravity is fundamental to astronomy, resolution of this issue is paramount.

The essential initial ingredient for any study of this issue is an estimate of the magnitude of the discrepancy between the mass that is inferred from dynamics and that which is estimated by assuming a standard stellar mass-to-luminosity ratio, M/L . The discrepancy between the two mass estimates is generally attributed to the faulty assumption that all the matter in the system has a standard stellar value of M/L . Because the standard stellar value of M/L is of order 1, dark matter is evidently present wherever M/L is inferred to be $\gg 1$. Therefore, estimates of

M/L or of the mass, as a function of position, provide information on the amount and distribution of dark matter. Unfortunately, accurate and precise estimates of mass distributions are difficult to obtain. Despite much work, the amount and distribution of dark matter remains poorly constrained. In this dissertation, we confine our attention to determining the distribution of dark matter in one specific type of environment — the region surrounding the luminous component of isolated unbarred late-type spiral galaxies. Once the distribution of dark matter is accurately determined, we can begin to try to determine the nature of the dark matter. In this chapter we present a brief review of studies of the dark matter problem in galaxy halos. For a comprehensive introduction to the material we suggest Binney and Tremaine (1987), and for more extensive reference material we suggest Faber and Gallagher (1979), Brück, Coyne, and Longair (1982), Setti and van Hove (1984), Kolb *et al.* (1986), Kormendy and Knapp (1987), Trimble (1987), and Kormendy and Yu (1988).

1.2 Dark Matter and Satellite Galaxies

Evidence for dark matter usually comes from the study of the dynamics of objects, presumably test particles, within the system of interest. In general, dark matter is invoked when the gravitational force produced by the luminous material is insufficient to generate the observed motions of the test particles. The inference of dark matter rests on the assumptions that Newton's law is valid on astronomical scales and that the simple dynamical models employed are adequate. We believe that the conservative approach is to adopt Newtonian physics until all other plausible solutions, such as dark matter, are rejected; therefore, we shall adopt the former assumption. Hereafter, any discrepancy between the inferred (from dynamics) and estimated (assuming $M/L \sim \text{few}$) mass will be attributed to the presence of dark

matter (see Milgrom (1983) for an alternative perspective on this issue). The latter assumption is more questionable because the conclusions drawn from this analysis are often model dependent. Understanding the biases inherent in selecting a sample of objects, improving the dynamical models, and quantifying uncertainties are primary emphases of this study.

The data for dynamical analyses of systems beyond the Local Group consist only of radial velocities and projected positions of objects considered to be test particles in the potential of interest. In galaxy clusters, the member galaxies are the test particles; in dwarf spheroidals, stars perform the same role; and in spiral galaxies, the test particles are either stellar tracers (stars, planetary nebula, or globular clusters), atoms or molecules of gas generally distributed in clouds, for example H II regions, or companion galaxies. The analysis is more straightforward when the analogy to a test particle is more appropriate. Therefore, the study of satellite galaxies, companion galaxies that are significantly less massive than the primary galaxy, presents an improvement over the study of binary galaxies, in which the galaxies are of roughly equal mass. Furthermore, using satellites to probe the potential at large galactocentric distance presents an improvement over observations of the disk rotation curve, which are limited in extent to a few tens of kpc. Finally, satellites are more luminous than any of the stellar tracers. These advantages, convolved with a proper analysis, should help shed light on the dark matter halos of spiral galaxies. In the following chapters, we present our study of satellite galaxies of our galaxy and of other galaxies.

In the next sections, the topics of dark matter and satellite galaxies temporarily diverge as evidence for dark matter in galactic halos is discussed and results from previous studies of satellite galaxies are presented.

1.3 Dark Matter in Galactic Halos

1.3.1 Rotation Curves

Consider a test particle, for example a star, in circular orbit about the center of a spherical galaxy. For that particle to remain in circular orbit, the gravitational force must be balanced by the centrifugal term in its reference frame,

$$\frac{GM(r)}{r^2} = \frac{v^2}{r}, \quad (1.1)$$

where $M(r)$ is the mass interior to radius r , v is the velocity of the test particle, and G is the gravitational constant. If the mass is concentrated at the center, then $M(r) = M$, and the result is a Keplerian rotation curve,

$$v = \sqrt{\frac{GM}{r}}. \quad (1.2)$$

However, if $M(r) \propto r$, then the rotation curve is flat, $v = \text{constant}$. Because most well-studied spiral galaxies have rotation curves that are flat rather than Keplerian (see Faber and Gallagher (1979) for a review), one infers that spirals have extended mass distributions.

Observations of neutral hydrogen in individual galaxies provide conclusive evidence for the presence of significant amounts of dark matter (*i.e.*, more than can be accounted for by known forms of dark matter such as the gas itself). In many spiral galaxies, neutral hydrogen rotation curves are flat to a galactocentric distance of several tens of kpc, which implies that $M(r) \propto r$ to this distance (cf. Rogstad and Shostak (1972) for H I rotation curves of 5 Scd's; Bosma (1978) for H I rotation curves and mass models for 7 spirals; and Rubin, Ford, and Thonnard (1978) for a comparison of rotation curves among different spiral types). Furthermore, because

at these radii there is little luminous matter, the existence of dark matter is inferred¹ (Freeman 1970). Unfortunately, neutral hydrogen cannot be observed to arbitrarily large radii, and even at the largest observed radius most rotation curves show no sign of a Keplerian decline. Therefore, while considered to be the strongest evidence for the presence of dark matter in spiral galaxies, rotation curves only place a lower bound on the amount of dark matter.

Progressing beyond the inferences from the H I studies requires observations of test particles at greater galactocentric distance than the farthest measurement of H I. Because the distance between a primary galaxy (*e.g.*, a large spiral) and its companion(s) is typically larger than the measurable extent of the H I disk, companions are well-suited for a dynamical study of the region beyond that already examined. However, unlike with the H I disk, for which the orbits are known to be nearly circular, the companions' orbits cannot be determined uniquely if given only the projected separations, r_p , and radial velocity differences, Δv . Therefore, it is especially important to collect Δv 's and r_p 's, for as many companions as possible. Unfortunately, only our galaxy and M31 have more than a few known bound companions; and so for galaxies outside the Local Group, the analysis must be done using companions to many "look-alike" galaxies. Observational considerations in such studies have limited previous work to bright companions. Often, the primaries and companions have been of similar brightness, and presumably similar masses. These systems are called binary galaxies.

¹The material at large radii might not be in circular orbit. Many galaxies have warps and other asymmetries at large radii (*e.g.*, M33 (Rogstad, Wright, and Lockhart 1976) and M101 (Bosma, Goss, and Allen 1981). However, it is unlikely that in most spirals the material in non-circular or non-planar orbits conspires to construct rotation curves that appear flat.

1.3.2 Binary Galaxies

The history of the study of binary galaxies is one of an increasing realization of the complexity of the problem. Holmberg (1937) published a treatise on the subject of binary galaxies, part of which details the determination of masses. Page (1952; hereafter P52) constructed a mass estimator statistic by assuming that the two galaxies are on circular orbits, that the viewing angles are randomly distributed, and that the galaxies have random orbital positions. He also discussed the effect of selection biases on his analysis. Turner (1976a,b; T76) used a well-defined sample, for which the selection biases could be modeled, to discriminate between various halo models. More recently, the most significant studies have been that of White *et al.* (1983; WHLD83) and Schweizer (1987a,b,c; S87). The former used a new, more flexible, set of models (from White (1981)) and precise velocities ($1\sigma = 29 \text{ km s}^{-1}$) for a well-defined sample. The latter used a smaller, but more precise, dataset ($1\sigma = 9 \text{ km s}^{-1}$) and a quantitative method for selecting isolated pairs. Results are compared in Table 1.1.

A comparison of the conclusions from recent studies is confusing at best. For example, van Moorsel (1987; vM87) concluded that a point mass model was inadequate even for companions at large separations (100 to 200 kpc) and that $M/L \sim 15^2$. On the other hand, S87 concluded that point mass models provide a good approximation for the orbits of companions and that $M/L = 28^2$ for Sc-type galaxies. Erickson *et al.* (1987; EGH87) concluded that no additional mass to that inferred from the rotation curve was necessary to explain the dynamics of objects in their sample, but WHLD83 concluded that there are extended halos consistent with a flat extrapolation of the rotation curve out to radii $\sim 100 \text{ kpc}$.

² M/L 's have been scaled to $H_0 = 75 \text{ km s}^{-1} \text{ Mpc}^{-1}$

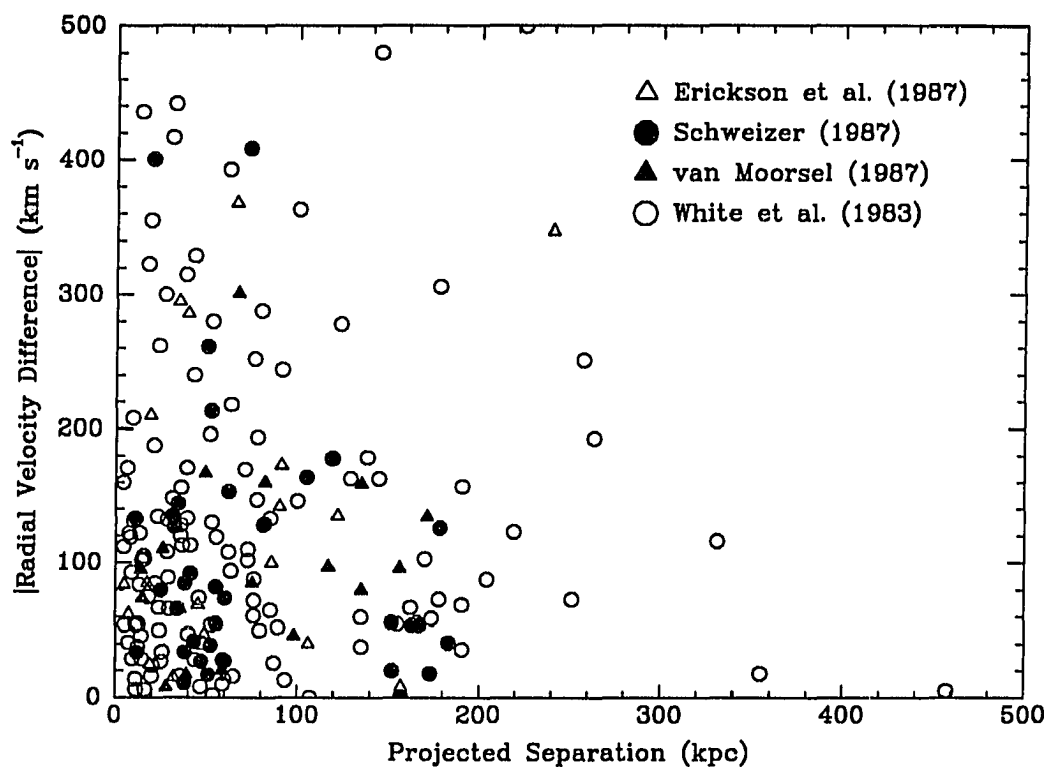


Figure 1.1: *Comparison of Data from Previous Studies : The WHLD83 sample is the largest, so more objects are expected at large r_p and $|\Delta v|$ than in other samples; however, the bulk of the data from the four samples is clearly clustered in the lower left corner of the diagram. A few data outside the bounds of the figure are not shown.*

Table 1.1: Results from Binary Galaxy Studies^a

Sample	P52	K72	T76	P79 ^b	WHL83 ^c	S87	vM87
M/L	50	8	98	50	28	32	15

^a These numbers are intended for rough comparison only. Model assumptions and sample selection are important, so one should refer to the original reference before adopting any particular M/L . Holmberg (1937) found similar masses as P52, but did not calculate an M/L . EGH87 also do not present a global M/L value for their sample, and so their result has not been placed in the Table. All M/L values have been converted to $H_0 = 75 \text{ km s}^{-1} \text{ Mpc}^{-1}$. There has been no attempt to select results from models of similar characteristics, so the comparison is for illustrative purposes only.

^b Peterson 1979a, b.

^c The value presented is for $r = 100 \text{ kpc}$, isotropically distributed velocities, and for L_* galaxies.

The data are not radically different among the various studies (see Figure 1.1), so the conflicts must arise primarily from interpretation. Except for the results of Karachentsev's 1972 study (K72) and T76, M/L varies by factors of only a few among the different studies. A major difficulty is that most studies are based on a small number of pairs (S87 43, EGH87 20, and vM87 16), few of which have projected separations greater than 100 kpc. Studies that concentrate on companions with projected radii $< 100 \text{ kpc}$ and on large spiral primaries, which have flat rotation curves out to at least several tens of kpc, will produce intermediate M/L ratios (*i.e.*, $M/L \sim 30$) even if the primaries have isothermal halos. Consider an L^* galaxy ($L_B^* = 2.06 \times 10^{10} L_\odot$; Efstathiou *et al.* 1988) with a circular velocity of $\sim 170 \text{ km s}^{-1}$ and extrapolate the flat rotation curve out to 100 kpc. The enclosed mass at 100 kpc for this galaxy is $6.4 \times 10^{11} M_\odot$ and $M/L_B = 31$. It is far more interesting to examine the potential at $r > 100 \text{ kpc}$ because the differences between different mass models becomes significant. Unfortunately, for $r_p > 100 \text{ kpc}$, the

existing data are much sparser (WHL 28 pairs with radial velocity differences of less than 500 km s^{-1} ; S87 10 pairs; EGH87 9; and vM87 6), and contamination by projected background galaxies is more likely (see §3.3.1). Hence, conclusions regarding the mass distribution beyond 100 kpc, where one hopes to detect convincingly differences between extended and compact halo models, are subject to large uncertainties. A sample of companion galaxies to be used for dynamical analysis should contain many galaxies at large separations but be defined to minimize contamination from projected galaxies and nearby group or cluster members.

Contamination must be minimized because existing mass analyses are most sensitive to the few test particles with largest $|\Delta v|$'s or r_p 's. Consider the 43 pairs in the S87 sample. By applying the Bahcall and Tremaine (1981) projected-mass estimator (cf. §4.2.1, Eq. 4.3), the average mass of a pair of galaxies is estimated to be $41 \times 10^{11} M_{\odot}$ ³. If the two galaxy pairs with $|\Delta v| > 500 \text{ km s}^{-1}$ are removed from the sample, because presumably they are not physical pairs, then the estimated mass decreases to $21 \times 10^{11} M_{\odot}$. Furthermore, if two more pairs are removed (Nos. 27 and 48 in S87; which have the next highest values of $r_p(\Delta v)^2$), then the estimated mass decreases further to $13 \times 10^{11} M_{\odot}$. In such analyses, the criteria used to decide whether companions with large $r_p(\Delta v)^2$ are physical companions or interlopers is obviously important. Accurate modeling of contamination can only be done if the sample is well-defined, and the effect of interlopers can only be precisely determined if the sample is sufficiently large. Both sample definition and size play an important part in the work detailed in Chapter 3.

Once a sample of companions is obtained, the aim of such work is to discriminate between the following basic galactic halo models:

³S87 used a different analysis technique. This exercise is meant only to show the effect of interlopers on one technique, albeit one that does not attempt to minimize the influence of interlopers.

- 1) no dark halo, the entire mass of the galaxy is located within the optical component (Keplerian model: $M/L \sim \text{few}$);
- 2) the halo extent is a few tens of kpc, the entire mass is located within the region probed by H I observations (small halo model: $M/L \sim \text{few} \times 10$);
- 3) the halo extent is a few hundreds of kpc (medium halo model: $M/L \gtrsim 100$);
- 4) the halo is approximately an isothermal sphere whose extent is determined by its nearest neighbors (extent of order 1 Mpc; large halo model: $M/L \gtrsim 1000$).

The first model is referred to as Keplerian. Although it is not a point mass model, most companion galaxies have r_p 's that are larger than the size of the primary's optical disk, and so the primary is effectively a central point mass (with a correction of order unity to account for the deviation from spherical symmetry). This model is ruled out by observations of H I rotation curves. The second, or small halo model, remains popular because it allows for flat rotation curves over the inner few tens of kpc, but is still nearly a point mass model because most companions have r_p 's greater than the observed extent of primary's H I disk. No conclusive evidence against this model exists, although many companion galaxy studies imply slightly larger M/L 's than predicted by this model. The third, or medium halo model, corresponds roughly to a current density parameter, Ω_0 , of 0.1 to 0.2 if the mass in the Universe is concentrated in galaxies. Values of Ω_0 in this range are inferred from the analysis of clusters of galaxies by Press and Davis ($\Omega_0 = 0.15$; 1982) and from the analysis of positions and velocities of galaxies in the CfA redshift catalog by Davis and Peebles ($\Omega_0 = 0.2e^{\pm 0.4}$; 1983a). Values in this range are also particularly interesting because they lie near the upper bound on the current

baryon fraction of the critical density, Ω_b , derived from nucleosynthesis models ($9.73 \times 10^{-3} < \Omega_b h^2 < 1/6 \times 10^{-2}$; Olive *et al.* (1990)⁴). The final model, the large halo model, is most appropriate if $\Omega_0 \approx 1$. There is some observational evidence from a recent study of binary galaxies drawn from the CfA catalog supporting this model (Charlton and Salpeter 1991). However, the principal motivation for this model is that the standard inflationary cosmology model predicts $\Omega_0 \approx 1$ to a high degree of accuracy if $\Lambda = 0$ (Guth 1981).

There has been little progress in discriminating between models 2 through 4; previous work has generally concentrated on discriminating between models 1 and 2. In most previous studies, point mass models, which are even only marginally applicable to model 2, have been used to model the dynamics of companion galaxies. In none of those studies has the possibility of models 3 or 4 been investigated. In addition, there are few data at $r_p > 100$ kpc and the samples are often poorly defined. Except for WHLD83, all previous authors obtained fits only to a pure point mass or an isothermal sphere model. In Chapter 4, we formulate a different analysis technique, based on secondary infall models of halo formation. This technique accurately simulates the dynamics of objects that decoupled from the Hubble flow and had sufficient time to relax dynamically in the potential of the primary (*i.e.*, settle into periodic orbits), of objects that decoupled from the Hubble flow but have had insufficient time to relax fully, and of objects that have not decoupled from the Hubble flow. By varying Ω_0 , we can use these simulations and the data described in Chapter 3 to discriminate between the various halo models. These models have a variety of additional advantages, which are described in Chapter 4.

⁴Non-homogeneous nucleosynthesis models can produce agreement with the observations for values of $\Omega_b h^2 > 1.6 \times 10^{-2}$ (cf. Applegate, Hogan, and Scherrer (1988) and references therein for a discussion of non-homogeneous nucleosynthesis).

1.3.3 Theoretical Prejudices

Theoretical prejudice has provided support and impetus for much of the observational work on dark matter. Regarding galaxy halos, the fundamental example is the work on disk stability. Numerical simulations have shown that thin disks of stars, like those in spiral galaxies, are strongly unstable to the formation of central bars (Hohl 1971; Ostriker and Peebles 1973). However, only about one-third of galaxies in the revised Shapley-Ames catalog (Sandage and Tammann 1981) are classified as barred. As a solution to this apparent discrepancy, Ostriker and Peebles (1973) proposed that disks are embedded in a dynamically hotter system, possibly a large dark matter halo, which inhibits bar formation. However, Sellwood (1982) has argued that large halos are not required to maintain a stable disk, and so this argument, originally a popular one in favor of large halos, has been weakened.

Halos have also been invoked to produce and maintain warps in the outer regions of galactic H I disks. Many galaxies, such as M33 (Rogstad, Wright, and Lockhart 1976) and M101 (Bosma, Goss, and Allen 1981), have large warps in the outer disks. It is theorized that the disk and the postulated aspherical halo have misaligned symmetry axes (see Toomre (1983) for a review of the topic). The halo potential dominates at large radii and forces the disk material to collapse onto one of its preferred planes, which differs from that defined by the inner disk. There are some problems with this model, especially concerning generation and maintenance of the warps. However, it has been successful at reproducing morphology (cf. Fig. 12 of Sparke and Casertano 1988).

The formation of large galactic halos is an active area of investigation. Many have investigated whether nearly isothermal halos should be expected (*e.g.*, Lynden-Bell 1967; Gott 1973; Gunn and Gott 1972; Blumenthal *et al.* 1986; Frenk *et al.* 1988). These studies have involved analytic calculations of violent relaxation

(Lynden-Bell), N-body simulations of collapsing spherical “top-hat” fluctuations (Gott), analytic solutions of the slow accumulation of material in a secondary infall process onto a small perturbation (Gunn and Gott), simulations of the combination of infalling dissipational and dissipationless material (Blumenthal *et al.*), and simulations of the growth of halos in an Einstein-de Sitter universe dominated by cold dark matter (Frenk *et al.*). These are only a few of the studies of the process of halo formation. The resulting halo density profiles range from $\propto r^{-2}$, for violent relaxation, to $\propto r^{-3.5}$, for Gott’s collapsing “top-hat”. Therefore, nearly-isothermal halos are within the expected range. These results further support the concept of large halos.

Most models of galaxy formation and dynamics include a dark matter component. However, there are almost no observational constraints on the extent or mass of the dark matter component. It is fundamental that observations provide the critical input for future theoretical work. We believe that satellite galaxies are the best currently available observational probe of galactic halos.

1.4 Satellite Galaxies

1.4.1 Observational Studies of Satellite Galaxies

Satellite galaxies are common in the local universe. The two largest satellites of our galaxy are beautiful naked eye objects in the southern sky. The Small and Large Magellanic clouds are well studied and provide data on topics from stellar to galactic evolution. There are at least 8 other companions to our galaxy: Carina, Draco, Fornax, Leo I, Leo II, Sculptor, Sextans, and Ursa Minor. M31, the other principal galaxy in the Local Group, has at least seven companions: M32, M33, NGC 147, NGC 185, NGC 205, And I, And II and And III. Other nearby galaxies

also have known companions, for example M51 has NGC 5194, and M101 has NGC 5474 and NGC 5477.

By counting the number of galaxies within annuli around a primary galaxy and correcting for background contamination by counting galaxies at much larger projected distances, Holmberg (1969) first estimated the number of companions per spiral galaxy. He concluded that down to his absolute magnitude limit, estimated to be about -10.6 , field spirals have a few companions (1 to 5). A similar study by Bothun and Sullivan (1977) concluded that the typical elliptical galaxy has no companions. Lorrimer *et al.* (1991), using APM-scanned UK Schmidt plates, concluded that there are between 1 and 2 satellites down to $M_B = -16.5$ within 375 kpc of the typical late-type galaxy. Therefore, although one advantage of using satellite galaxies is that primaries with multiple companions can be studied (since satellites are test particles they presumably do not interfere with each other), we expect to find typically only 1 to 2 satellites per primary.

1.4.2 Theoretical Studies of Satellite Galaxies

Satellite galaxies will interact with the primary since they are not perfect test particles. If large halos exist, massive satellites moving through the halo will produce a trailing wake of material. This material will pull back on the satellite, which will cause the satellite orbit to decay. This phenomenon, known as dynamical friction, has been quantitatively described for a particle moving through a uniform medium by Chandrasekhar (1943). While his particular formulation is strictly not applicable to the orbit of a satellite in a spherical self-gravitating halo, the estimated decay time is in good agreement with results from numerical simulations, and can be less than a Hubble time (cf. White (1983), Bontekoe and van Albada (1987), Zaritsky and White (1988), and Weinberg (1989) for a lively discussion of dynamical friction in

self-gravitating spherical systems.). Tremaine (1976) estimated that the Milky Way could accrete companions about the size of the LMC in a few $\times 10^9$ yrs. Ostriker and Turner (1979) concluded that the distribution of separations of binary galaxies in the T76 sample was affected by dynamical friction (see White and Valdes (1980) for an alternative interpretation). Dynamical friction may be an important factor in the observed dynamics of satellite galaxies and the structure of the primary. For example, if the orbits of satellites residing within massive halos decay rapidly, and if upon merging the satellites significantly disturb the morphology of the primary, then a sample of primaries selected on the basis of its morphological appearance (*i.e.*, selecting late-type spirals) may be biased toward galaxies with small halos.

The effect of satellites on the disk component has also been explored. Hernquist and Quinn (1989) demonstrated that satellites can generate warps in the outer disk. Details of the interaction between satellites and disks have also been examined by Quinn and Goodman (1986). They determined the efficiency of dynamical decay for satellites on prograde and retrograde orbits and attempted to explain the origin of the Holmberg effect⁵.

The interaction between a companion and the disk and halo of the primary complicates the interpretation from a dynamical analysis. Because the magnitude of the interaction between the two galaxies scales with companion mass, it is best to observe low-mass companions. On the other hand, massive companions are more luminous and more easily observed; hence there is always a compromise. Because our sample includes relatively massive companions, up to $\sim 1/10$ th of the primary mass (if M/L is the same for primaries and companions), the interaction cannot be completely ignored. However, our adopted minimum magnitude difference criterion (*i.e.*, the difference in magnitudes between the primary and satellite galaxies) is

⁵This is the unconfirmed observational result that satellites preferentially lie near the minor axis of the primary (*i.e.*, out of the disk plane) (Holmberg 1969).

the most stringent ever used in a study of this kind. We will argue (cf. §4.3.5) that the effect of dynamical interactions, including dynamical friction, is minimal. The sample of satellites may provide constraints on the efficiency of the theorized processes described above.

1.5 Summary

28 The topic of dark matter in the Solar neighborhood, in galactic halos, in galaxy clusters, and in the Universe as a whole, has spawned a tremendous amount of work in the past twenty years. This dissertation focuses on the distribution of mass in the halos of late-type spiral galaxies. In this chapter, we presented an introduction to the most common investigative techniques: the study of rotation curves and of binary galaxies. We also discussed briefly some advantages of an analysis of a large, well-defined sample of satellite galaxies. In Chapter 2, we describe our work using the satellites of our galaxy and the small galaxies in the Local Group to determine the mass of our galaxy. In Chapter 3, we detail the collection of a large well-defined sample of satellite galaxies and examine the characteristics of the sample. In Chapter 4, we develop an analysis designed specifically for satellites at large galactocentric distances, which we use to model satellite dynamics. We also present our interpretation of the data regarding the mass distribution in galactic halos. In Chapter 5, we summarize our results and outline possible future directions for research.

Chapter 2

The Mass of the Galaxy

2.1 Introduction

The remote satellites of our galaxy provide an invaluable tool for measuring the mass and extent of the dark matter halo¹. Previous studies by Hartwick and Sargent (1978), Lynden-Bell, Cannon, and Godwin (1983, hereafter LCG), Peterson (1985), Olszewski, Peterson, and Aaronson (1986, hereafter OPA), Little and Tremaine (1987, hereafter LT), and Peterson and Latham (1989, hereafter PL) presented radial velocity measurements for some of the most distant satellites, either globular clusters or dwarf spheroidal galaxies, and also presented a variety of analysis techniques with which to estimate the mass of the Galaxy. The latest substantial increase to the database was presented by OPA who concluded that the mass of the Galaxy, M_G , is $(5 \pm 2) \times 10^{11} M_\odot$, if the velocities of the satellites are distributed isotropically. LT developed a more sophisticated mathematical treatment of the problem based on a statistical analysis technique that enabled them to quantify the uncertainties in the mass determination. Using the data presented by OPA, they concluded that $M_G = 2.4_{-0.7}^{+1.3} \times 10^{11} M_\odot$ ² for isotropically distributed satellite

¹A large portion of this chapter has been published elsewhere and is included for completeness (Zaritsky *et al.* 1989). Material in §2.4 is new and the statistical analysis presented in §2.3.1 has been redone with the inclusion of the newly discovered dSph, Sextans (Irwin *et al.* 1990).

²Except in this case for which the quoted error represents the 60% confidence limits as given by LT, all quoted errors on statistically determined mass estimates represent the 90% confidence

velocities. LT excluded some satellites from their preferred sample because of uncertainties in the measured velocities; however, the results from these studies are in agreement despite this exclusion. Uncertainties in the measured velocities were large for some of the remote systems, in particular Eridanus, Pal 14, Leo I, and Leo II. Since the farthest systems place the most stringent constraints, velocities for Leo I and Leo II, the two most distant known satellites, are possibly critical in estimating the mass of the Galaxy and the properties of the halo.

We present observations of red giant stars in Eridanus and Pal 14, and of carbon stars in Leo I and Leo II. The observations are described in §2.2. Our result for the mass of the Galaxy is presented in §2.3.

2.2 Observations

The data were taken at the Multiple Mirror Telescope (MMT), with the MMT spectrograph using either the 600 line mm^{-1} grating in second order, which we shall refer to as the low resolution mode, or the Echellette grating in 11th order (with an order-blocking filter), which we shall refer to as the high resolution mode, and the dual-channel intensified Reticon detector, which records spectra from two $2.5''$ apertures separated by $36''$ on the sky. The spectral coverage in the low resolution mode was approximately from 4700 Å to 6000 Å with a resolution of 1.3 Å. The spectral coverage in the high resolution mode was approximately from 5200 Å to 5600 Å, for the central portion of the order, with a resolution of 0.6 Å. The data are from observing runs during 1986 January, February, March, and September, and 1988 January and March, predominantly in the low resolution mode. The Pal 14 data, which are from 1988 March, were reduced independently in the manner described by Peterson and Foltz (1986).

limits.

Observing techniques varied slightly from run to run. Beam-switching, alternately observing the object through the right and then the left channel in subsequent exposures, was used only in the 1986 January and 1988 January runs. Typical exposure times for program objects were 900 seconds with no beam switching and 450 seconds per channel when beam switching was used. Comparison lamp, and etalon spectra for the low resolution observations, were taken before and after each object exposure, or pair of exposures when beam-switching was used, during all the runs. Several exposures were eventually combined to produce the final object spectra.

The data were reduced using NOAO IRAF³ Version 2.7 on a Sun 4 computer at Steward Observatory. The spectra were flat-fielded by dividing them by a spectrum of an incandescent lamp, observed through the corresponding channel, from which the continuum component had been removed. This procedure removed pixel-to-pixel sensitivity variations in the Reticon detectors. We note that the data from each channel were independently reduced and combined with the data from the other channel only after the wavelength calibration was complete.

For accurate wavelength calibration, a large number of strong lines distributed through the entire spectral range is essential. In the low resolution mode none of the three comparison lamps available for wavelength calibration, HgCd, FeNe and HeAr, have a sufficient number of lines of adequate brightness in the central region of the spectral range, 5100 Å to 5800 Å; therefore, wavelength calibration with comparison lamps is untrustworthy in that region. The lamps do have useful lines outside this area (see Figure 2.1). This fact, and the fact that we wished to measure velocities of C stars by using spectra in the region of the $\lambda 5363$ C₂ Swan band, motivated the use of the etalon for wavelength calibration.

³IRAF is distributed by the National Optical Observatory, which is operated by AURA, Inc., under contract to the NSF.

The etalon is simply a Fabry-Perot interferometer for which the gap distance is not tunable. It consists of two parallel partially transmitting mirrors separated by an air gap and illuminated by collimated white light. Light with wavelengths commensurate with the interplate spacing will interfere and produce the pattern seen in the spectrum of transmitted light shown in Figure 2.1 (for more detail about etalons see Hernandez (1986) and for more detail about the MMT etalon in particular see Foltz, *et al.* (1985)). Zaritsky *et al.* (1989) present more details on the etalon wavelength calibration technique.

The high resolution data were calibrated with the available calibration lamps. However, we had to limit ourselves to the spectral region between 5400 Å and 5600 Å because this was the only region with enough strong lines for precise wavelength calibration. This mode was used for observations of red giant stars. The wavelength solution used consisted of a medium order (~ 6) Chebyshev polynomial that was fit to approximately 15 lines and had an associated *rms* error of ≈ 0.05 Å.

Velocities were measured using a cross-correlation program based on the algorithm described by Tonry and Davis (1979). M3 AA was used as the velocity template for the high resolution data. Both HD77234 and HD76846 were used as carbon star velocity templates. The template that produced the larger correlation peak for a given program carbon star was used for that object. The spectrum of the star NGC 1904-300 was used as the giant star velocity template for the low resolution giant star spectra. The results from this analysis are presented in Tables 2.1 and 2.2 (Table 2.1 also contains references to the names of the standard stars and to their velocities). Velocities were only accepted if the correlation peak was at least 2.5 times stronger than the largest noise peak.

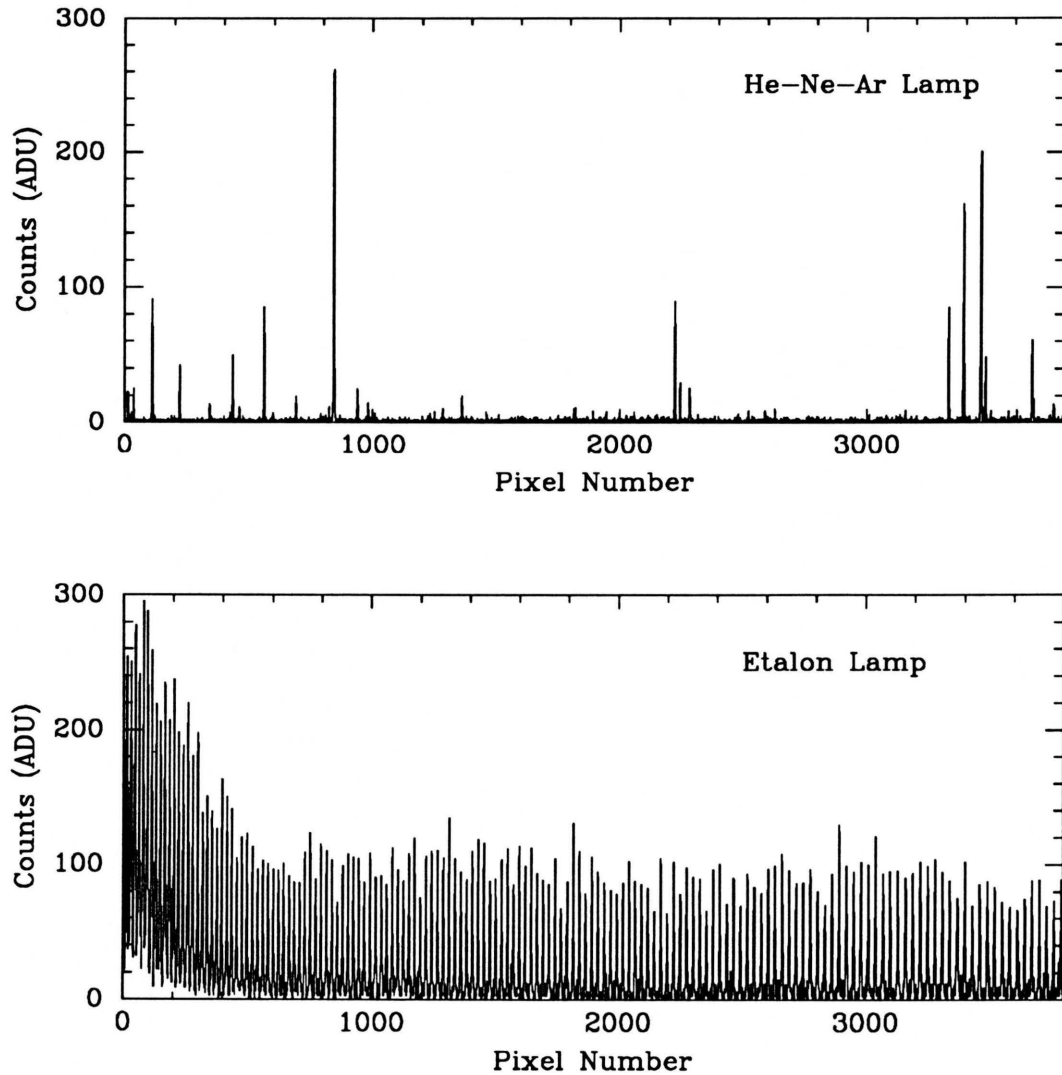


Figure 2.1: *Comparison of He-Ne-Ar and Etalon Calibration Spectra: The upper panel is the spectrum of the combination of HeAr, FeNe, and HgCd lamps from a 120 s exposure. Line centering is only sufficiently precise for lines with more than ~ 20 counts. The majority of lines seen in the central portion of the spectrum are third-order lines that have leaked through the filter. There are roughly 20 usable lines in this spectrum. The lower panel is the spectrum of the transmitted light through the etalon from a 60 s exposure. There are roughly 140 usable lines in this spectrum.*

Table 2.1: Measured Heliocentric Velocities for Standard Stars

Low Resolution Mode			High Resolution Mode		
Object	v Obs.	Std. v	Object	v Obs.	Std. v
	(km s^{-1})	(km s^{-1})		(km s^{-1})	(km s^{-1})
HD 156074 ^a	-20	-12.5	HD 112299 ^b	4	3.8
HD 30443 ^a	65	68	M 3 AA ^c	-148	-148
HD 32963 ^b	-56	-63	M 5 IV 34 ^d	56	51.0
HD 76846 ^a	19,31	24.6	M 15 K825 ^d	-104	-96
	31,26				
HD 77234 ^a	10,7	7.3	M 67 F170 ^e	35	34.3
	14,8				
M 3 AA ^c	-151	-148	M 67 S 995 ^e	31	33.3
NGC 1904-241 ^d	224	209	NGC 288-20C ^d	-47,-51	-48
NGC 1904-300 ^c	200	211	NGC 1904-15 ^d	207,206	207
				208,196	
NGC 288-20C ^d	-52	-48	NGC 1904-241 ^d	210,211	209
				210,204	
			NGC 1904-300 ^d	212,212	211
				210	
			NGC 4147 II 30 ^d	182	183.5
			NGC 4388 ^b	-30	-28
			NGC 5053 E ^f	40	43.4
			NGC 5053 L ^f	44	43.7
			NGC 5053 - 72 ^f	37	43.3
			NGC 6366 II 70 ^g	-119	-122.6
			NGC 6366 III 8 ^g	-120	-122
			NGC 6366 III 55 ^{g,h}	-118	-119.5
					-122.4

^a Carbon star; Velocities are from private communication from R. McClure to M. Aaronson several years ago, and from numerous measurements by E. Olszewski and M. Aaronson using the MMT echelle.

^b F-K stars; velocities quoted are from Transactions of the IAU, vol. 15A, p. 409, 1973, and from numerous measurements by E. Olszewski and M. Aaronson using the MMT echelle.

^c M 3 AA = VZ 238; velocities from Pryor, Latham, and Hazen (1988) and a similar number of measurements by M. Aaronson and E. Olszewski using the MMT echelle.

^d See Table I in Peterson, Olszewski, and Aaronson (1986) for velocities and star identifications; E. Olszewski has also made follow-up measurements of the velocities of these stars using the MMT echelle.

^e Velocities from Mathieu *et al.* 1986.

^f Velocities are from multiple unpublished MMT echelle measurements by E. Olszewski, C. Pryor, and R. Schommer. Star identifications from Sandage, Katem, and Johnson (1977).

^g Velocities from single MMT echelle measurements by E. Olszewski. Star identifications from Pike (1976).

^h Da Costa and Seitzer (1989).

Observational uncertainties were estimated from our measurements of standard star velocities (cf. Table 2.1) and from multiple observations of program objects. The velocities obtained from the low resolution mode standard star spectra indicate that the standard deviation of a single measurement in this mode is 7 km s⁻¹; therefore, we were able to maintain uncertainties below 1/10th of a resolution element using the etalon wavelength calibration technique. Although the standard star spectra have a much larger signal-to-noise ratio than the program objects, the uncertainties in the derived velocities for the program objects do not appear to be much larger. The standard deviation among the velocities for stars with multiple measurements is 8 km s⁻¹, which is in acceptable agreement with the uncertainty derived from observations of standard stars. We stress that this measurement includes any internal velocity dispersion in these systems; however, we adopted 8 km s⁻¹ as the single measurement velocity uncertainty. We feel that with greater S/N in the etalon exposures, with spline fitting routines that are optimized for the etalon wavelength calibration technique, and with shorter object exposures (flexure during the exposure is not negligible for the longer exposures) wavelength calibration could

be further improved. The velocities obtained from the high resolution standard star spectra indicate that the velocity errors for stars in this data set is 4 km s^{-1} . This is again approximately equivalent to 1/10th of a resolution element. For the observation of Pal 14 HS 54, which has lower S/N, the velocity uncertainty increases to 6 km s^{-1} .

2.3 Results and Discussion

In Table 2.2 we present our measurements of the heliocentric velocities of stars in Leo I, Leo II, Eridanus, and Pal 14. The systemic velocity of a particular system is the average of the observed velocities of stars in that system and the associated uncertainty is the standard deviation of the mean. The systemic velocity of Pal 14, $72 \pm 4 \text{ km s}^{-1}$ is a weighted average of the velocity for the star we observed, HS 54, and the velocity presented by OPA for HS 24, $73 \pm 4 \text{ km s}^{-1}$. Our measurement of the systemic velocity of Leo II is based on five stars, $70 \pm 4 \text{ km s}^{-1}$, and is in agreement with the previously published value, $95 \pm 25 \text{ km s}^{-1}$ (Suntzeff *et al.* 1986). The result for Eridanus is based on three stars, $-21 \pm 4 \text{ km s}^{-1}$, and also confirms a previously published values, $-20 \pm 5 \text{ km s}^{-1}$ (OPA). However, our result for Leo I based on six stars, $285 \pm 3 \text{ km s}^{-1}$, is in significant disagreement with the previously published value, $185 \pm 25 \text{ km s}^{-1}$ (Suntzeff *et al.* 1986). The previous Leo I observations were at roughly ten times lower resolution and therefore have random errors that are approximately ten times greater; in addition, the quoted error does not represent the possible systematic errors present in low resolution velocity work. To obtain Galactocentric velocities we converted from heliocentric velocities to local standard of rest, LSR, velocities by using a peculiar solar motion of 16.5 km s^{-1} toward $(l, b)^{\text{II}} = (53^\circ, 25^\circ)$, or in u, v, w notation $(-9, 12, 7) \text{ km s}^{-1}$ (Delhaye 1965). We then corrected for the rotation of the LSR about the center of the Galaxy using

Table 2.2: Measured Heliocentric Velocities for Program Stars^a

Leo I ^b		v_{\odot} (km s ⁻¹)
ALW 2		289(2/86),267(3/86)
ALW 5	291(1/88),289(2/86),273(3/86)	
ALW 7		288(2/86)
ALW 14	292(2/86),303(1/88)	
ALW 15		286(2/86)
ALW 20		280(3/86)
Leo II ^c		
ALW 1		59(1/86)
ALW 3	68(2/86),56(1/88)	
ALW 4		73(1/86)
ALW 5		82(1/86)
ALW 6	67(2/86),78(1/88)	
Eridanus ^d and Pal 14 ^e		
Eridanus 25		-20(1/88)
Eridanus 26		-22(1/88)
Eridanus 27		-21(9/86)
Pal 14		67(3/88)

^a Date of observation follows value in parenthesis.

^b Although some of these stars in Leo I were discovered independently by E. Olszewski and M. Aaronson, since the charts by Azzopardi, Lequeux, and Westerlund (1985 and 1986) have been published we refer to them by their ALW names. Data from 600 gpm spectra.

^c For convenience we again use the numbering scheme of Azzopardi, Lequeux, and Westerlund (1985). These stars were independently confirmed by M. Aaronson and E. Olszewski as C stars from candidates supplied by R. Schommer. Data from 600 gpm spectra.

^d Identification from DaCosta (1985). Data for Eri 25 and 26 from low resolution mode and data for Eri 27 from high resolution mode.

^e Identification from Hartwick and Sargent (1978). Data from high resolution mode.

220 km s⁻¹ for the circular rotation speed at the radius of the Sun, and using for our displacement from the center of the Galaxy 6.8 kpc (Frenk and White 1982). The Galactocentric velocity and distance for all the remote systems are listed in Table 2.3. Note that Leo I's large Galactocentric radial velocity and distance make it invaluable for placing limits on the mass of the Galaxy.

2.3.1 Statistical Analysis

We begin our analysis by applying a technique developed by LT. Briefly, the technique evaluates the probability that the values of the quantity $v^2 r / G$ ($\equiv \mu$) observed for the outer satellites would have been found for a given Galactic point mass potential, $\Phi = -GM/r$. This probability is expressed as $P(\mu|M)$. The desired quantity is $P(M|\mu)$, which one evaluates by using $P(\mu|M)$ and $P(M)$, and applying Bayes's theorem. $P(\mu|M)$ is evaluated assuming either isotropic or radial orbits for the satellites and no selection effects, of either an observational or physical nature. The recommended choice for $P(M)$ when the variable in question, M , can vary from 0 to ∞ , and when no other information is available, is $P(M) \propto M^{-1}$, although a constant $P(M)$ is also a reasonable choice. As LT demonstrated, using a constant for $P(M)$ increased the derived mass by less than 25% for their sample. Since the effect for our larger sample should be smaller, since adopting $P(M) \propto M^{-1}$ is recommended, and since it produces the lower, more conservative, mass estimate, we

Table 2.3: Velocities and Distances of Remote Satellites of the Milky Way^a

Object	v_{\odot} (km s ⁻¹)	v (km s ⁻¹)	Reference	r (kpc)	Reference
Pal 15 ^b	69	148	1	36	10
LMC + SMC	245	61	2	51	11
Ursa Minor	-249	-88	3	65	12
Pal 14	72	166	4	75	13,14
Draco	-289	-95	3	75	15
Sculptor	107	74	5	79	16
Eridanus	-21	-138	4	85	17
Sextans	230	78	6	88	18,19
Carina	230	14	7	93	20
Pal 3	89	-59	8	95	21
NGC 2419	-20	-26	8	98	22
Pal 4	75	54	8	108	23
AM-1	116	-42	9	117	24
Fornax	55	-34	3	140	25
Leo II	70	16	4	220	26,27
Leo I	285	177	4	230	26,28,29

^a Velocity, v , and distance, r , are Galactocentric.

^b The distance of Pal 15 not well determined due to the possibility of galactic absorption (Seitzer and Carney 1988). To be conservative, we adopt the smaller distance for the galactic mass analysis.

REFERENCES - (1) PL. (2) Yahil, Tammann, and Sandage 1977. (3) Aaronson and Olszewski 1988. (4) This paper. (5) Armandroff and Da Costa 1986. (6) Da Costa *et al.* 1991. (7) Cook, Schechter, and Aaronson 1983. (8) OPA. (9) Suntzeff, Olszewski, and Stetson 1985. (10) Seitzer and Carney 1990. (11) Schommer, Olszewski, and Aaronson 1984. (12) Olszewski and Aaronson 1985. (13) Harris and van den Bergh 1984. (14) Da Costa, Ortolani, and Mould 1982. (15) Stetson 1979. (16) Da Costa 1984. (17) Da Costa 1985. (18) Irwin *et al.* 1990. (19) Mateo *et al.* 1991. (20) Mould and Aaronson 1983. (21) Gratton and Ortolani 1984. (12) Racine and Harris 1975. (23) Christian and Heasley 1986. (24) Aaronson, Schommer, and Olszewski 1984. (25) Buonnano *et al.* 1985. (26) Hodge 1971. (27) Demers and Harris 1983. (28) Fox and Pritchett 1987. (29) Reid and Mould 1991.

adopted $P(M) \propto M^{-1}$. LT also presented an analysis using isothermal sphere models for the Galactic halo potential, $\Phi = v_c^2 \ln(r)$. In this case, the desired probability is $P(v_c^2 | v_r^2)$, which is the probability of having a halo with circular velocity v_c , if the observed radial velocity of the satellite is v_r . Analogously to the point-mass case, we adopted $P(v_c^2) \propto v_c^{-2}$. Unfortunately, when LT did their analysis, precise and accurate velocities were not available for some of the distant satellites, including the two farthest satellites, Leo I and Leo II. The distant satellites are the most likely not to be orbiting within an extended halo and also the most likely to contain all the mass of the Galaxy interior to their orbit. We present results from analyses with radial or isotropic orbits, with a point mass or isothermal sphere Galactic mass distribution, and with the enlarged database.

The data used in the analysis are presented in Table 2.3. All the systems have Galactocentric distances greater than 50 kpc, except for Pal 15. We included Pal 15 because although the most recent determination of the distance (Seitzer and Carney 1990) places it closer than 50 kpc, it has historically been thought to be substantially more distant (*e.g.*, Webbink 1985). The value we have adopted for the distance (from Seitzer and Carney 1990) is the most conservative one in the framework of our analysis. We have added from our own observations the velocities of Eridanus, Pal 14, Leo I and Leo II to the database, and the position and velocity of Sextans from Irwin *et al.* (1990) and Da Costa *et al.* (1991) respectively. We show the results from analyses done with and without Leo I (Figure 2.2 and 2.3, and Table 2.4). Adding Pal 15 (from PL), Eridanus, Pal 14, Sextans, and Leo II to LT's preferred sample increases the mass of the Galaxy by a factor of two. Assuming isotropically distributed satellite velocities, the median result (*i.e.*, the value of M for which the probability that the mass of the Galaxy is larger than M is 50%) is $4.7 \times 10^{11} M_\odot$ [3.1×10^{11} , 8.4×10^{11}], where the values in brackets are the endpoints

Table 2.4: Results of Statistical Analysis

Sample	Mass of the Galaxy (Point Mass Model)	
	$(10^{11} M_{\odot})$	
	Radial Orbits	Isotropic Orbits
LT Preferred Sample (Sample 4) ^a	1.1 [0.8,2.0]	2.3 [1.3,5.0]
Entire Sample Excluding Leo I	2.8 [2.3,4.2]	4.7 [3.1,8.4]
Entire Sample Including Leo I	9.2 [8.1,13.0]	12.3 [9.2,19.9]

Sample	Halo Circ. Velocity (Isothermal Sphere Model)	
	(km s^{-1})	
	Radial Orbits	Isotropic Orbits
LT Preferred Sample (Sample 4) ^a	62 [45,96]	107 [77,165]
Entire Sample Excluding Leo I	89 [65,126]	153 [115, 216]
Entire Sample Including Leo I	98 [73,136]	168 [127, 233]

^a Our results for LT's preferred sample.

of the 90% confidence interval. This is to be compared with LT's preferred sample result of $2.4 \times 10^{11} M_{\odot} [1.4 \times 10^{11}, 5.2 \times 10^{11}]$. With the increase of the median mass by 95% the results now discriminate against the LT result at over the 90% confidence level. Adding Leo I to the analysis, again assuming isotropically distributed velocities, *further increases the estimated mass of the Galaxy by nearly a factor of three* to $12.3 \times 10^{11} M_{\odot} [9.2 \times 10^{11}, 19.9 \times 10^{11}]$. Including Leo I in the analysis produces a Galactic mass estimate of roughly $10^{12} M_{\odot}$ even with the assumption of radial satellite orbits (cf. Table 2.4).

The mass estimate resulting from the analysis of the sample including Leo I was previously discriminated against at the 99% confidence level. The LT probability analysis, while offering a statistically "robust" estimate of the Galactic mass and its associated confidence interval, is susceptible to some uncertainties resulting from the small sample of satellites: in particular assumptions regarding the distribution of orbital eccentricities for satellites in the sample and the form of the Galactic potential. Principally, one does not know the relationship between the parameter distribution of the known satellites and that of the adopted model family.

When the assumption of a point mass potential is replaced by that of an "isothermal" potential, the results from the analysis for sets of satellites that include and exclude Leo I *are* in agreement within the errors (cf. Table 2.4). This agreement indicates that the Galactic halo is better represented by an isothermal sphere model than a point mass model. As shown graphically in Fig. 2.4, the theoretical probability distribution from the isothermal sphere model for $\ln(v_r^2)$ is consistent with the observed data distribution. In this model the theoretical curve is independent of the assumption of isotropic or radial orbits. However, even if the model is valid and the derived characteristic velocity is correct, we cannot calculate the total Galactic mass because we do not know the extent of the halo.

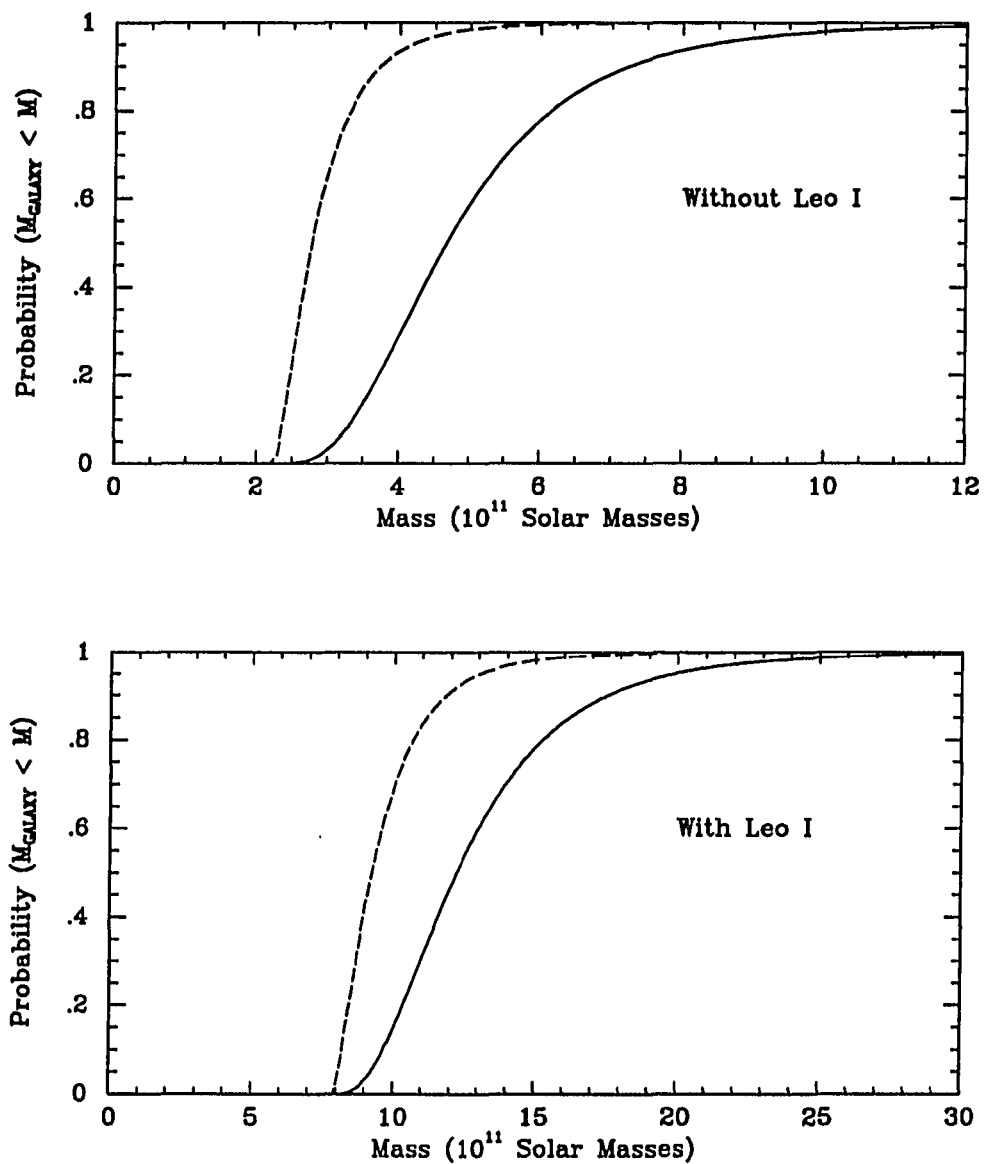


Figure 2.2: *Point Mass Model Results : The results from the statistical analysis using the satellite sample with and without Leo I. The dashed curve is from the analysis assuming radial satellite orbits and the solid line is from the analysis assuming isotropic orbits.*

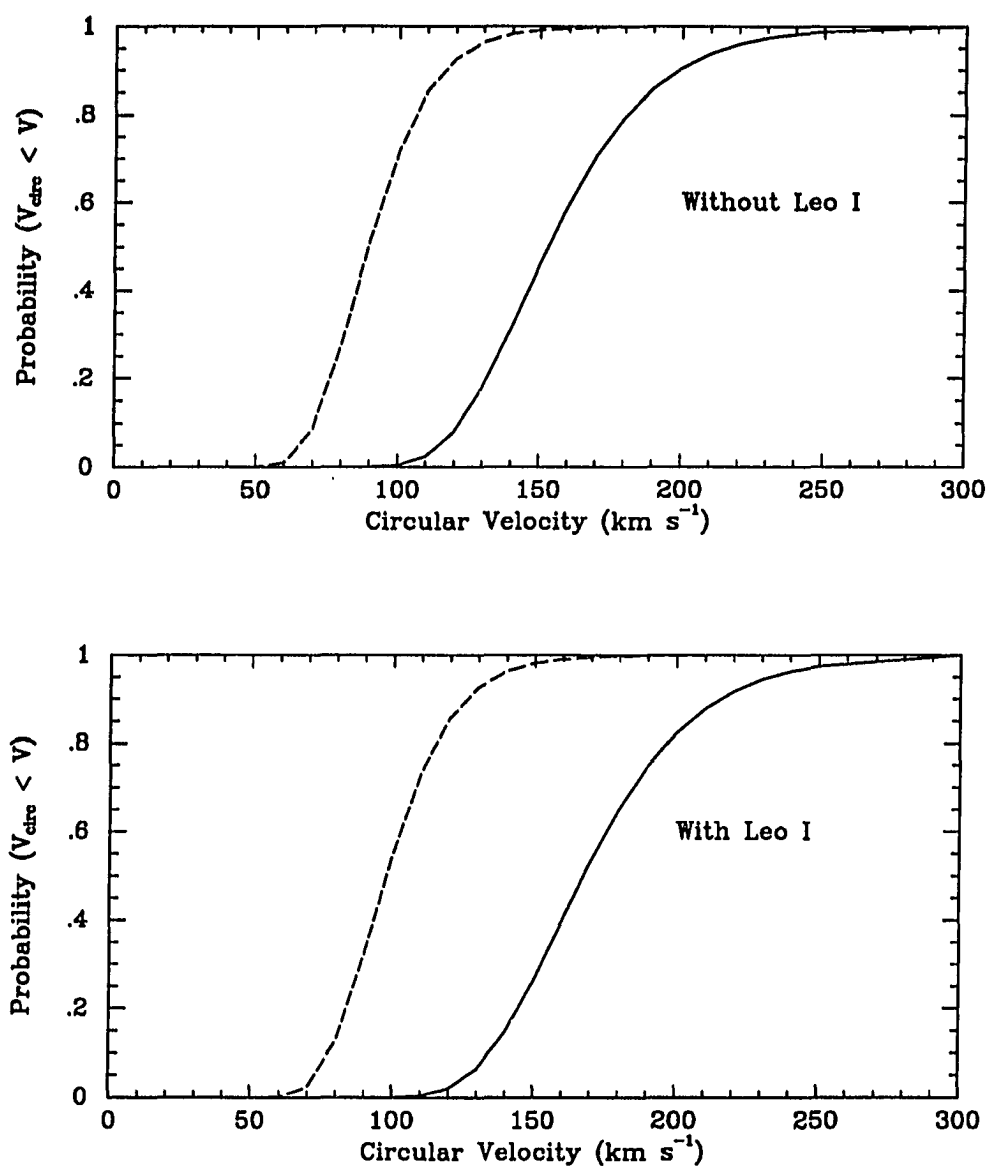


Figure 2.3: *Isothermal Sphere Model Results : The results from the statistical analysis using the satellite sample with and without Leo I. The dashed curve is from the analysis assuming radial satellite orbits and the solid line is from the analysis assuming isotropic orbits.*

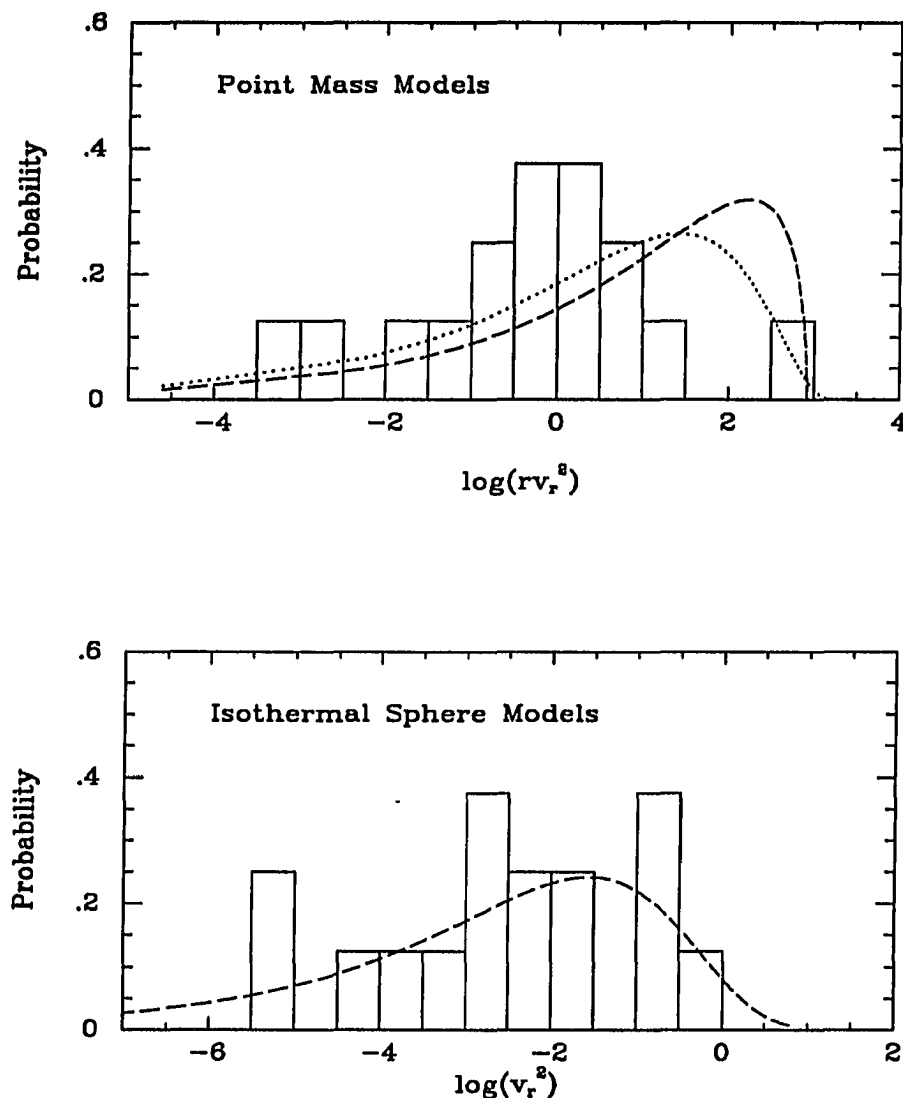


Figure 2.4: Observed vs. Theoretical Distributions : In the upper panel we show the theoretical distribution of the natural logarithm of rv_r^2 for the point mass Galactic potential models, and the observed distribution of satellites. Radial orbit models are represented by the dashed curve and isotropic orbit models by the dotted curve. The analogous comparisons for isothermal sphere Galactic potential models are shown in the lower panel. The dashed curve represents both a model with $v_c = 169 \text{ km s}^{-1}$ and isotropic satellite orbits and one with radial satellite orbits and $v_c = 90 \text{ km s}^{-1}$. Note that Leo I (the rightmost datum in both panels) is not as peculiar in the isothermal sphere models as in the point mass models.

The LT analysis, and almost all other analyses, presume that the entire satellite population can be characterized by a single type of orbit family, *e.g.*, radial or circular; however, little is known about the orbits of these remote satellites. Some argue that the outer satellites are not on circular orbits because they fail to lie in a plane (LT) and because galaxy collapse models lead to predominantly radial orbits (van Albada 1982; McGlynn 1984). However, circularization of orbits and tidal disruption are processes that could in principle decrease the mean eccentricity of the sample. Circularization of orbits by dynamical friction in the halo can be pronounced for massive satellites, *e.g.*, $M = 0.1 M_G$ (cf. Bontekoe and van Albada 1987), although presumably is only important for satellites that have completed several orbits. The effect would be proportionally less important for the less massive satellites that are considered here. LCG suggested that the eccentricity of the sample is smaller now than it was in the past because satellites on eccentric orbits pass close to the center of the Galaxy and suffer tidal disruption, thereby removing themselves from the sample. However, recent work (Allen and Richstone 1988) suggests that for objects on highly radial orbits the classical tidal radius formula significantly overestimates the effect of tidal stripping, primarily because of the relatively short time for which the satellite is near pericenter. Nevertheless, it has been shown that bulge shocking during the early history of the Galaxy could “significantly alter the observed kinematics of the surviving population” (Aguilar, Hut, and Ostriker 1988). To complicate matters further, the magnitude of the effects discussed above may depend on Galactocentric distance. Therefore, one might expect that satellites would have different orbital characteristics as a function of mean Galactocentric distance. These effects conspire to make the situation quite uncertain. Because we do not know the initial conditions of this system or the current space velocities of remote systems, the nature of the orbits of the outer satellites is not well determined.

Completeness is usually difficult to quantify. The dramatic change caused by the addition of one datum, from Leo I, to the point mass models demonstrates the inherent weakness of any statistical analysis of this small dataset. We therefore believe that the following timing arguments represent a more prudent approach to the derivation of the Milky Way's mass.

2.3.2 Timing Arguments

Leo I has an extreme velocity and distance among the satellites of our galaxy. If it is gravitationally bound to the Milky Way then it is the key object in a mass analysis because it imposes the largest lower mass limit. Assuming that Leo I 1) is bound, 2) is on a purely radial orbit, and 3) is only gravitationally influenced by the Milky Way, we recalculated, using basic timing arguments, the mass of the Galaxy. Note that because Leo I is currently receding rapidly, but is relatively nearby, we are required to assume that it has already passed at least once through the pericenter of its orbit. Because Leo I and M31 are separated by $\sim 115^\circ$ on the sky, the third assumption is approximately valid⁴. The first two assumptions produce results from timing arguments that are *conservative*. In addition, timing arguments have the advantage that generalizing assumptions concerning a set of data (*e.g.*, radial orbits for all the satellites) are not made.

⁴To justify this assertion we examined the effect of M31 on the orbit of Leo I using numerical simulations. The importance of the inclusion of M31 to the timing argument was estimated by examining one model with M31 and one without. In both of these the MW and M31 were represented by "heavy" point masses (as for model 2 in Table 2.5) and the orbits of the MW, M31, and Leo I were integrated backward in time assuming that their observed radial velocities equal their current space velocities. The model with M31 was done first and the integration was stopped when M31 reached a distance of 300 kpc from the MW. Let this time be t_1 . At this point, the halos presumably overlap and the point mass assumptions breaks down. Then we integrated the model without M31 until Leo I reached the Galactocentric distance it had at the end of the previous model. Let this time be t_2 . A comparison of t_1 and t_2 provides a measurement of the influence of M31 on the orbit of Leo I. The difference between the times was 5%. For comparison, a change of $1 \times 10^{11} M_\odot$ in the mass of the Galaxy, for models without M31, produces a 15% change in the corresponding times. The omission of M31 appears to introduce a relatively small error.

Equations that describe the orbit of a test particle emitted radially at $t = 0$ and attracted by a mass M at the origin have been derived and used to estimate the mass of the Local Group (Kahn and Woltjer 1959; Sandage 1986). The description of the test particle's orbit is given by

$$r = \frac{GM}{-2E}(1 - \cos \theta), \quad (2.1)$$

and

$$t = \frac{GM}{(-2E)^{3/2}}(\theta - \sin \theta), \quad (2.2)$$

which imply

$$v = \frac{GM}{(-2E)^{1/2}} \frac{\sin \theta}{r}, \quad (2.3)$$

where the "known" quantities are r , the present distance to the test particle, v , the radial velocity of the test particle, and t , the age of the Universe. The unknown quantities are M , the mass of the object to which the test particle is bound, E , the energy of the test particle, and θ , a parameter that describes the orbital position of the test particle. The equations can be rewritten to provide expressions for r , t , and M in terms of θ

$$r^3 = \frac{GMt^2(1 - \cos \theta)^3}{(\theta - \sin \theta)^2}, \quad (2.4)$$

$$\frac{r}{vt} = \frac{(1 - \cos \theta)^2}{\sin \theta(\theta - \sin \theta)}, \quad (2.5)$$

and

$$M = \frac{r^3(\theta - \sin \theta)^2}{t^2(1 - \cos \theta)^3}. \quad (2.6)$$

These equations can be used for the Leo I-Milky Way system and for the M31-Milky Way system. Although the latter is not a case that can be described as a test particle system, the equations above are valid if M31 and the Milky Way are bound to each other and on radial orbits. For the Leo I-Milky Way analysis M represents the mass of the Milky Way and for the M31-Milky Way analysis M represents the

total Local Group mass, *i.e.*, M31 + Milky Way. For both systems we present the solutions with the smallest value of θ , *i.e.*, the minimum number of complete orbits, which also leads to conservative mass estimates. The adopted solution for M31 and the Milky Way has the galaxies having just passed their maximum separation for the first time and falling back toward each other. On the other hand, the adopted solution for Leo I and the Milky Way has the galaxies approaching their maximum separation for the second time.

We solved the equations above to determine the range of allowed Galactic mass and the results are given in Table 2.5. In column (7) we present the mass of the Galaxy as derived from the Leo I-Milky Way timing argument. In column (8) we present the mass of the Local Group derived from the M31-Milky Way timing argument. In column (9) we present the mass of the Local Group as predicted by the Leo I-Milky Way timing argument if the mass of the Local Group is concentrated entirely in M31 and the Milky Way, if M31 and the Milky Way have the same value of M/L , and if the absolute magnitudes of M31 and the Milky Way are -21.1 and -20.5 , respectively (from van den Bergh 1980).

The models show that for the preferred parameters, *i.e.*, a distance of 710 kpc to M31 (Welch *et al.* 1986), a Galactocentric radial velocity of M31 of -118 km s^{-1} (Dean and Davies 1975), a Galactocentric distance of 230 kpc for Leo I (Hodge 1971), a Galactocentric velocity for Leo I of 177 km s^{-1} (this work) and an age of the Universe of 1.4×10^{10} years (model 2), the agreement between the mass of the Local Group predicted from the application of the timing argument to Leo I and the Milky Way, and the mass of the Local Group predicted from the application of the timing argument to M31 and the Milky Way is remarkable. In models 4 - 5 we probe the sensitivity of the results to changes in the adopted LSR velocity. Because of the geometry of the system (*i.e.*, that the angle between the Galactocentric radius

Table 2.5: Timing Argument Models

Model No.	t 10 ⁹ yrs.	v_c km s ⁻¹	r_{Leo} kpc	r_{M31} kpc	v_{LeoI} km s ⁻¹	v_{M31} km s ⁻¹	M_G 10 ¹¹ M _⊙	M_{LG} 10 ¹¹ M _⊙	M_{M31+MW} 10 ¹¹ M _⊙
	(1)	(2)	(3)	(4)	(5)	(6)	(7)	(8)	(9)
1	10	220	230	710	178	-115	15	49	41
2	14	220	230	710	178	-115	13	37	36
3	18	220	230	710	178	-115	12	30	33
4	14	200	230	710	162	-105	11	33	30
5	14	240	230	710	194	-124	15	40	41
6	14	220	230	685	178	-115	13	34	36
7	14	220	150	710	178	-115	7	37	19

vectors to Leo I and M31 is 105° when projected onto the rotation plane of the Galaxy and that Leo I is moving away while M31 is moving toward the Galaxy) changes in the adopted circular velocity increase or decrease the magnitude of both velocities and therefore affect both mass estimates in the same sense. The final models examine the dependence of the estimated mass on the adopted distance to Leo I and M31. The distance to Leo I is probably the worst determined quantity of all those required in this analysis. Model 7 demonstrates that to decrease the estimated mass of the Galaxy by a factor of two requires that the distance to Leo I be 150 kpc.⁵

We stress that mass estimates from these timing arguments are lower limits because we have excluded the tangential components of the velocities of Leo I and M31 and because we treat the galaxies as point masses. A timing argument analysis of the Local Group that does allow for a tangential component in the velocity of M31 is described by Einasto and Lynden-Bell (1982) and predictably gives somewhat larger masses than the purely radial models. They conclude that the mass of the Local Group is between 3 and $7 \times 10^{12} M_\odot$. However, the Leo I timing argument mass estimate for our galaxy is also a lower limit. Because of the uncertainties

⁵The distance to Leo I quoted in the literature is based on the assignment of an absolute magnitude to the brightest red giants, or for Fox and Pritchett (1987) on the assignment of $M_v = 0.6$ to a feature at the limit of their data that they identify as the horizontal branch. Both methods give distances greater than 200 kpc. In addition, Aaronson and Mould (1985) measured infrared magnitudes for some of the stars discussed in this chapter, as well as for others. Changing the adopted distance from 230 kpc to 150 kpc changes the distance modulus by one magnitude. As can be seen from Aaronson and Mould's (1985) Figures 3-5, a decrease of one magnitude for the bolometric magnitudes of these stars would make the abundances derived from IR photometry substantially larger than those measured by Suntzeff *et al.* (1986) from spectra of oxygen-rich giants. While an error in distance modulus of 0.5 magnitudes (which drops the distance to 180 kpc) is not out of the question (for which the timing arguments suggest a Galactic mass $\geq 9 \times 10^{11} M_\odot$ for $t_0 = 1.4 \times 10^{10}$ years), we believe that an error of 0.3 mag (which drops the distance to 200 kpc) is the largest reasonable error. Similarly, increasing the distance to Leo I makes the mass of the Galaxy even larger than proposed in this section and also makes the derived abundances from IR photometry very low. Lastly, Reid and Mould (1991) recently produced a new CM diagram of Leo I. From the luminosity of the tip of the giant branch they inferred a distance of 234 ± 16 kpc.

this presents, it is not judicious to discriminate closely between models presented in Table 2.5. The agreement between mass estimates from the Leo I and M31 timing arguments with the preferred input parameters, albeit without the inclusion of the tangential velocity components, is encouraging and removes the discrepancy between the previous mass estimates based on remote satellites (*e.g.*, OPA and LT) and Local Group timing arguments. From this analysis we conclude that $M_G = (13 \pm 2) \times 10^{11} M_\odot$ if all of our conservative assumptions are true.

By adopting $M_G = 13 \times 10^{11} M_\odot$, we can estimate the size of the Galactic halo. If the characteristic circular velocity of the halo is 170 km s^{-1} , which is approximately the result from the statistical analysis for isotropic satellite orbits and an isothermal sphere Galactic potential (cf. Table 2.4), then the halo extends to $\sim 210 \text{ kpc}$. Alternatively, if the rotation curve remains constant at the R_0 value of 220 km s^{-1} , the halo extends to about 120 kpc . These numbers are significantly larger than some previous results (*e.g.*, 50 kpc ; LT), and so we must address whether such a halo would have a dramatic effect on the satellite orbits. Because dynamical friction will have the greatest effect on the most massive satellite, the LMC is the natural choice for study. Tremaine (1976) demonstrated that if the LMC is currently at apocenter then its orbit will decay on a timescale between 2×10^9 and $4 \times 10^9 \text{ yrs}$ ⁶. The lower boundary corresponds to a halo with $v_c = 200 \text{ km s}^{-1}$ and a size of 30 kpc and the upper boundary to a halo with $v_c = 250 \text{ km s}^{-1}$ and a size of 200 kpc . The effect on the orbit is similar whether there is a relatively small or large halo, and provides no discriminatory power between these two halo models. In addition, since we do not know the radius at which any satellite originated, it is doubly difficult to infer the mass profile of the halo from current satellite positions and velocities.

⁶The orbit is currently believed to be much larger than that adopted by Tremaine (cf. Murai and Fujimoto (1980) or Mathewson *et al.* (1987) for current models of LMC-SMC orbits). Therefore, the decay time is significantly larger.

The effect on the more distant and less massive satellites is certainly significantly less than that derived by Tremaine for the LMC.

2.3.3 An Unbound Leo I ?

The above analysis is invalid if Leo I is not gravitationally bound to the Milky Way. If Leo I is unbound, then it probably has a place of origin other than the Milky Way, because at the observed velocity it would have traveled far beyond its current position in a Hubble time. The possible exception is that it was recently ejected from the Milky Way's system of satellites through a multibody encounter. However, none of the other satellites seems massive enough to have produced such an ejection. Another possible "birthplace" for Leo I is the M31 system. To examine this possibility, we have searched for orbits that would take Leo I near M31 when evolved backward in time.

If Leo I is unbound to the Milky Way, then from the remainder of the sample we infer that our galaxy's mass is approximately $4 \times 10^{11} M_{\odot}$. If M31 is roughly twice as massive as the Milky Way then its mass is approximately $8 \times 10^{11} M_{\odot}$. In order to avoid conflict between these masses and the Local Group (LG) mass inferred from the M31-Milky Way timing argument, one must postulate that the LG has a dark matter component (DMC) that is unassociated with either M31 or the Milky Way (MW). To model the effect of this component we assumed that it has uniform density and extends beyond M31, the MW, and Leo I. In the models, the DMC experiences expansion and contraction commensurate to that of M31 and the MW. Therefore, the enclosed mass within the positions of M31 and the MW remains constant⁷. This model neglects the perturbing influence of each of these

⁷The enclosed mass within Leo I's position does not remain constant because Leo I orbits the MW. The DMC mass enclosed by Leo I's position is calculated at each timestep using the DMC density calculated by requiring that M31 and MW reach the LG barycenter in 14 Gyr.

galaxies on the background dark matter component. The positions of the MW, with an adopted mass of $4 \times 10^{11} M_{\odot}$, and of M31, with an adopted mass of $8 \times 10^{11} M_{\odot}$, were evolved backward in time in a set of numerical simulations. The force each galaxy experiences is that due to the other galaxy plus that due to the enclosed DMC mass. For an age of the Universe of 1.4×10^{10} years, we determined that the required DMC has a mass of $7.0 \times 10^{11} M_{\odot}$ interior to the position of the MW (*i.e.*, between the MW and the LG barycenter). This defined the density of the DMC.

To study the possible orbits of an unbound Leo I in such a LG, we ran a set of numerical simulations with M31, the MW, and Leo I modeled as point masses, and the uniform DMC discussed above. Five thousand test particles were placed at Leo I's current position with randomly chosen velocities that satisfy the following conditions: the radial component as viewed from the MW is 177 km s^{-1} , and the total space velocity is less than 300 km s^{-1} . If the total space velocity exceeds 300 km s^{-1} then either the Leo I binding energy argument predicts a much larger mass for the LG than does the M31-MW-DMC timing argument, or Leo I is not bound to the LG (discussed below). The Leo I particles are influenced by the gravitational attraction of M31, of the MW, and of the uniform DMC. The particles representing Leo I, M31, and the MW are evolved backward in time for 1.1×10^{10} years by integrating Newton's equations of motion. No Leo I test particle reached within 200 kpc of M31 during the simulation; therefore, we conclude that Leo I did not originate in the M31 system.

Because we have concluded that the place of origin of Leo I could not have been the M31 system, and since we have no viable model for the recent ejection of Leo I from the MW's system of satellites, we must conclude, if we believe Leo I is unbound, that Leo I originated outside the Local Group and is coincidentally passing by us. While possible, this scenario appears improbable. We conclude that the most reasonable assumption is that Leo I is bound to the MW.

2.4 Timing Arguments for the Local Group

In §2.3, timing arguments were applied to the Leo I-MW and the M31-MW systems. The results from an analysis of the former system are sensitive to the mass of the MW, while those from an analysis of the latter system are sensitive to the combined mass of M31, the MW, and any additional mass contained interior to the orbits of M31 and the MW. While the agreement between the analysis of the two systems is reassuring, it would be valuable to have other galaxies with which to test the model.

To constrain the LG mass distribution out to a distance of ~ 1 Mpc, we examined the dynamics of the outer LG systems. The analysis is straightforward, provided there are no close encounters between galaxies before they reach the LG barycenter as their orbits are integrated backward in time. Note that because of the large distances involved none of these objects has yet completed an orbit. Restricted three-body simulations for LG dwarf galaxies were done by Mishra (1985), but the mass of the LG was determined from the two-body analysis of the M31-MW system. In some of our models, we include a dark mass component unassociated with either M31 or the MW, and used the outer LG members to constrain the mass model of the LG. As described in detail below, we judged our models on the degree of self-consistency between results for the various remote LG members. Peebles *et al.* (1989) did similar simulations. However, in an attempt to model galaxy formation, they allowed for accretion from a uniform background with density equal to the mean cosmological density onto two primordial seed masses that represented M31 and the MW. In the work by Peebles *et al.* there was no inclusion of a dark matter concentration unassociated with either M31 or the MW, and in ours there is no attempt to model the growth of structure. The DMC discussed here is similar to that discussed in the previous section.

2.4.1 The Models

The dynamics of remote LG galaxies were examined by specifying the current LG mass distribution, reflecting the observed radial velocities, and integrating the orbits backward in time. For plausible models, the members reach the LG barycenter at a time that is approximately equal to the age of the Universe.

The model LG consisted of M31, the MW, a uniform background dark matter component (DMC), and a “satellite” of interest. Candidate “satellites” were the apparently independent members of the Local Group (*i.e.*, not associated with either M31 or the MW) that have negative Galactocentric recessional velocities: IC 10, IC 1613, DDO 69 (Leo A), DDO 210 (Aquarius), DDO 216 (Pegasus), DDO 221 (WLM), and Sagittarius. Negative recessional velocities suggest that these systems have separated from the universal expansion and are bound members of the LG. Because the smallest possible space velocity is chosen for these objects (*i.e.*, we set space velocity = observed radial velocity), these objects were used to determine a lower mass limit. On the other hand, objects with positive recessional velocities could not be used to determine corresponding upper limits (*e.g.*, by assuming that they are unbound), because the tangential velocity component is unknown. The adopted distances and Galactocentric velocities of the satellites are given in Table 2.6. We opted for the smallest published distances because these decrease the estimated LG mass. The ratio between the adopted luminosities for M31 and the MW ($M = -20.5$ for the MW and $M = -21.1$ for M31; van den Bergh 1980) was assumed to determine the mass ratio (*i.e.*, we assumed equal M/L 's). The mass ratio may also be determined from the ratio of the squares of the maximum rotational velocities ($V_{MAX} \sim 225 \text{ km s}^{-1}$ for the MW (Clemens 1985) and $V_{MAX} \sim 270 \text{ km s}^{-1}$ for M31 (Rubin and Ford 1970)). The derived mass ratio is then 1.4, but we adopted the larger ratio obtained from the luminosities, 1.8, which is more

Table 2.6: Parameters of Remote Local Group Members^a

Name	r (Mpc)	l	b	v_{GAL}^b (km s ⁻¹)	v_{LG}^c (km s ⁻¹)
DDO 69 (Leo A)	1.1	196.9	52.4	-15.0	-25.4
DDO 210 (Aquarius)	1.0	34.1	-31.4	-17.6	-1.1
DDO 216 (Pegasus)	1.0	94.8	-43.5	-17.2	46.4
DDO 221 (WLM)	0.9	75.7	-73.6	-65.8	-25.8
IC 10	1.3	119.0	-3.3	-141.9	-71.5
IC 1613	0.7	129.9	-60.6	-157.1	-99.6
Sagittarius	1.1	21.1	-16.1	-2.1	-7.0

^a The galactic coordinates are from Mishra (1985) and references therein. The distances from Lynden-Bell and Lin (1977) and references therein.

^b Galactocentric velocities for LSR rotation speed of 220 km s⁻¹.

^c Includes only velocity component which is oriented toward the MW.

conservative when estimating the mass of the MW. The density of the DMC and the mass of the MW are free parameters. The adopted Galactocentric distance of M31 is 710 kpc (Welch *et al.* 1986) and its Galactocentric velocity is -118 km s⁻¹ (Dean and Davies 1975). The age of the Universe was taken to be 1.4×10^{10} years.

Because the orbits of most of the satellites were severely influenced by gravitational interactions with M31 or the MW (as determined in our test simulations), only three satellites, Leo A, Aquarius, and Sagittarius, which do not have a close encounter with either M31 or the MW before reaching the LG barycenter, were ultimately used. The remainder of the sample was not used because the analysis is ill-defined when there are close encounters between galaxies. The current space velocities of the three remote satellites are assumed to be equal to the observed

radial velocities. The code was the same as used for the Leo I simulations.

2.4.2 Discussion

Timing arguments can now be applied to systems at all relevant scales in the LG. Leo I can be used to examine the mass of the MW; M31 and the MW can be used to constrain the combined mass of the MW, M31 and the DMC between the two galaxies; and Leo A, Aquarius, and Sagittarius can be used to examine the combined mass of the MW, M31, and the DMC out to radii of ~ 1 Mpc. The results from a variety of models are presented in Table 2.7. In column (1) the model number is given. The name of the relevant satellite is in column (2). In columns (3) and (4) the assumed mass of the MW and that of the DMC interior to the satellite's current position are given. In columns (5) and (6) the times required for M31 and the satellite to reach the LG pericenter are presented. For acceptable models, these times will be approximately equal.

“Light” Galaxies

Before the work described in §2.2 and 2.3, the mass of the MW was estimated to be between 2 and $7 \times 10^{11} M_{\odot}$ (OPA; LT). We began this set of models by assuming that the mass of the MW is $4 \times 10^{11} M_{\odot}$ and that of M31 is $7.1 \times 10^{11} M_{\odot}$. If there is no additional mass in the LG, then M31, IC 1316, and IC 10 are unbound to the LG, yet have negative recessional velocities. In addition, the self-gravity of the LG cannot account for the low velocities of Aquarius, Sagittarius, and Leo A (cf. Model 1), nor does it account for the dynamics of Leo I (see earlier discussion). Therefore, this mass distribution is acceptable only if one postulates large peculiar velocities for M31, the outer systems, and Leo I. It is difficult to imagine a scenario in which all these objects have velocities that are substantially different from those produced

Table 2.7: Local Group Timing Model Results

Model No.	Satellite	M_{MW} $10^{11} M_{\odot}$	M_{DMC}^a $10^{11} M_{\odot}$	t_{M31}^b	t_{SAT}^b
1 ^c	Leo A	4.0	0.0	...	>>400
	Aquarius	4.0	0.0	...	>>400
	Sagittarius	4.0	0.0	...	>>400
2	Leo A	4.0	74	296	141
	Aquarius	4.0	74	296	141
	Sagittarius	4.0	74	296	132
3	Leo A	4.0	26	294	294
	Aquarius	4.0	13	294	294
	Sagittarius	4.0	14	294	297
4	Leo A	13.7	0.0	297	> 400
	Aquarius	13.7	0.0	297	290
	Sagittarius	13.7	0.0	297	340
5	Leo A	12.4	15.7	285	294
	Sagittarius	12.7	5.9	297	300
6	Leo A	10.1	7.9	396	402
	Sagittarius	10.7	1.3	402	402

^a Mass of DMC interior to satellite.

^b In units of 4.7×10^7 years (14 Gyr = 300).

^c The ellipsis denote unbound orbit.

by universal expansion, especially if there are no large mass concentrations in the LG.

The next model (model 2) includes a DMC that was modeled as a uniform sphere centered at the LG center-of-mass, which extends out to the farthest LG member and participates in cosmological expansion and gravitational contraction (*i.e.*, the

mass within the position of any galaxy remains constant⁸). The DMC density was chosen such that M31 and the MW reach the LG barycenter 1.4×10^{10} years in the past. This choice of DMC produces a gravitational force that causes the outer systems to reach pericenter in about half the age of the Universe⁹his model is not self-consistent when the remote systems come within the orbits of either M31 or the MW. A self-consistent solution for this model is attainable only if the remote systems have always been more distant from the Local Group barycenter than have M31 or the MW.. Because we are being conservative in our mass estimates by presuming that each satellite should just now be returning after its first apocenter passage, this model is unsatisfactory. However, if one allows for multiple pericenter passages or a truncated DMC, this model may be acceptable.

In model 3, the DMC mass interior to each LG member is chosen so that the member reaches the LG barycenter in 1.4×10^{10} years. We adopted a DMC with mass $\gtrsim 1.1 \times 10^{11} M_{\odot}$ inside the present position of M31 ($r \sim 250$ kpc), $\gtrsim 6.4 \times 10^{11} M_{\odot}$ inside the position of the MW ($r \sim 450$ kpc), and between 13 and $26 \times 10^{11} M_{\odot}$ for $r \sim 1$ Mpc. Although by using this model we can account for the dynamics of LG members, such a mass distribution is entirely *ad hoc*, does not account for the dynamics of Leo I, and requires nearly as much dark matter as do the “heavy” galaxy models.

“Heavy” Galaxies

The “heavy” galaxy models are those that have $M_G > 10^{12} M_{\odot}$. In Model 4, the mass of the MW is set at $13.7 \times 10^{11} M_{\odot}$, the mass of M31 is correspondingly $24.1 \times 10^{11} M_{\odot}$ and there is no DMC. These values are in accordance with the results from the Leo

⁸This is unambiguous because we are modeling only the initial expansion and contraction phases. The galaxies have not completed one orbit and so there have been no orbit crossings.

⁹T

I-MW and the M31-MW timing arguments (see Table 2.5). The results from model 4 indicate that there is insufficient total mass to account for the dynamics of Leo A and Sagittarius; however, the distances to these systems are uncertain. The distance to Sagittarius has been measured using several methods and appears to be accurate to within 30% (Cook 1987). The other two satellites have widely discrepant quoted distances. The discrepancies between t_{SAT} and t_{M31} can be diminished by adopting alternative satellite distances. However, to decrease the discrepancy both Leo A and Sagittarius need to have smaller distances, and we have already adopted the smallest distance estimates. The magnitude of the inferred errors is not beyond possibility; although, it is disturbing that both distances need to be decreased further. More likely, the discrepancy indicates that the mass of the LG is slightly larger than that adopted in the model.

The LG mass can be increased by either increasing the mass of M31 and the MW, or by including a DMC. If the maximum allowed distance error is 10%, which is probably not an underestimate in the direction of decreasing distance, and if the MW mass is increased until $t_{SAT} \sim 300$ (~ 14 Gyr), then $M_G \gtrsim 17.6 \times 10^{11} M_\odot$ according to the Leo A data, $M_G \gtrsim 17.3 \times 10^{11} M_\odot$ according to Sagittarius, and $M_G \gtrsim 14 \times 10^{11} M_\odot$ according to Aquarius. If $M_G = 17.6 \times 10^{11} M_\odot$, then the mass of the LG is $\sim 48 \times 10^{11} M_\odot$. In order for the M31-MW timing argument to produce a consistent mass estimate, a tangential velocity component must be added to the motions of M31 and the MW. By integrating orbits for different adopted current tangential velocity components, we found that for this model the MW has a tangential velocity component $\sim 55 \text{ km s}^{-1}$. This is in excellent agreement with the tangential velocity component derived for the MW from LG kinematics, $60 \pm 30 \text{ km s}^{-1}$ (Einasto and Lynden-Bell 1982). The result of torques generated by nearby galaxies on the LG was originally studied by Thuan and Gott (1977), but has more recently received a thorough examination by Raychadhury and Lynden-Bell (1989)

and Raychadhury (1990). They conclude that substantial angular momentum in the LG (on the order of that quoted above) is generated by torques from nearby mass concentrations. The second way to increase the LG mass is to have between 15 and $20 \times 10^{11} M_{\odot}$ of dark matter distributed uniformly out to radii of 1 Mpc (see model 5). This model does not have the same difficulties as the light-galaxies-and-massive-DMC model (models 2-3) because the DMC density is much lower, the DMC is not centrally condensed, and M31 and the MW are much more massive.

Uncertainties

Uncertainties in a variety of parameters, such as the distances, the age of the Universe, the velocities, the M31-to-MW mass ratio, the assumed orbits, and the LSR circular velocity, propagate through the calculations to the estimated masses. The effect of changing the age of the Universe is shown in model 6. Even for $t = 1.9 \times 10^{10}$ years the required masses are substantially larger than those in the light galaxy model. Errors in the velocities are $\lesssim 10 \text{ km s}^{-1}$ for these systems (cf. Table 1 in Mishra 1985) and increasing the velocity by 10 km s^{-1} decreases the mass estimate by only 10 to 20%. The uncertainty in the mass ratio contributes primarily to the determination of the MW mass, but does not substantially affect the orbits of the outer satellites since they spend most of their time far outside the orbits of M31 and the MW, and since none of the three satellites interact strongly with either galaxy. The same is true for the effect of the tangential velocity components of M31 and the MW. Changes in the circular velocity of the LSR are likely to be only $\sim 20 \text{ km s}^{-1}$ (e.g., Knapp *et al.* 1978) and would have a small effect (see Table 2.5 for the results of a 20 km s^{-1} change in the Leo I arguments). The proper combination, which includes stretching all the uncertainties to their limits in the appropriate direction, eliminates the need for “extra” mass in the “heavy” galaxy model. Because of the

large uncertainties, these models should be viewed as supporting evidence to the conclusions presented in §2.2 and 2.3; specific inferences can be drawn at one's own risk.

2.5 Conclusions

In this chapter we have done the following:

- 1) We have derived from measured velocities of three stars in Eridanus, two stars in Pal 14, six stars in Leo I, and five stars in Leo II that the heliocentric systemic velocities of these systems are -21 ± 4 , 72 ± 4 , 285 ± 3 , and 70 ± 4 km s⁻¹, respectively. The values for Leo II, Eridanus, and Pal 14 agree with some of the previously published values. The value for Leo I is in significant disagreement with the previous value.
- 2) We applied the analysis technique devised by Little and Tremaine (1987) to the enlarged data set. The large effect of Leo I on the results demonstrates how vulnerable this technique is to incompleteness, and to its assumptions about the eccentricity of orbits. Using LT's techniques we find the Galactic mass to be $M_G = 9.2^{+3.8}_{-1.1} \times 10^{11} M_\odot$ if satellite orbits are radial, and $M_G = 12.3^{+7.6}_{-3.1} \times 10^{11} M_\odot$ if they are isotropic. These numbers were derived assuming a point source Galactic mass distribution. Our formal error estimates correspond to the 90% confidence limit, but the dramatic effect of including or excluding one object, *i.e.*, Leo I, demonstrates that this is a poor characterization of the true uncertainties. However, the results are in agreement with the lower limit obtained from timing arguments. We also conclude that the isothermal sphere halo models appear to be more self-consistent than the point mass models.

- 3) We used Leo I in classical timing arguments. These bypass certain weaknesses in the statistical analysis and lead to stringent constraints on the estimated mass of the Galaxy because of the large velocity and distance of this object. In our analysis we assumed purely radial orbits and point mass distributions, both of which lead to lower limits on the mass of the Galaxy. For our preferred model parameters, we estimate that the Galaxy has a mass of at least $13 \times 10^{11} M_{\odot}$. This is in excellent agreement with results from the application of the timing argument to the orbits of M31 and the Milky Way (Kahn and Woltjer 1959, Einasto and Lynden-Bell 1982, and this chapter), from an analysis of the Magellanic Stream that suggests $M_G \geq 8 \times 10^{11} M_{\odot}$ (Lin and Lynden Bell 1982), and from binding arguments using the fastest local star, $M_G > 5 \times 10^{11} M_{\odot}$ (Carney, Latham, and Laird 1988). We conclude that $M_G = (13 \pm 2) \times 10^{11} M_{\odot}$, if Leo I has a radial orbit. If $v_c = 220 \text{ km s}^{-1}$ this implies that the halo extends to $\sim 120 \text{ kpc}$.
- 4) We argued against the possibility that Leo I is unbound to the Milky Way. Using simple models of the Local Group, which are consistent with the mass implied from the M31 - Milky Way argument, we demonstrated that Leo I could not have originated in the M31 system. We also argue against a recent ejection of Leo I from the Milky Way system, against Local Group membership if it is unbound to the Milky Way, and against the coincidental passage of Leo I through the Local Group. We concluded that the most reasonable assumption is that Leo I is bound to the Milky Way.
- 5) Based on the agreement between "heavy" galaxy models ($M_G > 10^{12} M_{\odot}$) using six different Local Group galaxies, we conclude that the hypothesis that either M31 or Leo I is an interloper in the Local Group and has a random velocity relative to the Milky Way is incorrect.

- 6) We conclude that the classic notion of the Local Group, of two galaxies that have masses of a few $\times 10^{11} M_{\odot}$, is inconsistent with the observed velocities of the satellites of our galaxy, of M31, and of Leo A, Aquarius, and Sagittarius. The “light” galaxy model ($M_G \sim \text{few} \times 10^{11} M_{\odot}$) is acceptable if one includes an additional dark matter component with a contrived radial density profile. However, these models have roughly the same total mass as the “heavy” galaxy models.
- 7) The “heavy” galaxy models are much more self-consistent than the “light” galaxy models. Using the remote Local Group members, we found marginal evidence for a slightly more massive Local Group than that inferred from the M31-Milky Way timing argument. The necessary extra mass may be located in M31 and the Milky Way, if the Milky Way has a transverse velocity of $\sim 55 \text{ km s}^{-1}$, or it may be in a DMC that would have little consequence on the dynamics of M31, the Milky Way, and Leo I. The uncertainties involved weaken the argument for “extra” mass beyond that in the two principal “heavy” galaxies.

Accurate and precise radial velocities are now available for all the known remote systems of our galaxy; therefore, future improvements in the mass determination of our galaxy will come primarily from improved knowledge of the orbits. Even with the rather crude determination of the Galactic mass presented here, it is evident that our galaxy has a large dark matter component, $\sim 10^{12} M_{\odot}$, and that the dark matter halo must extend to Galactocentric distances of $\gtrsim 100 \text{ kpc}$. More precise observations of the distance to Local Group systems and measurements of proper motions of Galactic satellites will lead to improvements in our knowledge of the Local Group mass distribution. Observations of satellite galaxies of other late-type spirals should lead to a better general understanding of galaxy halos.

Chapter 3

Spiral Galaxies and Satellite Dynamics: Data

3.1 Introduction

In the previous chapter we discussed the Galactic halo. For both confirmation and extension of that work, we now proceed to study other galaxies similar to our own. As mentioned in Chapter 1, the use of radial velocities and projected positions of companion galaxies to study galactic halos has a checkered history¹. Possible improvements to this line of work include the use of satellite galaxies, more coverage at large separations ($r_p > 100$ kpc), and improved modeling. While there have been several previous studies of satellite galaxies (*e.g.*, Einasto, *et al.* 1974; Dressler, Schechter, and Rose 1986; Erickson, Gottesman, and Hunter 1987), these studies had either no significant minimum magnitude difference criterion, scant data at large separations, or an emphasis on primaries with many apparent satellites. Magnitude differences between the primary and satellite that are greater than a couple of magnitudes are necessary to lend credence to the assumption that the satellites are test particles. Also, the lack of test particles with projected separations

¹We use the term companion to denote a nearby physically associated galaxy with a mass smaller than that of the primary. We use the term satellite to denote a companion that is significantly less massive than the primary.

greater than 100 kpc makes it difficult to use the data to discriminate between interesting halo models (cf. Chapter 1). Finally, the presence of many apparent companions around distant galaxies is likely to be the result of contamination by projected background galaxies (cf. §3.3.1). In this Chapter, we attempt to remedy the deficiencies of previous samples by compiling a new sample of satellite galaxies. A principal component of this work is the use of multiaperture spectrometers as an efficient tool for identifying satellites. We describe those observations and also follow-up observations done to obtain precise velocities (1σ errors $\leq 20 \text{ km s}^{-1}$) for all our primary and satellite galaxies. We also discuss other characteristics of the database.

3.2 The Data

3.2.1 The Selection of Primary Galaxies

Our aim is to obtain a large ensemble of satellite galaxies that can be treated as a collection of satellites of a single prototypical late-type spiral. Hence, the sample of primaries must be homogeneous. The following selection criteria for primary galaxies were adopted:

- 1) $-22 < M_B < -18$,
- 2) unbarred,
- 3) Sb to Sc,
- 4) $1000 \text{ km s}^{-1} < v_R < 7000 \text{ km s}^{-1}$, and
- 5) isolated,

where M_B is the blue absolute magnitude and v_R is the recessional velocity. The first condition was stipulated to maintain homogeneity in the sample. The magnitude range allowed is large (4 mag), but 63% of the primaries lie in a much more restricted

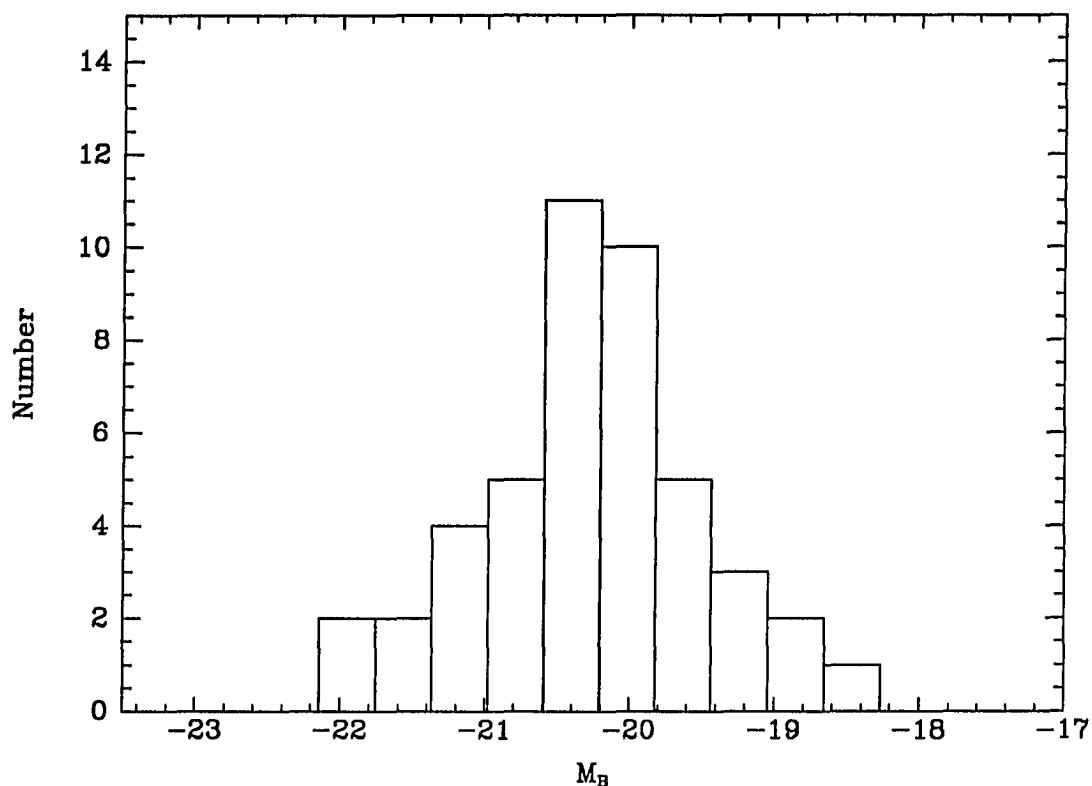


Figure 3.1: *Absolute Magnitude Histogram for Primary Galaxies with Satellites*

range, $-20.5 < M_B < -19.5$, and 77% in a slightly less restricted range, $-21 < M_B < -19$. (see Figure 3.1). From previous work (White *et al.* 1983; Charlton and Salpeter 1991) there appears to be little or no real correlation between luminosity and any other property of binary galaxy pairs; therefore, one might infer that this criterion is superfluous. However, the lack of correlations, especially between the absolute value of the radial velocity difference between primary and companion, $|\Delta v|$, and the absolute luminosity of the primary, is surprising considering that the Tully-Fisher relationship (Tully and Fisher 1977) implies a connection between the

luminosity and potential well of spirals. We must presume that at least to some degree light does trace mass (otherwise this project is futile), and so we retained the criterion. The second criterion was applied because barred spiral galaxies might have different halo properties than unbarred spirals. We examined all primaries in our sample on POSS or ESO plates, and are satisfied that none are clearly barred. While some have been classified as barred or mixed-type by other investigators, classifications often disagree between various sources. For homogeneity, we place the greatest weight on our own visual inspection. The third criterion was adopted because a relationship might exist between Hubble type and halo properties. The low-velocity cutoff in the fourth criterion was applied so that accurate redshift distances could be obtained from the recessional velocities. Peculiar velocities are estimated to be between 300 to 400 km s⁻¹ (Davis and Peebles 1983a) and should be smaller for our isolated galaxies. Distance errors produced for galaxies with recessional velocities of at least 1000 km s⁻¹ are likely to be of the same order (*i.e.*, 10-20%) as the uncertainty in the adopted Hubble constant (75 km s⁻¹Mpc⁻¹). The high-velocity cutoff is applied so that some of the satellites of the farthest galaxies are still brighter than our detection limit. At a distance corresponding to a Hubble velocity ($v_R = H_0 r$) of 7000 km s⁻¹, an observational magnitude limit of ~ 18.5 corresponds to an absolute magnitude limit of -16.4 . Because this is barely 2 mag fainter than the faintest primaries, primaries at greater distances are not included in the sample. Most of the primaries have recessional velocities between 2000 to 4000 km s⁻¹ (see Figure 3.2) and only some of the primaries (those from AAT and WHT surveys of Frenk and Smith, *priv. comm.*) have $v_R > 5000$ km s⁻¹. The criterion was also imposed so that the field-of-view of the multiobject spectrographs matched a reasonable physical scale (a few hundreds of kpc). The last criterion (No. 5), which is described below, is the most complex and probably the most important.

It is necessary to select isolated primary galaxies so that companions are influenced solely, or at least primarily, by the central galaxy. The mean density of galaxies brighter than $M_B = -18$, estimated by assuming a Schechter luminosity function,

$$\phi(L) dL = n \left(\frac{L}{L_*} \right)^\alpha \exp(-L/L_*) \frac{dL}{L_*} \quad (3.1)$$

where $L_* = 2.06 \times 10^{10} L_\odot$, $n = 6.6 \times 10^{-3} \text{ Mpc}^{-3}$ and $\alpha = -1.07$ for B magnitudes (Efsthathiou *et al.* 1988), is $1.2 \times 10^{-2} \text{ Mpc}^{-3}$. Therefore, an average primary has a “bright” (*i.e.*, $M_B < -18$) neighbor at a distance of 4.4 Mpc. Galaxies are clustered, so the true separation is lower; however, because we are constraining our primaries to be in sparse environments (*i.e.* no nearby bright neighbors), the separation should be greater than the typical separation of galaxies in groups, ~ 0.7 Mpc (Huchra and Geller 1982). Therefore, one might expect the average separation between bright galaxies in our sample to be between 1 and 2 Mpc. The average separation determines the volume around each primary that can be considered its domain. With this in mind, the adopted isolation criteria were:

- 1) that all other galaxies within 500 kpc projected separation from the primary are at least 2.2 magnitudes (a factor of 8) fainter than the primary, and
- 2) that all other galaxies within 1 Mpc projected separation from the primary are at least 0.7 magnitudes (a factor of 2) fainter than the primary.

These criteria are applied to galaxies with $|\Delta v| < 1000 \text{ km s}^{-1}$.

The Local Group can be used to judge our criteria. As discussed in Chapter 2, the Local Group is dominated by the Milky Way and M31, which are separated by 0.7 Mpc and have a magnitude difference of 0.6 mag. Therefore, the Local Group would not satisfy our criteria even at the most favorable viewing angle, and yet, at

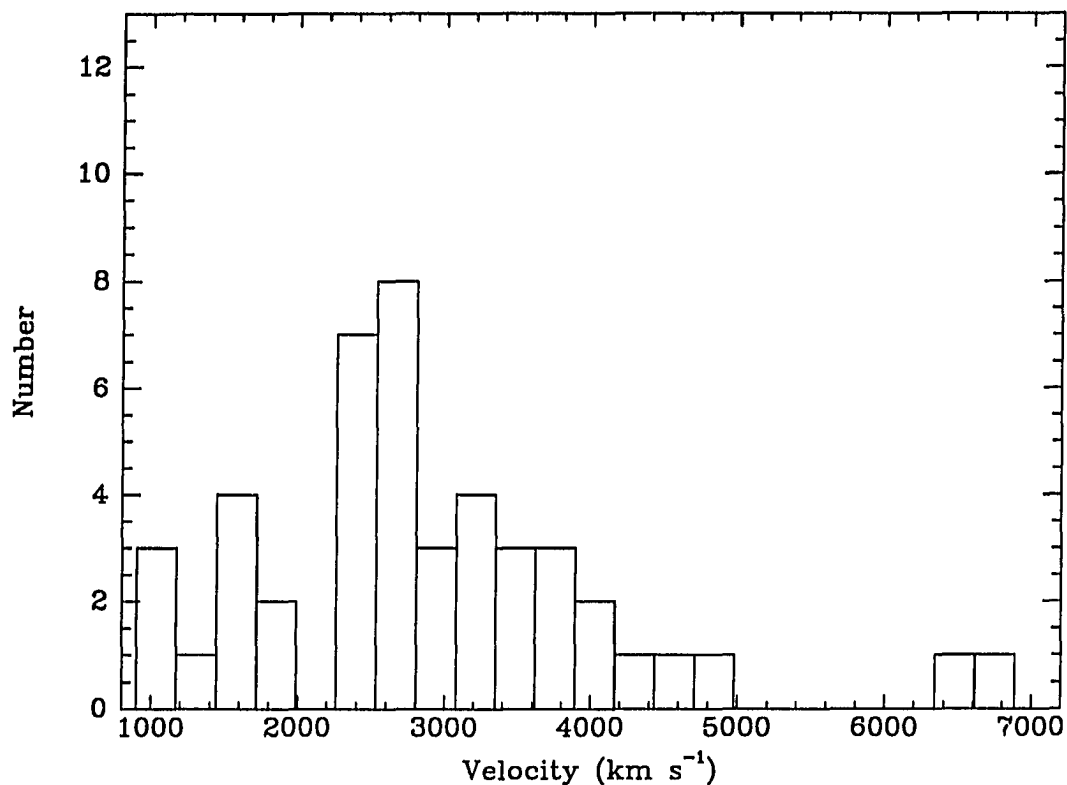


Figure 3.2: *Histogram of Recessional Velocities for Primaries with Satellites : The two objects with recessional velocities $> 5000 \text{ km s}^{-1}$ are from Frenk and Smith (priv. comm.).*

least to a distance of 200 kpc from each galaxy, the dynamics appear to be dominated by the nearer galaxy (see Leo I discussion in Chapter 2). Hence, we conclude that our criteria are conservative.

In an attempt to quantify and generalize such discussions, Schweizer (1987c), in her Eq. 2, described the fractional error produced in a mass estimate by a third nearby massive galaxy. Although the estimate is derived for point masses, it is still

useful for comparison. Considering an average satellite (projected separation = 200 kpc) and the two “worst case” scenarios, a galaxy as massive as the primary 1 Mpc away or a galaxy half as massive 500 kpc away, the induced fractional errors in the mass determinations are 0.02 and 0.1, respectively. Despite being the “worst case” scenarios (if light traces mass), neither perturbation is disturbingly large. In addition, note that a minimum projected separation of 1 Mpc generally corresponds to a much larger real separation, and that the exclusion volume in depth is much larger than in width because 1000 km s^{-1} corresponds to 13 Mpc.

We assert that primary galaxies that satisfy the isolation criteria are either isolated field galaxies or the dominant member of loose groups. In either case, they should be the principal influence on satellite galaxies, if light traces mass. Because redshift and magnitude catalogs are incomplete to the magnitude depth involved in our survey, our criteria may unknowingly be violated. In order to eliminate such uncertainties, visual inspections of every field on POSS or ESO survey plates were made. Where there was serious cause for suspecting a violation, the field was removed from consideration. In addition, several fields which satisfied the criteria, but which had nearby populous galaxy clusters were rejected.

The primaries were drawn from several sources, but primarily from Z-cat (Huchra 1987). Z-cat and the Huchtmeier-Richter catalog (hereafter HR; Huchtmeier and Richter 1989) were searched for bright galaxies that are near the candidate primaries. The fields surrounding the candidate primaries that passed this preliminary screening were inspected on POSS or ESO plates for nearby companions that might not have appeared in the catalogs. We also searched for the presence of bars and nearby galaxy clusters. We identified nearly 100 primaries that satisfied all the criteria. While this is not a complete sample, we do not believe that there are more than twice as many galaxies that would qualify as primaries. The 45 primaries

around which we identified satellites are presented in Table 3.2. Primaries for which no satellites were found are listed in Table 3.3.

3.2.2 The Search for Satellites

Selection Criteria

We now discuss the adopted definition of a satellite galaxy and the acquisition of our sample. Satellite galaxies were defined to be at least 2.2 magnitudes fainter than the primary, with projected separations, r_p , less than 500 kpc, and with $|\Delta v| < 500 \text{ km s}^{-1}$. There were no qualitative criteria (*e.g.*, morphology) applied. A natural magnitude difference cutoff is 2.5, a factor of ten in luminosity. However, because we found a few apparent satellites just slightly brighter than this limit and because there is no compelling reason to have the cutoff at 2.5 mag instead of 2.2 mag, we chose 2.2 mag. Only 14% of the satellites in our sample have magnitude differences smaller than 2.5 mag (see Figure 3.3 for the distribution of magnitude differences). Because separations between large non-interacting galaxies are ~ 1 Mpc, a natural cutoff for satellite separations is 500 kpc. Holmberg (1969), in his Figure 1, demonstrated that there are few satellites with $r_p > 400$ kpc. The multiaperture redshift surveys, which will be discussed below, typically extended out to $r_p \sim 250$ kpc and the catalog survey extended to 500 kpc. Therefore, projected separations beyond 250 kpc will be more sparsely sampled. Distances were estimated using the primary's recession velocity. The heliocentric velocities listed in Table 3.2 were corrected for Galactic rotation, assuming an LSR rotational speed of 220 km s^{-1} , and for Virgocentric infall, assuming an infall velocity of 300 km s^{-1} (a rough average from values presented by Davis and Peebles 1983b). The infall correction used was $v_C = 300(\sin \delta_i \sin \delta_V + \cos \delta_i \cos \delta_V \cos(\alpha_i - \alpha_V))$, where α_i and δ_i are the RA and Dec of the primary galaxy and α_V and δ_V are the RA and Dec of M 87

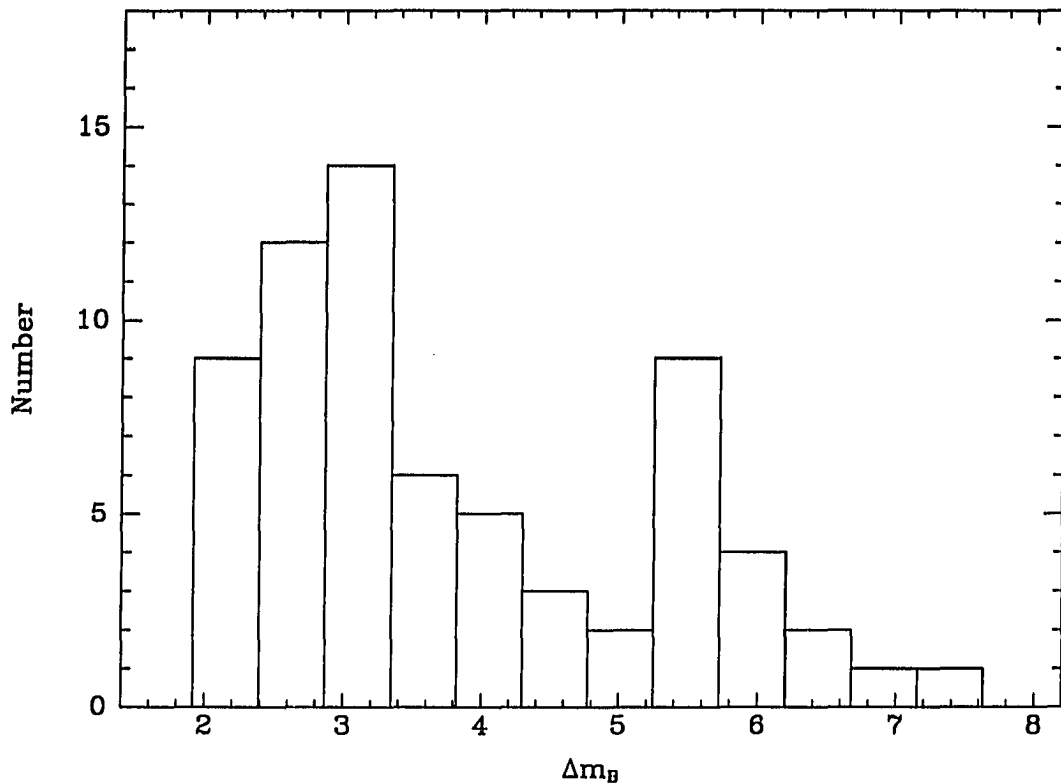


Figure 3.3: *Histogram of Magnitude Differences Between Primaries and Satellites*

(the center of the Virgo cluster). The velocity difference cutoff, 500 km s^{-1} , is a compromise between setting it too low and eliminating real companions or setting it too high and surveying such a large volume that interlopers overwhelm the sample. A lack of satellites in our sample with $300 \text{ km s}^{-1} < |\Delta v| < 500 \text{ km s}^{-1}$ at small separations, where one expects the largest $|\Delta v|$'s, would demonstrate *a posteriori* that this criterion does not disqualify many physical companions. However, the $|\Delta v|$ limit does place an upper bound on the derived mass. The mass within 50 kpc required to gravitationally bind a satellite with $|\Delta v| = 500 \text{ km s}^{-1}$ at this radius

is about $2.7 \times 10^{12} M_{\odot}$. Our estimates for the mass within 50 kpc, $M(50 \text{ kpc})$, are significantly smaller than this (see Chapter 4); therefore, we assert that this criterion will not artificially produce low mass estimates.

Candidate satellite galaxies for the multiaperture redshift survey were obtained from either APM-scanned UK Schmidt plates or from visual scans of POSS or ESO plates using a 2-axis Grant machine. In fields scanned both visually and with the APM, coordinates agree to well within one arcsec, although star-galaxy classification differed. Machine classifications had to be confirmed by visual inspection. Down to a magnitude of 18.9, which is only slightly fainter than our nominal magnitude limit of 18.5, each typical field of radius 20 arcmin contains roughly 20 galaxies (Seldner *et al.* 1977; and personal experience). Based on Holmberg's (1969) study and more recently on the work of Lorrimer *et al.* (1991), we expect about one satellite galaxy per such field to the limits of our survey. Hence the discovery rate of a satellite survey is likely to be low, and especially inefficient if a single aperture spectrograph is employed. This project has only become feasible with the development of multiobject spectrographs.

By using multiobject spectrometers, we were able to double the size of the satellite sample over that available from existing redshift surveys. However, the foundation for this work was the Z-cat and HR catalogs. Z-cat was heavily used in preliminary searches. The HR catalog data is incorporated into our database. Many positions and all H I velocities are from the HR catalog. H I velocities with quoted errors $< 20 \text{ km s}^{-1}$ and those without a quoted error, but which differ from the average of all velocity measurements by less than 60 km s^{-1} , were averaged using σ weighting. For values without quoted errors we adopted $\sigma = 30 \text{ km s}^{-1}$, which is in agreement with an empirical determination. Velocity widths are also adopted from data in the HR catalog. Velocities from the HR catalog are compared with

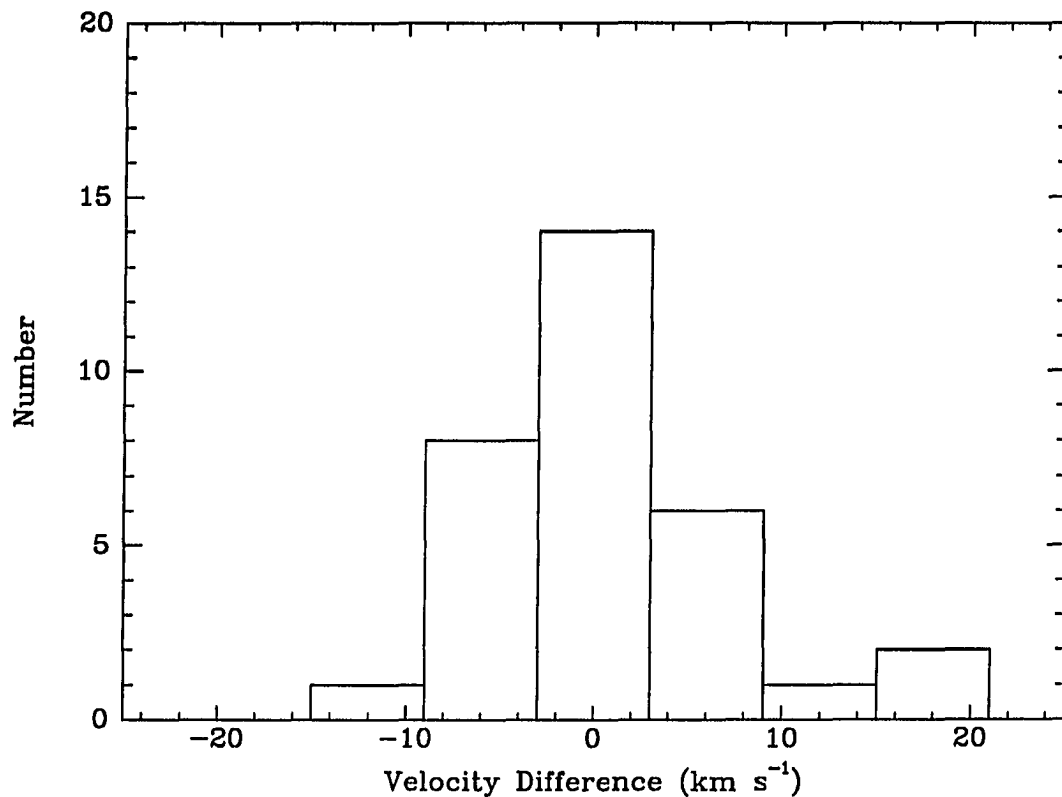


Figure 3.4: *H I Velocity Uncertainties* : This is a comparison between the *H I* velocities obtained from the HR catalog as described in the text, and *H I* velocities obtained by Tifft (priv. comm.) for galaxies in our sample. Notice that $1\sigma < 10 \text{ km s}^{-1}$.

independent values obtained by Tifft (priv. comm.) in Figure 3.4, and the excellent agreement is obvious. The uncertainties² in the *H I* velocities are clearly $< 20 \text{ km s}^{-1}$. Below we describe the multiaperture observations and additional spectroscopy undertaken to have 20 km s^{-1} precision for all velocities.

²There is the possibility of systematic errors in the *H I* velocities due to beam contamination from the primary or companion galaxy. We found only one case where this appeared to be a problem (NGC 772/NGC 770).

MX Observations

MX is a multi-object spectrometer designed and built by John Hill at Steward Observatory (Hill 1984) and used with the Steward Observatory 2.3m telescope on Kitt Peak. Optical fibers are attached to 32 mobile micro-processor-controlled probes. Each probe has a two and a four arcsec fiber plus a dedicated sky fiber. Of all the sky fibers, 28 are two arcsec fibers and 4 are four arcsec fibers. The 2 arcsec fibers are arranged in one slit and the 4 arcsec fibers are arranged in another slit. The observer can select between slits by rotating a cover plate. We used the two arcsec fibers. The probes can travel radially to the center of the 45 arcmin diameter field and azimuthally to 12.5° to either side of the center position.

A standard B & C Spectrograph with a 300 l/mm grating was used to produce spectra from 3800 Å to 6000 Å with a resolution of about 8Å. The detector was a TI CCD with readout noise of about $9e^-$. Velocity errors are $\sim 70 \text{ km s}^{-1}$, which is sufficient precision with which to identify satellites, but not sufficient for the dynamical analysis. Because this survey was used only to identify satellites, there will be no detailed discussion of uncertainties. The principal spectral features used for redshift identification were the Ca H & K lines at $\sim 4000\text{Å}$ and the emission lines H β , and [O III] $\lambda\lambda 4959, 5007$. For each field, two one-hour exposures were obtained. Because of the low surface brightness of some of our targets, the inefficiency of the spectrograph, the mismatch of the spectrograph-spectrometer system, and the blind operation of probe positioning, the survey is not complete to the expected depth, *i.e.*, 18th mag. The probe positioning improved with time because new observing techniques were implemented, but although the system improved, it did not perform entirely to expectations.

Each exposure was reduced independently using IRAF³. Bias subtraction and

³IRAF is distributed by the National Optical Observatory, which is operated by AURA, Inc., under contract to the NSF.

flat-fielding were done in the standard manner. Calibration lamp spectra taken before and after each exposure were used for wavelength calibration. The spectra were rescaled for differences in fiber throughput by using a twilight sky exposure. A master sky spectrum was composed from all the sky fiber spectra and then subtracted from each object spectrum. Cross-correlation analysis (cf. Simkin 1974; Tonry and Davis 1979) was applied to all the spectra to obtain velocities. The spectra were also visually inspected.

Out of 24 fields observed after probe pointing problems were corrected, 12 had at least one satellite. There was a total of 15 confirmed satellites. Implications for the number of satellites per primary will be discussed in §3.3.3. Because we expected ~ 24 satellites, we infer that the survey was roughly 60% complete to ~ 18 th magnitude. The ARGUS observations, discussed below, demonstrate that our expectation of 1 satellite/primary based on the work of Holmberg (1969) and Lorrimer *et al.* (1991) is at worst slightly conservative.

ARGUS Observations

ARGUS is a multiobject spectrometer at the Cerro Tololo Interamerican Observatory (see Ingerson 1987, 1988). It is placed at the prime focus of the 4-m telescope and at the time had 24 object fibers plus 24 sky fibers. Fiber diameters correspond to apertures of 1.8 arcsec. It, like MX, is based on the probe system. We used the bench mounted spectrograph with the red camera and the KPGL 3 grating, which is a 527 l/mm grating with 3.4 Å resolution and a coverage of 1860 Å. The detector for this system is a GEC CCD. The spectra were centered at roughly 5100 Å, which allows viewing of some of the principal features observed in galaxy spectra (Sandage 1978): $H\beta$, [O III], and Mg I.

Besides being on a larger telescope, ARGUS has several advantages over MX. First, the observer can interactively check the probe positioning. ARGUS is equipped

with a robot arm that carries imaging optics and a fiber bundle. This arm can be placed in front of an individual probe. A clever design (for details see Ingerson *et al.* 1991) allows the observer to use this robot arm to look at the object on the sky *and* the fiber, which is illuminated from the back end. The probe can then be moved so that the illuminated fiber, which can be distinguished from the object because the intensity of the illuminating light source oscillates, is coincident with the target object in the sky. We do not have measured magnitudes for the objects in the southern fields, but we estimate that the faintest targets have an integrated B magnitude of ~ 19.5 mag. Under the best conditions we could see about 90% of our objects through the periscope camera. For objects that we could not see on the TV, we either applied no probe shift or, if a particular shift had been necessary for many probes, a blind shift. The periscope greatly increased our success rate. Shifts comparable to the fiber size or greater were necessary for most targets. The plate solution was known to be poor, but there had been no effort to correct it in software because a new corrector had been ordered and because the periscope was available. The second significant advantage ARGUS provided was the bench-mounted spectrograph. The stability provided by this type of spectrograph allows one to spend less time on calibration and to remove cosmic rays by direct comparison of two consecutive one-hour images. The wavelength drift on the detector during a night is of order 0.01 of a pixel, primarily due to the evaporation of LN_2 in the CCD dewar which in turn causes flexure in the camera-dewar assembly (Suntzeff, priv. comm.). For any given two hour period the flexure should be less than during the entire night. Two consecutive images can be added with no noticeable degradation of the data. Emission lines are the best redshift diagnostic for these objects, consequently cosmic rays are a problem. Because flexure is minimal, emission lines appear in the same pixels in two different images, while cosmic rays are unlikely to appear in the

same pixel in two exposures. Therefore, by comparing two consecutive exposures of the same objects, we removed almost all of the cosmic ray induced defects.

The observing procedure consisted of two, 1 or 1.5 hour exposures of each field. Standard star observations were taken at the beginning, middle, and end of each night through different fibers. All exposures were bias-subtracted and flat-fielded in the standard manner. Each set of two object exposures was then combined using the cosmic ray filtering described above. The spectra were traced using a sky flat (continuum lamp observed through all the fibers) and the same trace was applied to the object exposures. Spectra were wavelength calibrated using calibration lamp exposures from that night. The 24 sky spectra in each exposure were median combined into one high S/N master sky spectrum. The master sky spectrum was scaled and subtracted from each individual object spectra. The *rms* deviations around the sky line at 5577Å in each spectra were evaluated and a new scaling and subtraction was done for each spectrum. This was continued until a minimum was found, typically in about 5-8 iterations. A truly typical sky-subtracted sky spectrum is shown in Figure 3.5. While there is some residual scatter around the 5577Å line, the remainder of the continuum is flat and equal to zero. Velocities were measured using cross-correlation techniques for absorption line systems and Gaussian line fitting for emission line systems. Nightly systematic velocity shifts were derived from observations of standard stars and were typically less than 10 km s⁻¹.

We claim that velocity errors for the ARGUS data are < 20 km s⁻¹. Velocity errors for standard stars are < 10 km s⁻¹. Independent observations of a few of the galaxies observed with ARGUS are available from the H I catalog or from MMT observations. The differences among observed velocities are consistent with 1σ errors of 20 km s⁻¹.

We observed 22 fields with ARGUS. In most we found at least one satellite, and a total of 20 satellites was identified. These numbers, given our expectation of 1

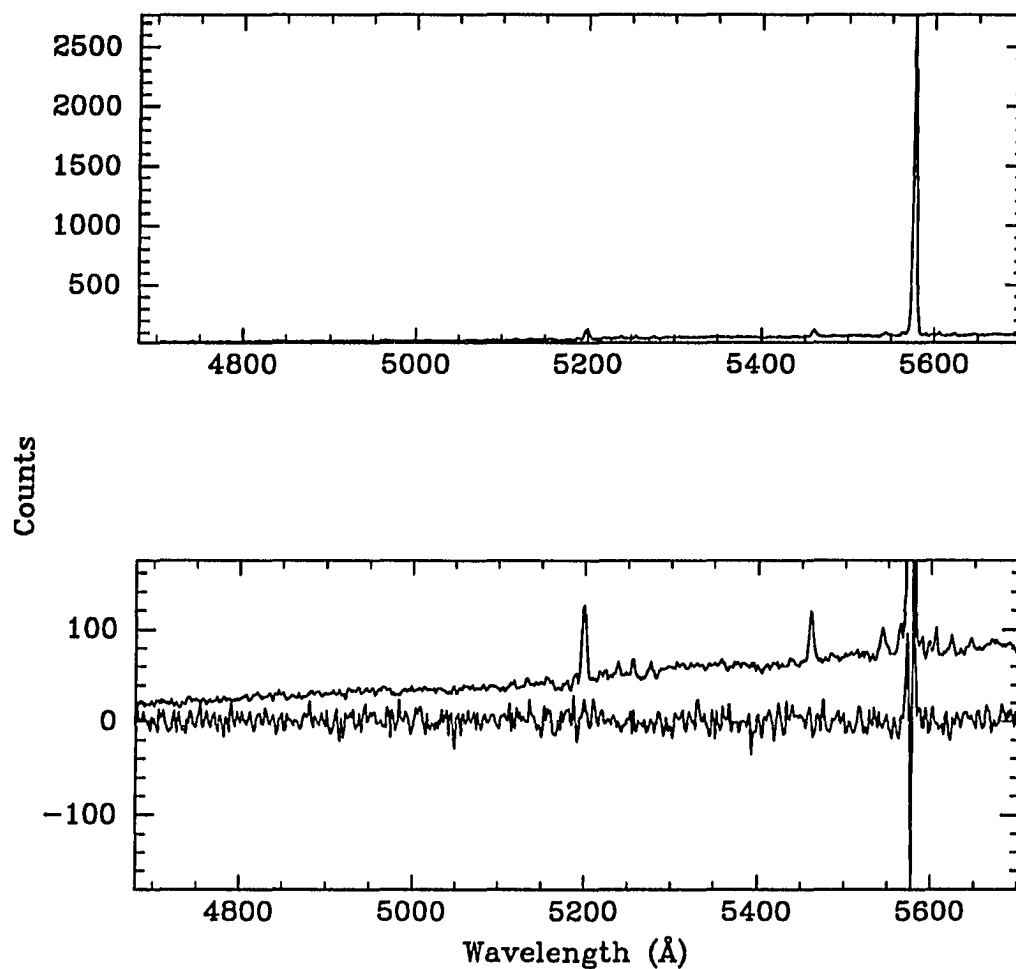


Figure 3.5: *Argus Sky Subtraction* : The top panel shows a truly typical sky spectrum taken with ARGUS. The bottom panel shows a master sky spectrum (upper spectrum) and the sky subtracted version of the spectrum shown in the upper panel. Notice that the continuum in the sky subtracted spectrum is flat, has an average of 0, and that all sky lines, except that at 5577 Å, have disappeared down to the level of the noise in the spectrum. The bottom plot is scaled vertically to the largest deviations in the sky subtracted spectrum.

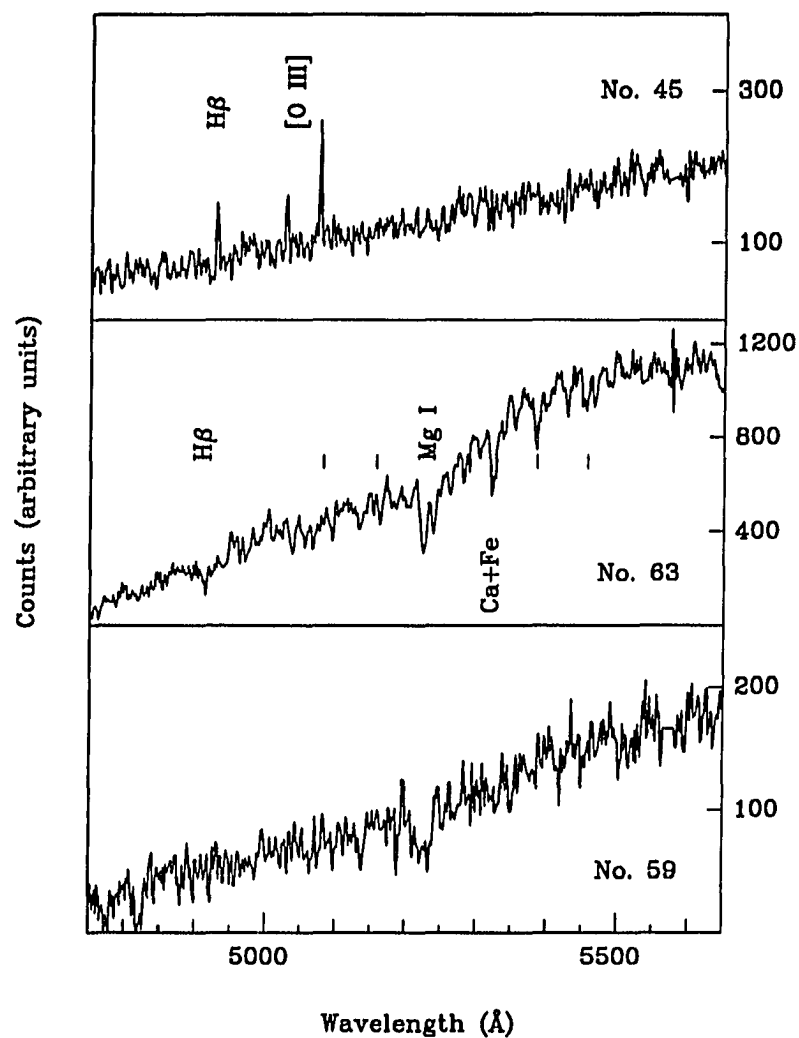


Figure 3.6: *Representative ARGUS Satellite Spectra : Spectra of 3 satellites identified with ARGUS. The identification number of each object is given in the upper or lower right hand corner. Some of the brighter lines are identified and some fainter lines are marked (identifications from Sandage 1978).*

Table 3.1: Satellites Identified With MX and ARGUS^a

Spectrometer	Emission Line Objects ^b	Absorption Line Objects ^b
MX	9,15,16,21,24,26,33,28,41,67	5,26,27,41
ARGUS	6,23,34,42,43,45,54,55,57,60,62	1,3,40,44,56,58,29,61,63

^a Refer to Table 3.2 for satellite identification numbers.

^b Some satellites have both prominent emission and absorption lines.

satellite/field, imply that the ARGUS survey was nearly 100% complete to ~ 18 th magnitude. These numbers are discussed in more detail in §3.3.3. In Figure 3.6 we show some representative satellite spectra obtained with ARGUS. The top panel has a moderate S/N spectrum of an emission line satellite (No. 45). The intermediate panel has the spectrum of a bright satellite (No. 63; $M_B = 14$), with the most prominent absorption lines identified. The bottom panel shows one of our lowest S/N spectra. Because cross-correlation utilizes the entire spectrum and because this region of the spectrum is rich in absorption lines, we were able to measure a velocity for this object (No. 59), which has $M_B = 19.8$!

In Table 3.1 we list the satellites which were identified with either MX or ARGUS. The satellites are divided into two groups based on their spectral characteristics.

Other Data

This section outlines the acquisition of supplemental data: observations using other than Steward Observatory or CTIO facilities (C. Frenk and R. Smith, priv. comm.)

or the observations of primary galaxy rotations using the Steward Observatory 90" telescope.

As described by C. Frenk and R. Smith, the observations were carried out on both the Anglo-Australian telescope (AAT) or the William Herschel telescope (WHT). The small number of satellites from these observations is due primarily to bad weather (satellites Nos. 7,22,47,48). There were two runs at the AAT. The AAT field-of-view accessible with the spectrometer has a diameter 40 arcmin. The first set of AAT observations were carried out with AUTOFIB (Automatic Fibre Positioning System) and the RGO spectrograph. AUTOFIB has 64 object fibers and 6 guide-star fiber bundles. Guide stars typically need to be brighter than 15th magnitude. In general, about 50 fibers were assigned objects and 10 were used for sky determination. A 1200 l/mm grating blazed in the blue provided a resolution of $1\text{\AA}/\text{pixel}$. The spectral region between 3580\AA and 4600\AA was observed with the Image Photon Counting System. During the second run they used the same detector system, but with FOCAP instead of AUTOFIB. FOCAP, Fibre-Optic Coupled Aperture Plate, is a plug board system. FOCAP has 50 fibers, seven which were used for sky. They switched to the FOCAP system because FOCAP uses 3 arc-sec fibers (instead of AUTOFIB's 2 arcsec fibers) and seeing was poor on the first run. The 600 l/mm grating was used which provided a $2\text{\AA}/\text{pixel}$ resolution between 3460 and 5495\AA . The WHT observations were done with a version of the FLEX spectrograph and the AUTOFIB system. The WHT AUTOFIB has 55 fibers, but is otherwise like the AAT AUTOFIB. A 632 l/mm grating blazed at V was used. The wavelength coverage was 2000\AA wide centered at 4480\AA . This setup provided a resolution of $1.73\text{\AA}/\text{pixel}$. The detector was a EEV CCD (1172×760 pixels). Satellites of NGC 1459 (AAT 1st run), NGC 3154 (WHT), and A1416 (AAT 2nd run) are from these observations. The data were reduced using FIGARO and the cross-correlation package from DUSDERS (Durham University Spectral Data Evaluation

and Reduction System). The errors are estimated from the fit to the correlation peak. These error estimates have been calibrated to standard stars prior to this work.

The direction of rotation of some of the primary disks was measured using the Steward Observatory 90" telescope and the Bollens and Chivens spectrograph. A 1200 l/mm grating was used in long-slit mode. The observations are extremely straightforward, we simply identified which side of the galaxy has the greater recessional velocity. The primaries are quite bright and short exposures, ~ 15 min, usually sufficed.

MMT Observations

The MMT Red Channel spectrograph was used for follow-up velocity measurements. Our goal was to reduce all velocity uncertainties below 20 km s^{-1} . The Red Channel has long-slit capability, with high throughput, and a CCD detector (for details see Schmidt, Weymann, and Foltz 1989). Galaxies without reliable velocities (only H I velocities with errors $< 20 \text{ km s}^{-1}$, AAT, and ARGUS velocities are deemed reliable), required follow-up observations. We also measured the sense of rotation (*i.e.*, which side is moving away from us) for many of the primary galaxies. We used a 1200 l/mm grating centered at 5100\AA , which has a coverage of 650\AA and a resolution of 2.1\AA . Standard calibration frames, biases and flat fields, were obtained at the beginning of the night. Standard star or galaxy observations were always obtained at the beginning and end of the night, and occasionally during the night. Calibration lamp spectra were obtained before and after each exposure. Object exposure times were limited to 15 min, after which the flexure of the spectrograph can become important.

The data were reduced in the standard manner. Bias correction and flat fielding were done initially. The frames were rectified using wavelength calibration lamps.

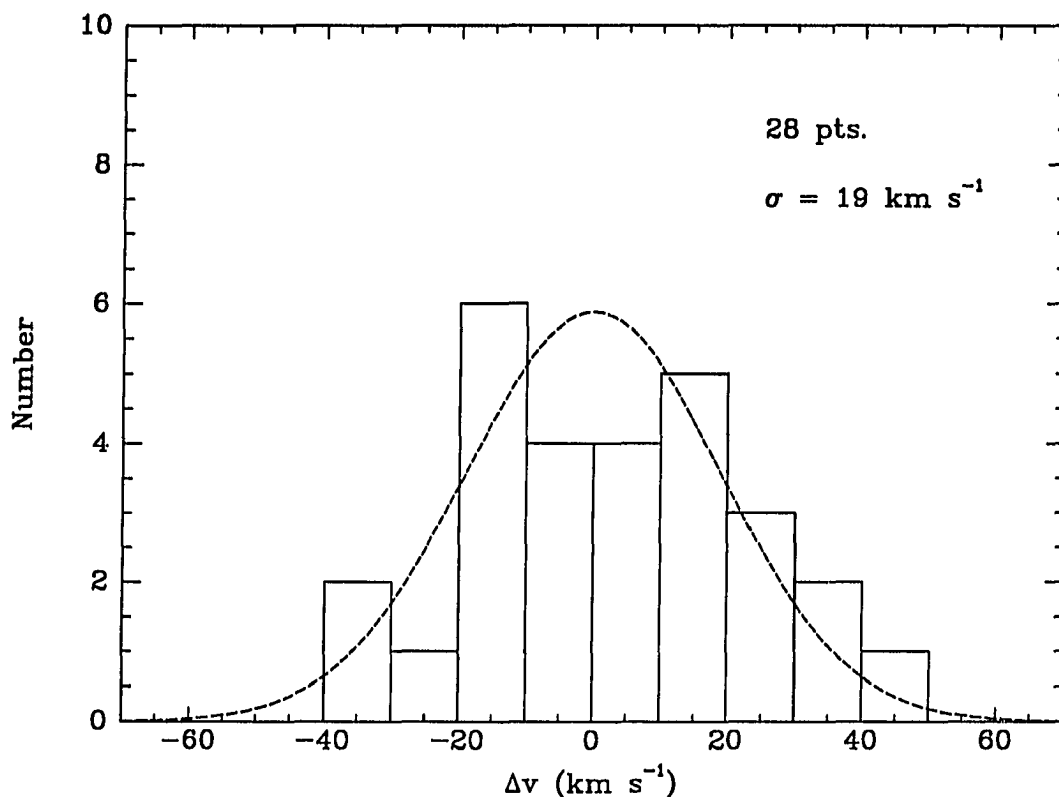


Figure 3.7: *MMT Velocity Error Distribution : Comparison of our MMT measurements with H I velocities for objects in common. Notice that $\sigma = 19 \text{ km s}^{-1}$ includes both the uncertainties in our measurements and those in the H I velocities.*

Typically 12 to 15 lines were identified and a Chebyshev polynomial of order 4 or 5 was fit to the lines. Sky subtraction was done along rectified columns with a low-order fit. The aperture was extracted and a cross-correlation analysis was used to measure velocities of absorption line systems while Gaussian line fitting was used to measure velocities of emission line systems. Heliocentric corrections were then applied. Differences between our determined velocities and H I velocities are

presented in histogram form in Figure 3.7. The standard deviation of the velocity differences is slightly lower than 20 km s^{-1} . Note that the distribution shown in Figure 3.7 includes the observational errors in the H I data. Most of the galaxies for which there are measurements in the HR catalog are primaries. These galaxies have large amplitude rotation curves; therefore, the few points with the largest differences are possibly due to a slight misplacement of the slit. This should be less of a problem for satellite galaxies, which have smaller internal velocities. In Figure 3.8 we show the results of the velocity determinations (from our observations and the HR catalog) for the entire satellite sample.

Supplementary Data

Table 3.2 contains information about both the primary and satellite galaxies in our sample. The galaxies are presented in groups with the primary first, followed by its satellite(s). In column (1) the name of the primary or the identification number of the satellite is given. The right ascension and declination in 1950.0 coordinates are in columns (2) and (3). The blue apparent magnitude is in column (4), and the heliocentric recessional velocity is given in column (5). In column (6) we present the projected separation. The projected separation was calculated using the angular separation and the distance to the primary. The distance to the primary was estimated from the recessional velocity using $H_0 = 75 \text{ km s}^{-1} \text{ Mpc}^{-1}$, assuming a 220 km s^{-1} LSR rotation velocity, and a 300 km s^{-1} Virgocentric infall. In columns (7), (8), (9), and (10), the galaxy type, the major axis, the H I line width (uncorrected for inclination), and the inclination are listed. The galaxy types are T-types as described in the Second Reference Catalogue of Galaxies (de Vaucouleurs, de Vaucouleurs, and Corwin, Jr., 1976). The angle between a line connecting the nuclei of the primary and satellite, and the major axis of the primary is referred to

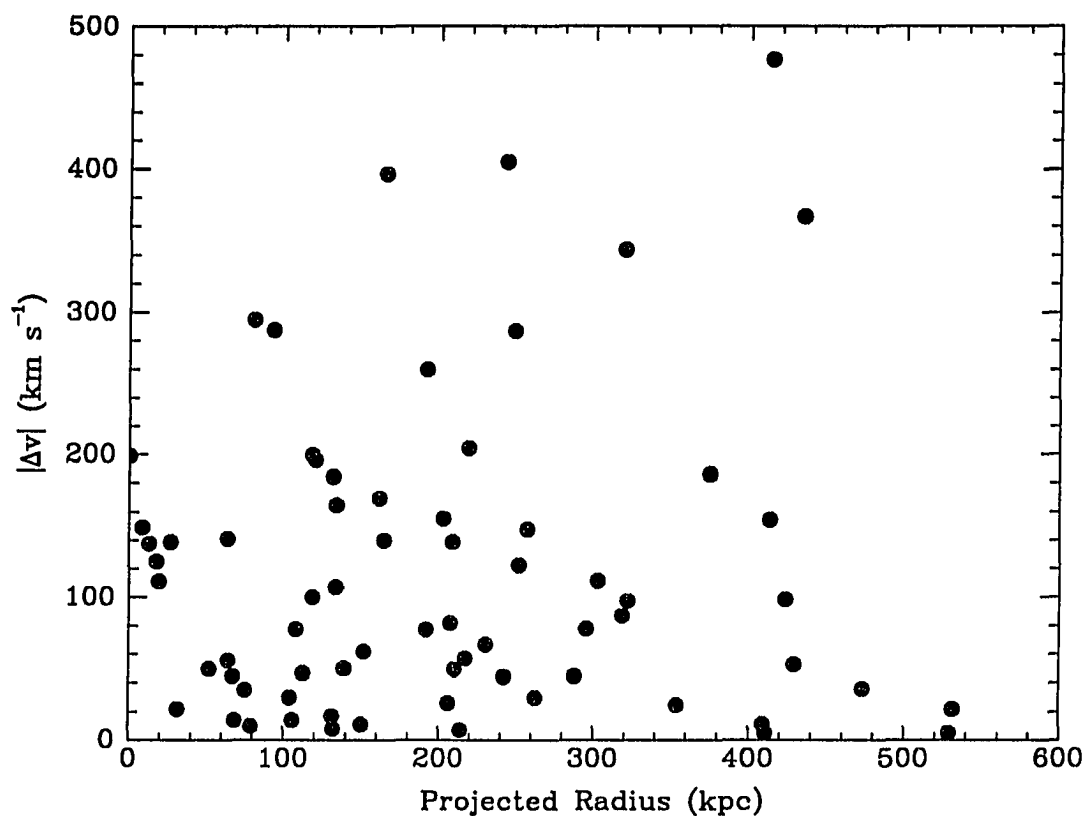


Figure 3.8: r_p vs. $|\Delta v|$: Note that two satellites have $r_p > 500$ kpc. These satellites had $r_p < 500$ kpc before Virgocentric infall corrections are applied. Because of the uncertainties in the distance due both to uncertainties in H_0 and Virgo infall models (note that a 10% uncertainty is more than that required to bring them under 500 kpc), we decided to retain these two satellites. Because of the small values of $|\Delta v|$ for these objects, this will not artificially increase the mass estimates.

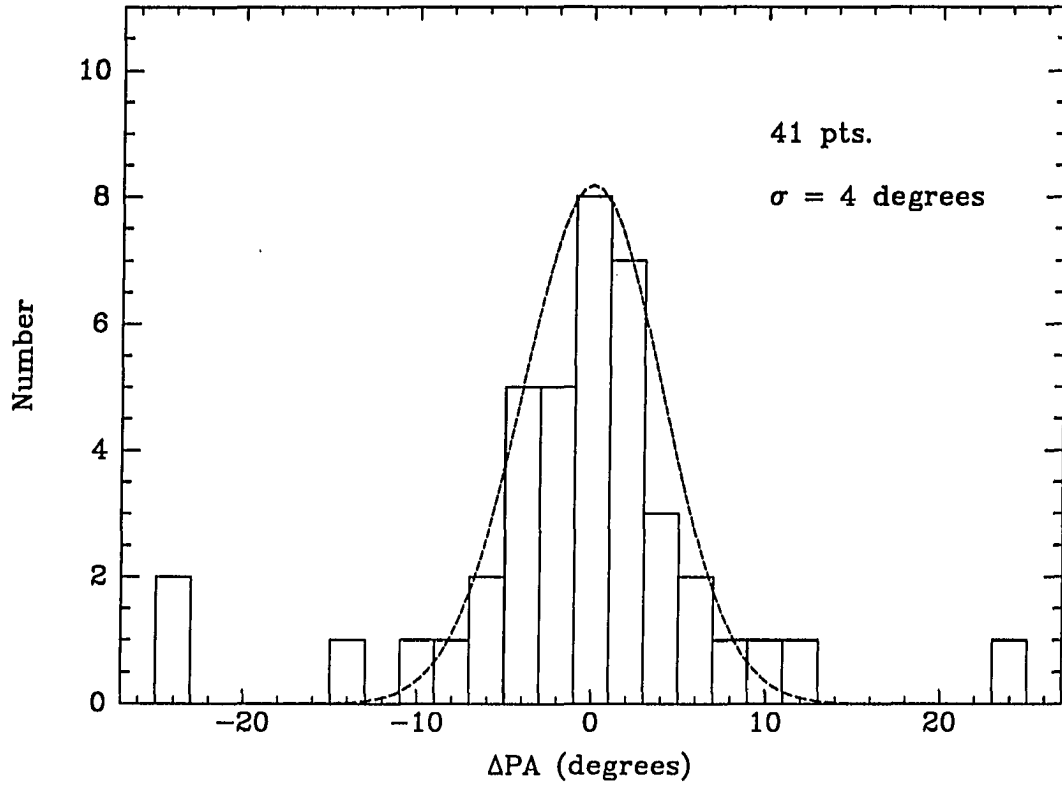


Figure 3.9: *Primary Galaxy Position Angle Error Distribution*

as the position angle (PA) and is given column (11). Notes regarding spectral characteristics are given in column (12). The references for some of the magnitudes, coordinates, and types is Z-cat (Huchra 1987). The HR Catalog (Huchtmeier and Richter 1989) is the reference for H I velocities and velocity widths, inclinations, types, and coordinates. Some coordinates are from our own plate scans. The position angles and some magnitudes were measured visually from POSS and ESO plates and are described below.

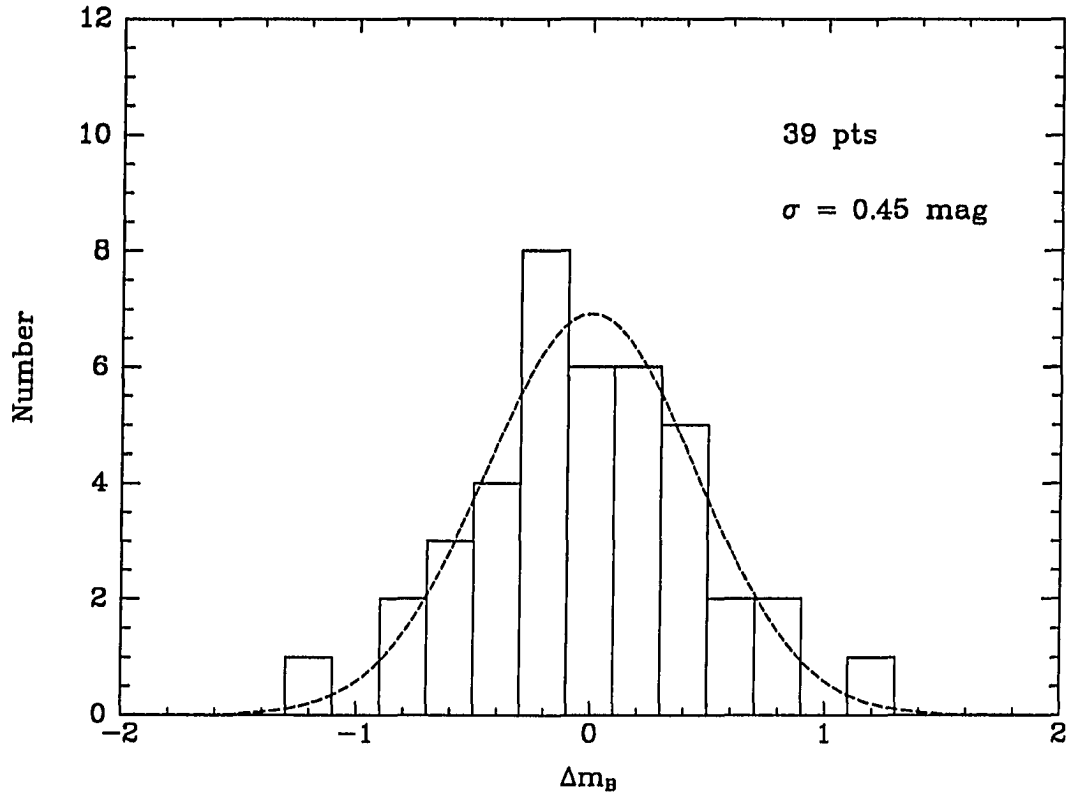


Figure 3.10: *Blue Magnitude Error Distribution*

The uncertainty in our determination of position angles was estimated from a comparison of our measured major axis position angles with those in the literature (see Figure 3.9). The errors in the major-axis position angles are due to slight misplacement of north, and in the determination of the major axis of the galaxy. The 1σ uncertainty in any primary's PA is 5° . Uncertainties in the relative position angles of primaries and satellites should be smaller because the errors in the determination of north cancel.

For many satellites measurements of blue magnitudes are not available in the literature. We estimated by eye, using a field in the Coma cluster (from Godwin *et al.* 1983) to calibrate ourselves, the blue apparent magnitude of each satellite. Figure 3.10 is a histogram of differences between the estimated magnitude and that presented in the literature for those objects for which this data is available. The 1σ uncertainty is 0.45 mag, and the error distribution is shown in Figure 3.10. The large errors are due primarily to variations in surface brightness between objects in the calibration field and the satellites (there are no low surface brightness extended objects near the center of the Coma cluster). Errors are smaller for high surface brightness objects. Because of the low precision, the visually estimated magnitudes are only used for objects which do not have published magnitudes.

Sizes and types were also estimated visually for many objects. A histogram of differences between the estimated sizes and those in the literature is presented in Figure 3.11. The estimated 1σ uncertainty is 0.5 arcmin. To preserve homogeneity, all satellite sizes given in Table 3.2 are from our measurements. Galaxy types are extremely uncertain, especially for galaxies of small angular extent. The types should be taken as approximate.

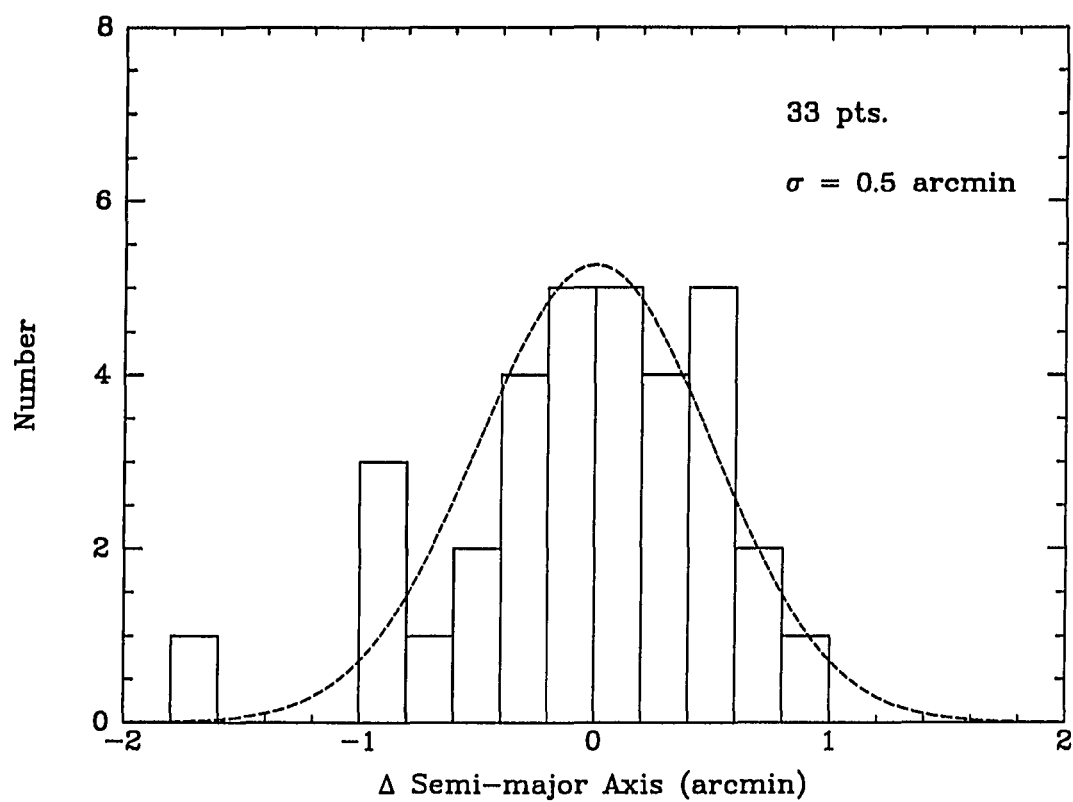


Figure 3.11: *Semi-Major Axis Error Distribution*

Table 3.2: Data for Primary and Satellite Galaxies

Name (1)	α^a (2)			δ (3)			m_B (4)	v_{\odot}^b (5)	r_p^c (6)	T^d (7)	a^e (8)	W_0^f (9)	i^g (10)	θ_S^h (11)	S^i (12)
N259	0 45	30.0	-3	2 50	12.5	3808	...	4	3.2	456	81	ab
1	0 44	44.6	-2	49 4	18.3	3518	252	9	0.5	2	...	ab
2	0 46	20.6	-2	39 5	15.5	3996	380	10	0.5	67	...	em
N488	1 19	10.9	4	59 36	11.6	2268	...	3	6.0	463	42	ab
3	1 19	30.0	5	6 0	15.6	2212	66	-4	1.9	17	...	ab
4	1 17	48.0	5	33 48	17.0	2170	329	10	1.6	108	50	44
N772	1 56	35.3	18	45 50	11.3	2468	...	3	8.0	480	51	ab
5	1 56	28.2	18	42 46	14.2	2490	32	-4	1.0	...	42	76	ab
N895	2 19	5.9	-5	45 0	11.5	2290	...	6	3.5	284	41	ab
6	2 19	15.1	-5	45 47	17.3	2402	20	11	0.3	1	em
N1459	3 44	50.8	-25	40 24	13.6	4160	...	6	3.5	...	48	ab
7	3 44	52.4	-25	40 51	18.8	4009	9	10	2.0	27
N1620	4 34	3.7	-0	14 42	13.6	3513	...	5	3.2	452	69	ab
8	4 35	0.0	-0	24 0	16.5	3720	220	6	1.1	69	ab
9	4 34	58.3	-0	22 17	15.6	3670	204	-4	86	em
N1961	5 36	33.9	69	21 16	12.2	3934	...	4	4.6	702	50	ab
10	5 38	54.0	69	16 0	15.4	3927	214	5	2.4	296	84	15
11	5 37	6.0	69	13 0	15.6	3884	139	10	1.2	143	70	63	em
12	5 37	54.0	69	24 0	14.5	4122	120	3	1.0	186	55	30	ab
13	5 40	12.0	69	2 0	15.1	4305	434	10	1.1	151	...	40	em
14	5 39	24.0	69	8 0	15.0	4282	319	2	2.2	298	50	35	em
N2424	7 37	16.4	39	20 58	13.9	3112	...	3	3.9	439	90	ab
15	7 37	42.1	39	16 55	18.5	2814	80	3	0.3	47	em
N2718	8 56	11.5	6	29 17	13.3	3842	...	2	2.3	135	15	ab
16	8 56	41.6	6	31 25	17.0	3640	117	15	0.6	18	em
17	8 55	48.3	6	31 21	15.5	3551	92	15	1.1	22	em

Name (1)	α^a (2)	δ (3)	m_B (4)	v_{\odot}^b (5)	r_p^c (6)	T^d (7)	a^e (8)	W_0^f (9)	i^g (10)	θ_S^h (11)	S^i (12)
N2997	9 43 27.4–30	57 35 11.0	1086	...	5	13.2	276	35	...	ab	
18	9 41 55.0–31	56 6 15.2	1209	245	10	2.4	70	...	56	...	
19	9 42 37.0–31	35 42 13.2	1256	157	10	2.6	164	30	59	...	
20	9 43 18.0–30	6 42 14.6	1004	202	7	4.9	148	79	78	...	
N3043	9 52 41.3	59 32 40	13.3	2998	...	3	1.9	319	71	...	ab
21	9 53 51.0	59 13 46	16.6	3028	260	3	0.7	70	em
N3154	10 10 18.1	17 16 42	14.5	6508	...	4	63	...	ab
22	10 10 15.2	17 16 42	16.3	6636	18	5	0.9	59	em
N3464	10 52 13.6–20	47 55 13.2	3750	...	4	4.3	386	46	...	ab	
23	10 51 24.0–20	56 59 18.8	3807	214	10	0.2	77	em	
N3614	11 15 35.2	46 1 16	12.7	2332	...	5	4.6	318	52	...	ab
24	11 15 40.1	45 56 11	18.5	2282	51	8	0.3	55	em
N3629	11 17 51.9	27 14 13	12.9	1514	...	5	2.1	249	43	...	ab
25	11 21 46.5	27 43 54	16.0	1503	398	3	1.3	165	...	33	...
N3646	11 19 5.2	20 26 43	12.1	4250	...	5	3.8	540	55	...	em
26	11 19 36.6	20 29 0	14.7	4417	132	–2	1.7	25	em + ab
N3735	11 33 4.8	70 48 42	12.4	2696	...	5	4.3	513	78	...	ab
27	11 30 12.1	70 40 2	15.3	2618	190	7	1.1	72	ab
28	11 31 6.7	70 52 13	17.6	2595	118	11	0.6	21	em
N4030	11 57 50.3	–0 49 22	11.6	1460	...	4	4.2	354	41	...	ab
29	11 56 12.0	–1 10 30	14.6	1486	200	10	2.3	169	58	11	...
30	11 58 18.0	–0 15 18	17.0	1939	402	10	1.9	72	39	31	...
31	11 58 36.0	–1 1 6	14.4	1490	101	10	1.5	113	28	83	...
32	12 1 47.0	–1 15 7	17.0	1465	398	10	1.4	130	33	76	...

Name (1)	α^a (2)			δ (3)			m_B (4)	v_{\odot}^b (5)	r_p^c (6)	T^d (7)	a^e (8)	W_0^f (9)	i^g (10)	θ_S^h (11)	S^i (12)
N4162 33	12	9	19.4	24	24	5	12.6	2559	...	4	2.5	334	52	...	ab em
	12	9	2.3	24	18	25	16.5	2524	74	2	0.6	43	
N4679 34	12	44	46.0–39	17	54		13.3	4647	...	4	4.4	436	61	...	ab em
	12	46	10.4–39	17	9		16.5	4568	294	10	1.2	79	
N4725 35	12	47	59.9	25	48	20	10.2	1207	...	2	12.0	419	43	...	ab ...
	12	49	18.6	26	2	45	13.2	1109	127	10	4.0	215	64	12	
36	12	50	43.5	25	32	58	15.5	1140	223	11	0.7	75	em + ab
N5073 37	13	16	42.0–14	36	0		13.0	2736	...	5	3.5	416	90	...	ab em
	13	16	48.0–14	52	0		15.5	2876	177	2	33	
N5085 38	13	17	33.5–24	10	42		12.1	1957	...	5	5.0	245	42	...	ab ...
	13	21	19.0–24	24	12		17.8	2056	416	10	3.2	113	28	52	
N5248 39	13	35	2.4	9	8	23	10.9	1153	...	5	6.8	285	45	...	ab ...
	13	33	12.0	9	13	24	15.5	1164	145	10	3.4	150	83	24	
N5254 40	13	36	58.5–11	14	29		13.0	2311	...	5	2.6	354	57	...	ab ab
	13	34	24.0–11	35	0		15.8	2467	406	7	1.8	117	31	62	
N5297 41	13	44	19.0	44	7	23	12.3	2406	...	4	5.8	451	80	...	ab em + ab
	13	44	13.7	44	5	0	15.0	2266	27	–2	0.9	...	45	81	
N5324 42	13	49	29.1	–5	48	42	12.6	3044	...	4	2.2	232	24	...	ab ...
	13	49	29.1	–5	48	43	–9.9	3245	0	75	45	...	
43	13	48	46.7	–5	49	23	16.5	3036	131	3	0.7	57	em
I4351 44	13	55	2.0–29	4	18		12.3	2664	...	4	11.8	...	81	...	ab ab
	13	54	36.7–29	9	18		18.8	2674	78	10	0.2	34	
45	13	54	36.2–29	1	6		17.8	2650	68	10	1.9	74	em
46	13	52	4.0–28	53	30		17.8	2717	424	3	1.1	89	em

Name (1)	α^a (2)	δ (3)	m_B (4)	v_{\odot}^b (5)	r_p^c (6)	T^d (7)	a^e (8)	W_0^f (9)	i^g (10)	θ_S^h (11)	S^i (12)
A1416	14 16 29.6–26	24 52 12.8	6809	4.8	...	48	...	ab	
47	14 16 19.3–26	35 57 15.3	6695	301	4	2.1	83	...	
48	14 16 18.4–26	24 38 15.6	6855	67	11	0.7	16	...	
N5768	14 49 2.3 –2	19 27 13.0	1959	...	5	2.0	206	32	...	ab	
49	14 50 0.0 –3	21 0 15.2	1954	520	8	3.3	178	38	53	...	
N5899	15 13 14.9	42 14 1	12.6	2576	...	5	2.8	551	76	...	ab
50	15 13 16.4	42 23 31	15.0	2562	105	3	2.1	457	71	20	em + ab
N5965	15 32 50.1	56 51 8	13.4	3413	...	3	6.0	612	87	...	ab
51	15 32 58.0	57 28 4	15.6	3391	528	11	0.6	48	em
N6181	16 30 9.4	19 55 48	12.5	2371	...	5	2.5	395	61	...	ab
52	16 29 12.8	20 17 30	14.7	2520	255	7	2.4	273	80	32	em
N6384	17 29 59.0	7 5 43	11.5	1655	...	3	7.0	394	46	...	ab
53	17 25 41.9	7 27 40	15.0	1691	471	5	3.1	150	25	73	...
N6948	20 39 48.0–53	32 18 13.2	3228	...	3	2.3	...	65	...	ab	
54	20 39 12.6–53	12 16 16.8	3637	245	8	1.0	49	em	
N6943	20 39 48.0–68	55 42 11.9	3142	...	5	...	437	63	...	ab	
55	20 38 51.5–68	45 13 16.6	3328	132	6	1.2	29	em	
56	20 42 36.4–68	44 59 18.8	3092	212	–4	0.5	6	ab	
N7038	21 11 46.0–47	26 56 12.4	4940	...	5	3.3	545	56	...	ab	
57	21 13 40.0–47	25 48 18.3	4965	356	–4	0.3	37	em	
58	21 13 2.3–47	29 50 17.8	4985	244	–4	0.3	21	ab	
A2120	21 19 56.0–45	59 6 12.6	2686	...	4	3.5	425	73	...	ab	
59	21 19 55.5–45	57 44 19.8	2825	13	10	0.2	62	ab	

Name (1)	α^a (2)	δ (3)	m_B (4)	v_{\odot}^b (5)	r_p^c (6)	T^d (7)	a^e (8)	W_0^f (9)	i^g (10)	θ_S^h (11)	S^i (12)		
A2125	21 25	9.0–38	5 48	12.9	2567	...	5	4.1	...	60	...	ab	
60	21 24	9.6–38	4 20	16.0	2645	110	2	0.6	...	72	1	em	
61	21 25	29.6–37	48 20	15.4	2708	167	8	0.9	3	ab	
N7083	21 31	48.0–64	7 54	11.8	3113	...	5	3.8	410	53	...	ab	
62	21 31	9.1–64	24 36	18.3	3375	194	–6	0.2	3	em	
63	21 36	10.2–64	8 8	14.0	3201	322	2	1.5	78	ab	
N7137	21 45	54.1	21 55	43	13.3	1641	...	5	1.6	187	30	...	ab
64	21 45	12.0	21 55	53	17.0	1833	66	9	1.3	123	66
N7177	21 58	18.5	17 29	50	12.2	1155	...	3	3.3	319	53	...	ab
65	21 56	42.0	17 56	0	15.1	1093	156	8	2.9	130	28	57	...
N7290	22 26	0.8	16 53	35	13.8	2900	...	5	1.7	271	53	...	ab
66	22 26	24.0	16 45	0	17.0	2947	114	10	1.5	3	em
67	22 27	19.8	16 35	35	17.9	2855	292	11	0.5	9	em
N7678	23 25	58.2	22 8	50	12.7	3486	...	5	2.5	317	42	...	ab
68	23 26	14.9	21 57	0	15.4	3887	167	3	1.9	191	52	26	...
N7716	23 33	57.2	0 1	14	12.9	2570	...	3	2.3	239	35	...	ab
69	23 34	50.0	0 6	53	15.7	2678	136	8	3.5	143	51	32	...

^a RA and Dec are for 1950 epoch.

^b Heliocentric velocity in km sec^{-1} . Source of velocities given for MX (+ MMT) and ARGUS observations in Table 3.1. The remainder of the velocities come from the HR catalog except for satellites 7, 22, 47, and 48 (from Frenk and Smith priv. comm.)

^c Projected separation in kpc.

^d Hubble type designated by T-types (cf. RC2).

^e Major axis in arcmin.

^f H I line width in km sec^{-1} , not corrected for galaxy inclination.

^g Inclination in degrees. 0° indicates face on.

^h Position angle in degrees. Described in text.

ⁱ Spectral characteristics of spectrum (ab = absorption, em = emission).

Notes to Table 3.2

Satellite No. 5 - H I measurements give a much lower velocity (2437 km s^{-1}) ; however multiple optical measurements agree on the value presented in the Table. The separation between primary and satellite is small and the H I velocity determination of the satellite may have been affected by contaminating emission from the primary.

Satellite No. 7 - Probably an outer disk H II region.

NGC 1961 - This galaxy is peculiar in several respects. First, it is among the most rapidly rotating disks known. Second, it has five companions, which is an abnormally large number of companions. Third, all five companions are located in the same quadrant with respect to the primary, suggesting that the companions belong to a group, possibly just seen in projection. We suggest later (§3.3.2) that at least two of the companions (Nos. 13 and 14) are interlopers.

NGC 2424 - Our optical determination of the recessional velocity of this galaxy is significantly larger (3360 km s^{-1}) than the value quoted in the table from H I observations (Staveley-Smith and Davies 1987). The H I signal is convincing and samples the emission from the entire galaxy; however, further observations are necessary to resolve the discrepancy.

Satellites No. 16 and 17 - These two satellites appear to be interacting.

NGC 3646 - Possibly an outlier of a relatively nearby cluster seen in projection.

Satellite No. 42 - This satellite was identified from H I line profile and so its position is not well determined. There is an optical companion near to NGC 5324 that could correspond to the observed H I emission. However, we have adopted a projected separation of 0 kpc.

A1416 - Has a relatively nearby cluster.

Satellite No. 50 - Anomolously large far-infrared flux ($L_{IR}/L_B > 14$). Bolometric magnitude for this satellite is greater than that of the primary. Should probably be rejected from sample.

NGC 5768 - Only one H I velocity available for this galaxy (1959 km s^{-1} with unknown uncertainty); however, optical measurement from Z-cat is 1951 km s^{-1} .

NGC 6384 - Crowded environs. Although the primary satisfies the isolation criteria, there is a nearby concentration of galaxies.

NGC 7038 - Crowded environs. Same as above.

NGC 7177 - Uncertainty in primary velocity estimated to be greater than 20 km s^{-1} (25 km s^{-1}).

Table 3.3: Primaries Without Known Satellites^a

NGC 803+, IC 1783, A0407-48*, IC 2070, NGC 2359, NGC 2608,
 NGC 2701, NGC 2713, NGC 2870+, NGC 2939, NGC 2989, NGC 2990+,
 NGC 3200*, NGC 3320, NGC 3463, NGC 3464, NGC 3549+, NGC 3735,
 NGC 3976, NGC 4602, NGC 4682, NGC 4793, NGC 4939+, NGC 5162,
 NGC 5172+, NGC 5362, NGC 5492+, NGC 5633, NGC 5665, NGC 5875+,
 IC 5071*, NGC 6368+, NGC 6808, NGC 7124, NGC 7448, NGC 7541,
 NGC 7606, NGC 7721*+, NGC 7755

^a These primaries have satisfied the criteria described in §3.2.1. Those that have been observed have undergone the most extensive scrutiny. Primaries denoted with (*),(+), or (**) have been observed with ARGUS, MX, or AAT, respectively. This is not a complete sample.

3.3 A Look at the Data

3.3.1 Asymmetric Velocity Distribution

The majority of satellite galaxies in our sample have recessional velocities greater than that of their respective primary galaxy (cf. Figure 3.12). Given the tacit assumption that all of these satellites are gravitationally bound to the primary and have well-mixed orbits, this result, if statistically significant, seems inexplicable. The same result observed in an independent sample prompted Arp and Sulentic (1985) to postulate that the measured redshifts of satellite galaxies contain a non-Doppler component. Therefore, it is imperative to evaluate the statistical significance and origin of the observed asymmetric relative velocity distribution.

For further confirmation and analysis, we have collected additional data from two binary galaxy surveys: the revised Turner catalog (White *et al.* 1983) and the Schweizer catalog (Schweizer 1987). A principal difference between the satellite

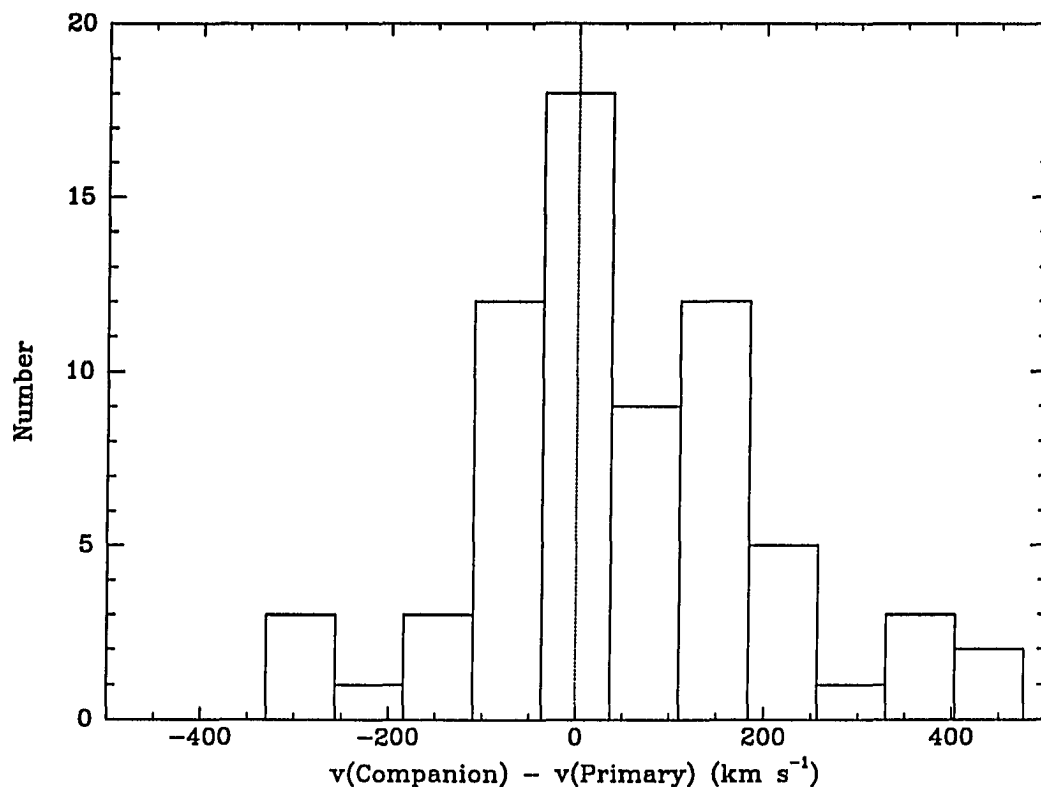


Figure 3.12: *Velocity Difference Histogram for Satellite Sample*

samples (Arp and Sulentic's and ours) and the binary samples (White *et al.*'s and Schweizer's) is that the former include systems with multiple companion galaxies. To facilitate comparison between the published data and our own, we have imposed the following selection criteria to the published data: $r_p < 500$ kpc, $|\Delta v| < 500$ km s⁻¹, $v_R > 1000$ km s⁻¹, and $\Delta m > 0.3$, where v_R is the primary recessional velocity and Δm is the magnitude difference between primary and satellite. The reasoning behind all except the last of these criteria was discussed in §3.2.2. We have adopted the last criterion to distinguish unambiguously between primary and companion.

Table 3.4: Observed P/T Values

Sample	P/T	Prob. of Observed P/T or Greater	Significance
Ours	0.594	0.048	1.7σ
ASR	0.595	0.065	1.5σ
Schweizer	0.542	0.368	0.3σ
White <i>et al.</i>	0.554	0.190	0.9σ
Ours + ASR	0.594	0.015	2.2σ
All Four	0.575	0.009	2.3σ

The fraction of each sample with $\Delta v > 0$ is designated as P/T (the number of satellites with positive Δv divided by the total number of satellites). P/T's and statistical significance levels for various galaxy samples are given in Table 3.2. All four independent samples have $P/T > 0.5$. The effect, while apparently real, has received little attention, except in the Arp and Sulentic work, because the effect is marginally significant in any one sample alone and because the asymmetry is hidden since the distribution of $|\Delta v|$ is examined, as is usually the case in dynamical analyses.

Before appealing to non-standard physics, we attempt to explain the effect in terms of biases created by the selection criteria. First, the assumption that all companion galaxies are gravitationally bound to their respective primary galaxy is incorrect. Some apparent companions are at a much different distance than the associated primary and only appear close on the sky. Additionally, some apparent companions are possibly near, but unbound to the primary. Second, it is incorrect to presume that the selection criteria have not affected the sample. We will demonstrate that significant asymmetries in the velocity distribution can develop as a result of the inclusion of projected companions and the choice of selection criteria.

There are two types of biases created by the selection criteria, which we shall refer to as volume and magnitude biases, that when combined with the presence of projected companions can skew the Δv distribution. First we consider the volume biases. Since the projected separation criterion, $r_p < 500$ kpc, is equivalent to an angular separation criteria, it produces a selection cone in space centered on the primary and truncated at the near and far ends by the velocity difference criterion. The difference in the selection volume in front of the primary (*i.e.*, nearer to the observer) and that behind the primary creates a bias in the Δv distribution. P/T will also be affected by the magnitude-type biases. The 500 km s^{-1} velocity difference cutoff corresponds to 6.7 Mpc, if the velocities are purely due to universal expansion. Because this distance is a significant fraction of the distance to the primaries, which range from 13.3 to 92.0 Mpc, the apparent magnitude difference between the front and back of the selection volume can be significant and affect the selection process. For example, a possible companion might be excluded from the sample for being too bright were it located at the near edge of the volume, but would be included if located at the far edge. On the other hand, a galaxy near the faint magnitude limit, might be found if at the near edge, but not if at the far edge. In addition, when companions and primaries are defined by small magnitude differences (*e.g.*, 0.3 magnitudes, as is true for most samples except ours), the nearer galaxy is more likely to be identified as the primary than the more distant one.

For illustration of the volume-type bias, we consider its effect on the two populations in the sample: physical satellites and interlopers. The physical satellites are those galaxies that are within the sphere of influence of the primary, which presumably extends to between 1 and 2 Mpc. Companions at these distances are not necessarily bound to the primary. However, their velocities do contain information about the mass of the primary and they are principally influenced by the primary.

On the other hand, interlopers are beyond the range of the primary's dominant influence; therefore, their velocities do not strongly reflect the primary's gravitational influence. For the physical satellites, there exists a range of radii where the satellites are expanding away from the primary (they are either unbound or have not yet reached their initial turnaround). Consider a shell of expanding companions, that has an outer radius larger than the projected radius cutoff. We treat the physical satellites in terms of shells because the distribution of companions is presumably nearly spherical about the primary. Because the portion of the shell that lies within the selection volume and behind the primary is larger than that which lies within the selection volume and in front of the primary, more companions will be found behind the primary, hence with positive Δv . If the satellites are distributed uniformly and extend out to separations of 2 Mpc, then companions within the expanding shell will have a P/T between 0.5 and 0.6 depending on the associated primary's distance and the size of the shell. For primaries in our sample, the P/T of companions in the expanding shell ranges between 0.5 and 0.55, depending on model assumptions. Because galaxies are strongly correlated, we expect galaxies to be on average closer to the primary than in a uniform distribution model, and so we expect P/T's to be only slightly greater than 0.5. Now consider a uniform background of galaxies⁴. Because of the disparity in front and back volumes, one is predisposed to find projected companions that are more distant than the primary, hence with positive Δv since velocities are $\approx H_0 r$. If galaxies are distributed uniformly in space and no other selection effects are important, then interlopers will have P/T's that are proportional to the ratio of the volume behind the primary to the total volume. For a typical galaxy in our sample, this ratio is ~ 0.60 . However, the magnitude

⁴Background is used as a generic term for galaxies that are physically unassociated with the primary. Note that some of the "background" galaxies will be in the foreground. Because these galaxies are unassociated with the primary, these galaxies are treated as a uniform distribution — not as in shells.

bias and clustering become important when considering the P/T of the background sample.

Galaxy clustering has an additional effect on P/T for two reasons. First, clustering increases the noise in P/T because fewer random selections are needed to account for the same number of interlopers. The second reason is more complex. If the luminosity function were flat (*i.e.*, equal numbers of galaxies in any equal magnitude bin) then regardless of the distance to the background cluster, one would find the same number of galaxies within a fixed apparent magnitude range. Additionally, for the sake of the argument assume that one finds equal numbers of clusters behind and in front of the primary. Then $P/T = 0.5$. Now consider the case where there exist no galaxies brighter than some absolute magnitude cutoff. Then, if this cutoff falls within the allowed apparent magnitude range, the more distant sample of interlopers will have fewer galaxies and so $P/T < 0.5$. However, recall that galaxies brighter than the upper limit of the allowed apparent magnitude range disqualify their associated primary from the sample (because the primary is no longer isolated). The more distant sample of interlopers will contain no galaxy brighter than the upper apparent magnitude limit because of the cutoff in the luminosity function, but the nearer sample might. However, these galaxies will not only disqualify themselves but also the other members in that cluster. This creates a deficit of foreground clusters. While the interplay between the effects is complicated, and the result for our sample is not obvious, it is clear that given a suitably chosen scenario either $P/T > 0.5$ or $P/T < 0.5$ can be created by the combination of the magnitude bias and clustering.

Computer simulations were used to determine the effect of the combination of observational biases and galaxy clustering. To model clustering first one has to determine the number of galaxies per cluster and the size of clusters. We used

the observed clustering properties of galaxies in small groups to determine N , the number of galaxies per cluster, and R , the radius of the cluster. There is strong evidence that most galaxies reside in small groups with diameters of order 1 Mpc (cf. Gott and Turner 1977; Soneira and Peebles 1977; Huchra and Geller 1982; Geller and Huchra 1983). We adjusted the size and number of galaxies per group in our simulations, which are described below in detail, until an acceptable match to the observations was obtained. The criteria for judging the choice of N and R included a comparison of the occurrence of single, binary, and group galaxies in our models with the results presented by Huchra and Geller (1982), and a comparison of the simulated and observed mean pairwise separation. The relative fractions of model clusters that contained one, two, or more observed galaxies (*i.e.*, those galaxies which satisfy the selection criteria of the cluster studies) for our preferred model are 0.22, 0.12, and 0.66 respectively. The observed fractions are 0.27, 0.12, and 0.61 (Huchra and Geller 1982). The mean pairwise separation in our model is 0.6 Mpc and that found by Huchra and Geller (1982) is 0.7 Mpc. This model has $R = 0.75$ Mpc and $N = 16$ down to an absolute magnitude of -12.0 . We used this model to determine the background P/T 's quoted in Table 3.4 for the satellite models. The binary galaxy models are for $N = 1$. This is because if an interloping cluster with more than 1 galaxy were observed, then the system would no longer be classified as a binary.

To estimate the P/T of the background, we used the following procedure to simulate background galaxies. First, a primary galaxy was selected at random from the list of observed primaries. Second, a cluster center was positioned at random within a cube that is 1500 kpc wide and 1400 km s^{-1} deep centered on the primary. Third, N galaxies were located at random within a sphere of radius R , centered on the position determined in the previous step. N is set to 1 for simulations that include no clustering or is set to 12 for simulations that include clustering. Fourth,

the luminosities were drawn from a Schechter luminosity function (Eq. 3.1) that was truncated at the faint end at a fixed absolute magnitude, which corresponds to an apparent magnitude well below the limiting apparent magnitude. Fifth, apparent magnitude and minimum apparent magnitude difference criteria were applied to simulate the selection criteria imposed on the observed sample. If none of the cluster galaxies violate the isolation criteria imposed on the primary, then the galaxies in the simulated cluster that satisfied the remaining criteria constituted a background cluster. This process was repeated thousands of times and a list of background clusters was generated. To evaluate the distribution of P/T for a background of 10 galaxies, we drew background clusters from the master list of clusters until we had 10 or more galaxies and evaluated P/T . From the distribution of P/T , we evaluated the means and standard deviations presented in Table 3.4.

For the binary galaxy samples, although the observed excess of companions with $\Delta v > 0$ is statistically insignificant (*i.e.*, $< 1\sigma$), models 1-4 demonstrate that $P/T > 0.5$ is expected. Because the number of background galaxies is expected to be small, and because in our satellite models (models 5-9) the interlopers come in groups, these models produce a larger scatter in P/T than the models with no clustering (models 1-4). However, clustering does not noticeably increase P/T . If heavily populated groups (≥ 3 members only; model 9) are preferentially observed, then the background P/T rises slightly. This is important because populous groups might be preferentially observed, especially when searching for companions — as was the case for the ASR sample.

We infer from these models that primaries with multiple apparent satellites are most likely to harbor interlopers. Interlopers come in groups and supplement physical companions. Furthermore, due to the magnitude bias, populous background clusters are more likely to have $\Delta v > 0$. For example, for model 4 the P/T of

Table 3.5: Simulated Interloper P/T Values

Model	Sample ^a	m_B^b cutoff	Δm^c	$\langle P/T \rangle$	$\sigma_{P/T}^d$
1	Binary	14.0	0.3	0.60	0.16
2	Binary	14.0	2.2	0.59	0.17
3	Binary	15.5	0.3	0.60	0.16
4	Binary	15.5	2.2	0.57	0.16
5	Satellite	14.0	0.3	0.60	0.25
6	Satellite	14.0	2.2	0.61	0.26
7	Satellite	15.5	0.3	0.61	0.25
8	Satellite	15.5	2.2	0.60	0.25
9 ^e	Satellite	15.5	2.2	0.64	0.30

^a $N = 1$ for the binary models. $R = 0.75$ Mpc and $N = 16$ down to $M = -12$ for the satellite models.

^b The apparent magnitude cutoff used for the model.

^c The minimum allowed magnitude difference between primary and companions.

^d The standard deviation of P/T evaluated from 50 realizations.

^e This model uses only background clusters with 3 or more galaxies.

clusters with only 1 or 2 galaxies is 0.55, but is 0.64 for clusters with 3 or more members. For those primaries with three or more satellites in the combination of the ASR and our sample, $P/T = 0.67$. This is significantly larger than in the sample as a whole. On the other hand, for those primaries in the combined sample with a single satellite, $P/T = 0.46$. The significant biasing by groups is also evident in the observation that the binary samples (1 companion) have lower P/T 's than the satellite samples.

Unfortunately, the highly populated systems are the most attractive ones, since they appear to have many satellites. Previous studies using satellites to determine masses have focused on a few well populated individual systems (cf. Dressler,

Schechter, and Rose 1986; Erickson, Gottesman, and Hunter, Jr. 1987) and as a result have skewed velocity distributions and probably a high level of contamination. The Dressler, Schechter, and Rose sample (six satellites around one primary) has $P/T = 0.17$ (such a low P/T is only expected 11% of the time in a sample of this size). In addition, the velocities of the five galaxies with slower recessional velocities than the primary are clumped at a velocity $\sim 300 \text{ km s}^{-1}$ less than the primary. The EGH87 sample (20 satellites around 6 primaries) has $P/T = 0.7$, and such a high P/T is only expected 6% of the time in a sample of that size.

Using the background P/T obtained from the simulations, we estimated the background fraction necessary to produce the observed P/T in our sample. Assuming that true satellites are evenly distributed between those receding and approaching the primary, in Figure 3.13 we plot the minimum background P/T , as a function of sample background fraction, required to account for the observed P/T for a model with no galaxy clustering. With dashed lines, in the same figures, we plot the 1 and 2 σ confidence limits on the background P/T necessary to account for the observed P/T , again for models without clustering. With solid triangles we denote the 1σ lower limits on the required background fraction for our clustering model and a variety of other model assumptions, which are described in the figure caption. We conclude that background fractions between 10 and 15% can account for the observed P/T .

The minimum amount of background contamination inferred from the P/T considerations ($\sim 10\%$) is fairly large and highly uncertain. For an average field from the multiaperture survey, and assuming that background galaxies are distributed uniformly and drawn from a Schechter luminosity function (Eq. 3.1), we estimate that 1 in 20 fields will contain an interloper. Therefore, we might expect 2 interlopers in our sample of 45 primaries or 3% of the total sample of 69 satellites; however,

this estimate is based on the parameters of the multiobject spectrographic survey. Because only primaries with satellite systems are listed in Table 3.2, the total number of primaries examined is significantly larger than the number of primaries listed in Table 3.2.

To estimate the number of background galaxies, independently from the P/T calculations, we present the following argument. The principal redshift catalog we used was Z-cat. We reidentified primaries that satisfy our criteria, given only the data in Z-cat, and compiled samples of isolated primary and primary+satellite(s) system⁵. There are 144 isolated primaries and 27 primary+satellite groups; a ratio of 5.3 isolated primaries for every primary+satellite systems⁶. Twenty of the primaries with satellites in our sample are purely from existing redshift catalogs, although not all from Z-cat. Assuming that the ratio of isolated primary to primary+satellite systems is 5.3, then we infer that in effect we searched 126 primaries. If one in twenty contributes an interloper, then there are 6 interlopers from this portion of the sample. There were 43 primaries involved in the MX and Argus searches. Because these were not selected on the grounds of having apparent companions, these contribute only 2 interlopers (from the earlier estimate of 1/20th of an interloper/primary). Eight interlopers correspond to 12% of the sample, which is in accordance with the estimates from the P/T argument.

In conclusion, we find that there is indeed an overabundance of apparent satellites with positive recessional velocities, and that the presence of background galaxies in the sample, whose distribution in velocity space has been distorted by the

⁵Recall that when selecting primaries for the sample we also examined the fields visually on POSS or ESO plates for nearby companions and searched through additional redshift and magnitude catalogs.

⁶The appropriate number is probably lower since the redshift search in fields where satellites were found is likely to be more complete (i.e., there is a positive correlation between the completion level of the redshift search in a given field and the probability of finding a satellite).

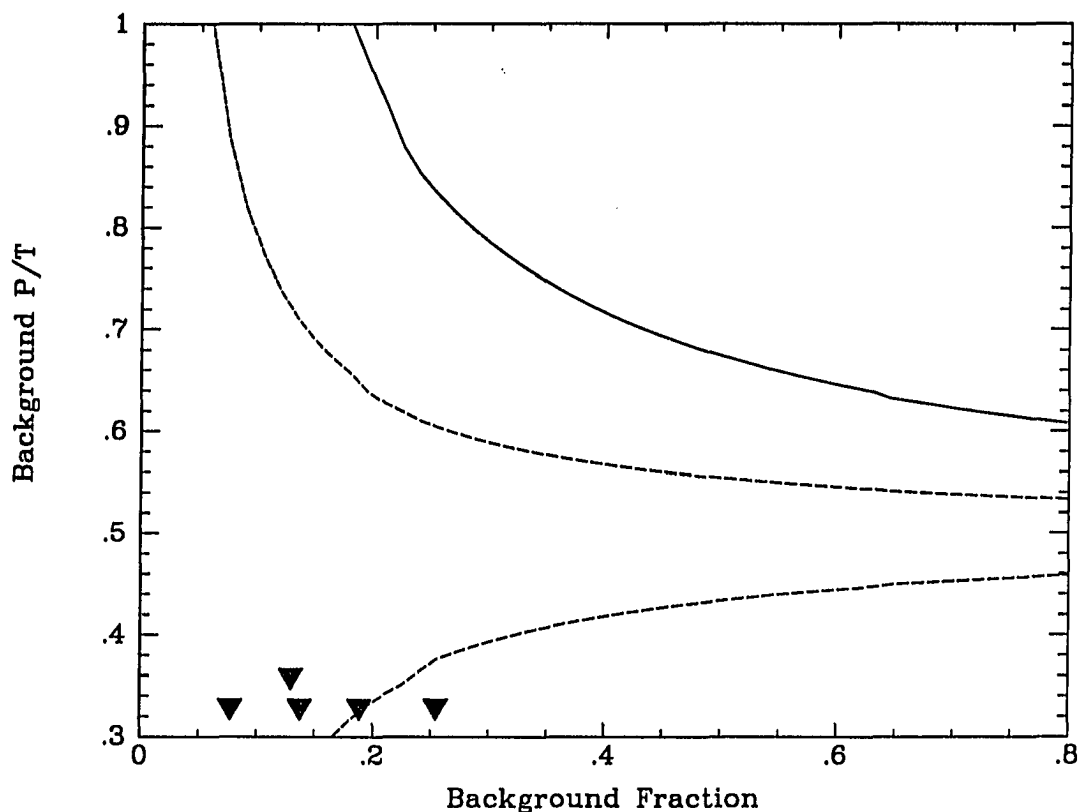


Figure 3.13: *Minimum P/T of Background vs. Background Fraction* : Minimum background P/T required to account for the observed P/T , for a particular background fraction, is plotted for 0 (solid line) and 1 and 2 σ confidence limits. The curves plotted correspond to models with no galaxy clustering. The triangles denote the background fraction required to produce the observed P/T for chosen clustering properties and adopted P/T 's for physical satellites ($\equiv P/T_S$). The cluster model is that discussed in the text. From left to right the triangles represent the following models (1σ lower limits on required background fraction in parenthesis): Clustering and $P/T_S = 0.52$ (0.078); Clustering and $P/T_S = 0.51$ (0.130); Clustering (only including clusters with more than 3 observed members and $P/T_S = 0.50$ (0.138); Clustering and $P/T_S = 0.50$ (0.189); No clustering and $P/T_S = 0.50$ (0.255; this model corresponds to the plotted curves).

selection effects and by their propensity to cluster, can produce a similar result. If the percentage of contamination is as expected, then the significance of the observed effect is reduced to $\sim 1\sigma$.

3.3.2 Identifying Interlopers

Unfortunately, there is no guaranteed method for culling interlopers. The properties of interlopers are difficult to quantify. An interloper is a galaxy that appears to be close to the primary on the sky, but whose real distance is sufficiently large that its motion is not dominated by the potential of the primary. Hence, interlopers contain little or no information about the potential of the primary and dilute the information provided by physical companions. To help us identify the interlopers, we compiled the following list of their characteristics:

Preferentially positive velocities - Most likely, 60% or more of the interlopers will have positive recessional velocities with respect to the primary.

Preferentially large projected separations - Because there is more sky at large separations, the background galaxies are preferentially found at large projected separation.

Crowded Environs - As demonstrated in §3.3.1, interlopers are most likely found in systems with many apparent companions. Also, a crowded nearby environment suggests that the candidate satellite may be a projected background galaxy.

Off-line in the Tully-Fisher diagram - If the rotation width and inclination data exist for the candidate satellite, the absolute magnitude derived from the H I width can be compared with that implied by

its association with the primary. Unfortunately, H I widths are unavailable for most satellites and inclinations are poorly determined.

Precise observations are needed for this technique.

When identifying interlopers, we prefer to err in the direction that will minimize the derived mass. Because the aim of the project is to determine if a definitive case for medium to large halos in spiral galaxies exists, any suspicious data that would lead to that conclusion must be rejected. However, one must be especially careful not to create artificially a sample that agrees with a preconceived notion of a Keplerian falloff. We have divided the background candidates into three groups based on their position in the $r_p - |\Delta v|$ plane. In Figure 3.14 all satellites are plotted in the $r_p - |\Delta v|$ plane and coded according to our opinion of the likelihood that they are interlopers. The open circles denote likely interlopers; satellites 13,14,30,54, and 68. Besides being the five objects with the largest $|\Delta v|$'s, they all have positive velocity differences, three belong to satellite groups of 3 or more members, another lies in a field classified as crowded, and, as would be expected from our model, 4 out of 5 come from existing redshift catalogs. The open triangles denote objects which *may* be interlopers (chosen entirely by prejudice); satellites 1,2,8,15,17,40 and 62. Rejecting these satellites creates a Keplerian falloff, decreases the maximum $|\Delta v|$ to 200 km s^{-1} , and removes more galaxies from the sample than the estimated number of interlopers. Eliminating these is an example of how background rejection can make a sample appear as if it were drawn from a small point mass potential. Unlike the first five objects, this sample does not have any particularly peculiar qualities, again arguing that at least most of these should not be removed. We only examine this sample to place conservative lower limits on our results. Our preferred sample excludes *only* the first group of five objects. We have removed these objects from the sample for the remainder of this chapter.

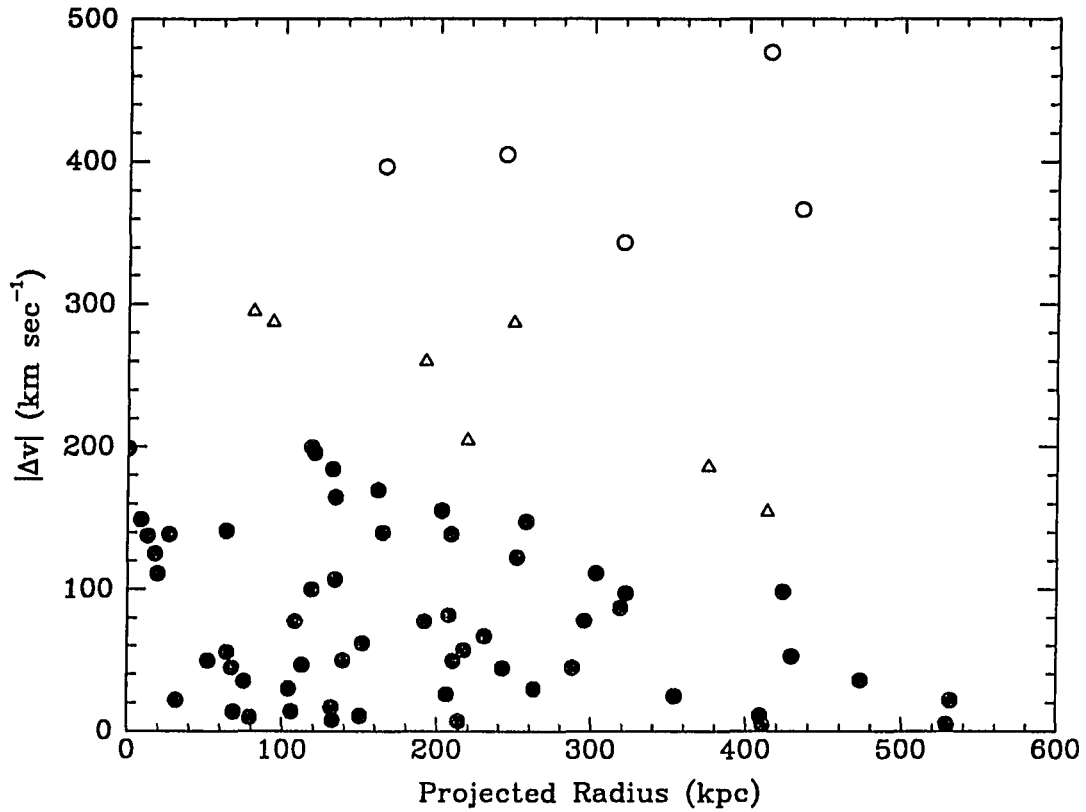


Figure 3.14: *Possible Interlopers in the $r_p-|\Delta v|$ Plane : The open circles represent the objects that are almost certainly interlopers. The open triangles represent an overly liberal selection of interlopers. The closed circles represent the remainder of the satellites.*

3.3.3 The Number of Satellites

Using our data we have estimated the number of satellites per late-type spiral galaxy. Unfortunately, this was not straightforward because the sample was drawn from a variety of sources. The most reliable data come from the ARGUS survey because

it is almost complete to its magnitude limit for a known area of sky around each galaxy. The MX survey is the next best subsample. Although it is less complete than the ARGUS survey due to observational problems (cf. §3.2), it is superior to the catalog data. The catalog data are the poorest because the completeness level and selection parameters are unknown. The ARGUS survey covered 22 primaries, of which 14 had at least one satellite. The distribution of the number of satellites found per primary is presented in Figure 3.15. The average number of satellites found per primary is 1.05. For the MX sample, whose distribution is also presented in Fig 3.14, the mean drops to 0.71. The decrease is due both to pointing problems and to lower sensitivity. Both these numbers include satellites around primaries that were found solely in the existing redshift catalogs (3 for ARGUS primaries, 1 for MX primaries). They were not found in the multiobject surveys because they were beyond the range of projected separations probed by the spectrometers. For each of these surveys, as opposed to the existing catalogs, we know the number of primaries for which no satellite was observed. In §3.3.1, we claimed that 1 out of every 6.3 primaries in Z-cat, down to Z-cat's "magnitude limit", has at least one satellite. From this, we infer that for the catalog subsample there correspond 101 primaries with no satellites. Therefore, this subsample averages about 0.23 satellites/primary. This average is much lower than for the multiobject surveys because the sensitivity and completeness of the survey are much lower. We conclude from the multiobject surveys that Sc type galaxies average about 1 satellite brighter than 18.5 mag to projected radii between 200 and 300 kpc. This result is in agreement with the results of Lorrimer *et al.* (1991).

In Figure 3.15, we compare the distribution of satellites/primary with Poisson distributions. Both the ARGUS and MX data agree well with Poisson distributions. The catalog data appear to have a larger tail than expected, but the numbers are

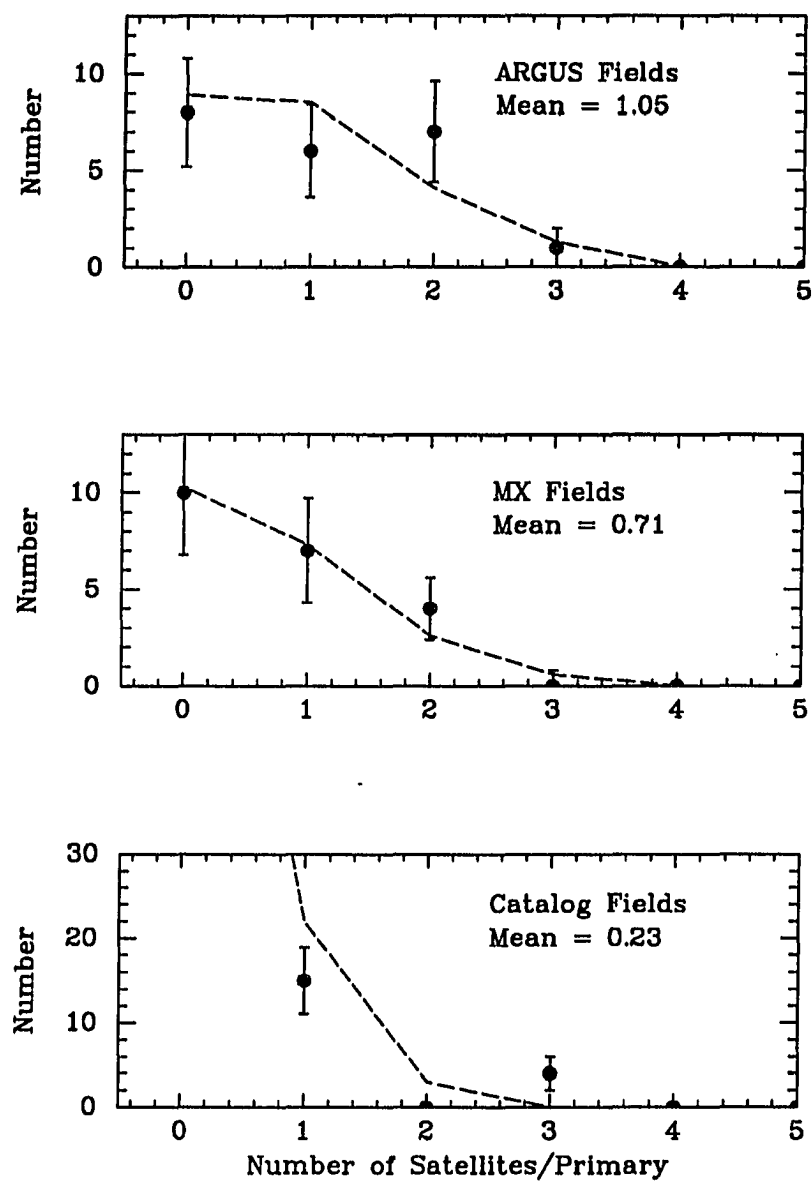


Figure 3.15: *Distributions of Satellites per Primary for Various Subsamples : Solid circles denote actual count and dashed lines denote Poisson distribution with given means.*

small. We suspect that the tail exists because of contamination by interlopers. As mentioned in §3.3.1 the largest groups are likely to possess some additional interlopers. Three out of the five galaxies most likely to be interlopers (cf. §3.3.2) belong to groups with three or more members, although these interloping satellites have already been removed. We find that the distribution of satellites is consistent with Poisson statistics. Using this conclusion, and a mean of 1 satellite per primary, we can demonstrate the true rarity of many-satellite systems. For example, the probability of having a five member group, like that around NGC 1961, among groups with one or more satellites, is 0.005, but we found 1 in 45 (a probability of 0.022).

It is possible that more massive galaxies have more satellites. Holmberg (1969) found no correlation between number of satellites and primary mass. However, his determination of number of satellites per primary has large uncertainties since he had no velocity information and only probed out to 50 kpc. We considered the possibility of a correlation between H I rotation width and number of satellites. In Figure 3.16 we display the number of satellites vs. H I line width, possibly a measure of mass, only for fields observed with a multiaperture spectrograph. There is a marked shift in both the mean H I line width (marked by the vertical bar) and the median line width (marked by the open triangle). However, the hypothesis that the distributions have the same mean can be ruled out only with 84% confidence. Such a shift could be the result of our definition of a satellite, which would allow a brighter galaxy to draw companions from further up the luminosity function than could a fainter galaxy. However, because there is no significant difference among the magnitude distributions of the satellites in the two classes, this bias does not appear to be important.

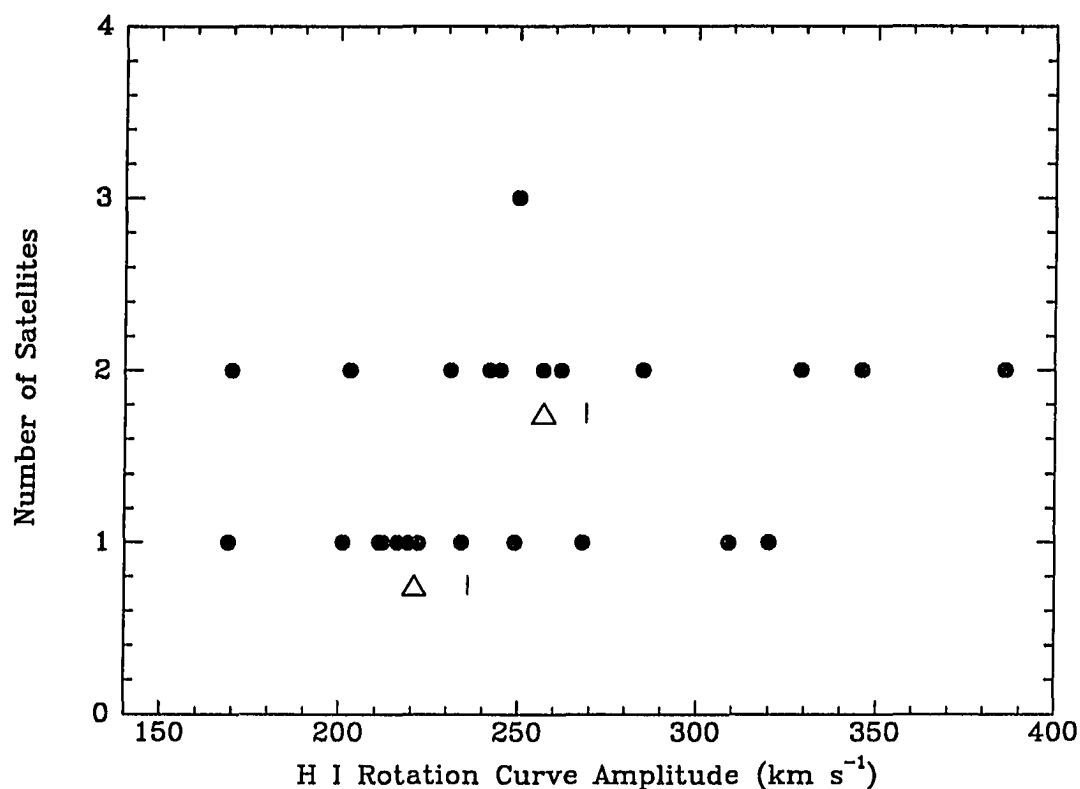


Figure 3.16: *Number of Satellites vs. Primary Rotation Curve Amplitude : The open triangles represent the medians of the distributions and the vertical bars the means.*

3.3.4 The Radial Distribution of Satellites

Studies of the correlation function at small separations have concluded that the correlation function can be modeled by a power-law with index ~ -1.8 (Lake and Tremaine 1980, Lorrimer *et al.* 1991). We display the projected radius distribution of satellites and the surface density of satellites in our sample in Figure 3.17. Also

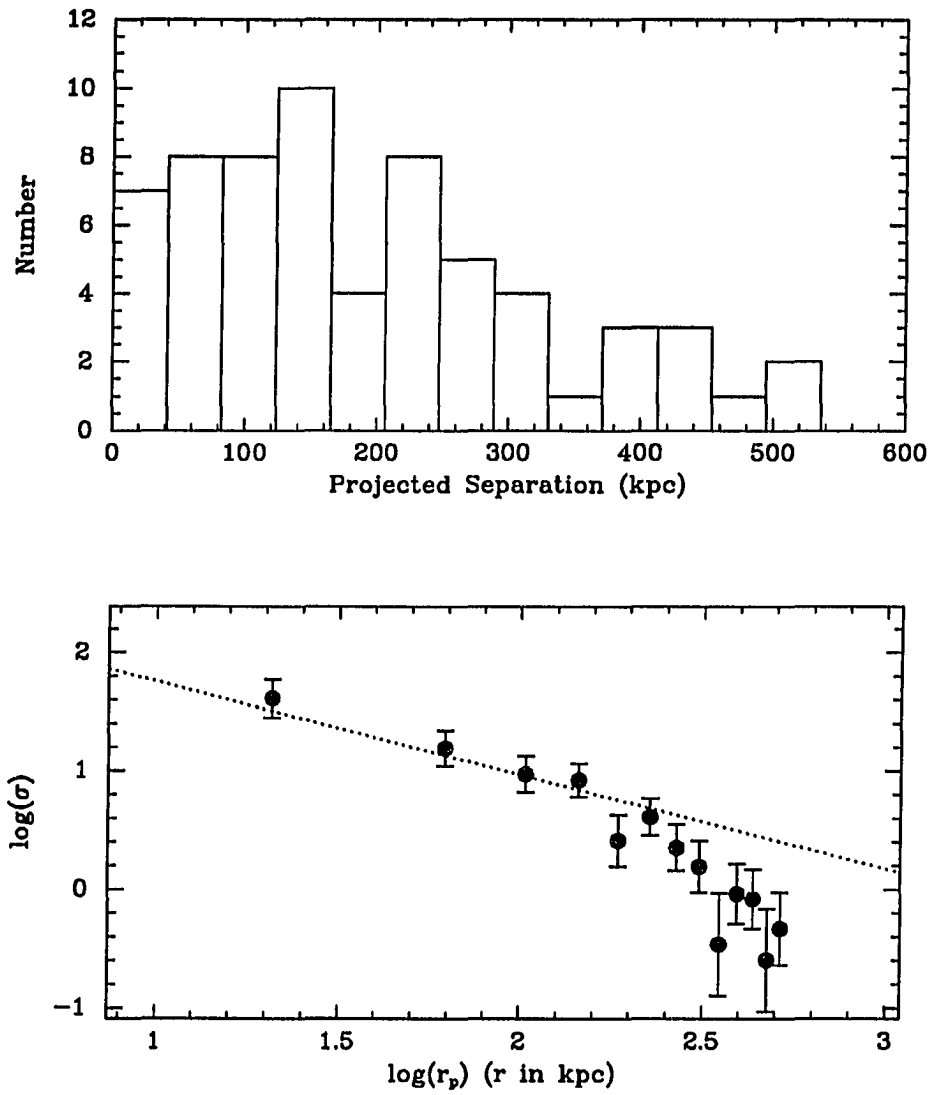


Figure 3.17: *Distribution of Projected Separations : Histogram of projected separations for satellites in the sample presented in upper panel. Number surface density of satellites vs. projected separations is presented in lower panel. Distribution from $\rho \propto r^{-1.8}$ (dotted line) is also shown.*

drawn is the surface number density corresponding to $\rho \propto r^{-1.8}$ (dotted line). This number density profile is consistent with our data for $r_p < 300$ kpc ($\log r_p < 2.48$). The best-fit power law to the radial surface density profile has an index of -1.0 ± 0.2 , which implies $\rho \propto r^{-2.0 \pm 0.2}$. There is a marked deviation from the straight power-law for $r_p > 300$ kpc that we attribute to lack of coverage at those radii in the multiaperture surveys.

3.3.5 The 2-Dimensional Distribution of Satellites

The 3-dimensional distribution of satellites contains important information for those studying the interaction between the disk, halo, and satellites. For example, one could ascertain if the satellites were formed in a disk system, if they formed on the same plane as the galactic disk, and if polar and disk orbits are stable. It would also allow us to refine the models presented in the next chapter. Unfortunately, only the projected distribution of satellites is observed, and so only some information can be retrieved. We investigated the azimuthal distribution of the satellites with respect to the disk major axis. Holmberg (1969) observed a statistical excess of objects along the disk minor axis out to a projected radius of 50 kpc. This has become known as the Holmberg effect; however, it lacks a quantitative physical explanation and observational confirmation. We attempted to confirm this effect and investigate whether it extends beyond 50 kpc. Major-axis position angles and satellite position angles were measured for all the primaries and satellites from POSS and ESO plates and are described in §3.1 and presented in Table 3.2. In Fig 3.18 we have plotted the distribution of satellite angles versus their projected separation for satellites of primary galaxies with inclinations greater than 45° . “Edge-on” galaxies were chosen

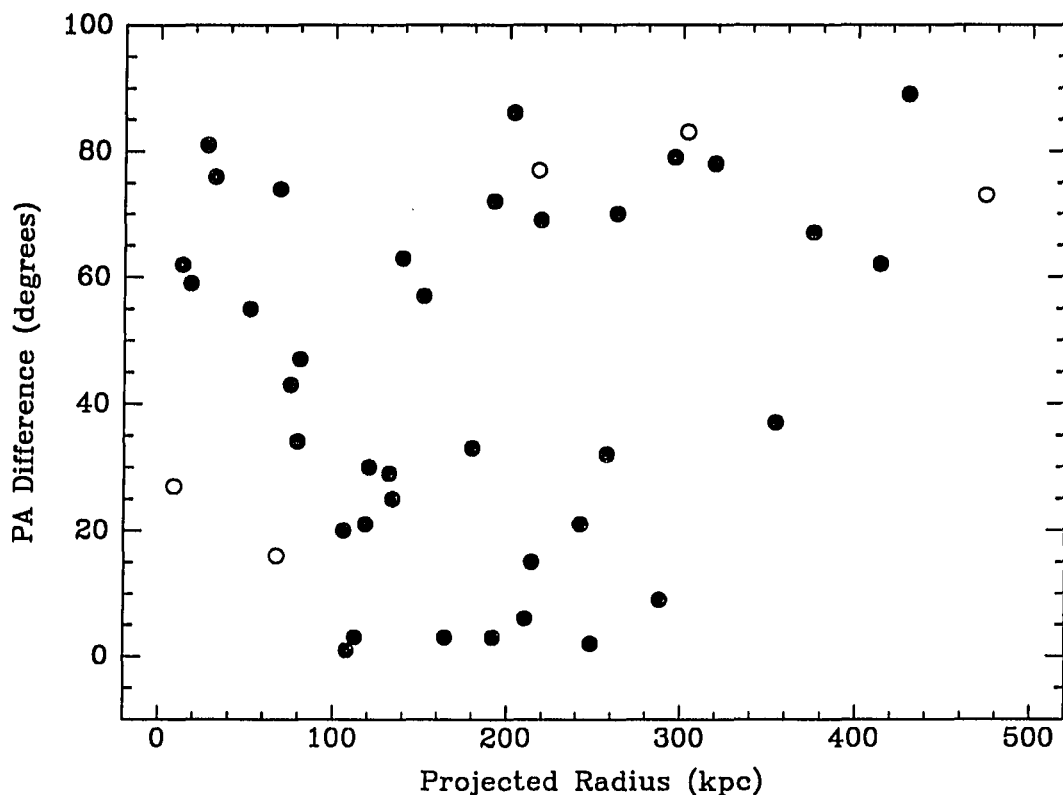


Figure 3.18: *Position Angle Difference Scatterplot : The difference between the primary's major axis PA and the satellite's position PA are given for primaries with inclinations greater than 50° (solid circles). The open circles denote data for primaries with inclinations less than 50° , but greater than 45° .*

so that there was a well-defined major axis. Satellites of primaries with inclinations less than 50° , but still greater than 45° , are designated with open circles. There is an apparent lack of objects for $r_p < 50$ kpc and small angles (*i.e.*, along the major axis); however, because of the few points in this region, a KS test does not significantly differentiate ($> 2\sigma$) between the observed distribution and a uniform one. We conclude that the data do not contradict Holmberg's result, but more

data are necessary to reach statistically significant conclusions. The distribution of angles appears uniform beyond radii of 100 kpc.

3.3.6 The Characteristics of the Satellites

We do not have the data to present a detailed study of satellites that includes surface photometry, chemical abundance determinations, and star formation rates, although such a study would be extremely informative. However, we do have some potentially interesting preliminary information about the satellites.

Morphological Type

From our visual inspection of the fields, we observed that there is a clearly identifiable subclass of objects (Nos. 4, 8, 32, 38, 40, 44, 45, 46, 49, 53, 65, 66, 69). This subclass is roughly defined as large satellites (>1 arcmin semi-major axis) of low surface brightness. The identifications were done visually, so the surface brightness results are not quantitative. We can only stress that the difference between these objects and the rest of the sample is obvious. In addition, these galaxies appear to lie at large projected separations, indicating that they are at large real separations from the primaries (see Figure 3.19). We conclude from a KS test that the hypothesis that these galaxies were drawn from the same distribution of projected separation as the rest of the sample can be ruled out with 98.8% confidence (2.5σ). However, we stress that these galaxies, while distinct from the remainder of the sample, are not the extremely low-surface brightness galaxies discussed by Impey, Bothun, and Malin (1988) and Bothun *et al.* (1990). All of these galaxies are easily seen on POSS or ESO survey plates.

We have also investigated the claim by Einasto *et al.* (1974) that early-type companions are located nearer to the primary than late-type companions. Certainly,

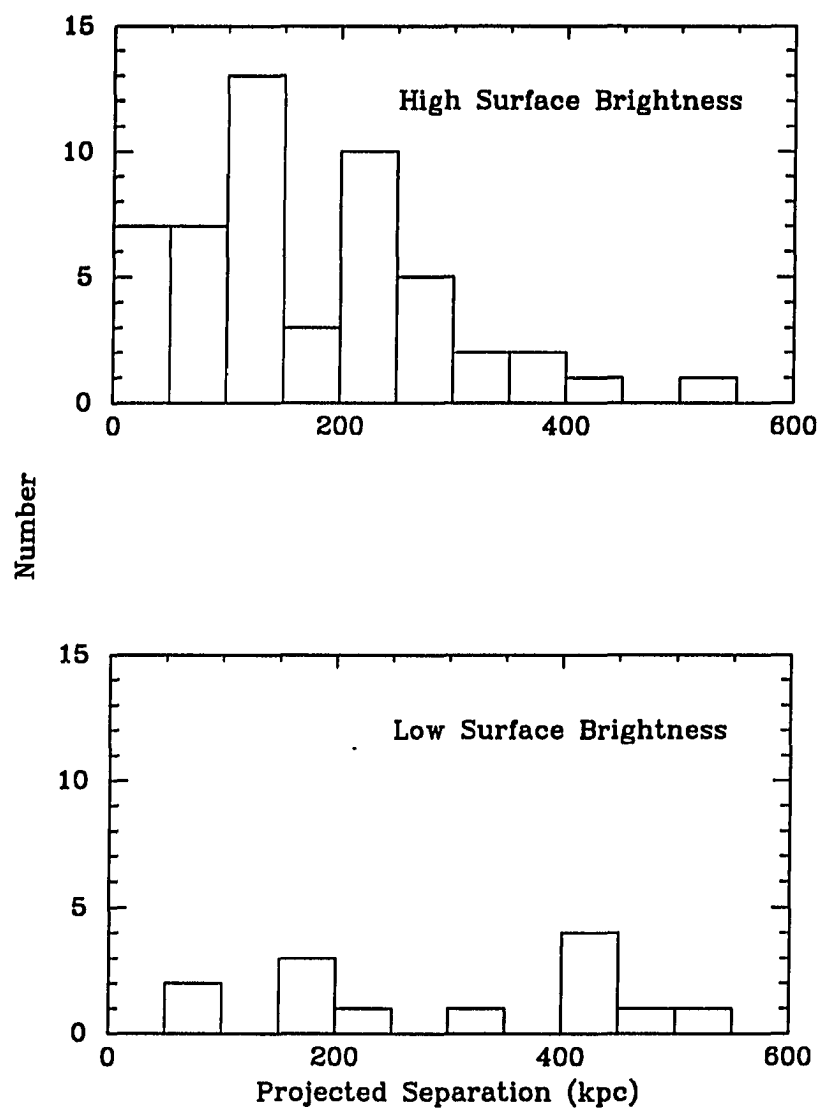


Figure 3.19: *Surface Brightness vs. Projected Separation*

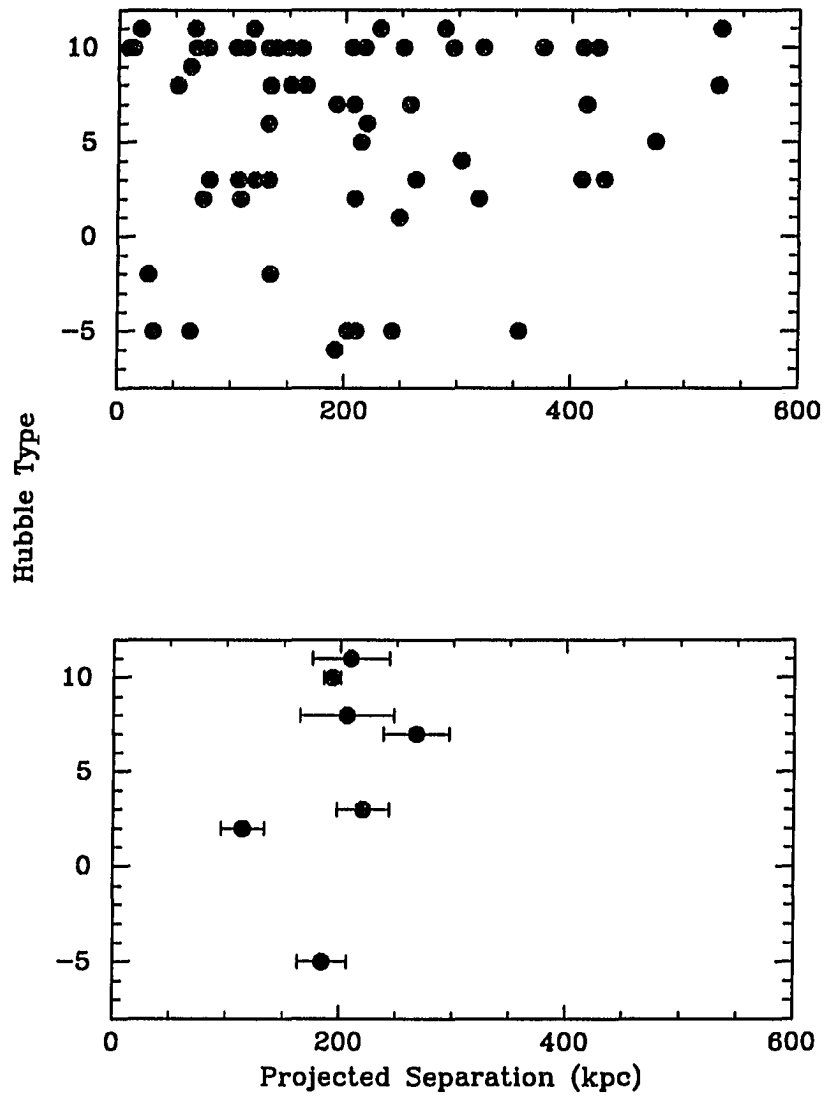


Figure 3.20: *Hubble Type vs. Projected Separation* : The upper panel contains the individual data. The bottom panel contains the averages for galaxy type bins with three or more members.

the class of objects described above supports their contention. In Figure 3.20 we have plotted Hubble type vs. projected radius for the satellites. In the top panel are the data from Table 3.2. Hubble types are denoted numerically according to the system described by de Vaucouleurs, de Vaucouleurs, and Corwin, Jr. (1976; RC2). Larger numbers denote later types. The means and standard deviations for types for which we have at least three member galaxies are shown in the bottom panel. There is a slight hint of a trend of increasing projected separation for later types. If the data are binned into early types (-6 to 3) and late types (7 - 11), then the means, 187 kpc for early types and 218 kpc for late types, are different (and in the claimed direction); however, from a Student t -test we cannot exclude the hypothesis that the means are the same with significant confidence. Therefore, we conclude that there is no quantitative support for the effect claimed by Einasto *et al.* (1974).

Emission vs. Absorption Spectra

We also classified satellites by their spectral characteristics. Crudely, the presence of emission or absorption lines is an indication of the age and star formation activity of the system. In Figure 3.21 we have plotted the distribution of projected separations for satellites whose spectra are dominated by absorption or emission lines, or whose spectra have both prominent absorption and emission lines. We could do this only for the 43 satellites for which we have spectra. Again we are hampered by small numbers, but there is no quantitative evidence of differing spatial distributions among the different classes of objects despite the apparent excess of emission objects at small r_p .

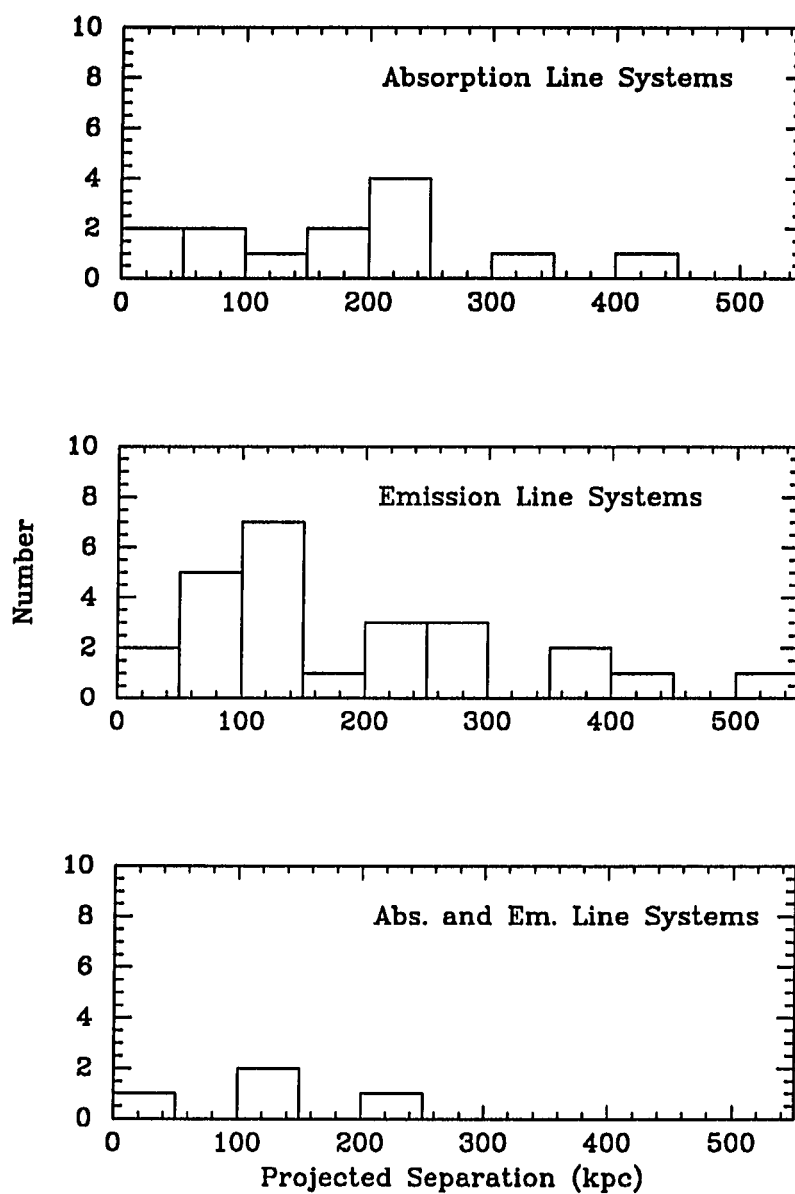


Figure 3.21: *Comparison of Absorption and Emission Line Systems*

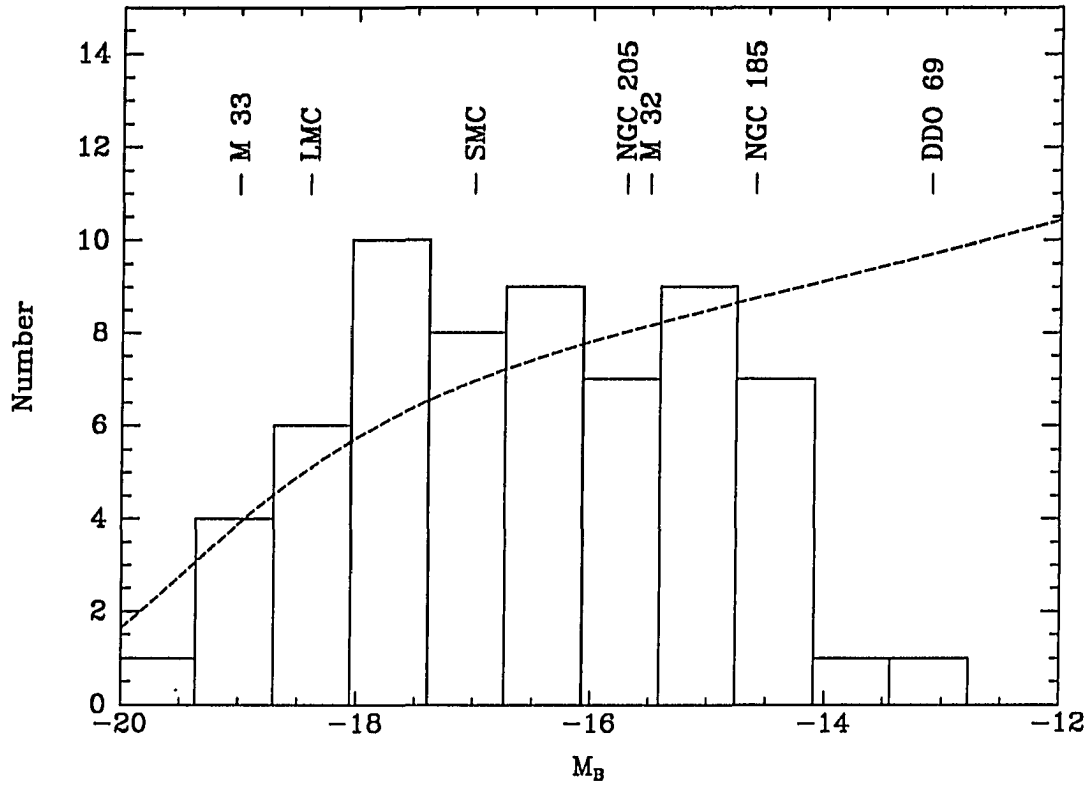


Figure 3.22: *Satellite Luminosity Function : Blue absolute magnitudes for Local Group members are designated for comparison. Also plotted is Schechter luminosity function.*

Luminosity Function

Despite some crudely determined magnitudes, we compiled the satellite luminosity function. This luminosity function is subject to variable incompleteness at the faint end. Uncertainties are also difficult to quantify at the bright end because of variable limits imposed by the selection criteria. We have used the data in Table 3.2 to

compile the luminosity function shown in Figure 3.22, but have not attempted to account for incompleteness. While the numbers are small, the shape is in general agreement with that of the Schechter luminosity function. This agreement is possibly fortuitous since the distribution of luminosities is strongly affected by selection effects at both the bright and faint ends. In Figure 3.22 we have plotted a Schechter function with $\alpha = -1.07$, $L_* = 2.06 \times 10^{10} L_\odot$ (cf. Eq. 3.1), and a normalization constant set to match the observations. The normalization constraint does not have physical significance because the completeness level is poorly determined for the entire sample. There is no evidence for strong peculiarities in the luminosity function. Note that most of the satellites are fainter than the LMC, but brighter than the major satellites of M31.

Size Distribution

The sizes of satellites, most notably globular clusters, have been used to deduce the mass of our galaxy by applying tidal radii arguments (cf. Innanen, Harris, and Webbink 1983). The precision of this type of argument is degraded by uncertainties in the orbits and by the details of the tidal stripping mechanism; however, a trend of increasing radii with increasing separation is observed (for globular clusters in our galaxy and M 31, see Cohen and Freeman 1991).

Signs of tidal limiting might be observable in our satellite galaxy data. In Figure 3.23, we plot the satellites' semi-major axes versus their projected separation from the primary. There is a marginally significant (0.90 confidence level) correlation present (rank correlation coefficient = 0.21). If we consider satellites with projected separations less than 200 kpc, then the correlation coefficient is 0.33 and the probability that such a correlation is produced by random fluctuations is only 0.06. Because projection effects decrease the significance of any existing correlation, we conclude that there is evidence for a correlation between size and projected radius

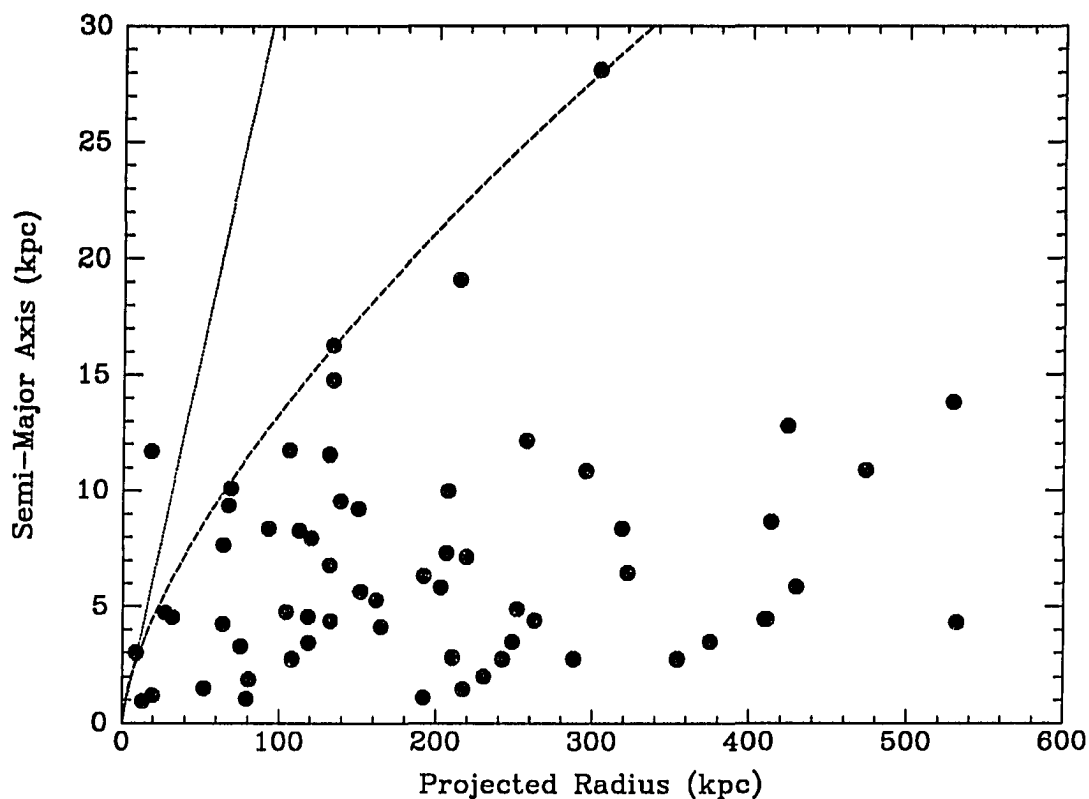


Figure 3.23: *Semi-Major Axis vs. Projected Separation*

in the satellite sample, at least to projected radii of 200 kpc.

To investigate whether such a correlation could be the result of tidal truncation, we also plotted in Figure 3.23 lines that indicate the radii predicted using the standard tidal radius formula (cf. Binney and Tremaine 1987) and assumed circular orbits. The dotted line was derived assuming that the ratio of the companion mass to primary mass is 0.01. Smaller ratios would move the line downward. The dashed line was derived assuming that the primaries can be modeled by an isothermal sphere with $v_c = 250 \text{ km s}^{-1}$, which is the average v_c for our sample, and that

the companions have a mass of $1 \times 10^{11} M_{\odot}$. These standard assumptions lead to tidal radii that are consistent with the observed radii (*i.e.*, only one object with a radius larger than the predicted tidal radius). Although most satellites are much smaller than predicted by the application of the tidal radius formula, we cannot discriminate between the possibility that the sizes reflect the tidal radii imposed when the satellites were much nearer the center of the galaxy (*e.g.*, pericenter on a radial orbit), or that their sizes were not determined by tidal truncation.

3.3.7 The Angular Momentum of Primaries and Satellites

An important part of the data we have obtained is the direction of rotation of most of the primaries. We can now determine whether satellite galaxy orbits are preferentially prograde or retrograde with respect to the disk. Because for nearly edge-on primary galaxies the distinction between prograde and retrograde orbits is clearer, we will again use the subsample of primaries with inclinations greater than 45° . In Figure 3.24 we present the distribution of satellites in the $r_p - |\Delta v|$ plane with retrograde satellites coded by open circles and prograde ones by filled circles, and in Table 3.6 we identify the satellites on prograde and retrograde orbits. Note that the number of satellites on prograde orbits (17) is approximately the same as the number on retrograde orbits (18). However, the prograde orbits appear to have on average greater $|\Delta v|$. A KS test rules out the hypothesis that the samples were drawn from the same parent population with 99.6% confidence. Keel (1991) reported a similar result for binary galaxies. The hypothesis that the projected separation distributions came from the same parent population cannot be ruled out with significant confidence. We examined whether there is a relationship between the nature of the orbit and the PA of the satellite (*e.g.*, prograde orbits lie in the disk plane), but found none. The only observable that appeared to be different among the prograde and retrograde samples was the absolute magnitude of the satellites.

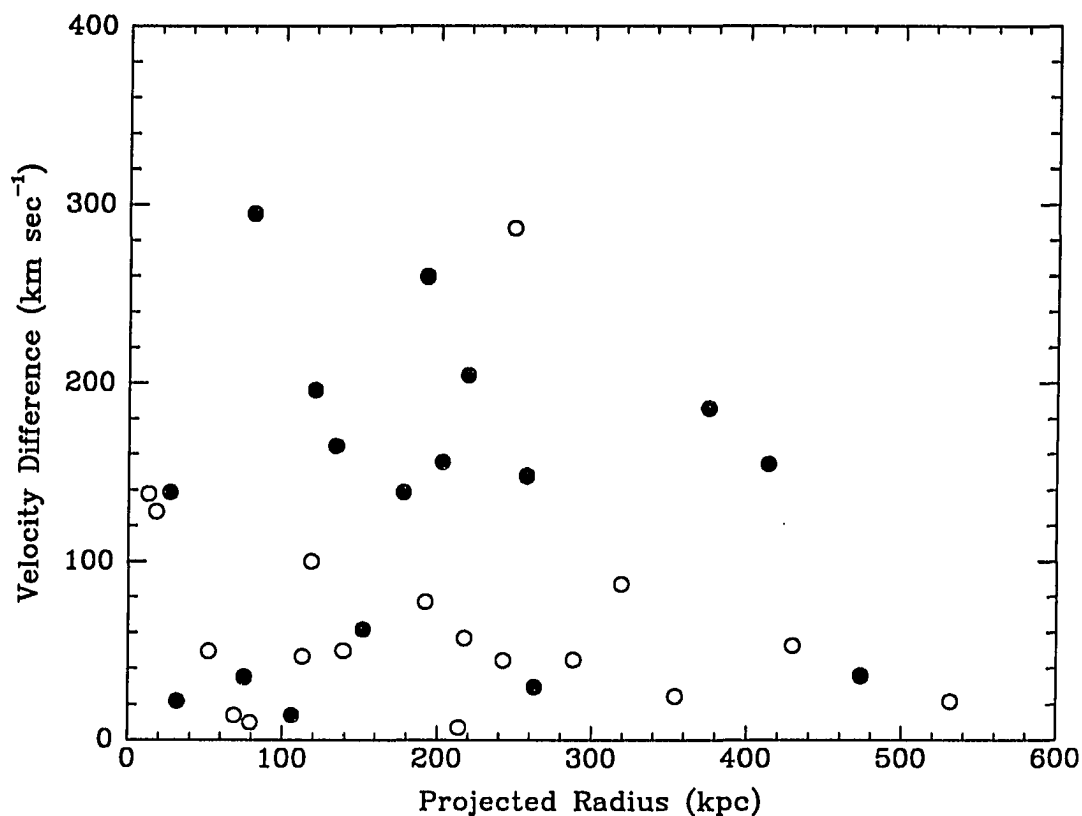


Figure 3.24: *Prograde and Retrograde Orbits : Satellites on prograde orbits represented by filled circles and those on retrograde orbits by open circles.*

The satellites on retrograde orbits are in general fainter than those on prograde orbits. A KS test rules out the hypothesis that both samples were drawn from the same parent distribution of magnitudes with 95.9% confidence. We conclude that there appears to be a deficit of fast retrograde orbits and that those satellites on retrograde orbits are fainter than those on prograde orbits. One explanation for the asymmetry in velocity differences is that the typical halo rotates with a velocity of $\sim 100 \text{ km s}^{-1}$ in the same sense as the disk. If the velocity dispersion of the system is then of order 100 km s^{-1} , then one would not expect to find satellites

with large retrograde velocities. However, the difficulty with this explanation is that the number of prograde and retrograde orbits are nearly the same.

Table 3.6: Prograde and Retrograde Satellites

Sample	Satellites
Prograde	2,5,8,9,12,15,21,26,33,37,40,41,50,52,53,62,65
Retrograde	1,10,11,22,23,24,27,28,44,45,46,51,57,58,59,63,66,67

3.4 Summary

In this chapter we have described the following:

- 1) our selection criteria, which are critical to providing a well-defined isolated sample of primary galaxies and a sample of satellite galaxies,
- 2) the multiobject spectroscopic redshift survey undertaken to find additional satellite galaxies,
- 3) the observations undertaken to obtain velocities with uncertainties less than 20 km s^{-1} for the primary and satellite galaxies,
- 4) the organization of a satellite database that was used to investigate the characteristics of satellite galaxies,
- 5) the excess of apparent satellites that have recessional velocities larger than the primary's velocity and the modeling done to understand how the effect arises from the combination of selection effects and interloping galaxies,

- 6) the distribution of satellites per primary,
- 7) the radial and azimuthal number density distributions of satellites around primary galaxies,
- 8) the general trend of finding more diffuse satellite galaxies at larger separations, and
- 9) the lack of fast retrograde orbits.

We have presented the collection and a first look at an interesting, yet almost entirely unexplored constituent of the family of galaxies. The collection of this data is the first and critical step in our determination of the mass of spiral galaxies. In the next chapter, we discuss the dynamical analysis of the data.

Chapter 4

Spiral Galaxies and Satellite Dynamics : Analysis

4.1 Introduction

We now proceed to use the data presented in the previous chapter to determine the mass distribution in the halos of late-type unbarred spiral galaxies. This is a specific case of a classic problem in astronomy: to derive the mass of one body from its gravitational effect on a nearby body. For many binary stars, one can observe a complete orbit within a reasonable amount of time and from those observations determine the orbital parameters and subsequently the total mass of the system. For galaxies, the issue is more complex because the orbital periods are far too long for one to observe a noticeable fraction of an orbit. Instead, observations of an ensemble of companions must be treated in a statistical manner. An example of this approach is the use of the virial theorem to estimate the mass of galaxy clusters using projected positions and radial velocities of member galaxies (*e.g.*, Zwicky 1933; Smith 1936).

More recently, alternatives to the virial theorem mass estimator have been presented. Page (1952) constructed a mass estimator based on the mean value of the projected mass, $r_p(\Delta v)^2/G$, where r_p is the projected separation between the two

galaxies, Δv is the radial velocity difference between them, and G is the gravitational constant. The average of this quantity over many representative systems is equal to the typical mass of these systems, provided one includes a proportionality factor k (*i.e.*, $M = k \langle r_p (\Delta v)^2 / G \rangle$). For example, one can observe many binary galaxy pairs to determine the mass of a typical binary *pair*. Because the mass of a satellite galaxy is negligible in comparison to the mass of a primary galaxy, the projected-mass estimator can be used in conjunction with our satellite galaxy sample to estimate the mass of typical *isolated* spiral galaxies. The constant k contains statistical corrections for projection, selection effects, and the nature of the orbits. For example, the value of k depends on whether the companions are on predominantly radial or circular orbits. Given a preferred model, one computes k analytically for simple models or computationally for more complex ones, and uses the observed mean value of $r(\Delta v)^2$ to determine M . Bahcall and Tremaine (1981) demonstrated that the projected-mass estimator is more statistically stable than the virial theorem estimator,

$$M = \frac{3\pi}{2G} \left(\sum_{i=1}^N (\Delta v)^2 \right) / \left(\sum_{i=1}^N \frac{1}{r_{p,i}} \right), \quad (4.1)$$

by using Monte-Carlo simulations of systems with known mass and comparing the results obtained with each technique. Projected-mass estimators have been applied to groups of galaxies (*e.g.*, Heisler, Tremaine, and Bahcall 1985) and to satellite and binary galaxy studies (*e.g.*, Erickson *et al.* 1987; Schweizer 1987; van Moorsel 1987). Another popular estimator is based on $(\Delta v)^2$ (hereafter the quantity $(\Delta v)^2$ will be written as Δv^2), which is appropriate for use with logarithmic potentials (*i.e.*, isothermal sphere models).

The estimator approach has several shortcomings. First, information is discarded when two dimensional data, $(r_p, \Delta v)$, are converted into a single number.

Two samples with the same mean value of the mass estimator, but with different distributions in the $r_p - |\Delta v|$ plane, are effectively indistinguishable. This shortcoming could be remedied by comparing the distributions, but typically is not. By ignoring the shape of the $r_p - |\Delta v|$ distribution information about the shape of the potential is squandered. Second, the estimator approach does not include the effects of the cosmological evolution of the halo. In a universe with a non-zero density parameter and a finite lifetime, dynamical evolution can significantly change the expected structure of the halo as a function of time (cf. Gott 1975), and thereby presumably affect the orbits of test particles, especially those at large separation. Third, the effect of practical difficulties such as observational uncertainties, selection criteria, and contamination have not been fully investigated and quantified. These difficulties become important in sample acquisition and could have serious consequences on inferences drawn from the data. Fourth, the orbits of companion galaxies are always assumed to have randomly distributed orbital phases. The strengths and weaknesses of this particular assumption are discussed in §§4.2 and 4.3. We believe that the secondary infall models, which we present in §4.3, represent progress in each of these trouble areas and that the sample of satellites discussed in Chapter 3 is superior for a variety of reasons to previous binary and satellite galaxy samples.

Our aim is to produce models that can be compared directly to the data. Often in this field, the expectations created by the “preferred” models have influenced the definition of the final working sample. The clearest example is the pruning of background contamination. We endeavored to provide an analysis that is as impervious to background contamination, and its removal, as possible. We also made a concerted effort to incorporate all of the information present in the data into our analysis. To accomplish this, we “observed” our models in a manner that allowed direct comparison to the data. The problem we are addressing is ambiguous and subtle; it is important to be as direct as possible with the analysis.

The discussion in this chapter progresses from the most popular, and most basic models, to the secondary infall models that we have developed and utilized. First, we examine the reliability and applicability of the random phase point mass estimator. We will conclude that the results obtained using this technique violate the assumptions incorporated into the technique. Then we examine the extended mass random phase models. We conclude that these are self-consistent, but that several possibly important aspects of the problem have been neglected. We believe that these aspects are especially important when analyzing the dynamics of a sample of objects at large separations. Unable to find a satisfactory existing model, we describe the development of models based on the models of halo formation described by Gott (1975), Gunn (1977), Fillmore and Goldreich (1984), and Bertschinger (1985). We discuss the development, properties, and implementation of these models. Finally, we conclude this chapter by discussing our inferences regarding the mass and extent of galactic halos.

4.2 Random Phase Models

Previous models of the dynamics of binary and satellite galaxies (except for timing arguments) have been based on the assumption of random orbital phases¹, which is that there is no relationship between the time at which the test particle is observed (*i.e.*, the current age of the system) and its orbital position. This assumption is valid for test particles that have completed many orbits because relatively small changes in the age of the system produce large changes in the particle's position. Because galaxies presumably formed at different times, the orbital phases of particles that have completed many orbits are randomly distributed. However, a satellite with a

¹The term orbital phase is equivalent to mean anomaly in the terminology of Keplerian orbits. See Goldstein (1980) for details of Keplerian orbits.

velocity of 100 km s^{-1} on a circular orbit of radius 100 kpc will have only completed slightly over 2 orbits in 14 Gyr. Therefore, the random phase assumption can only be entirely appropriate for samples where the mean separation between primary and companion is $< 100 \text{ kpc}$. Despite this, estimator techniques have been used to study samples of objects with mean separations $\gtrsim 100 \text{ kpc}$. We encountered a similar difficulty in the analysis of the mass of our galaxy in Chapter 2 and argued against the use of random phase statistical methods. There are three reasons why we begin our analysis with the random phase models: their prevalence in the literature, the lack of firm evidence that they do not work, and for the purpose of illustration.

4.2.1 Point-Mass Random-Phase Models

The point-mass random-phase models are the most popular because of their simplicity and because the null hypothesis is that galaxies do not have massive dark matter halos. For central point masses and no selection biases, Bahcall and Tremaine (1981) showed that

$$\langle q \rangle = \frac{\pi M}{32} (3 - 2 \langle e^2 \rangle), \quad (4.2)$$

where $q \equiv r_p \Delta v^2 / G$, M is the mass of the central object, and e is the orbital eccentricity of a test particle orbiting the central mass. They demonstrated that under the assumed circumstances this estimator is stable and reliable. Additionally, using

$$\langle q^2 \rangle = \frac{M^2}{35} (6 - 5 \langle e^2 \rangle), \quad (4.3)$$

the variance of q can be estimated. In principle, both M and $\langle e^2 \rangle$ can be determined using these equations. Unfortunately, because the averages cannot be calculated with sufficient accuracy given the small number of objects orbiting a single galaxy, e remains unknown. In our case, where we have an ensemble of satellites that orbit a variety of primaries, instead of many satellites orbiting a

single primary, we could not solve for e anyway since presumably the M 's are not all the same. Because the eccentricity of the orbits is unknown, M is generally determined using

$$M = \frac{24}{\pi} \langle r_p \Delta v^2 / G \rangle, \quad (4.4)$$

which corresponds to assuming that the orbital velocities are between purely radial and isotropically distributed. When treating an ensemble of primaries substitute $\langle M \rangle$ for M .

In practice many observational limitations affect the value of $\langle q \rangle$. For example, selection effects might cause a deficit of observed companions at small or large projected radii. Additionally, velocity difference criteria designed to minimize the number of interlopers may cause the rejection of physical companions with large $|\Delta v|$'s. The result of selection effects and the violation of model assumptions can only be fully investigated with the aid of computer simulations.

We used Monte-Carlo simulations of particles in Keplerian orbit to examine the importance of observational uncertainties, selection effects, and simplifying assumptions. Next we describe the prescription with which particles in Keplerian orbits were "observed". The orbital eccentricity was taken to be either fixed for all particles or was randomly drawn from a uniform distribution of values of e^2 . The latter choice corresponds to having isotropically distributed velocities at every radius. The energies were selected from the power-law probability distribution given by Bahcall and Tremaine,

$$p(E) = \begin{cases} (3-s)E^{s-4}/E_0^{s-3}, & \text{if } E > E_0; \\ 0, & \text{if } E \leq E_0, \end{cases} \quad (4.5)$$

where $s < 3$ and $E = (GM/r) - (v^2/2)$. This choice of $p(E)$ generates a number density profile of test particles that is proportional to r^{-s} for $E > E_0$. We chose $s = 2$ and $E_0 = 0.0065$ to have the simulated value of $\langle r_p \rangle$ match the observed one (~ 200 kpc). The mean anomaly (orbital phase) was selected from a uniform

distribution between 0 and 2π . This is the random phase assumption. Using the mean anomaly, the eccentric and true anomalies were calculated. The true anomaly is the more familiar polar angle, typically referred to as θ . Once the eccentricity, true anomaly, central mass, and energy were determined, the rest of the orbital parameters, most importantly velocity and position, were evaluated. The observed projected position and radial velocity were obtained by viewing the system from a random orientation. Any selection criteria and observational uncertainties were subsequently imposed. The projected-mass estimator was evaluated from the final set of simulated data.

We investigated the performance of the projected-mass estimator and the results are presented in Table 4.1. One hundred simulations were performed for samples of either 10, 100, or 200 particles, each of which orbits a different primary. From the hundred trials, we determined the mean and variance of the mass estimator for a particular model. Only one aspect of the standard model was varied at a time. The primary's mass was taken to be $10^{12}M_{\odot}$, except for model 11, for which we adopted a Gaussian distribution of masses with a mean of $10^{12}M_{\odot}$ and a dispersion of $3 \times 10^{11}M_{\odot}$. The secondary's mass was taken to be $5 \times 10^{10}M_{\odot}$, except for model 12, for which we adopted a mass of $2 \times 10^{11}M_{\odot}$. The orbital eccentricities were drawn from a uniform distribution of e^2 , except for models 7-10, for which we adopted fixed eccentricities. All models included an outer projected radius cutoff (500 kpc for all models except 6,7, and 8, which had a cutoff at 150 kpc) and an upper radial velocity difference cutoff (500 km s⁻¹). Observational uncertainties, when applied, were drawn from a Gaussian distribution with a dispersion of 20 km s⁻¹ for velocities and were uniformly distributed between $\pm 10\%$ for distances. The 10% distance uncertainty includes all sources of error, except the uncertainty in H_0 . Resulting masses and M/L 's scale with $1/H_0$ and H_0 respectively. For examining the internal consistency of the models, uncertainties in H_0 are irrelevant. For all

models except 4, where we used Eq. 4.4 (unknown e), we used Eq. 4.2 (known e) to determine the central mass. We used these models to demonstrate several important

Table 4.1: Point Mass Model Parameters and Results

Model No.	No. of Test Pts.	Description	Estimated Mass ^a ($10^{11} M_{\odot}$)
1	10	Idealized	9.7 ± 3.9
2	100	Idealized	10.1 ± 1.1
3	200	Idealized	10.0 ± 0.9
4	100	Unknown Eccentricity	14.9 ± 1.6
5	100	Vel. and Distance Errors	10.6 ± 1.3
6	100	r_p cutoff = 150 kpc	10.5 ± 1.4
7	100	r_p cutoff = 150, radial	13.5 ± 1.7
8	100	r_p cutoff = 150, circular	7.9 ± 0.9
9	100	Radial Orbits	9.8 ± 1.0
10	100	Circular Orbits	10.0 ± 1.1
11	100	Variable Primary Mass	10.1 ± 3.1
12	100	Massive Companion	11.1 ± 1.2
13	100	10% Background	34.2 ± 8.3
14	100	10% Background/Median	12.6 ± 2.7

^a True mass is 10. For models with variable mass, mean mass is 10.

points. The results from the first three models, the idealized models, support the claim of Bahcall and Tremaine (1981) that the estimator is accurate even with few test particles, and as expected the uncertainty decreases proportionally to the square root of the number of particles. There appears to be no compelling reason to obtain samples of more than 100 objects. Therefore, the remainder of the results are for 100 particle runs. To determine the mass for the next model (model 4) we used Eq. 4.4, which presumes no knowledge of the orbital eccentricities. The

result demonstrates, as does inspection of Eqs. 4.2-4.4, that a principal cause of uncertainty in this process is the unknown orbital eccentricity. Using the next model (model 5) we show that observational errors at the level present in this study are not a major cause of uncertainty in the mass determination. Observational scatter in the measured quantities decreases the precision slightly, but has a minimal effect on the accuracy. The next five models (6-10) demonstrate that observationally imposed projected radius cutoffs can produce significant errors for certain types of orbits. The “isotropic” orbits fare well, the more extreme models (7-8) have large errors. The discrepancies are not due simply to a difficulty with either radial or circular orbits (cf. models 9 and 10). As demonstrated with model 11, a normal distribution of primary masses with moderate dispersion ($3 \times 10^{11} M_{\odot}$) does not affect the accuracy of the result, but does decrease the precision. However, a pathological primary mass distribution could create a problem for this technique. For example, if there were two classes of galaxies in the sample, one with a small characteristic mass and the other with a large mass, the result from the projected mass estimator would not reflect that. Such a problem is unlikely for our sample because of the apparent homogeneity of primaries (see §3.1), but could be a problem with binary galaxies, which are typically less homogeneous (*e.g.*, pairs of mixed type). We also conclude that the projected mass estimator is reliable even when the companion’s mass is 20% of the primary’s mass (cf. model 12).

With model (13) we examined what is the most alarming problem. If 10% of the companions are background galaxies, then the estimated mass is several times greater than the true value. For our modeling, the background galaxies are assumed to be uniformly distributed in space. As discussed in Chapter 3, background rejection is a delicate process. The severity of the problem can be reduced by using a more stable statistical quantity (*i.e.*, less sensitive to outliers), such as the median

instead of the mean of q . The mean is traditionally used because it can be calculated analytically — an aesthetic, if somewhat anachronistic, reason. We present the result of the median projected-mass estimator for a model with 10% background contamination (cf. model 14). The correction factor k used for this model was derived from an idealized 200 particle run with isotropically distributed velocities. The result obtained by using the median estimator (model 14) is clearly superior to that obtained by using the average estimator (model 13). The eccentricity-dependence of the median projected-mass estimator is similar to that of the average estimator, about a factor of three change in k from radial to circular orbits. On the whole, the mass estimator *appears* to work well (errors $< 50\%$, usually better), especially when one models the selection effects involved in collecting the sample, when the model potential matches the real one, when the assumption of random phases is valid, and when interlopers have been removed or the median estimator is used. Unfortunately, these conditions do not usually apply.

Before proceeding, it is important to note that for our sample, information about the disk rotation velocity of each primary is also available. H I linewidths were taken from HR and references therein when available (for 37 primaries), or were estimated from M_B (for 8 primaries) using the Tully-Fisher relationship (Tully and Fisher 1977) normalized using the other 37 primaries. W 's, which are the primaries' inclination-corrected H I rotation curve amplitudes, complement the satellite data, which probe much larger galactocentric distances. The relationship between the disk rotation velocity, which depends on both the disk and halo mass distributions, and the halo circular velocity, which is the relevant parameter for most models, is unknown. We will treat two extreme cases. First, we postulate that there is so much scatter in the relationship between the halo velocity and W , that W contains almost no information about the halo circular velocity of that particular primary. In this case, we assume that all galaxies have the same mass or alternatively the

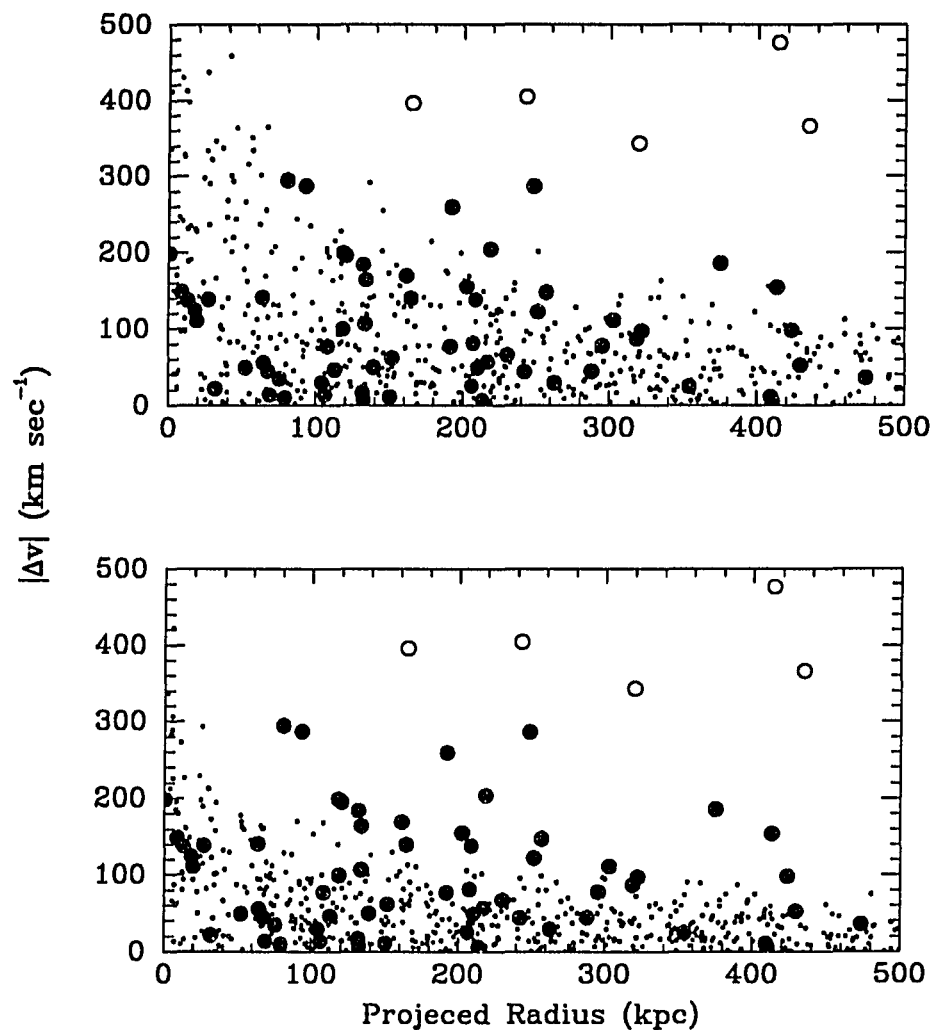


Figure 4.1: *Keplerian Simulations vs. Observations:* The top panel shows a comparison between the entire satellite dataset (filled circles are Sample 1) and the $M = 1.5 \times 10^{12} M_{\odot}$ Keplerian model (dots). The lower panel shows a comparison between the data and the $5 \times 10^{11} M_{\odot}$ Keplerian model.

same circular velocity at a given radius exterior to the disk region (case I). This case corresponds to using Eq. 4.4. We stress that such models should not imply rotation velocities that are grossly different from the observed W 's. Second, we postulate that W is directly proportional to the characteristic halo circular velocity. In this case, $M \propto W^2$ or $v_c \propto W$ (case II). For case II, Eq. 4.4 can be rewritten as

$$\langle M \rangle = \langle W^2 \rangle \frac{24}{\pi} \langle r_p \frac{\Delta v^2}{GW^2} \rangle. \quad (4.6)$$

Intermediate cases are also possible. Models that consider the contributions to the observed rotation curve from various mass components (*e.g.*, disk and halo) have concluded that the effects from the non-halo components can be significant (Bahcall, Schmidt, and Soneira 1982; Salucci and Frenk 1989). The case I and II nomenclature will be adopted for the remainder of this work to describe the adopted relationship between the halo characteristic velocity and the observed rotation amplitude.

Properly forewarned, we proceeded to analyze our data using the projected-mass estimator. The mass estimated for a typical primary in our sample using the average projected-mass estimator, no *a priori* knowledge of the orbital eccentricities, and a single primary mass (*i.e.*, Eq. 4.4; case I) is $1.0 \times 10^{13} M_{\odot}$. The mass estimated using the median estimator, assuming isotropically distributed orbital velocities, and case I is $1.5 \times 10^{12} M_{\odot}$. The estimated typical mass for case II, using the average projected-mass estimator given in Eq. 4.6, is $1.0 \times 10^{13} M_{\odot}$; using the median it is $2.2 \times 10^{12} M_{\odot}$.

The results from the average mass projected-estimator can easily be shown to

be unacceptably large. An isothermal halo that extends² to 500 kpc³ would need to have a rotation curve amplitude of 300 km s^{-1} , significantly greater than the average of the primaries in our sample (253 km s^{-1}), to have a total mass of $1.0 \times 10^{13} M_{\odot}$. Furthermore, since the average projected separation of the satellites is $\sim 200 \text{ kpc}$, most of the satellites do not sample the halo out to 500 kpc. If the typical halo extends to only 200 kpc, then the inferred rotation curve amplitude is 478 km s^{-1} . Because the models are for a point mass distribution, the discrepancy between the inferred rotation curve amplitude at small radii and the observed value is even worse. However, because we know that there is significant background contamination in our sample (cf. §3.3) and that background contamination inflates the mass estimate (cf. Table 4.1 model 13), it is not surprising that we derive such a large value for the mass. As shown previously, the median estimator is more robust; although, even these more conservative mass estimates imply that the halo extends beyond 100 kpc if the rotation curve amplitude is 250 km s^{-1} . Certainly this does not satisfy the point mass distribution assumption. Results for the other subsamples (defined in Table 4.2 and discussed in §3.3) are shown in Table 4.3.

We then investigated whether the point mass models provide a good fit to the satellite data despite the discrepancies with the observed W 's. In Figure 4.1, we overlaid the satellite data onto 1000 points drawn from a Keplerian model with a central mass of $1.5 \times 10^{12} M_{\odot}$, with isotropically distributed velocities, and with the appropriate selection criteria applied. Using the result from a KS test, we conclude

²The extent of dark matter halos has not been addressed by any direct observations. Typically a density profile is chosen and the extent is derived from the estimated total mass. The most popular choice for the halo density profile is $\rho \propto r^{-2}$ because this produces a flat rotation curve and is characteristic of isothermal spheres, which are simple to treat analytically. Both observationally (cf. Bahcall, Schmidt, and Soneira 1982) and theoretically (cf. Gunn 1977) halos are expected to have a nearly isothermal mass distribution, at least for the inner few tens of kpc. However, neither observationally nor theoretically can slightly different power-law density profiles be excluded (cf. Bahcall, Schmidt, and Soneira (1982); Lake and Feinswog (1989)).

³We consider 500 kpc as an upper limit of the halo, since we know that the majority of our satellites are not sampling the potential beyond 500 kpc (cf. §4.3.2 and Fig. 4.7).

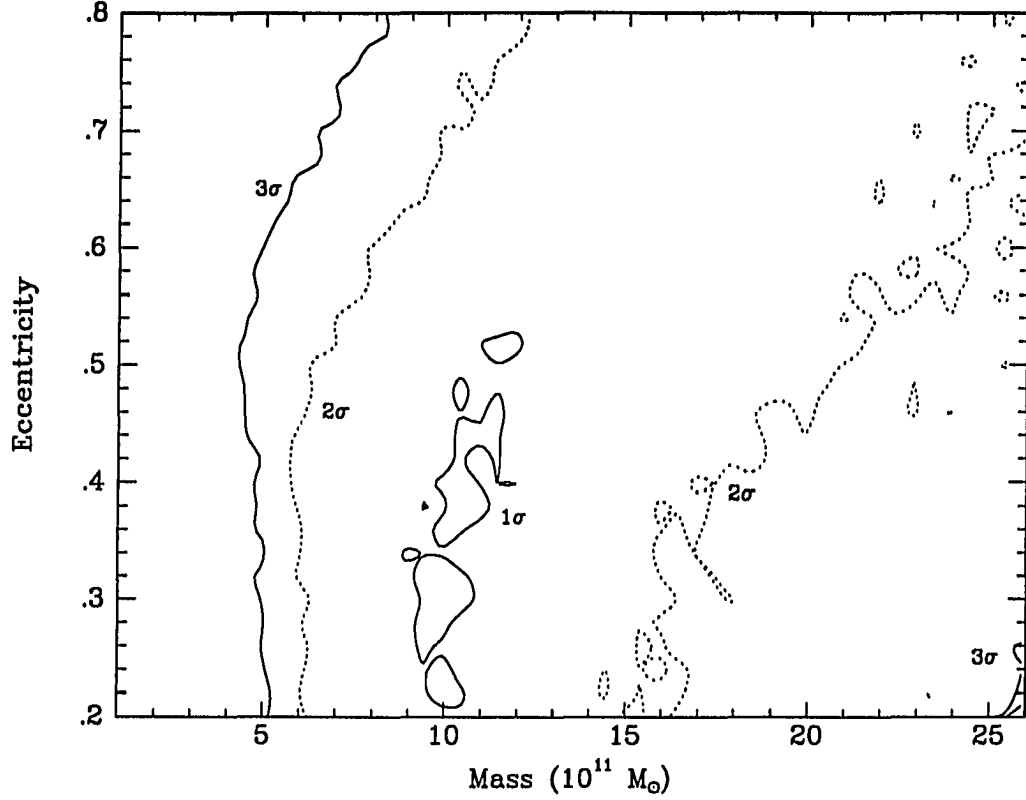


Figure 4.2: *Keplerian Simulations: 2-D KS Probe Through Parameter Space. Solid contours are 1 and 3 σ . Dotted contour is 2 σ .*

that the hypothesis that the r_p distributions are drawn from the same parent distribution cannot be excluded. However, the corresponding hypothesis regarding the $|\Delta v|$ distributions can be ruled out with 94% confidence. The difference in the distributions coming because of the large $|\Delta v|$ tail in the observed sample. These tests were done using the entire satellite sample. If the five most probable background objects are removed (Sample 1: cf. Table 4.2), then the confidence with which we

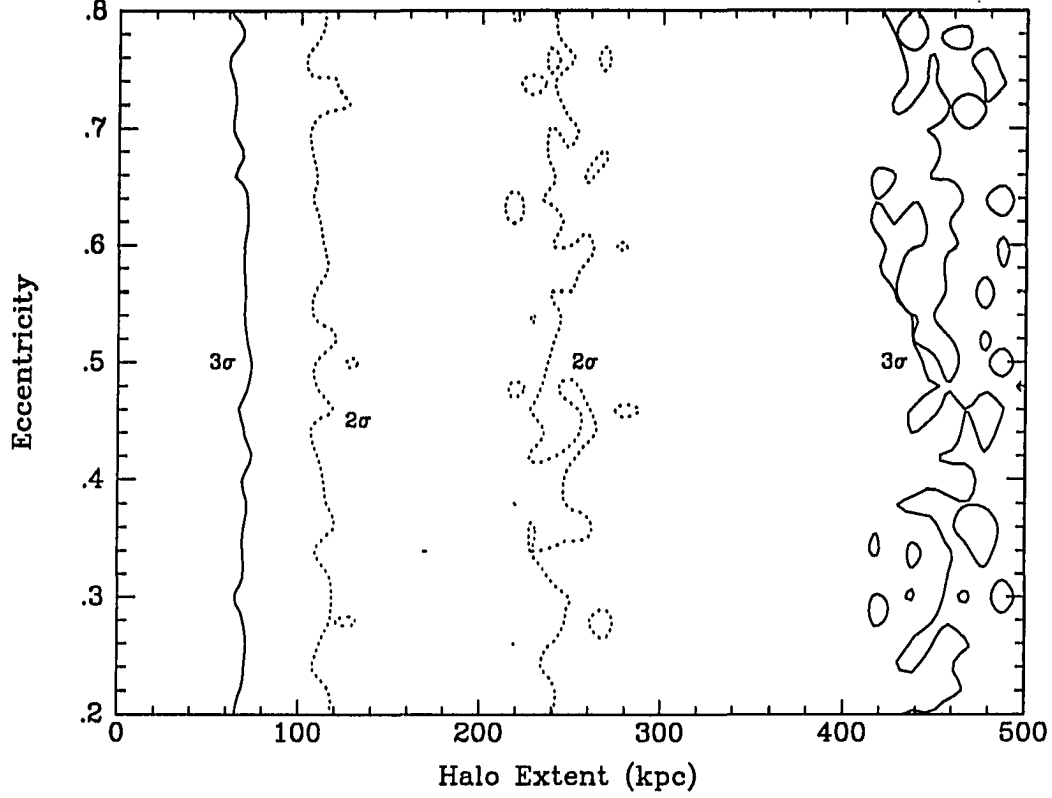


Figure 4.3: *Keplerian Simulations: 2-D KS Probe Through Parameter Space. Solid contours denote 3 σ contour. Dotted contour is 2 σ . There are no models that are discriminated against at less than the 1 σ level.*

can claim that the $|\Delta v|$ distributions were not drawn from the same sample decreases below 1 σ significance. However, $1.5 \times 10^{12} M_{\odot}$, even if it were distributed with density $\propto r^{-2}$ out to 30 kpc (a standard length scale probed by rotation curve studies), would produce a maximum rotation curve amplitude of 480 km s^{-1} . For a central mass of $5 \times 10^{11} M_{\odot}$, which if distributed with $\rho \propto r^{-2}$ out to 30 kpc is in

Table 4.2: Description of Satellite Samples

Sample Name	Number of Satellites	Satellites Removed
Sample 0 (entire sample)	69	None
Sample 1	64	13,14,30,54,68
Sample 2	57	1,2,8,13,14,15,17 30,40,54,62,68

marginal agreement with the observed rotation curves, the hypothesis that the observed and simulated velocity distributions were drawn from the same parent sample can be ruled out with 99.97% confidence if the observed sample is Sample 0 and with 98.9% confidence if it is Sample 1. We also examined the rank correlation of r_p vs. $|\Delta v|$. The simulated distribution has a Spearman rank correlation coefficient of -0.373 , while Sample 0 has a correlation coefficient of -0.0348 and Sample 1 has one of -0.171 . This is further evidence against the point mass models, which produce correlations in the $r_p - |\Delta v|$ plane that are at least twice as steep as the observed correlation.

Despite the poor showing by the point mass models, we made one final attempt to identify an acceptable model by probing the $M - e$ parameter space. The use of a quantitative criterion with which to estimate the range of acceptable models⁴ provides an alternative to the estimator technique. We chose to use the 2-D KS test as our quality-of-fit criterion (see Press and Teukolsky 1988).⁵ Model distributions

⁴Acceptable with respect to the distribution of satellites in the $r_p - \Delta v$ plane, not with respect to the rotation curves.

⁵Unlike its 1-D counterpart, the significance of a deviation in the cumulative distributions is not given in closed form. Instead, the significance is estimated using Monte-Carlo simulations and is somewhat sensitive to the shape of the parent distribution in the 2-D space. The 1-D KS statistic is the maximum difference between the two cumulative functions. The 2-D KS statistic is

Table 4.3: Estimates of Total Mass^a Using Bahcall-Tremaine Mass Estimator

Statistic	Sample 0	Sample 1	Sample 2
Average (case I)	99.6	40.6	22.1
Average (case II)	100.7	46.3	24.3
Median (case I)	15.0	12.7	11.0
Median (case II)	22.1	14.3	11.8

^a Mass given in units of $10^{11} M_{\odot}$.

of particles in the $r_p - |\Delta v|$ plane were compared to the observed distribution. As for the earlier models, the energy distribution among particles was chosen to obtain a good match between the simulated $\langle r_p \rangle$ and the observed one. For case I, models were calculated for masses between $1 \times 10^{11} M_{\odot}$ and $2.6 \times 10^{12} M_{\odot}$ in intervals of $5 \times 10^{10} M_{\odot}$, and were calculated for fixed eccentricities between 0.1 and 0.8 in intervals of 0.02. The probability of distinguishing among the simulated and observed samples is given by the average of the 2-D KS probability from 40 realizations of 100 particles each, at each (M, e) . The observed distribution was taken to be Sample 1. In Figure 4.2 we show a contour plot of our results. Contours represent the 1, 2, and 3 σ confidence limits for rejection of models. For case II, we varied the “extent”⁶ of the halo between 10 and 500 kpc, with 10 kpc spacing (assumed to have a flat rotation curve) and used $M = rW^2$. A contour plot of confidence limits on r and e is given in Figure 4.3.

taken to be the maximum difference in the number of data points in corresponding quadrants in the two samples, where the origin is moved to all data points. If the correlation coefficients for the two samples are nearly the same, then the probability of an observed deviation greater than D is given by an approximation presented by Press and Teukolsky (1988). If the correlation coefficients are significantly different, then the two samples were not drawn from the same parent population.

⁶Extent in terms of $M = rW^2$, recall that these models are for point-mass distributions.

The best-fitting models lie along the ridge at $M \sim 10^{12} M_{\odot}$ and low eccentricities for case I and at $r \sim 180$ kpc for case II. The small halo models ($5 \times 10^{11} M_{\odot}$) are rejected at about the 3σ level. Note that low eccentricity orbits appear to be preferred for case I models. This is caused by the fairly uniform vertical distribution of observed points in the $r_p - |\Delta v|$ plane at any r_p . Radial orbit models have $|\Delta v|$ distributions at fixed r_p with large wings and so provide poorer matches to the observations. Note also that all case II models are at least marginally unacceptable (significance $> 1\sigma$). Case II models are less acceptable than case I models.

The mass estimate from this exercise, even when Sample 0 is used ($\sim 10^{12} M_{\odot}$), is closer to the result from the median projected-mass estimator than to that from the average projected-mass estimator. This demonstrates an important result: that the median is much less sensitive to interlopers, to peculiar objects, and to objects with poorly determined observational parameters than the average mass estimators. Because the K-S test is most sensitive to differences near the medians of the distributions, it, whether of the 1 or 2-D variety, provides stability against outliers as does the median projected-mass estimator. This reason is why the Sample 0 2-D KS result agrees with that from the median estimator.

However, even for a central point mass of $10^{12} M_{\odot}$, which is a lower bound on our estimates, the discrepancy between the predicted and observed rotational velocities at small radii is unacceptable. Hence, the point mass models, although providing a numerical answer that may eventually be proven roughly correct, are rejected.

4.2.2 Extended-Mass Random-Phase Models

Galactic halos must extend to at least several tens of kpc given the observed flat H I rotation curves and provided the results from the previous section are even remotely correct. The orbits of objects that lie within a halo cannot be described

with a Keplerian model. However, isothermal halo models, for which total mass diverges and which are the other common halo model, may also be inappropriate. A compromise between the models (*i.e.*, models where the velocity dispersion $\propto r^{-\alpha}$, where 0 (for isothermal models) $< \alpha < 1/2$ (for Keplerian models)) is more likely to be a good match to reality. Models that have the flexibility to examine a variety of potentials are desirable. The development of such models under certain simplifying assumptions was presented by White (1981) and applied to the study of binary galaxies by WHLD83. Because of the increased variety of available potentials, these models provide a clear advantage over the point mass models. However, these models, like the point mass models, do not model the dynamical evolution of the halo, and so depend on the assumption of random orbital phases.

The models are described in detail by White (1981). The principal assumption is that the clustering distribution of galaxies on small scales has no characteristic spatial scale. This assumption appears to be borne out by observational evidence (Lake and Tremaine 1980; Lorrimer *et al.* 1991). By further assuming that there are no biases in the distribution of galaxies along a line-of-sight, velocity differences can be calculated for a variety of potentials and power-law galaxy correlation functions.

We ran the following models of satellites in an isothermal potential for illustration. We do not intend to do an extensive analysis of the data using these models. The results presented in Table 4.4 are from isothermal sphere models where the satellite number density is proportional to $r^{-1.8}$. The orbital eccentricity was set to 0.3. The masses were estimated from the simulated data by using the average projected-mass estimator described in the previous section (Eq. 4.4), and the circular velocities were estimated from the quantity F defined by White (1981). Particles were drawn with projected separations less than 500 kpc (note that their true separations could be larger). In models 1-3 the total mass ($\equiv 5 \times 10^{12} M_{\odot}$) is

slightly underestimated, but the circular velocity is recovered with high precision. The mass is underestimated because most of the particle orbits enclose less than the total $5 \times 10^{12} M_{\odot}$ out to 500 kpc, which we chose to be the limiting projected radius of our simulations. Results from model 4 show that observational uncertainties at the level present in this study are not one of the principal sources of uncertainty in the mass or characteristic rotational velocity determination. Projected radius cutoffs (model 5) have an effect on the estimated mass, but not on the estimated circular velocity because its determination is based on line-of-sight properties. Results from model 6 demonstrate that if rotation curve values are normally distributed with a dispersion of 50 km s^{-1} then the results are still accurate. Model 7 includes background interlopers. As expected the estimated mass and circular velocity increase. Because we adopted a value for the rotation curve amplitude that is nearly half of the allowed maximum velocity difference and because projected separations (which tend to be large for interlopers) are not a factor in the determination of circular velocities, the effect on the estimated circular velocity is not as pronounced as that on point-mass estimates. The last model also illustrates that if interlopers are present, it is best not to use a statistic that depends on both r_p and $|\Delta v|$ because both of these quantities tend to be larger for interloping galaxies than for physical companions.

In WHLD83, the extended models are judged on their ability to reproduce particular correlations in the data. One of these is denoted as R where,

$$R^2 = (\rho_{|\Delta v|, W}^2 + \rho_{|\Delta v|, r_p}^2 - 2\rho_{|\Delta v|, W}\rho_{|\Delta v|, r_p}\rho_{W, r_p}) / (1 - \rho_{W, r_p}^2), \quad (4.7)$$

and ρ denotes the Spearman rank correlation coefficient between the two quantities in subscript. R is the rank correlation coefficient between $|\Delta v|$ and the combination of r_p and W . The other two correlations that were examined have the following

Table 4.4: Extended Mass Model Parameters and Results

Model No.	No. of Test Pts.	Description	Estimated ^a Mass ($10^{11} M_{\odot}$)	$\frac{V(\text{est.})}{V(\text{true})}$
1	10	Idealized	38.2 ± 19.4	0.98
2	100	Idealized	42.1 ± 8.1	0.99
3	200	Idealized	41.9 ± 5.5	0.99
4	100	Vel. and Distance Errors	43.2 ± 7.7	1.00
5	100	r_p cutoff = 150 kpc	13.0 ± 2.3	0.99
6	100	Variable Prim. Mass	44 ± 8.7	1.00
7	100	Background	59.8 ± 9.3	1.08

^a True mass = 50.

partial correlation coefficients:

$$\rho_{|\Delta v|, W; r_p} = (\rho_{|\Delta v|, W} - \rho_{|\Delta v|, r_p} \rho_{W, r_p}) / [(1 - \rho_{|\Delta v|, r_p}^2)(1 - \rho_{W, r_p}^2)]^{1/2}, \text{ and}$$

$$\rho_{|\Delta v|, r_p; W} = (\rho_{|\Delta v|, r_p} - \rho_{|\Delta v|, W} \rho_{W, r_p}) / [(1 - \rho_{|\Delta v|, W}^2)(1 - \rho_{W, r_p}^2)]^{1/2}. \quad (4.8)$$

Partial correlation coefficients measure the correlation among the two variables to the left of the semi-colon, where the effect on the correlation of the variable given to the right of the semi-colon has been removed. These are as given by WHLD83 from Kendall and Stuart (1973). The correlation coefficients for the entire satellite sample and the two subsamples are given in Table 4.5. There is a slight negative correlation between $|\Delta v|$ and W , which is somewhat surprising, but not highly significant ($< 1.5\sigma$ for Sample 1). This slight anti-correlation is the reason why case I models, which predict no correlation between $|\Delta v|$ and W , are favored over the case II models, which predict a positive correlation. Our conception of what constitutes an interloper is why the correlation between v and r_p increases as interlopers are removed from the sample.

Table 4.5: Correlation Coefficients for Satellite Samples

Sample	R	$\rho_{ \Delta v , W; r_p}$	$\rho_{ \Delta v , r_p; W}$
Sample 0	0.10	-0.09	-0.03
Sample 1	0.22	-0.15	-0.17
Sample 2	0.28	-0.11	-0.25

The values of the correlation coefficients for Sample 1, which is our preferred sample, can be compared with the results from models presented in Table 3 of WHLD83⁷. The best-fitting models are those with $\beta = 0.25$ and small α , where β describes the shape of the potential, $d\Phi/dr \propto r^{-2\beta-1}$ and α is the power-law exponent of the assumed relationship between luminosity and effective mass of pairs at a fixed separation. For clarification, Keplerian models have $\beta = 0.5$ and isothermal halos models have $\beta = 0$. For our sample of satellites, α is the power-law exponent of the relationship between primary luminosity and halo mass enclosed at a fixed separation. α near 0 implies no correlation between the optical and halo components of spiral galaxies (case I) and $\alpha = 1$ implies a direct relationship between the two components (case II). In Table 4.6 we show the results from extended mass models. The results are presented in terms of the fraction of the simulations that produced correlation coefficients (R , $\rho_{|\Delta v|, W; r_p}$, and $\rho_{|\Delta v|, r_p; W}$) that were less than the observed values of satellite sample 1. We ran 100 simulations of 64 satellites each. All runs include simulated observational errors. We adopted Gaussian distributed errors of 20 km s^{-1} in velocities and uniformly distributed errors of $\pm 10\%$ in distance. The models include no scatter in the relationship between luminosity

⁷Their models are applicable to our sample because their $|\Delta v|$ cutoff is 500 km s^{-1} and because the radial cutoff is unimportant in a scale-free model.

Table 4.6: Results Using White *et al.*'s Models

α	β	Ecc.	$P(R < 0.22)$	$P(\rho_{ \Delta v , L; r_p} < -0.15)$	$P(\rho_{ \Delta v , r_p; L} < -0.17)$
0	0	0.3	0.81	0.16	0.07
1	0	0.3	0.85	0.08	0.05
0	0.25	0.3	0.22	0.15	0.80
1	0.25	0.3	0.26	0.13	0.79
0	0	0.6	0.68	0.22	0.15
1	0	0.6	0.78	0.14	0.29
0	0.25	0.6	0.12	0.11	0.91
1	0.25	0.6	0.10	0.04	0.96

and halo velocity. Models are for a satellite number density profile $\propto r^{-1.8}$. We conclude that models with $0 < \beta < 0.25$ are preferred and that $\alpha \sim 0$ is also preferred. Therefore, we conclude that there is evidence for extended halos out to the median separation of the satellites (~ 200 kpc). Since the models scaled to the average circular velocity (*i.e.*, $\alpha = 0$) are acceptable, we conclude that the results from this analysis are consistent with halo masses of $2 - 3 \times 10^{12} M_\odot$. To reach such a conclusion definitively requires more extensive statistical discussions; however, we defer those until we discuss the secondary infall models. More importantly, such modeling, while interesting, is unconnected to the processes that formed the halo and does not address how those time-dependent processes affect the current mass profile. In addition, we still have not addressed our concern that random phase modeling may be flawed. Would the result obtained (*i.e.*, $\beta = 0.25$ and small α) rule out an $\Omega = 1$ universe? Could density profiles with the required extent arise in universes with $\Omega_0 = 0.1$ or 0.01 ? These are the types of questions we hope to address with the secondary infall models.

We have explored the two most popular versions of the random-phase dynamical

models. The point-mass models are clearly deficient for several reasons. Primarily, the resulting estimated masses violate the point-mass assumption. The extended models appear to provide a better fit to the data, but also lack a dynamical connection to the development of the halo. However, both types of models suggest that the mass of a typical halo is $\gtrsim 10^{12} M_{\odot}$, which in turn implies that the halos extend at least to beyond 100 kpc. We now present the development and implementation of the secondary infall models.

4.3 Secondary Infall Models

The evolution of galaxy halos within the context of an expanding universe has been examined by many including Gott (1975), Gunn (1977), Fillmore and Goldreich (1984), Bertschinger (1985), and Hoffman and Shaham (1985). There are several important issues addressed by that work; although, for our purpose the most important is the expected mass density profile of halos.

The secondary infall model is conceptually simple. In the framework of the standard big bang cosmology, the catalyst for the formation of structure is an initial density perturbation present at the epoch of recombination, $z \sim 1000$ (cf. Shipman and Strom 1970). At the time that matter and radiation decouple, the velocity field is nearly that of uniform Hubble flow. Subsequently, the expansion surrounding the initial perturbation, or seed mass, is slowed by the gravitational attraction of the seed mass. Material within the region of the perturbation collapses quickly; however, material at larger radii, which is also gravitationally bound, expands away initially and collapses much later — hence the name secondary infall.

The perturbed region is assumed to be a small spherical region with a slightly larger-than-ambient density (cf. Gott 1975). Because our particular interest lies in the dynamics surrounding the initial collapse region, the results from such a model

are insensitive to the exact nature of the density profile of the initial perturbation. The central region will virialize early during the formation of the outer halo. The mean mass density in a spherical region of radius r centered on the seed mass decreases as larger r 's are considered. Because the turnaround time (the time at which a particle reverses its initial expansion and begins to fall back toward the seed mass) is proportional to $\delta\rho^{3/2}$, where $\delta\rho$ is the overdensity of the region interior to the position of the particle, the evolution of the halo is envisioned as a progression of shells, at larger and larger radii as time increases, decoupling from the Hubble flow and collapsing onto the seed mass. These shells eventually cross shells that collapsed earlier and undergo dynamical relaxation. This process forms a structure that has a steady-state density profile interior to a radius that increases with time.

Gott (1975) and Gunn (1977) recognized that infalling material can produce physically interesting profiles, $\rho \propto r^{-2} - r^{-3}$. In a model where the expansion of mass shells is artificially stopped at some particular fraction of their turnaround radius, the density profile is proportional to $r^{-2.25}$ (Gott 1975). Such a profile is similar to that of an isothermal sphere, $\rho \propto r^{-2}$. The isothermal sphere potential is appealing because it has a corresponding flat rotation curve and is mathematically simple. However, the Gunn and Gott models are artificial because they do not include the relaxation that occurs as mass shells cross. A full n -body simulation of halo formation supported the earlier results by producing profiles with $\rho \propto r^{-2.25}$ (Dekel, Kowitt, and Shaham 1981). Fillmore and Goldreich (1984) and Bertschinger (1985) confirmed those results by convincingly demonstrating that the relaxed portion of the halo develops a $\rho \propto r^{-2.25}$ profile. Bertschinger also argued that the shape of the density profile within the relaxed region was independent of Ω_0 . However, the shape of the unrelaxed portion of the halo must depend on the value of Ω_0 because the outer regions of the halo consist of unmixed infalling material. In the extreme case where $\Omega_0 \approx 0$ there is little infalling material, while if $\Omega_0 \approx 1$ there is

a significant amount of infalling material. As we will show, the shape of the density profile in the unrelaxed region depends on the choice of Ω_0 , while specifying the current turnaround radius, the enclosed mass at the current turnaround radius, or the central mass determines the extent of the relaxed region at a given time. There is a variant of these models described by Fillmore and Goldreich (1984). In these models the perturbing mass is not a central mass concentration, but instead has extent. The ideas are similar to those in the secondary infall models, but the models are not true secondary infall models because they do not describe material falling onto an already collapsed perturbation (*i.e.* a point mass). A specific case of their models is equivalent to the secondary infall model. We shall refer to our version of these models, which are described below, as the modified secondary infall models. In our modified models the density profile at small radii is self-similar (*i.e.* *already virialized*), but for computational convenience the mass at small radii is placed in a central mass. The models can then be discussed in terms of a central mass, although the term central mass has a slightly different definition than in the standard infall model.

The secondary infall and modified secondary infall models are attractive for several reasons. First, such growth of structure, albeit idealized to the isolated case, must occur given the standard big bang cosmology and the existence of galaxies. Second, the modeling is straightforward with few free parameters. Third, it removes the assumption of random orbital phases that was present in previous work. Fourth, it allows us to probe a variety of halo profiles, not just point mass and isothermal spheres. Fifth, it relates these mass profiles to the cosmological mass density.

4.3.1 “Analytic” Solution

Secondary infall for $\Omega = 1$ was treated fully by Fillmore and Goldreich (1984) and Bertschinger (1985), although in slightly different ways. In an $\Omega = 1$ universe and for

the standard model material is continually accreting onto the central perturbation and the turnaround radius is $\propto t^{8/9}$. Because there is no fixed preferred scale length or time in the problem, the solutions are self-similar in time. This self-similarity makes it possible to solve the equations for the density profile. As Bertschinger showed, material on concentric shells settles into periodic orbits whose maximum radius is 0.81 of their initial turnaround radius. Therefore, as Gott (1975) had shown and Bertschinger confirmed, if each particle settles into an orbit whose maximum radius is a fixed fraction of the particle's initial turnaround radius, then the density profile is $\propto r^{-2.25}$ in the fully relaxed core.

For $\Omega_0 < 1$, there is a last bound shell. Because the evolution is time dependent, no completely self-similar solution is available. However, because we need neither to scale the models in time nor to solve the equations analytically for the density profile, self-similarity in time is not critical for our purpose. We do want to be able to scale models at a fixed time to different values of the total bound mass, or equivalently different values of the current turnaround radius or central mass. If such scaling relationships exist, then additional computer simulations are not necessary for each choice of total mass. Such relationships simplify the examination of a wide variety of models. Below we discuss the infall models and show how some scaling relations are preserved for $\Omega_0 < 1$ models by using a variant of the Gunn and Gott (1972) formalism.

Consider a homogeneous universe into which a seed mass is placed at redshift z_i . Initially, the energy of a shell of radius r , which encloses a seed mass of mass m and a region of uniform density of mass M surrounding the seed mass, is given by

$$E = \frac{1}{2} H_i^2 r_i^2 - \frac{G(M + m)}{r_i}, \quad (4.9)$$

where H is the Hubble constant and the subscript i denotes initial epoch. In this formalism, we have adopted a centrally concentrated perturbing mass. The alternative, as presented in the models of Fillmore and Goldreich (1984) (hereafter FG),

is to model an extended mass perturbation. Their models reduce to the standard seed mass models with the appropriate choice of parameters. We shall refer to their mass profile variable ϵ as ϵ_{FG} ⁸. The advantage of their models is that by altering ϵ_{FG} , one can alter the shape of the mass profile in the relaxed core. We shall return to this point below. Returning to Eq. 4.9 and the standard secondary infall models, since there is no shell crossing in the initial expansion phase, each shell conserves energy at least until its initial turnaround at r_t . Therefore, we can write

$$\frac{1}{2} H_i^2 r_i^2 - \frac{G(M+m)}{r_i} = -\frac{G(M+m)}{r_t}. \quad (4.10)$$

Substituting

$$H_i^2 = \frac{8\pi G\rho_i}{3\Omega_i} \quad (4.11)$$

and solving for r_t gives,

$$r_t = r_i \left(\frac{\left(1 + \frac{m}{M}\right) \Omega_i}{\left(1 + \frac{m}{M}\right) \Omega_i - 1} \right). \quad (4.12)$$

By substituting

$$r_i(1+z_i) = \left(\frac{2GM}{\Omega_0 H_0^2} \right)^{1/3} \quad \text{and} \quad \Omega_i = \Omega_0 \frac{1+z_i}{1+\Omega_0 z_i} \quad (4.13)$$

where subscript 0 indicates current time, and z_i is the redshift of the initial epoch, into Eq. 4.12 and by taking the limit as $z_i \rightarrow \infty$ and $m \rightarrow 0$, we can derive the asymptotically accurate value of r_t . Let $mz_i \rightarrow q$ (q is unspecified yet), then

$$r_t = \left(\frac{2GM}{\Omega_0 H_0^2} \right)^{1/3} / \left(\frac{q}{M} + 1 - \frac{1}{\Omega_0} \right). \quad (4.14)$$

If we examine the marginally bound shell (*i.e.*, $r_t = \infty$) and define the mass enclosed to be M_* (*i.e.*, the total bound mass), then the radius which encloses M_* currently, can be written using Eq. 4.13 as

$$r_* = \left(\frac{2GM_*}{\Omega_0 H_0^2} \right)^{1/3}. \quad (4.15)$$

⁸The exact definition of ϵ_{FG} is $\delta M/M = (M/M_0)^{-\epsilon_{FG}}$, where M_0 is a reference mass.

Because the denominator in Eq. 4.14 must $\rightarrow 0$, as $r_t \rightarrow \infty$, q is given by

$$q = M_*(\Omega_0^{-1} - 1). \quad (4.16)$$

Using Eqs. 4.14-4.16, we can now express the ratio of the turnaround radius corresponding to mass M to the current radius that encloses M_* as

$$\frac{r_t}{r_*} = \frac{\Omega_0(M/M_*)^{4/3}}{(1 - M/M_*)(1 - \Omega_0)}. \quad (4.17)$$

Now we proceed to find an expression for the turnaround time t_t . From definitions we can express the density inside the sphere at turnaround as

$$\rho_t = \frac{M}{M_*} \left(\frac{r_*}{r_t} \right)^3 \rho_0. \quad (4.18)$$

The free-fall time, t_{ff} , for a uniform sphere with radius r_t is given by

$$t_{ff} = \left(\frac{3\pi}{32G\rho_t} \right)^{1/2}. \quad (4.19)$$

Recognizing that the timescale for expansion is the same as for free-fall, and using Eqs. 4.11, 4.17-4.19, we find that the turnaround time is given by

$$H_0 t_t = \frac{\pi\Omega_0}{2(1 - \Omega_0)^{3/2}} \left(\frac{M}{M_*} \right)^{3/2} \left(1 - \frac{M}{M_*} \right)^{-3/2}. \quad (4.20)$$

We now have expressions for the turnaround radius and time, as functions of M and M_* for a chosen cosmology.

The principal quantities of interest for each shell are the mass which that shell encloses and its energy. Again consider the placement of a seed mass at time t_i into an otherwise homogeneous universe, then the energy of any given shell centered on the seed mass is

$$E(M) = \frac{1}{2} H_i^2 r_i^2 - \frac{G(M + m)}{r_i}$$

$$= \frac{GM}{r_i} \left(\frac{1}{\Omega_i} - 1 - \frac{m}{M} \right), \quad (4.21)$$

where again M is the mass of uniformly distributed material and m is the mass of the seed mass. We will also need the standard equations

$$\rho_i = \frac{3H_i^2 \Omega_i}{8\pi} \quad \text{and} \quad \Omega_i = \frac{\Omega_0(1+z_i)}{1+\Omega_0 z_i}. \quad (4.22)$$

Using Eq. 4.22 and $\rho_i = \rho_0(1+z_i)^3$, we can rewrite Eq. 4.21 as

$$E(M) = GM \left(\frac{4\pi\rho_0}{3M} \right)^{1/3} \left(\Omega_0^{-1} - 1 - (1+z_i) \frac{m}{M} \right). \quad (4.23)$$

For $\Omega_0 < 1$, $M_* \equiv \lim_{z_i \rightarrow \infty} (z_i m / (\Omega_0^{-1} - 1))$ and the expression for E as $z_i \rightarrow \infty$ is

$$E(M) = GM \left(\frac{4\pi\rho_0}{3M} \right)^{1/3} (\Omega_0^{-1} - 1)(1 - M_*/M). \quad (4.24)$$

Recall that for $\Omega_0 < 1$, M_* is the total bound mass. This asymptotic expression for E is valid until shell crossing occurs. The analog of Eq. 4.24 for $\Omega = 1$ is

$$E(M) = -GM_* \left(\frac{4\pi\rho_0}{3M} \right)^{1/3}, \quad (4.25)$$

where $M_* \equiv \lim_{z_i \rightarrow \infty} (m z_i)$. However, for the $\Omega = 1$ case, M_* has no direct physical interpretation.

These expressions correspond to the standard secondary infall models that produce $\rho \propto r^{-2.25}$ in the relaxed core. Therefore, the relaxed core has a circular velocity that is $\propto r^{-0.25}$. Since there is no observational evidence supporting slightly decreasing rotation curves over flat rotation curves, and certainly none for rotation curves that diverge as $r \rightarrow 0$, we wish to have models that produce flat central rotation curves⁹. Gunn (1977) modified initial mass profiles in an attempt to find

⁹The observations do not strongly constrain the density profile of the halo (Bahcall, Schmidt, and Soneira (1982); Lake and Feinswog (1989)).

a case which produced flat rotation curves. However, in his models he assumed that all particles had orbits with a maximum radius that was a fixed fraction of the initial turnaround radius. FG found that this assumption is invalid for almost all initial mass profiles that produce flat rotation curves. However, they found that there are a wide variety of initial mass profiles that should produce $\rho \propto r^{-2}$ if $e = 0$.

To produce resulting mass distributions that are different from those in the standard infall models, we need to alter the binding energy of each shell. Because the enclosed mass is the only independent variable in these models, for a given choice of cosmological parameters, we suggest the scale-free perturbation $\Delta E(M) \propto M^{-\alpha} E(M)$. If we consider that energy perturbation arises from a difference in the initial mass profiles (as in FG), then for choices of mass profiles between uniformly distributed and centrally concentrated α lies between 0 and 1. We expect the standard model to be a specific case of this more generalized formulation. Since the energy of a shell enclosing mass M in a Friedmann-Robertson-Walker (FRW) universe with $\Omega_0 < 1$ is given by

$$E(M) = -GM \left(\frac{4\pi\rho_0}{3M} \right)^{1/3} (\Omega_0^{-1} - 1) \quad (4.26)$$

we can write

$$\Delta E(M) = -GM \left(\frac{4\pi\rho_0}{3M} \right)^{1/3} (\Omega_0^{-1} - 1) (M/M_*)^{-\alpha}. \quad (4.27)$$

The total binding energy is then given by

$$E(M) = -GM \left(\frac{4\pi\rho_0}{3M} \right)^{1/3} (\Omega_0^{-1} - 1) ((M/M_*)^{-\alpha} - 1). \quad (4.28)$$

Notice that $\alpha = 1$ corresponds to the standard models. For $\Omega = 1$, we then write by analogy

$$E(M) = -GM \left(\frac{4\pi\rho_0}{3M} \right)^{1/3} (M/M_*)^{-\alpha}. \quad (4.29)$$

If $\alpha = 1$, then the expressions for E , for both $\Omega = 1$ and $\Omega_0 < 1$, are equivalent to those for the standard model. As such, they are directly analogous to the energies obtained from the timing arguments in Chapter 2. Asymptotically, the two methods of determining E , and subsequently v and r , should yield identical results.

The turnaround radius and time can be derived straightforwardly from the expressions for the energy. For radial orbits, at turnaround in the asymptotic case $E(M) = -GM/r_t$ (recall that as $z_i \rightarrow \infty, m \rightarrow 0$), where r_t is the turnaround radius. Therefore,

$$r_t(M) = \begin{cases} (3M/4\pi\rho_0)^{1/3}(\Omega_0/(1-\Omega_0))((M/M_*)^{-\alpha} - 1)^{-1}, & \text{if } \Omega_0 < 1; \\ (3M/4\pi\rho_0)^{1/3}(M/M_*)^\alpha, & \text{if } \Omega_0 = 1 \end{cases} \quad (4.30)$$

and from arguments similar to those given previously,

$$H_0 t_t(M) = \begin{cases} (\pi/2)(\Omega_0/(1-\Omega_0))^{3/2}((M/M_*)^{-\alpha} - 1)^{-3/2}, & \text{if } \Omega_0 < 1; \\ (\pi/2)(M/M_*)^{3\alpha/2}, & \text{if } \Omega_0 = 1, \end{cases} \quad (4.31)$$

where t_t is the turnaround time. As expected, if the shells are made less bound (*i.e.*, $\alpha < 1$), then the turnaround radius and time increase in comparison to the values for the standard model.

Our modified models are a hybrid between the standard secondary infall models and the models of FG. Our models have a central mass, not an extended mass distribution. Before turnaround, each shell is modeled exactly as in the FG models. That is, $\epsilon_{FG} = \alpha$ and one can imagine that the difference in binding energy arises from a difference in the mass profile. However, a real difference between the models lies in the shell masses. Therefore, once shells start to cross, the evolution will be slightly different. However, as $z_i \rightarrow \infty$ and $m \rightarrow 0$ the models asymptotically become the same. As FG concluded, particles will settle into orbits whose maximum radius is a fixed fraction of their initial turnaround distance if $\epsilon_{FG} \geq 2/3$. Note that

our α is almost equivalent to ϵ_{FG} ($\alpha \rightarrow \epsilon_{FG}$ as $z_i \rightarrow \infty$). The FG models have two difficulties: the overdensity in the inner region diverges and the total mass of the perturbation diverges for $\epsilon \neq 1$. Because of the placement of the perturbation into a central mass, our models do not have these difficulties. However, we then lose the physical interpretation for the decrease in binding energy. Our slight modification of the FG model is primarily for computational convenience. The two versions are essentially equivalent since we begin our simulations at a large value of z_i .

To determine the shape of the mass profile as a function of α , we examined the relationship between the turnaround radius and enclosed mass given by Eq. 4.30. Recall that the particles settle into orbits whose maximum radius is a fixed fraction of their initial turnaround radius if ϵ_{FG} (or α) $\geq 2/3$. For $\Omega_0 < 1$ models, we consider the region of the halo for which $M_*/M \gg 1$, in which case the $\Omega_0 < 1$ and $\Omega = 1$ cases have the same behavior, namely,

$$M \propto r_i^{1/(1/3+\alpha)}. \quad (4.32)$$

We see that we get the expected profile, $M \propto r^{0.75}$, for $\alpha = 1$ and also that we get the desired profile, $M \propto r$, for $\alpha = 2/3$. In fact, we derive exactly the same dependence of the mass profile on α that FG derived for $\epsilon_{FG} \geq 2/3$.

On reflection, there are several points of note. First, the models are well-defined in that $m \rightarrow 0$ as $z \rightarrow \infty$. Second, $\Omega_0 < 1$ models can be categorized either by total bound mass, turnaround radius for enclosed mass M , turnaround time for enclosed mass M , or seed mass and z_i . Third, all models will have a region for which the enclosed density is larger than the critical density. This region will develop a central relaxed core that has a $\rho \propto r^{-2.25}$ profile (Bertschinger 1985) for standard models and a $\rho \propto r^{-9\alpha/(1+3\alpha)}$ profile for the modified models. Fourth, for a given total mass and Ω_0 the flat rotation curve models will have a smaller v_c at any particular

radius interior to r_* than the standard model. This in turn implies that for a chosen value of v_c at a particular interior radius, the modified models will produce halos with a greater total bound mass. Therefore, using the modified infall models will produce a *lower* estimate of Ω_0 than would the standard infall models. Finally, the radial scale of the model depends only on M_* , Ω_0 , and H_0 . Therefore, for a chosen cosmology and fixed time, mass profiles corresponding to different M_* must be self-similar (*i.e.*, of the same shape) since they depend on no other quantity. This self-similarity will be important in our use of these models because it will enable us to rescale between models of different total mass. However, as noted before, because the density profile is time dependent, no analytic solution exists. We must employ numerical simulations, described below, to obtain a density profile for an initial model, which can then be rescaled to any particular M_* .

4.3.2 Numerical Solution

It may seem to some that computer simulations, especially those involving just gravity, are devoid of scientific choices; just a matter of letting the computer go to work. Unfortunately (or fortunately depending on one's point of view), this is not the case. Both the choice of initial conditions and the choice of computational scheme can seriously affect the outcome. Subtle effects can produce not only quantitative but qualitative differences in the outcome (cf. Zaritsky and White 1988). In this and the following sections we describe the code, the initial conditions, and tests with which we determined the reliability of the code.

All models of secondary infall assume spherical symmetry. In general, the halo of an isolated galaxy is assumed to be spherical, although some recent work has focused on the possibility of triaxial halos. Velocities of material in polar rings have been used to probe the shape of the potential (Schweizer, Whitmore, and Rubin 1983;

Whitmore, McElroy, and Schweizer 1987). The agreement between the rotational velocities in and perpendicular to the disk, implies that the halo is nearly spherical; however, projection effects complicate the interpretation. As supporting evidence we cite the observational result that the distribution of stellar halo tracers, such as globular clusters, is approximately spherical at large radii (cf. Harris 1987). In addition, H I flares in disks at large radii (Sancisi and Allen 1979) demonstrate that the dark matter is not confined in a disk on the same plane as the luminous matter. Gunn (1980) derived that the axial ratio of the Galactic halo is > 0.5 from the thickening of the Galaxy's disk at large radii. Steiman-Cameron, Kormendy, and Durisen (1991) have analyzed the disturbed disk of NGC 4753 and argued that the mass distribution is no flatter than E1.6 ($b/a \geq 0.84$). While theoretical models of dissipationless collapse (Binney 1976) and numerical simulations of halo formations in CDM (Frenk *et al.* 1988) imply that halos should be triaxial, observational evidence suggests they are probably only mildly triaxial. We assume for simplicity that the halo potential is spherically symmetric.

Because the adopted potential is spherically symmetric, we chose to use a spherical shells code. In this type of code, unlike in N-body simulations, the force of each particle on every other particle is not calculated directly. In a spherically symmetric system, the force at a radius r is given by $GM(r)/r^2$, where $M(r)$ is the mass enclosed in a sphere of radius r centered on the seed mass. Therefore, at each timestep the program works its way outward in radius through all the particles, recording the enclosed mass at each radius, and evaluating the total force on each particle with just *one* calculation. This produces a substantial saving in computational expense¹⁰. Because of noise in the initial conditions, full N-body simulations, unlike spherical shells simulations, could be prone to the growth of nonaxisymmetric features during

¹⁰The computational time required by a full N-body code with N particles is proportional to N^2 , while in a shells code it is proportional to N .

infall¹¹. An additional benefit of the spherical shells code is that it is less subject to two-body relaxation effects, because the potential diverges only at the center, not at each particle.

Next we describe the details of the code. The equation of motion for particle j is

$$\frac{d^2 \vec{r}_j}{dt^2} = \frac{G \left(\sum_{i, r_i < r_j} m_i \right) \vec{r}_j}{(r_j^2 + \epsilon^2)^{3/2}}, \quad (4.33)$$

where ϵ is the softening length adopted (10 kpc) to prevent the potential from diverging at the center, and m_i is the mass contained in shell i . The particular choice of the softening radius is not critical. The softening radius should be as large as possible while not seriously affecting the dynamics on scales of interest. Because galactic disks dominate on scales of 10 kpc, it is observationally difficult to find satellites with $r_p < 10$ kpc. We also expect that the satellite-primary system is unlikely to survive such close passages unscathed. On the other hand, by 20 or 30 kpc we might expect such effects to become significantly less important. We compromised and adopted $\epsilon = 10$ kpc. Each shell is tracked by one particle. The typical integration timestep is of order 10^5 yrs and the orbits for 25000 particles are integrated from $z \sim 1000$ until the present time using a 4th-order Runge-Kutta algorithm. Figure 4.4 shows the final distribution of particles (not mass) for the central region of one model. Notice the strong shell structure due to particles “piling up” near apocenter. The results of the simulations are then “observed” with the same selection criteria that were applied to the real observations. Our procedure for reproducing both the 3-D satellite density profile and the distribution of projected separation for the observed satellites is described in §4.3.4.

¹¹Such instabilities may arise in nature, but the increase in complication without the knowledge to constrain the models prompts us to continue with the simple model.

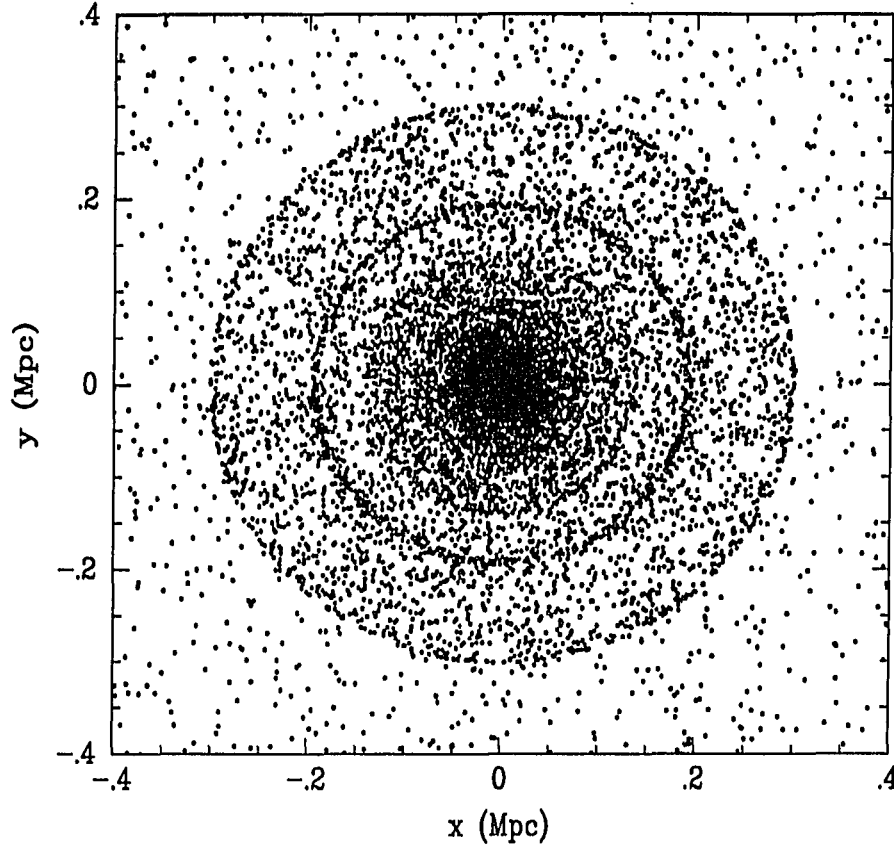


Figure 4.4: *Distribution of Point Particles for a Secondary Infall Model : The inner region of the model with $\Omega_0 = 1$ and $e = 0.5$.*

In the following sections we describe in detail the major technical issues involved in the simulations: the generation of angular momentum, the volume to be covered by the simulations, the initial conditions, and the comparison to previous work.

Generating Angular Momentum

Orbital eccentricity is an important parameter in any discussion of the dynamics of companions. Therefore, our modeling must include a provision for adding angular

momentum to the particles. Angular momentum is believed to have been 'generated' in galaxy halos through the gravitational interaction of the quadrupole moment of the protogalaxy with the tidal field produced by its neighbors (first suggested by Hoyle 1949; analytic treatment of the interaction given by Doroshkevich (1970) and White (1984)). Theoretical work on the acquisition of angular momentum in galaxy halos has been verified and expanded by the application of numerical simulations (cf. Efstathiou and Jones 1979; Aarseth and Fall 1980; Barnes and Efstathiou 1986; Quinn and Zurek 1988). The efficiency with which angular momentum is transferred to the growing protogalaxy increases as the density contrast increases, but decreases as the separation between distinct systems increases. Because of this interplay, the majority of the angular momentum is acquired prior to the decoupling of the material from the universal expansion. Therefore, we assumed that no additional angular momentum was transferred to a particle in our simulation after its initial turnaround.

To create halos consisting of material on orbits with a chosen eccentricity, we have adopted the following prescription. For each particle of energy E , there is a corresponding circular orbit with the same energy and a corresponding angular momentum $J_{max}(E)$. We have adopted the crude assumption that all particles in a given model will have the same fraction, ϵ_P , of $J_{max}(E)$, where ϵ_P is a free parameter. This scheme has the advantage that all particles have similar orbits and self-similarity is retained, but is otherwise artificial. Below, we describe the prescription in detail and its application.

Consider a test mass in orbit around mass M with energy E and angular momentum J . Also consider another test particle with the same energy but on a circular orbit, then for the latter we can define

$$v_c \equiv \sqrt{-2E} \quad (4.34)$$

and

$$\begin{aligned} r_c(E) &\equiv \frac{GM}{v_c^2} \\ &= -\frac{GM}{2E}, \end{aligned} \quad (4.35)$$

where v_c is the circular velocity and r_c is the radius of the circular orbit. Because this particle is on a circular orbit, it has the maximum angular momentum possible corresponding to its energy, and so

$$J_{max}(E) = v_c(E)r_c(E), \text{ or} \quad (4.36)$$

$$J_{max}(E) = \frac{GM}{\sqrt{-2E}} \quad (4.37)$$

For the particle on a non-circular orbit, at apocenter, where r_a is the distance between the central mass and the apocenter,

$$E = -\frac{GM}{r_a} + \frac{J^2}{2r_a^2}. \quad (4.38)$$

If $J \equiv \epsilon_P J_{max}$, then

$$E = -\frac{GM}{r_a} - \epsilon_P^2 \frac{G^2 M^2}{4Er_a^2}. \quad (4.39)$$

This is a quadratic equation in r_a for which the solution is

$$r_a = \frac{GM}{-2E} (1 + \sqrt{1 - \epsilon_P^2}). \quad (4.40)$$

Now consider a torque acting on this system. We have chosen to define the tangential force, F_t , and the radial force, ΔF_r , from the perturbing mass distribution as follows,

$$F_t = K \frac{GM}{r} v_r \quad \text{and} \quad \Delta F_r = -K \frac{GM}{r} v_t \quad (4.41)$$

so that $\mathbf{v} \cdot \Delta \mathbf{F} = 0$, then at its initial apocenter passage,

$$J = \int_{t(r_0)}^{t(\text{apo})} F_t r \, dt \quad (4.42)$$

where r_0 is the initial radius, and the orbit was assumed to be radial prior to the initial time. Alternatively after substitution of variables,

$$J = \int_{r_0}^{r_a} KGM \, dr, \quad (4.43)$$

which is trivially solved to derive,

$$J = KGM(r_a - r_0). \quad (4.44)$$

By substituting from Eq. 4.37 we determined that

$$K = \frac{\epsilon_P}{\sqrt{-2E}(r_a - r_0)} \quad (4.45)$$

Therefore, specifying ϵ_P determines the angular momentum that the test particles acquire on their initial outward orbit because all particles acquire a fraction ϵ_P of the maximum allowed angular momentum. The forces due to the external torque are applied to each particle until its initial turnaround. An eccentricity can be defined as $e \equiv \sqrt{1 - (J/J_{\text{max}})^2}$, which is $\sqrt{1 - \epsilon_P^2}$. We examined the range of eccentricities from 0.5 to 0.9. This range includes the resulting mean eccentricity of halo particles in simulations of the formation of galactic halos under the influence of external torques ($\langle e \rangle \sim 0.71$, Quinn and Zurek 1988). The effect of including a softening radius is complicated, but of negligible importance except for particles with small apocenter distance.

The choice of ϵ_P has only slight effects on the mass profiles. In Figure 4.5 we have plotted profiles from $\Omega_0 = 0.3$ models for eccentricities of 0.5, 0.7, and 0.9. There are minor differences in the position of the last caustic and in the slope of the mass

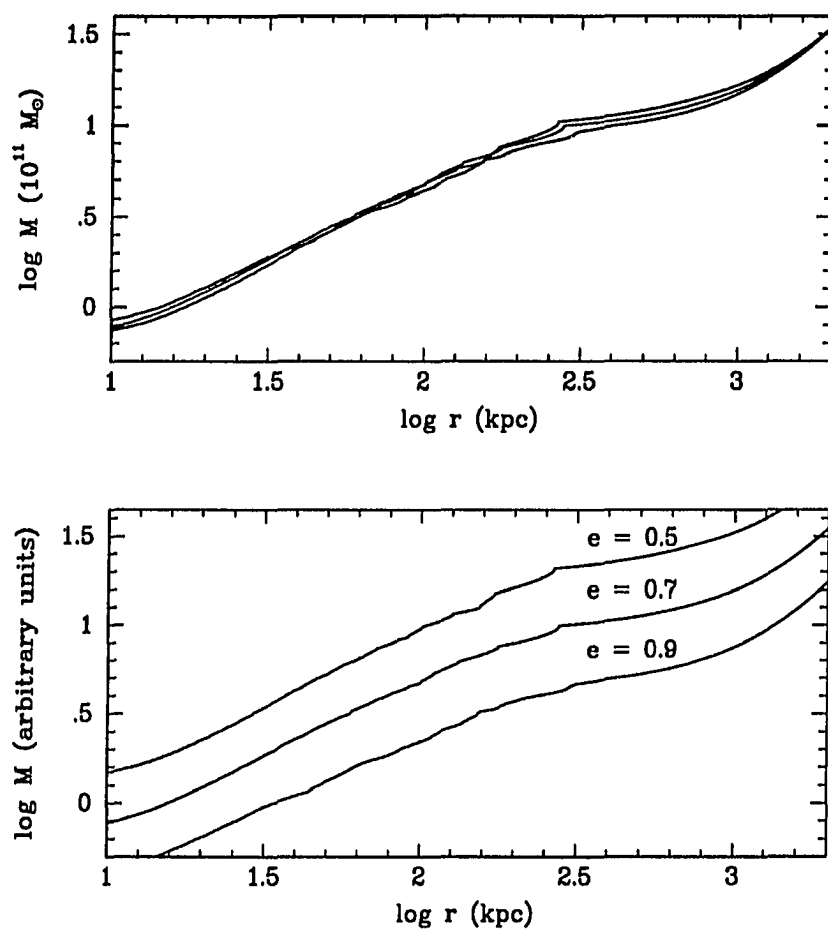


Figure 4.5: *Mass Profiles vs. Orbital Eccentricity:* In the top panel we have overlaid the mass profiles from $\Omega_0 = 0.3$ simulations with eccentricities of 0.5, 0.7, and 0.9. In the bottom panel we have arbitrarily shifted the profiles vertically to facilitate comparison.

profile near the last caustic. Note that with increasing eccentricity the outermost caustic moves outward and the profile just beyond the outermost caustic flattens. By construction all profiles will converge at very large radii. The differences in the profiles are caused by the relaxation properties of particles on different orbits. For radial orbits the relaxation arises from shell crossing. For more circular orbits shell crossing is less important and particles are more nearly virialized by the time they reach turnaround (*e.g.*, consider the case for $\epsilon_P = 1$). The radial orbit model requires more time for relaxation and so the core is not as fully relaxed. However, the turnaround radius at a particular time is larger in the radial orbit models.

Determining r_{max}

Particles at any true distance can appear close to the center due to projection. Therefore, the appropriate spatial extent of the modeled satellite distribution is not well-defined, especially for an isolated system. If the density of satellites is $\propto r^{-2}$ and if there is no projected separation or radial velocity difference criteria, then the number of satellites per thin shell is constant regardless of the radius of the shell. Therefore, one would need to simulate satellites at all distances to match the distribution of observed satellites. However, the velocity difference criterion creates an upper bound, r_{max} , on the necessary extent of the simulated volume because galaxies at distances greater than $H_0/|\Delta v|_{max}$ from the primary will not be included in the sample (assuming pure Hubble flow). The projected separation criterion further reduces the number of objects at distances greater than the maximum allowed projected separation because it truncates the search volume (see Fig. 4.6). The result of these two criteria on the spatial distribution of satellites is discussed below.

Velocities of apparent companions at large distances from the primary ($>$ several Mpc) are unlikely to be influenced strongly by the primary. Therefore, barring

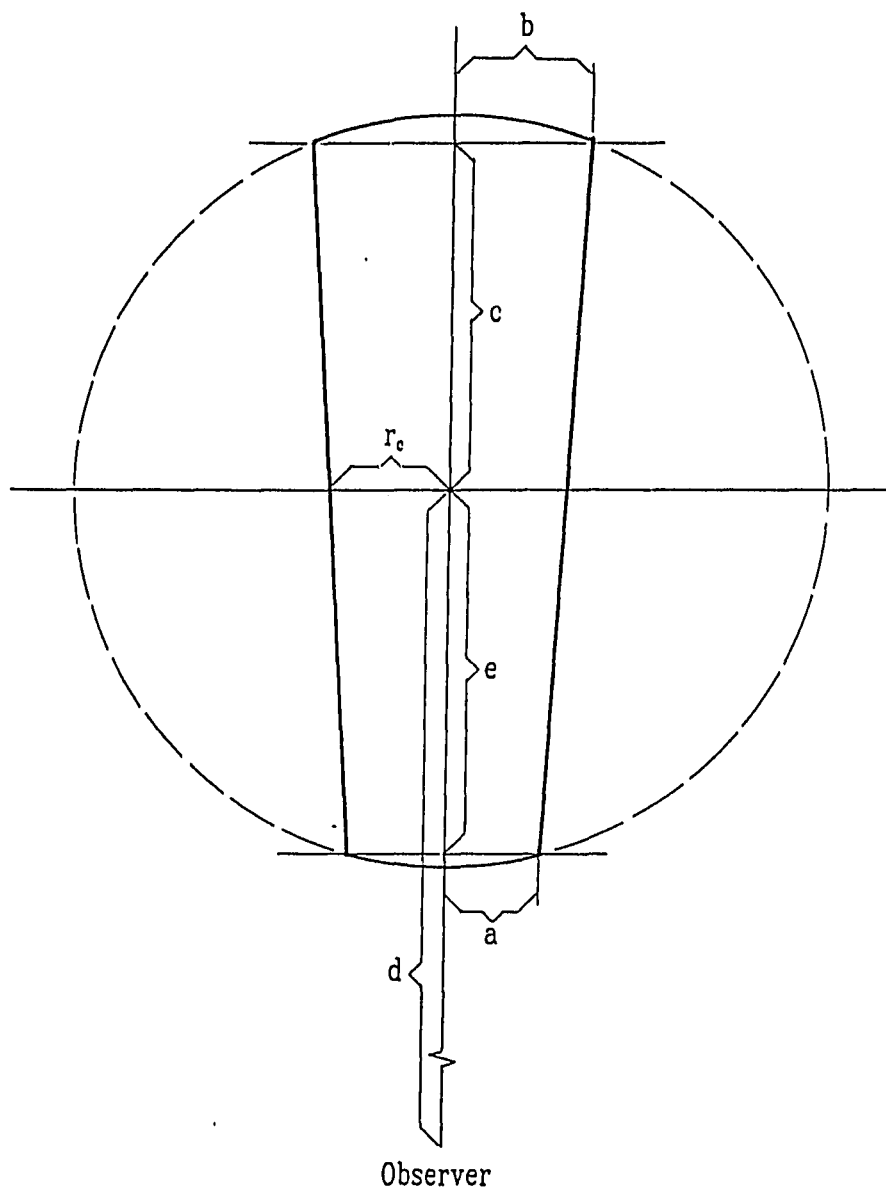


Figure 4.6: *Satellite Search Volume : Satellites that are within the conical volume satisfy the selection criteria. The cone is truncated by a sphere of radius r centered on the primary. The primary is located at the intersection of the vertical and horizontal axes. For small r all the satellites within the sphere are within the cone; as r increases only a fraction of the spherical volume is within the cone (drawing courtesy of I. Zaritsky).*

any large external perturbation on their motion, $v_r \approx H_0 r$. Because the 500 km s^{-1} velocity difference criterion corresponds to a maximum true separation of 6.7 Mpc along the line of sight, 6.7 Mpc is an upper bound on r_{max} . There is no evidence of correlated companion galaxies to these distances; however, the galaxy-galaxy correlation function does have a correlation length of $\sim 5 \text{ Mpc}$ (Davis and Peebles 1983). Lorrimer *et al.* (1991) examined the correlation properties of satellite galaxies and concluded that to a galactocentric distance of 0.75 Mpc (the limit of their sampling for $H_0 = 75 \text{ km s}^{-1} \text{ Mpc}^{-1}$) the correlation function has a slope of 1.8 ± 0.2 , which agrees with the previously determined galaxy-galaxy correlation function (Davis and Peebles 1983a). Therefore, at least to 0.75 Mpc, but possibly to much larger distances, the density of “satellites” is proportional to $r^{-1.8}$. By adopting $\rho \propto r^{-1.8}$ at all distances up to 6.7 Mpc and using our survey parameters, we calculated the expected relative proportion of satellites in our sample from various galactocentric distances. For smaller values of γ the percentage of satellites contained within a particular radius decreases.

To calculate the number of objects in each shell, we need to know the density in the shell and the volume of the shell. The density was discussed above. The volume will now be treated. Consider the progression of spherical volumes beginning with a shell of radius $r = 0$ and moving outward. Initially, the projected radius cutoff has no relevance. For a shell of width dr the volume of that shell within the selection cone is $4\pi r^2 dr$. For radii larger than the projected radius cutoff, the volume of a shell of width dr that is within the selection cone is not $4\pi r^2 dr$. The shell is truncated at the sides by the “walls” of the selection cone created by the projected separation cutoff (the projected separation criteria is equivalent to an angular separation cutoff). A representative volume element is drawn in Figure 4.6. We integrated analytically over the region within the intersection of the spherical

shell and the interior of the selection cone to arrive at the following expression for the volume of the region,

$$V = \frac{\pi r_c^2}{3d^2} \left((d+e)^3 + (d+c)^3 - 2d^3 \right) + \pi \left(c^3/3 + e^3/3 - r_{sph}^2 c - r_{sph}^2 e \right),$$

where

$$\begin{aligned} a &= \frac{2d^2/r_c - \sqrt{4d^4/r_c^2 - 4(d^2/r_c^2 + 1)(d^2 - r_{sph}^2)}}{2(d^2/r_c^2 + 1)}, \\ b &= \frac{2d^2/r_c + \sqrt{4d^4/r_c^2 - 4(d^2/r_c^2 + 1)(d^2 - r_{sph}^2)}}{2(d^2/r_c^2 + 1)}, \\ c &= \sqrt{r_{sph}^2 - a^2}, \\ e &= \sqrt{r_{sph}^2 - b^2}, \end{aligned} \tag{4.46}$$

d is the distance from us to the primary, r_{sph} is the radius of the sphere in question, r_c is the projected separation cutoff, and the remaining quantities are as shown in Figure 4.6. We numerically integrated the product of density and volume to estimate the proportion of satellites in our sample from each physical radius. The cumulative distributions for projected radius cutoffs of 0.3 and 0.5 Mpc are presented in Figure 4.7. We conclude that if the simulations extend to radii of 2 Mpc at the current time, they will include 90 to 95% of the observed sample. Because the background contamination was estimated to be $\sim 10\%$ of the sample (cf. §3.3), there is no compulsion to achieve greater completeness. Therefore, we adopted $r_{max} = 2$ Mpc. Note that although our cutoff radius is 0.5 Mpc (and for the data from the multiobject surveys between 0.2 and 0.3 Mpc) many of the satellites are probing the potential to much larger distances.

At 2 Mpc the particles may be unbound. To estimate whether this occurs for mass models of interest, we calculated the current radial distance of the last bound

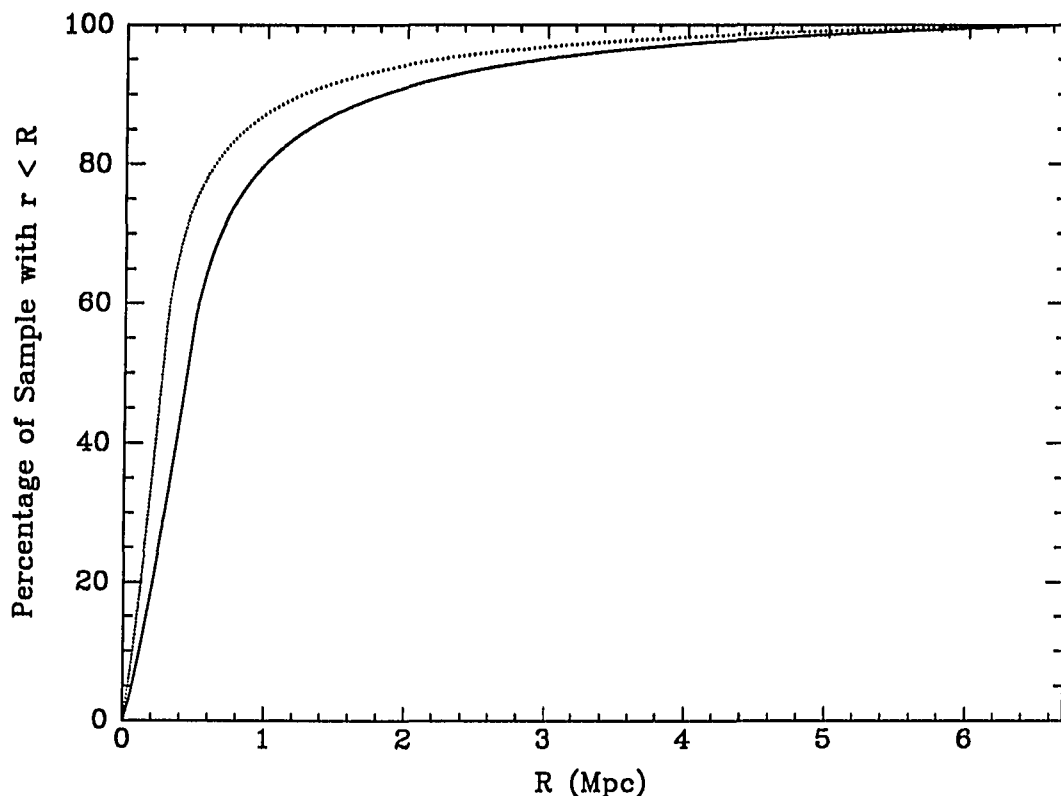


Figure 4.7: *Distribution of Satellites in True Distances : The cumulative distribution of satellites vs. their galactocentric distance. The solid line is for an observational cutoff of 500 kpc projected separation. The dotted line for an observational cutoff of 300 kpc.*

orbit as a function of enclosed mass for $\Omega_0 < 1$ models¹². Before the initial turnaround, a shell will not have crossed any other shell, and so we can treat the orbit of a particle in that shell as Keplerian. For Keplerian orbits Eq. 2.5,

$$r^3 = \frac{GMt^2(1 - \cos\theta)^3}{(\theta - \sin\theta)^2},$$

¹²Recall that all shells are bound in the $\Omega = 1$ models.

can be used. The least bound orbit will have $\theta \approx 0$. Using

$$\lim_{\theta \rightarrow 0} \frac{(1 - \cos \theta)^3}{(\theta - \sin \theta)^2} = 4.5, \quad (4.47)$$

we determined that the position of farthest bound shell, r_b , as a function of time and enclosed mass is given by,

$$r_b = (4.5GMt^2)^{1/3}. \quad (4.48)$$

Therefore, if the last bound shell is at 2 Mpc at $t = 14$ Gyr, then the enclosed mass is $2 \times 10^{12} M_\odot$. Because some of our models are for smaller total masses, we expect those models to have unbound particles. An important advantage of the secondary infall models is that they can be used to model the dynamics of unbound particles. We treat the orbits of unbound particles as purely radial. Random phase models cannot treat unbound particles.

Initial Conditions

If the mass of galaxies is only that inferred from H I rotation curves, then galaxies have global M/L 's between 10 and 20. If such galaxies contain all the mass in the Universe, then $\Omega_0 \sim 0.01$. We will consider such models in addition to those with $\Omega_0 = 0.03, 0.1, 0.3$ and 1.0.

The evolution of a FRW universe can be written in terms of a development angle, θ (see Weinberg 1972 for details). For open universes, θ is imaginary and it is convenient to define Ψ such that $\Psi \equiv i\theta$. We can then write,

$$H_0 t = q_0(1 - 2q_0)^{-3/2}(\sinh \Psi - \Psi), \quad (4.49)$$

where H and q are the Hubble constant and deceleration parameter, respectively, and the subscript 0 denotes current value. Once t_i , H_0 , and q_0 were prescribed, we

evaluated Ψ_i . The ratio of scale factors, R_i/R_0 , was calculated using

$$\frac{R_i}{R_0} = \frac{q_0}{1 - 2q_0} (\cosh \Psi_i - 1). \quad (4.50)$$

The $\Omega = 1$ case is slightly different. In an Einstein-de Sitter universe the evolution is given by

$$\frac{R_i}{R_0} = \left(\frac{3}{2} H_0 t_i \right)^{2/3}, \quad (4.51)$$

and $\Omega_i = 1$ for all z_i . By combining the previous equations with the equation for the redshift,

$$z_i = \frac{R_0}{R_i} - 1, \quad (4.52)$$

we converted between time and redshift.

We now describe the initial conditions, r_i and v_i , for each shell as a function of the enclosed mass. At the initial time, we can approximate the density as uniform, implying that

$$r_i(M) = \left(\frac{3M}{4\pi\rho_0} \right)^{1/3} \left(\frac{1}{1 + z_i} \right). \quad (4.53)$$

Notice that the assumption of uniform density is where we deviate from the FG models. Given the enclosed mass, position, and energy (cf. §4.3.1), we can now produce an expression for the initial radial velocity of the shell,

$$v_i(M) = \left(2E(M) + \frac{2G(M + m)}{(r_i^2 + \epsilon^2)^{1/2}} \right)^{1/2}. \quad (4.54)$$

We now describe the remaining details of how the simulations were begun. The initial time was chosen so that $z \sim 1000$. M_* was determined using the $\alpha = 1$ case. As mentioned above, the initial energies and velocities for this case should be equal to those derived using the Keplerian orbit equations given in §2.3.2. Once M_* was determined and r specified, the quantities E , $M(r)$ and v were calculated using Eqs. 4.28, 4.29, 4.53, 4.54 and $\alpha = 2/3$. Using M , E , and Eq. 4.45, we calculated the

torquing factor K . The minimum radius at which to place particles was determined by the requirement that $G^2 M^2 / 4E^2 > \epsilon^2$ (cf. Eq. 4.45) and that the maximum radius of the innermost orbit be between 10 and 20 kpc. Since the softening was 10 kpc, there was no need to have particles with maximum radii smaller than 10 kpc. The largest initial radius was determined by our requirement that the final distribution extend to 2 Mpc. Twenty-five thousand particles spaced evenly in radius were used for the simulations. Each shell/particle had a mass of $\rho_i \times (\text{shell volume})$. The orbits were integrated until $H = H_0$ in an otherwise undisturbed universe of chosen Ω_0 . H_0 was adopted to be $75 \text{ km s}^{-1} \text{ Mpc}^{-1}$, as throughout this dissertation.

Testing and Comparison to Earlier Work

Internal checks on the code included verifying that the system conserved energy and angular momentum. Because of the relaxation process, each shell does not necessarily conserve energy. However, the entire system should conserve energy. During the runs, we evaluated the system's total energy approximately every simulated million years. $\Delta E/E$ between the beginning and end of any run is $\lesssim 1\%$, and *rms* deviations are $\ll 1\%$. Because of the imposed spherical symmetry, each shell should conserve angular momentum once the tangential force is switched off. To test this aspect of the code, we examined the orbits of particles that were initially the 50th, 2500th, and 7500th when ordered by radius. Angular momentum in all runs was conserved to $\ll 1\%$. Additionally, the final angular momentum of the particles was always well within 1% of $\epsilon_P J_{\text{max}}$.

The integration numerics were examined by comparing a single particle radial orbit around a point mass with the analytic expression for a Keplerian orbit, and by examining the orbits of many particles in the full simulation until they reached

their initial turnaround. Recall that particles are on Keplerian orbits until they cross other shells, which only happens after their initial turnaround. In both instances there was excellent agreement with the analytic calculations.

External checks on the code involved verifying that the results agree with previous analytic work. However, we note that inside a particular radius the mass density is not accurately described in our models. Interior to the innermost shell, the mass is treated as if it were concentrated at the center of the system. This material (if treated correctly) would develop a relaxed core and envelope structure of its own. However, treating smaller scales requires more particles and smaller integration time steps, which increases the computation time. For simulations with strongly radial orbits, this omission becomes somewhat more important because more particles penetrate within the region with the incorrect density profile. Errors arise only in the radial density profile at radii $< \epsilon$ and to some extent radii just beyond ϵ . The mass profiles within the relaxed core have the correct shape for $r > 15$ kpc in all models.

The best external check of the initial conditions is provided by the final density profiles. In Figure 4.8 we have plotted the resulting halo mass profiles¹³ within the core from runs with $\Omega_0 = 0.1, 0.3$, and 1.0 . We have also plotted the representative profile of a fully relaxed core (*i.e.*, $\rho \propto r^{-2}$) with a dashed line. In Figure 4.9 we have plotted mass profiles from $\Omega = 1$ models with $e = 0.5$ for $\alpha = 2/3$ and $\alpha = 1$. The differences in profiles are apparent within the relaxed core (*i.e.*, compare the slopes of the dashed lines). In addition, we have overlaid the rescaled results from Bertschinger (1985) onto the $\alpha = 1$ model. The agreement between the simulated profiles of the relaxed core region and the expected profile for all values of Ω_0 , both

¹³We have plotted the mass profiles instead of the density profile because the density profiles are much noisier. However, the density profiles are also consistent with the expected r^{-2} power-law.

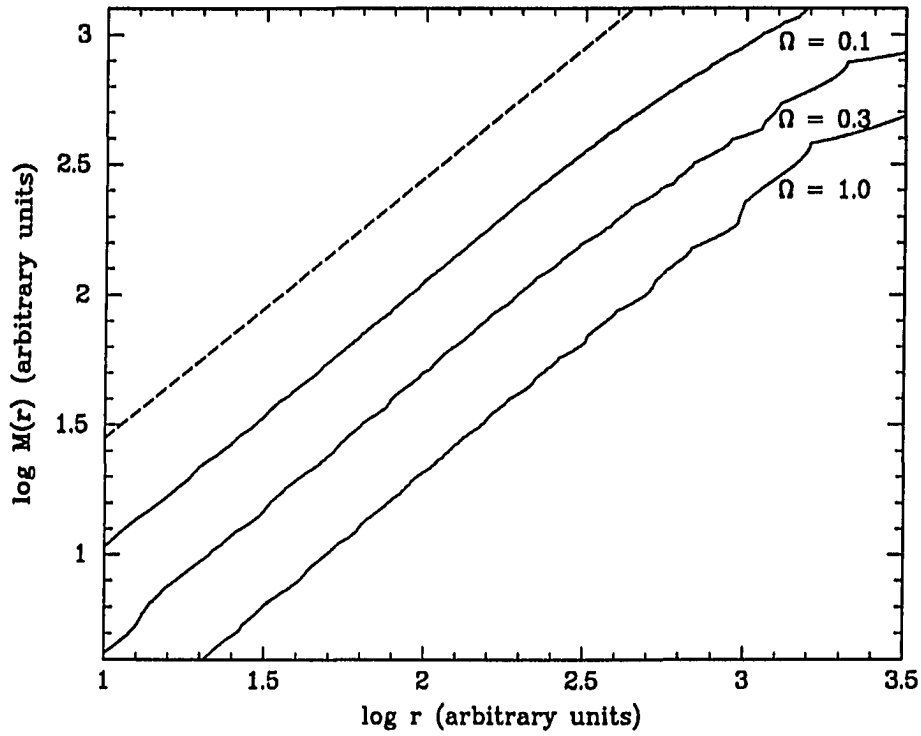


Figure 4.8: *Mass Profiles of Secondary Infall Models: Relaxed Core.* We have plotted the rescaled simulated mass profiles for $\Omega_0 = 0.1, 0.3$, and 1.0 models. The expected $\rho \propto r^{-2}$ profile is designated by the dashed line.

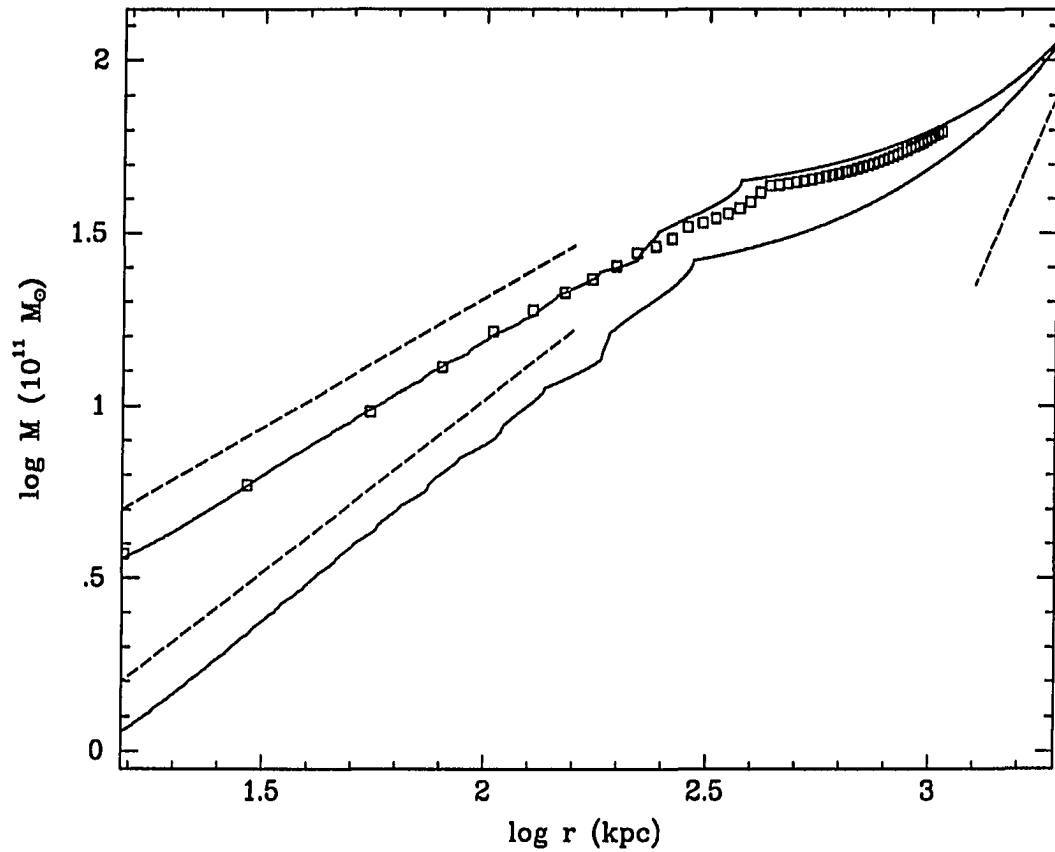


Figure 4.9: *Mass Profiles of Secondary Infall Models: Dependence on α .* We have plotted mass profiles for $\Omega = 1$ models with $\alpha = 2/3$ and 1. Dashed lines represent the expected mass profiles. The profile from Bertschinger (1985) is denoted by open boxes. The Bertschinger profile is for a model with radial orbits. The differences between it and our profile are similar to those seen among profiles from models with different eccentricity orbits (e.g., the outermost caustic is at a slightly larger radius and the profile beyond that is flatter for the model with more radial orbits).

in Figures 4.8 and 4.9, indicates that initial conditions and the code are working satisfactorily.

4.3.3 Scaling Properties

An important feature of the standard and modified secondary infall models is that the shape of the mass profile is independent of the total bound mass, M_* . This self-similarity enables us to scale among models of the same Ω_0 , but of different M_* 's. Therefore, once Ω_0 and ϵ_P are specified, only one model (*e.g.*, one with a particular M_*) is calculated numerically. The corresponding mass profile, and particle velocities and positions, for any other M_* model were derived by scaling the original computational results. The scaling procedure is described below.

We used the ratio of circular velocities at a fixed distance r_c to scale our models. Consider two models, denoted by subscripts 1 and 2, and that we want to scale model 1 to model 2. We know that $M_1(r_c)/M_2(r_c) \propto (v_1/v_2)^2$, where the velocities are measured at r_c and as usual M 's denote mass enclosed at that radius. After radial rescaling, $r_{c,1} \rightarrow r'_{c,1}$ and $M_1(r_c) = M'_1(r'_c)$. We defined S to be the scaling factor between r_c and r'_c (*i.e.*, $r'_c/r_c \equiv S$). From Eq. 4.15 we know that, $M_* \propto r_*^3$. Therefore, if r_* scales by a factor S , then M_* scales by a factor S^3 . Because of self-similarity (*i.e.*, because the shape of the mass profile remains the same), the same scaling must hold at all radii. The scale factor S can be derived analytically in special cases or empirically in general.

If both $r_{c,1}$ and $r'_{c,1}$ are smaller than the size of the fully relaxed core, then S can be calculated analytically. $M'_1(r_c)$ can be evaluated using

$$M'_1(r_c) = M'_1(r'_c) \left(\frac{r_c}{r'_c} \right)^\delta, \quad (4.55)$$

provided we know δ , which is defined by $M \propto r^\delta$ within the relaxed core. In addition, we know that

$$M'_1(r_c)S^3 = M_2(r_c) \text{ and that } M_2(r_c) = \left(\frac{v_2}{v_1}\right)^2 M'_1(r'_c), \quad (4.56)$$

so

$$M'_1(r_c)S^3 = \left(\frac{v_2}{v_1}\right)^2 M'_1(r'_c). \quad (4.57)$$

We combine the previous equations to derive that

$$M'_1(r'_c)S^3 \left(\frac{r_c}{r'_c}\right)^\delta = \left(\frac{v_2}{v_1}\right)^2 M'_1(r'_c). \quad (4.58)$$

Solving for S , we find that $S = (v_2/v_1)^{2/(3-\delta)}$. Model 1 is then rescaled by multiplying r by S and $M(r)$ by S^3 . For our purposes (*i.e.*, generally we want to scale a simulation to match an observed galaxy), v_2 is related to the observed rotation curve amplitude, W , and v_1 is the circular velocity of the simulated model. We shall refer to the circular velocity of the model at 30 kpc, our choice for r_c , as $v_c(30)$.

In general, the mass profile cannot be expressed as a radial power-law because r_c and r'_c are not within the fully relaxed core of the halo. The following is a description of the empirical derivation of S as a function of $v_c(30)$. A model was chosen and its mass profile was computed. For one hundred values of S , which span the range required by the observed W 's¹⁴, the mass profile was rescaled and the new $v_c(30)$ was evaluated. A polynomial was fit to the relationship between $v_c(30)$ and S . The polynomial fit was used to obtain the corresponding S for any choice of $v_c(30)$.

In Figure 4.10 we show the mass profiles for two full simulations of different total mass, for both $\Omega_0 = 0.01$ and 1.0. In addition, we have scaled the lower total mass model, for each value of Ω_0 , to match the higher mass model by using the circular

¹⁴ W 's provide information on the appropriate rescaling velocities. Therefore, the range of W 's is roughly matched to the range of velocities to which we shall want to rescale models.

velocities at 30 kpc. The results are overlaid in Figure 4.10. The agreement between the full simulations and the scaled ones is clearly excellent and demonstrates that rescaling is a reliable technique. The discrepancies are slightly larger in the upper panel (the $\Omega_0 = 0.01$ and $e = 0.9$ model). Models with large central masses and high eccentricities are the more difficult to model because the problem of modeling the central region becomes more important. Even though this combination of Ω_0 and e is the most difficult to model of all our combinations, the original and rescaled models are quite similar. We conclude that with rescaling we can accurately obtain a family of models, as a function of M_* , for a specified Ω_0 and ϵ_P .

Scaling Variable

In the previous section, we demonstrated that the models are easily rescaled to different characteristic velocities. However, the relationship between the scaling and observed velocities is not straightforward. As we have discussed in §4.2, the relationship between the inner rotation velocity, which is related to the observed H I line width, and the halo circular velocity, which is the relevant quantity for rescaling the models, is unknown. There might not be any relationship between primary luminosity (and H I rotation width) and halo mass. In this case, the simulated satellites should be drawn from a single model rescaled to a fixed characteristic velocity for the prototypical halo (case I). Alternatively, consider the natural presumption that more luminous galaxies, consequently those with greater H I widths, have more massive halos than fainter galaxies. If true, then the preferred velocity scaling for the simulated halo of a particular primary would be proportional to the observed

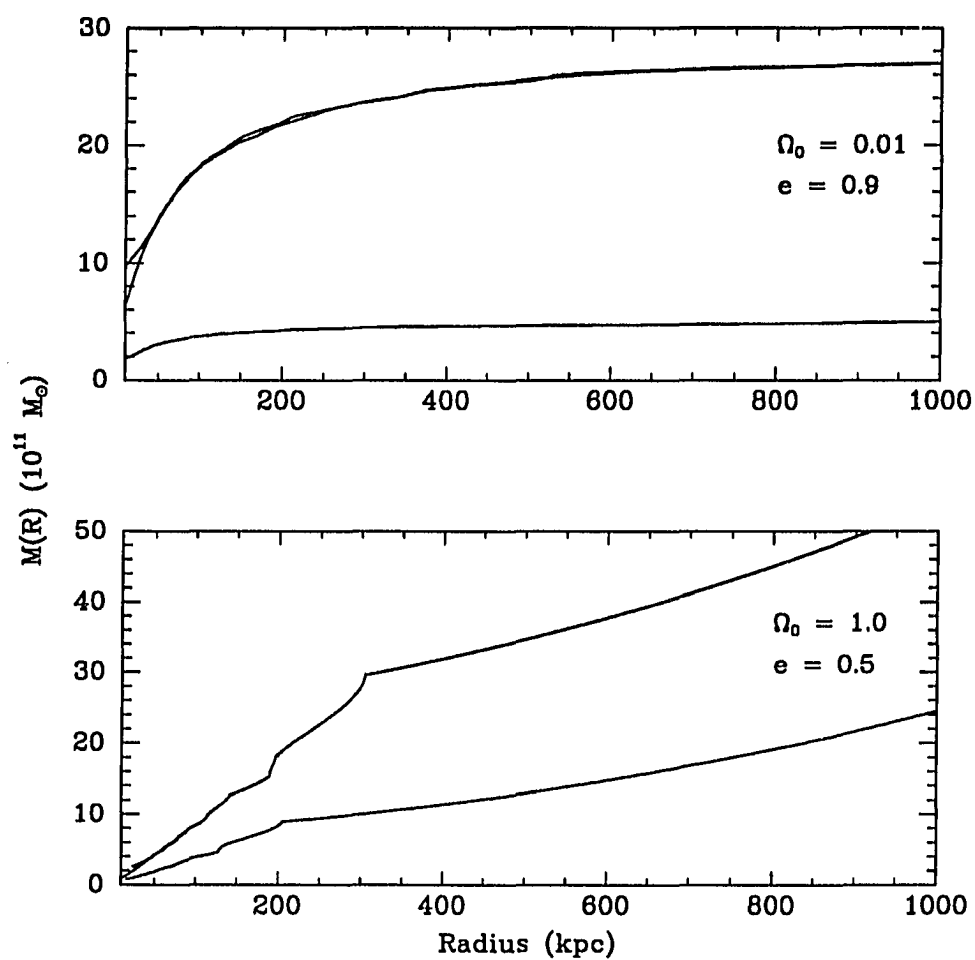


Figure 4.10: *On Rescaling the Models :* We show rescaling for both $\Omega_0 = 0.01$ and 1.0 models. Each panel includes mass profiles from a high and low mass full computer simulation. In addition, the low mass model has been rescaled to match the high mass model. In the lower panel, the upper curve contains both the original and the rescaled model.

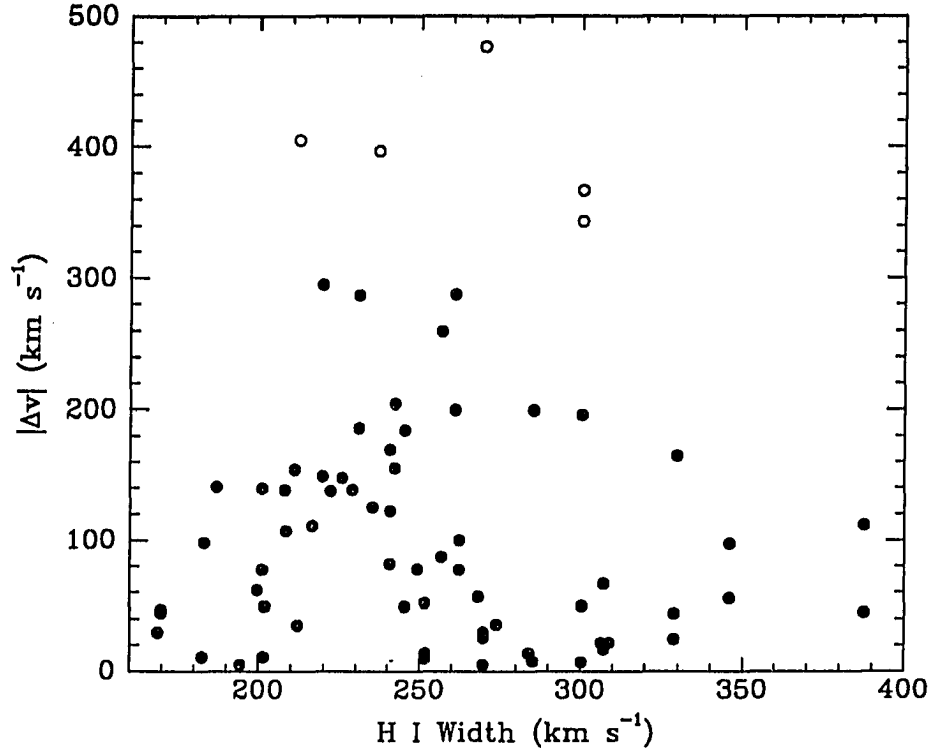


Figure 4.11: $|\Delta v|$ vs. Rotation Curve Amplitude : Entire satellite sample is plotted. Sample 1 is plotted with filled circles.

H I width of that primary. That is, simulated satellites belonging to a particular primary should be drawn from a model scaled to some fraction of the observed rotation width of that primary (case II). This choice of model would ensure that galaxies with larger H I widths would have more massive halos. Reality may lie somewhere between the two extremes with whatever relationship exists further complicated by scatter. However, for lack of more detailed knowledge, we only treated the two simple cases.

One observation that addresses this question of appropriate scaling is the distribution of observed $|\Delta v|$'s vs. rotation curve amplitudes, W 's. The scatterplot is shown in Figure 4.11. If more luminous galaxies have larger halos, then we expect brighter galaxies to have satellites with larger $|\Delta v|$'s. However, there is no visible trend between the two quantities and no significant rank correlation; although projection effects and observational errors decrease the significance of any existing correlation. Even though there appears to be no evidence of a positive correlation (actually there is marginal evidence for an anti-correlation), we calculated both case I and case II models.

Regardless of whether there is a one-to-one connection between W and the halo's characteristic velocity, it must be true that observations of W can aid us in constraining the halo scaling velocity. For example, the chosen halo circular velocity cannot be greater than W if $\rho \propto r^2$. One difficulty in relating the observations to the *standard* secondary infall models arises because those models are not an accurate depiction of galaxies at small scales ($< \text{few} \times 10 \text{ kpc}$). The rotation curve of the halos produced by those models diverges as $r \rightarrow 0$. This problem is possibly made more severe by the presence of dissipative matter that sinks deep in the potential well and further steepens the profile. These considerations led us to the modified infall models described in §4.3.1, which produce a flat central halo rotation curve. Again we stress that the modified models will result in slightly lower mass estimates than would the standard models. By having a flat rotation curve, we have eliminated the uncertainty associated with where to measure v_c . r_c must be beyond the inner region where the dynamics are not modeled accurately, but it should be within the relaxed core. We chose $r_c = 30 \text{ kpc}$.

Finally, we stress that the relevant quantity is the halo circular velocity, but the observed rotation curve reflects both the halo and disk potentials. By assuming that

W is the halo circular velocity, we have chosen a maximum halo solution. If the disk contributes to the potential, then we will have overestimated the halo circular velocity. This is true both for case I and case II models. The assumption of a massless disk will lead us to underestimate Ω_0 because for a given Ω_0 -model halo, we will have overestimated the halo's circular velocity.

4.3.4 Comparing Models and Data

The data are the collection of projected separations and radial velocity differences of satellite galaxies with respect to their associated primary galaxy and are described in Chapter 3. When comparing simulations with data, it is important to retain as much of the information in the data as possible. While this seems fairly obvious, many of the mass analysis techniques violate this maxim. For example, the mass estimator methods collapsed all the data into a single number (*e.g.*, $k < r\Delta v^2/G >$). The technique outlined below was constructed with this point in mind.

Each of our modified secondary infall models is defined by Ω_0 and e (the orbital eccentricity). Each model can be rescaled to arbitrary total mass by the appropriate choice of $v_c(30)$. As previously discussed, there are at least two possibilities regarding the relationship between $v_c(30)$ and the observed value of W . For one set of models we assumed that the halo velocities at 30 kpc were equal to $\langle W \rangle$, regardless of W for the particular primary galaxy being modeled (case I). For the other set models we adopted $v_c(30) = W$ (case II). In addition to Ω_0 , e , and $v_c(30)$, there is another free parameter. This fourth parameter arises from the conversion of the simulated particle distribution to the satellite distribution. The conversion requires an expression for the true distribution of satellites. We have assumed that the distribution is spherically symmetric and that the satellite radial density profile is given by a power-law of the form, $\rho \propto r^{-\gamma}$. The fourth free parameter is then γ .

Since the scaling velocities are constrained by the observed H I rotation widths, the only parameters left to constrain are Ω_0 , e and γ .

There are external constraints on γ . Observational studies conclude that $\gamma = 1.8 \pm 0.2$ (Lorrimer *et al.* 1991). On the other hand, if satellites formed in proportion to the local density, then standard secondary infall models predict that $\gamma = 2.25$, in the relaxed core, while our modified infall models predict $\gamma = 2$. We will study three cases: $\gamma = 1.6$, 1.8 and 2.0 .

Only Ω_0 and e now remain to be constrained. The observed $|\Delta v|$'s contain information on the intrinsic distribution of $|\Delta v|$ for each r_p at which a satellite was observed. The intrinsic distribution of $|\Delta v|$ can be derived from the secondary infall simulations. To constrain combinations of Ω_0 and e , we compared the observations to the data in the following manner. A model with a certain Ω_0 and e was chosen for comparison. The first satellite from the list of observed satellites was selected. The model was rescaled either to the mean rotation width of the entire sample of primaries, $\langle W \rangle$ (case I), or to the rotation width of the primary that corresponds to the observed satellite (case II). Using the chosen value of γ and the procedure detailed in the following section, we chose five thousand simulated satellites with a projected separation within 10% of the observed satellite's. The rank R of the observed value of $|\Delta v|$ within the simulated distribution of $|\Delta v|$'s was evaluated. To obtain R for every satellite in the observed sample, we proceeded to repeat the process for each observed satellite. The distribution of ranks (*i.e.*, the distribution between 1 and 5000) for the entire sample of observed satellites will be uniform for acceptable models. We used a 1-D KS test to compare the distribution of ranks against the expected uniform distribution.

By evaluating the distribution of ranks we have projected two-dimensional data onto a one-dimensional space, although in a more sophisticated manner than by

simply collapsing the data onto the $|\Delta v|$ axis. To regain some of the lost information, we examined the correlations among the ranks and the other observables, r_p and W . Acceptable models will produce no significant correlation between the ranks and either observable. To illustrate this consider a model that produces a uniform distribution of ranks by balancing the number of satellites at small r_p with small ranks, with the number of satellites at large r_p with large ranks. While such a model would have a uniform distribution of ranks, it would not accurately reproduce the observed distribution of points in the $r_p - |\Delta v|$ plane. Such a model would produce a significant correlation between r_p and R . Similar correlations arise between R and W if the adopted relationship between $v_c(30)$ and W is incorrect.

The models are deemed unacceptable if we can reject with 90% or greater confidence the hypothesis that the ranks were drawn from a uniform distribution, or if there is a 10% or smaller probability that the correlation between R and r_p or W arose from random fluctuations. All models included simulated observational uncertainties. We adopted a $\pm 10\%$ uncertainty in distance (uniformly distributed), and a dispersion of 20 km s^{-1} in the distribution of velocity errors. Uncertainties in W were taken to be $\pm 10\%$ (uniformly distributed). Again the distance uncertainties are meant to include all sources of uncertainty except those in H_0 .

Selecting Satellites

Each particle in the simulation represents a shell of test particles — not satellites — orbiting in the primary's potential. We must convert between particles and satellites in a manner that reproduces the correct satellite radial density profile (observed to be roughly $\rho \propto r^{-1.8}$; Lorrimer *et al.* 1991). In addition, to compensate for any selection biases in the projected separation distribution, we must ensure that the distribution of simulated satellites has the same projected separation distribution as

the observed satellite sample. Within the simulations there are three different radial distributions to consider: the particle distribution, the mass distribution, and the satellite distribution. The particle distribution depends on the initial distribution of particles and is further complicated by the development of shell structure. The mass distribution can be obtained from the particle distribution and the masses of the various shells. It is useful for comparison to the predicted radial density profiles (cf. §4.3.2) and for our final conclusions about the mass profiles of galaxy halos. The first two distributions are a direct result of the simulations; the third one is obtained by attributing to each shell the appropriate number of satellites¹⁵.

To select appropriately satellites from the simulated particle distribution, we first need to evaluate $P(r|r_p)$. $P(r|r_p)$ is the probability of selecting a satellite from a shell of radius r when only selecting satellites that have a projected separation r_p . To evaluate $P(r|r_p)$, we calculated the fraction of each shell that projects onto the radial position of the corresponding observed satellite to within 10%. The total number of satellites per shell was calculated to within a normalization constant by using $\rho_n \sim r_{turn}^{-\gamma}$, where r_{turn} is the initial turnaround distance of each shell/particle and ρ_n is the number density of satellites. It is more natural to weight the shells by their turnaround distance than by their current distance, which is time-dependent. However, the appropriate weight for unbound shells is unclear since they will never reach turnaround. We chose to weight shells that had not yet turned around and unbound shells by their current distance. This weighting scheme produces a density profile that is on average $\propto r^{-\gamma}$, because most satellites are currently at distances near their maximum radius. This weighting scheme also propagates the shell

¹⁵A satellite density profile that is flatter than the halo density profile (i.e., $\gamma < 2.0$) could be produced by a bias in the formation of satellites, by evolution of the satellite density profile, or by fluctuations in the initial density distribution (cf. Hoffman and Shaham 1985). If there was an initial power-law fluctuation spectrum, $p(k) \propto k^n$, then the modified relaxed-core density law is $\rho \propto r^{-\beta}$, where $\beta = [3(3+n)]/(4+n)$. The standard infall model reproduces the $r^{-2.25}$ profile and so corresponds to $n = 0$. Shallower slopes are predicted for $0 < n \lesssim -1$, which are standard assumed values of n . Our modified infall model corresponds to $n = -1$.

structure from the particle distribution to the satellite distribution and produces a continuous distribution of weights. An alternative is to weight all shells by their current distance. This scheme produces a noiseless $r^{-\gamma}$ profile throughout, but the weighting is time-dependent, which is unphysical. In addition, in this scheme the shell structure is not propagated to the satellite density profile¹⁶. The number of satellites from each shell that project onto the chosen r_p bin is the product of the total number of satellites in that shell and the fraction of the volume of that shell which projects onto that r_p bin. The projection volume integral was calculated analytically in a similar manner to that discussed in §4.3.2 for estimating r_{max} . Once these calculations are done for all shells and a particular r_p , the distribution of galactocentric radii of satellites in the r_p bin has been determined. The normalized version of this distribution is $P(r|r_p)$.

Five thousand simulated satellites, which all have the same particular r_p to within 10%, were selected using the probability function described above. The line-of-sight velocity of each particle is given by $v_{l.o.s.} = v_r \cos \theta + v_t \sin \theta \sin \phi$, where v_r and v_t are the radial and tangential velocity components of the particle with respect to the primary, $\theta = \arcsin(r_p/r)$, r is the distance from the primary to the satellite, and ϕ , which describes the direction of the tangential velocity component, is randomly chosen from a uniform distribution between 0 and 2π . Using the radial velocities, we compiled the $|\Delta v|$ distribution at an r_p that matched that of one of the observed satellites. The process is repeated for each observed satellite. Using the derived $|\Delta v|$ distributions, we calculated the ranks of the observed $|\Delta v|$'s.

¹⁶We ran a test set of models where all shells were weighted by their current distance. The 90% confidence lower bound on Ω_0 was slightly larger than with the turnaround radius weight. We conclude that of the two weighting schemes, the turnaround radius weighting is conservative.

Constraining Ω_0 and e

We are finally ready to begin constraining galactic halo models. We present results only from comparisons with the modified secondary infall models. Simulations were run for five values of Ω_0 (0.01, 0.03, 0.1, 0.3, 1.0) and three values of e (0.5, 0.7, 0.9). Samples of simulated satellites were drawn as described above to determine the $|\Delta v|$ distribution at the r_p of each observed satellite. The distribution of ranks corresponding to the observed $|\Delta v|$'s was compared to the expected uniform distribution. The probability that the ranks were drawn from a uniform distribution is given in Tables 4.7-4.9 for various models. Also given in these Tables are the probabilities that correlations of the observed magnitude among the ranks and either r_p or W could arise at random. We consider models that have values < 0.1 in either of the three rightmost columns unacceptable. The values in Table 4.7 were obtained through use of the entire sample of satellites. The values in Table 4.8 were obtained through use of our preferred sample, sample 1, and the values in Table 4.9 were obtained using sample 2. In addition to the Tables, we also present the results for the preferred models (sample 1, case I) in contour plots in Figures 4.12-4.14.

We begin by discussing the results obtained using sample 1. All case II models produce correlations among W and R that are too significant to be caused by random fluctuations. This conclusion is also true for the other samples. Therefore, we reject case II in favor of case I, which does not have this problem. This result does not imply that there is no relationship between W and $v_c(30)$; although the relationship, if one exists, must be more complex than that adopted for case II models. Probably, as suggested by Salucci and Frenk (1989), the disk contribution to the rotation curve distorts the relationship. The results from the KS tests for case I models imply slightly lower values of Ω_0 than do the corresponding case II models. Therefore, by continuing only with case I models, we will continue to obtain conservative limits on Ω_0 .

Table 4.7: Modified Secondary Infall Model Results : Sample 0

Ω_0	Ecc.	γ	Case	KS Test	$P(\rho_{r_p,R})$	$P(\rho_{w,R})$
0.01	0.5	1.8	I	0.000	0.289	0.584
0.01	0.7	1.8	I	0.000	0.017	0.715
0.01	0.9	1.8	I	0.000	0.055	0.966
0.03	0.5	1.8	I	0.001	0.442	0.786
0.03	0.7	1.8	I	0.000	0.352	0.945
0.03	0.9	1.8	I	0.000	0.098	0.395
0.10	0.5	1.8	I	0.019	0.764	0.800
0.10	0.7	1.8	I	0.011	0.110	0.874
0.10	0.9	1.8	I	0.000	0.007	0.889
0.30	0.5	1.8	I	0.118	0.986	0.705
0.30	0.7	1.8	I	0.065	0.141	0.646
0.30	0.9	1.8	I	0.000	0.014	0.809
1.00	0.5	1.8	I	0.303	0.578	0.607
1.00	0.7	1.8	I	0.674	0.442	0.736
1.00	0.9	1.8	I	0.032	0.017	0.659

Table 4.8: Modified Secondary Infall Model Results : Sample 1

Ω_0	Ecc.	γ	Case	KS Test ^a	$P(\rho_{r,p,R})$	$P(\rho_{w,R})$
0.01	0.5	1.6	I	0.002	0.830	0.222
0.01	0.7	1.6	I	0.000	0.220	0.107
0.01	0.9	1.6	I	0.000	0.424	0.413
0.03	0.5	1.6	I	0.008	0.653	0.268
0.03	0.7	1.6	I	0.004	0.244	0.582
0.03	0.9	1.6	I	0.000	0.069	0.254
0.10	0.5	1.6	I	0.199	0.974	0.277
0.10	0.7	1.6	I	0.306	0.112	0.633
0.10	0.9	1.6	I	0.007	0.023	0.612
0.30	0.5	1.6	I	0.792	0.353	0.379
0.30	0.7	1.6	I	0.971	0.359	0.263
0.30	0.9	1.6	I	0.118	0.016	0.382
1.00	0.5	1.6	I	0.043+	0.572	0.050
1.00	0.7	1.6	I	0.088+	0.878	0.225
1.00	0.9	1.6	I	0.390	0.995	0.020
0.01	0.5	1.8	I	0.000	0.466	0.393
0.01	0.7	1.8	I	0.000	0.146	0.294
0.01	0.9	1.8	I	0.000	0.319	0.366
0.03	0.5	1.8	I	0.006	0.726	0.182
0.03	0.7	1.8	I	0.005	0.164	0.180
0.03	0.9	1.8	I	0.001	0.055	0.167
0.10	0.5	1.8	I	0.519	0.524	0.665
0.10	0.7	1.8	I	0.192	0.212	0.304
0.10	0.9	1.8	I	0.003	0.009	0.840
0.30	0.5	1.8	I	0.806	0.883	0.214
0.30	0.7	1.8	I	0.888	0.529	0.106
0.30	0.9	1.8	I	0.145	0.014	0.154
1.00	0.5	1.8	I	0.022+	0.120	0.241
1.00	0.7	1.8	I	0.304	0.687	0.661
1.00	0.9	1.8	I	0.648	0.050	0.367

^a The + indicates that the cumulative distribution of ranks was above that of a uniform distribution of ranks for all values of the ranks. This implies that agreement between the two could be improved by decreasing $v_c(30)$.

Table 4.8 (continued)

Ω_0	Ecc.	γ	Case	KS Test	$P(\rho_{r,p,R})$	$P(\rho_{w,R})$
0.01	0.5	1.8	II	0.000	0.981	0.083
0.01	0.7	1.8	II	0.001	0.232	0.035
0.01	0.9	1.8	II	0.000	0.115	0.001
0.03	0.5	1.8	II	0.009	0.549	0.001
0.03	0.7	1.8	II	0.015	0.572	0.002
0.03	0.9	1.8	II	0.000	0.004	0.007
0.10	0.5	1.8	II	0.136	0.739	0.013
0.10	0.7	1.8	II	0.286	0.724	0.010
0.10	0.9	1.8	II	0.013	0.017	0.006
0.30	0.5	1.8	II	0.674	0.468	0.023
0.30	0.7	1.8	II	0.873	0.106	0.002
0.30	0.9	1.8	II	0.123	0.034	0.038
1.00	0.5	1.8	II	0.196	0.371	0.000
1.00	0.7	1.8	II	0.747	0.661	0.000
1.00	0.9	1.8	II	0.257	0.086	0.002
0.01	0.5	2.0	I	0.000	0.263	0.286
0.01	0.7	2.0	I	0.000	0.055	0.988
0.01	0.9	2.0	I	0.000	0.046	0.670
0.03	0.5	2.0	I	0.039	0.672	0.852
0.03	0.7	2.0	I	0.005	0.458	0.323
0.03	0.9	2.0	I	0.000	0.010	0.327
0.10	0.5	2.0	I	0.508	0.895	0.319
0.10	0.7	2.0	I	0.290	0.487	0.483
0.10	0.9	2.0	I	0.004	0.081	0.319
0.30	0.5	2.0	I	0.989	0.380	0.209
0.30	0.7	2.0	I	0.989	0.675	0.443
0.30	0.9	2.0	I	0.333	0.014	0.455
1.00	0.5	2.0	I	0.079+	0.207	0.499
1.00	0.7	2.0	I	0.214	0.800	0.192
1.00	0.9	2.0	I	0.310	0.141	0.445

Table 4.9: Modified Secondary Infall Model Results : Sample 2

Ω_0	Ecc.	γ	Case	KS Test	$P(\rho_{r_p,R})$	$P(\rho_{w,R})$
0.01	0.5	1.8	I	0.090	0.885	0.250
0.01	0.7	1.8	I	0.014	0.050	0.464
0.01	0.9	1.8	I	0.003	0.045	0.637
0.03	0.5	1.8	I	0.259	0.889	0.912
0.03	0.7	1.8	I	0.205	0.842	0.200
0.03	0.9	1.8	I	0.017	0.006	0.496
0.10	0.5	1.8	I	0.252	0.392	0.427
0.10	0.7	1.8	I	0.969	0.860	0.309
0.10	0.9	1.8	I	0.407	0.112	0.204
0.30	0.5	1.8	I	0.340	0.048	0.298
0.30	0.7	1.8	I	0.245	0.917	0.608
0.30	0.9	1.8	I	0.831	0.074	0.698
1.00	0.5	1.8	I	0.000+	0.184	0.711
1.00	0.7	1.8	I	0.010+	0.718	0.502
1.00	0.9	1.8	I	0.205	0.301	0.924

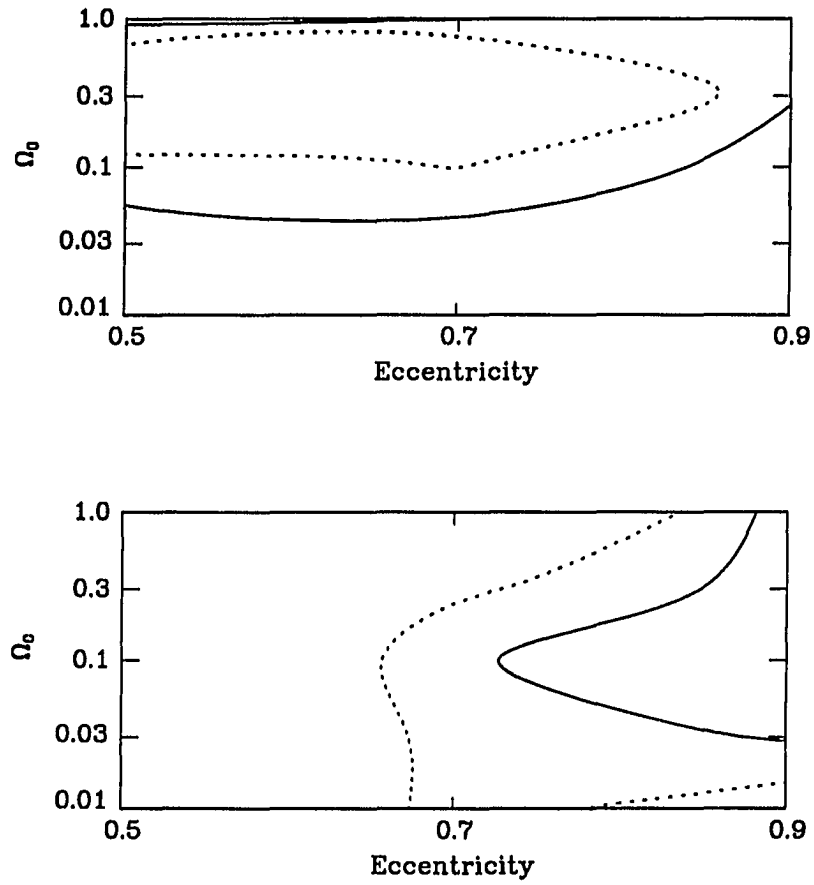


Figure 4.12: *KS Results from Modified Secondary Infall Models : In the upper panel, contours represent 60 and 90% confidence limits based on the distribution of ranks on acceptable models in the (Ω_0, e) subspace. In the lower panel, contours represent 60 and 90% confidence limits based on the correlation between r_p and R on acceptable models. These results are for case I, $\gamma = 1.6$, and satellite sample 1.*

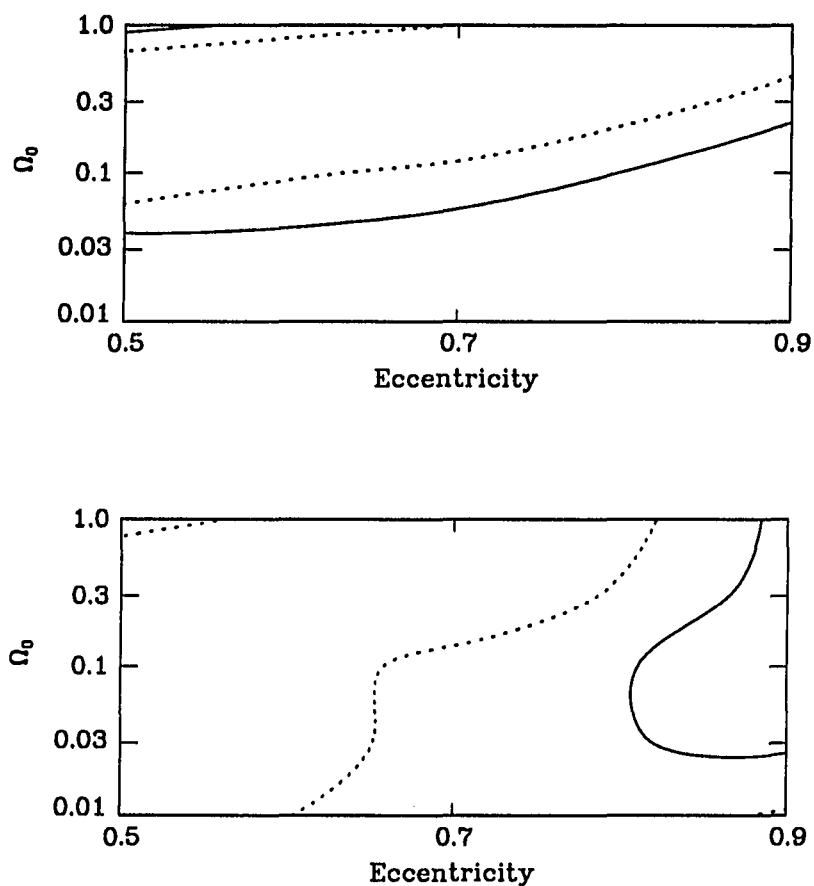


Figure 4.13: *KS Results from Modified Secondary Infall Models : In the upper panel, contours represent 60 and 90% confidence limits based on the distribution of ranks on acceptable models in the (Ω_0, e) subspace. In the lower panel, contours represent 60 and 90% confidence limits based on the correlations between r_p and R on acceptable models. These results are for case I, $\gamma = 1.8$, and satellite sample 1.*

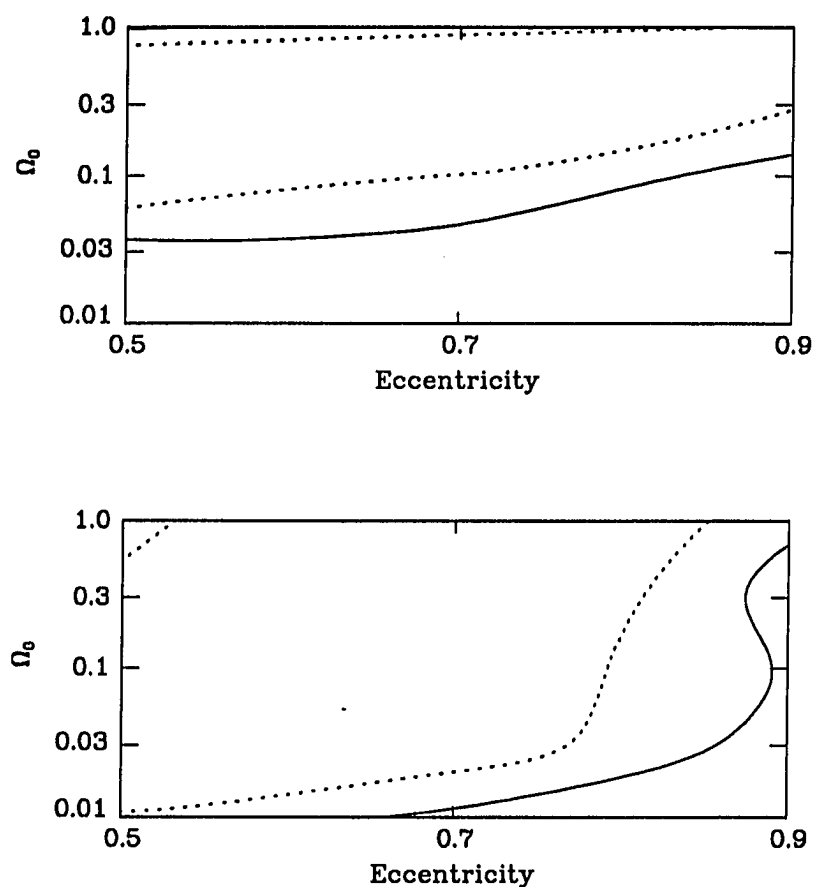


Figure 4.14: *KS Results from Modified Secondary Infall Models : In the upper panel, contours represent 60 and 90% confidence limits based on the distribution of ranks on acceptable models in the (Ω_0, e) subspace. In the lower panel, contours represent 60 and 90% confidence limits based on the correlation between r_p and R on acceptable models. These results are for case I, $\gamma = 2.0$, and satellite sample 1.*

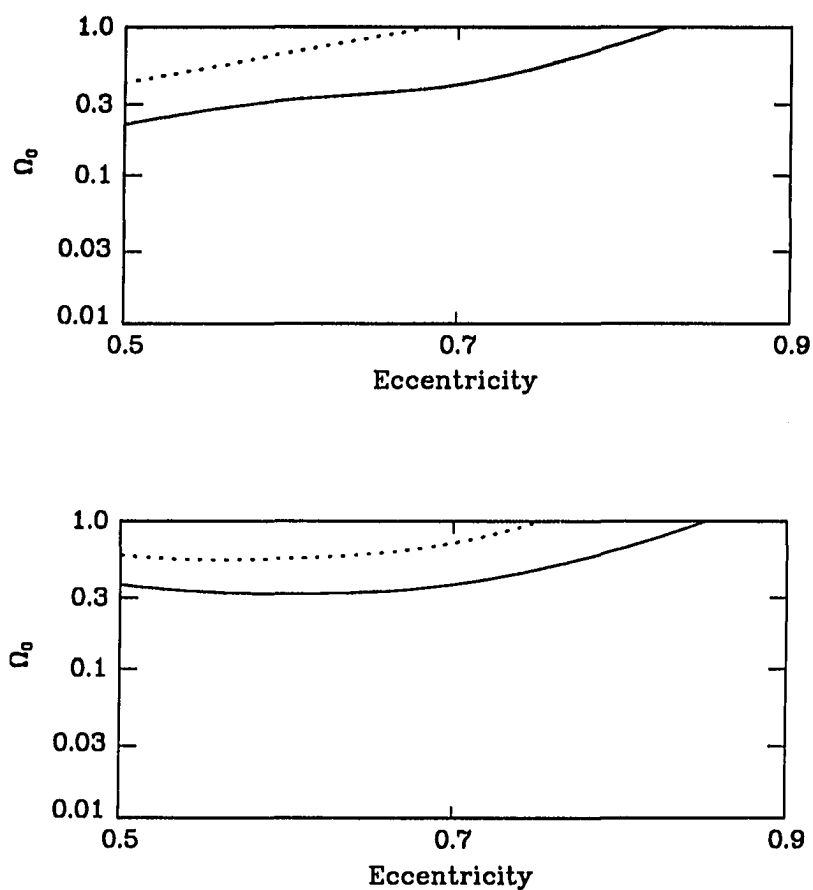


Figure 4.15: *KS Results from Modified Secondary Infall Models : v_c Dependence.* In the both panels, contours represent 60 and 90% confidence limits based on the distribution of ranks on acceptable models in the (Ω_0, e) subspace. Upper panel is for case I models ($v_c(30) = 0.8W$). Lower panel is for case II models ($v_c(30) = 0.8 \langle W \rangle$). These results are for $\gamma = 1.8$, satellite sample 1.

We now proceed to examine the dependence of our conclusions on γ . By examining the upper panels of Figures 4.12-4.14 (KS test results), we can see that the effects of changing γ are slight. We also conclude that all three models are consistent with the conclusion that we can reject, with 90% or greater confidence, models with $\Omega_0 \leq 0.03$. Quinn and Zurek (1988) concluded from their simulations of halo formation that $e \sim 0.7$. If $e = 0.7$, we can reject with at least 60% confidence models with $\Omega_0 < 0.1$. The effect of the choice of γ on the results presented in the lower panels (r_p vs. R correlation probabilities) is stronger. As γ increases, the upper bound on the eccentricity also increases. Generally, the difficulty with the radial orbit models is that they produce large positive correlations between r_p and R (*i.e.*, there are large values of R at large values of r_p). The large correlations are caused by the lack of fast-moving simulated satellites at large separations. Satellites at extremely large separations have had insufficient time to collapse back onto the galaxies and populate the high $|\Delta v|$ wings of the distribution at large r_p . Because higher values of γ give less weight to shells at greater galactocentric distance, large γ models are biased against the selection of satellites at large r . Therefore, high values of γ lead to smaller correlations between r_p and R . We conclude that models with $e \geq 0.9$ can be rejected with greater than 90% confidence for all allowed values of Ω_0 regardless of the choice of γ and that the preferred values of e are in general $\lesssim 0.7$.

Our final comment on Figure 4.13 is that one should not infer from it that models with $\Omega = 1$ and $e = 0.5$ can be rejected with 90% confidence. Recall that we have used maximum halo models. If one allows $v_c(30)$ to be smaller than $\langle W \rangle$, then one would obtain acceptable fits. For our galaxy the best fit halo circular velocity for isotropically distributed orbital velocities is 170 km s^{-1} , which is well below the LSR rotation velocity of 220 km s^{-1} (cf. Chapter 2). If this were true in general (*e.g.*, $v_c(30) = 0.8W$), then the lower bound on Ω_0 would be 0.3 (cf. Figure 4.15).

From the results of this test we see that much more stringent constraints on Ω_0 could be formulated if the relationship between $v_c(30)$ and W was better determined.

We have also compared the standard models to samples 0 and 2. There are substantial differences in the constraints on Ω_0 . We have argued that sample 1 represents the best compromise for interloper rejection. If we have been too liberal in the process of interloper rejection (*i.e.*, rejected objects that are physical companions), then our lower bounds will be too low. Since we are determining lower bounds, this is acceptable, although not desirable. If we have not removed all interlopers, then it is possible that our lower bound on Ω_0 will be too large. However, we believe that it is unlikely that we are still seriously affected by interlopers. We have already excluded the five satellites with the largest $|\Delta v|$'s. Recall that we estimated that there were eight interlopers in the entire sample. It is improbable that all eight have large $|\Delta v|$'s. In addition, the KS tests are not strongly susceptible to interlopers (see §4.2.1). Sample 2, which excludes the twelve satellites with the largest $|\Delta v|$'s, has definitely had too many satellites removed. Even so, using that sample $\Omega_0 = 0.01$ models can be rejected with greater than 90% confidence.

Galaxy Halos

What do the previous conclusions imply for the parameters of galaxy halos? First, it is clear that standard parameters (*e.g.*, M , M/L , and size) are not well-defined. Our modeled halos have no boundary and no well-defined total mass, other than the total bound mass. However, the total bound mass may be much larger than that realistically associated with a halo. As $\Omega_0 \rightarrow 1$, M_{BOUND} approaches the entire mass of the Universe. The only way to describe a halo fully is to provide the current mass profile. The mass profiles for the five different values of Ω_0 studied are shown in Figures 4.16 and 4.17. As expected, for lower values of Ω_0 the halo is more centrally concentrated. For convenience, although with loss of information, one may quote

Table 4.10: Halo Parameters for Secondary Infall Models

$$\Omega_0 = 1.0$$

	$v_c(30 \text{ kpc}) \text{ km s}^{-1}$				
	150	200	250	300	350
$M(200 \text{ kpc}) (10^{11} M_\odot)$	10.7	18.7	29.6	43.1	55.0
$M(500 \text{ kpc}) (10^{11} M_\odot)$	18.1	38.7	70.7	116.5	150.7
$r_t \text{ (Mpc)}$	0.93	1.26	1.59	1.91	2.21

$$\Omega_0 = 0.3$$

	$v_c(30 \text{ kpc}) \text{ km s}^{-1}$				
	150	200	250	300	350
$M(200 \text{ kpc}) (10^{11} M_\odot)$	7.2	13.3	21.8	31.6	42.0
$M(500 \text{ kpc}) (10^{11} M_\odot)$	10.6	22.6	40.5	64.4	83.4
$r_t \text{ (Mpc)}$	0.82	1.08	1.33	1.56	1.78

$$\Omega_0 = 0.1$$

	$v_c(30 \text{ kpc}) \text{ km s}^{-1}$				
	150	200	250	300	350
$M(200 \text{ kpc}) (10^{11} M_\odot)$	4.8	9.4	15.7	24.2	34.5
$M(500 \text{ kpc}) (10^{11} M_\odot)$	6.0	12.7	23.4	38.6	54.8
$r_t \text{ (Mpc)}$	0.69	0.90	1.11	1.33	1.53

Table 4.10 (continued)

$$\Omega_0 = 0.03$$

	$v_c(30 \text{ kpc}) \text{ km s}^{-1}$				
	150	200	250	300	350
$M(200 \text{ kpc}) (10^{11} M_\odot)$	3.2	6.4	10.7	16.0	22.7
$M(500 \text{ kpc}) (10^{11} M_\odot)$	3.6	7.4	13.0	20.4	29.8
$r_t \text{ (Mpc)}$	0.59	0.76	0.92	1.07	1.22

$$\Omega_0 = 0.01$$

	$v_c(30 \text{ kpc}) \text{ km s}^{-1}$				
	150	200	250	300	350
$M(200 \text{ kpc}) (10^{11} M_\odot)$	1.4	4.6	7.7	11.5	16.1
$M(500 \text{ kpc}) (10^{11} M_\odot)$	2.5	5.0	8.4	12.9	18.5
$r_t \text{ (Mpc)}$	0.53	0.67	0.80	0.93	1.04

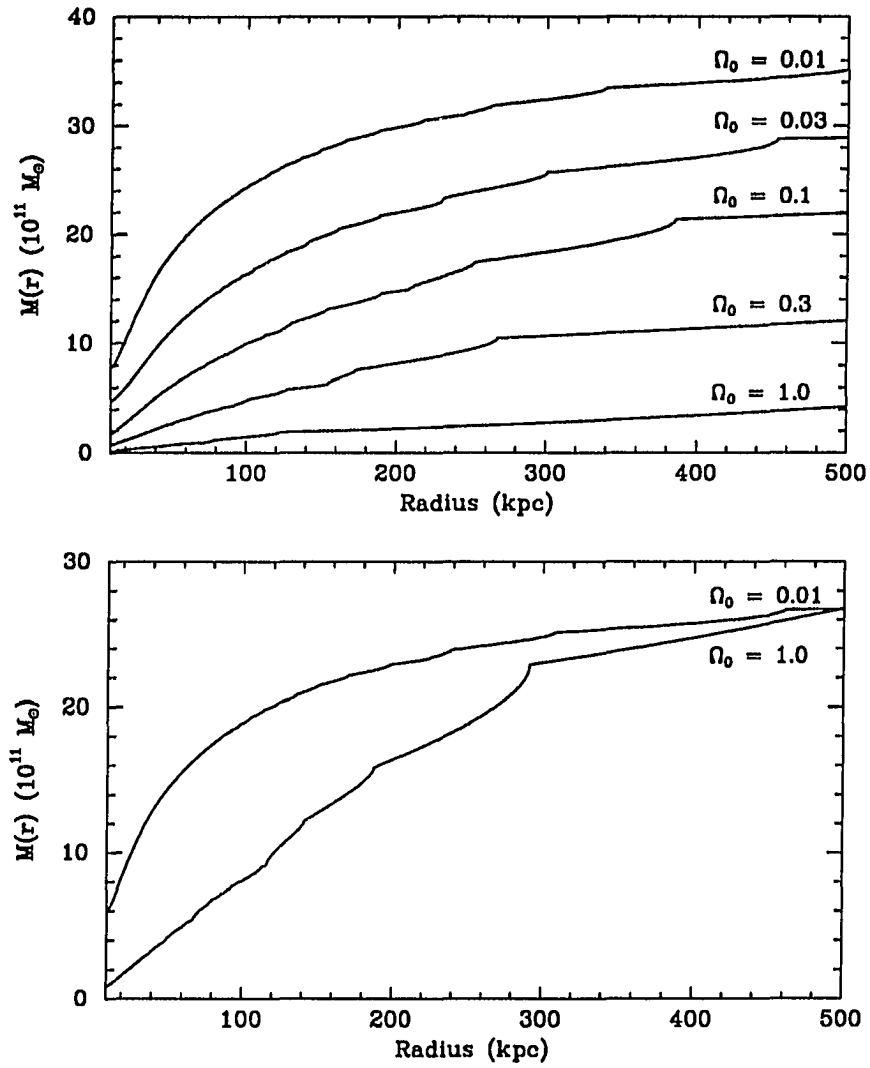


Figure 4.16: *Mass Profiles from Secondary Infall Models: Within 500 kpc. We have plotted mass profiles for models with $\Omega_0 = 0.01, 0.03, 0.1, 0.3$, and 1.0 within 500 kpc. These have been arbitrarily rescaled for illustrative purposes. In the bottom panel we have plotted the mass profiles for the $\Omega_0 = 0.01$ and 1.0 models scaled to have the same $M(500)$.*

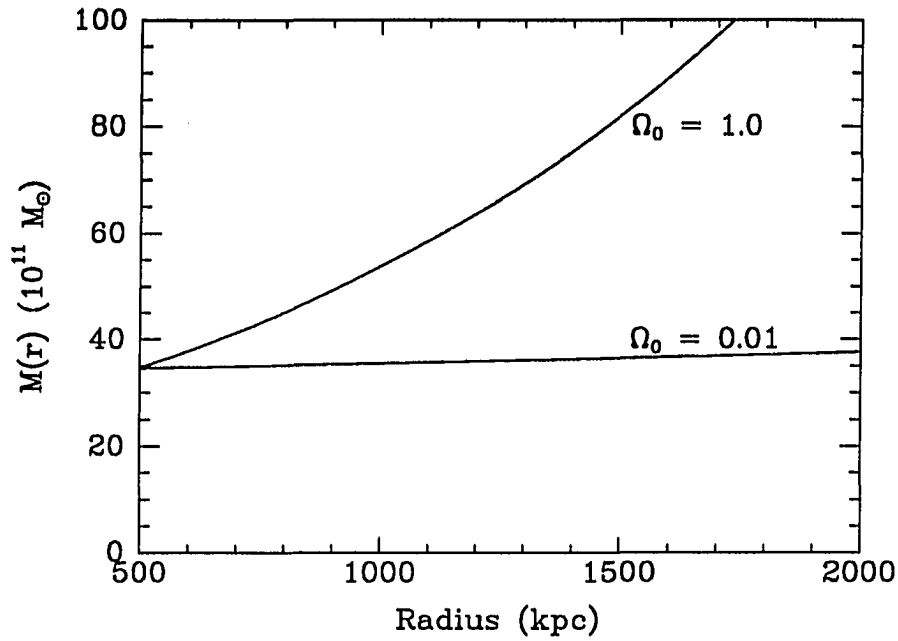


Figure 4.17: *Mass Profiles from Secondary Infall Models: Beyond 500 kpc. We have plotted mass profiles for models with $\Omega_0 = 0.01$ and 1.0 for $500 \text{ kpc} < r < 2 \text{ Mpc}$. These have been scaled to have the same $M(500 \text{ kpc})$.*

the enclosed mass within a sphere of radius r . For example, an $\Omega = 1$ model with $v_c(30) = 250 \text{ km s}^{-1}$ has an enclosed mass of $3.0 \times 10^{12} M_{\odot}$ at 200 kpc. An $\Omega_0 = 0.1$ model with $v_c(30) = 250 \text{ km s}^{-1}$ has an enclosed mass of $1.6 \times 10^{12} M_{\odot}$ at 200 kpc. We quote enclosed masses at 200 kpc, $M(200)$, because this is roughly the median projected separation of satellites and for $v_c(30) = 250 \text{ km s}^{-1}$ because this is $\langle W \rangle$ for the sample. Enclosed mass as predicted by the five different Ω_0 models is given

as a function of $v_c(30)$ for spheres of radius 200 and 500 kpc in Table 4.10. We can convert our constraints on Ω_0 to constraints on the halo mass profiles. For $\Omega_0 = 0.03$, which is a model that can be rejected with greater than 90% confidence, $M(200) = 1.1 \times 10^{12} M_\odot$ for $v_c(30) = 250 \text{ km s}^{-1}$. A smaller value of $v_c(30)$ would lead to stronger rejection confidence limits on the low Ω_0 models. Larger values of $v_c(30)$ are not allowed by our observations of W . We could also quote $M(500)$; however, because the median separation of our sample is 200 kpc, the models are not tightly constrained at 500 kpc. Preferred models (60% confidence limit) imply that $M(200)$ is $\gtrsim 1.6 \times 10^{12} M_\odot$ (i.e., $\Omega_0 \gtrsim 0.1$). These results are in agreement with the estimate of our galaxy's mass within 200 kpc, $M_G \gtrsim 1.3 \times 10^{12} M_\odot$. Also in the preferred range are models with $\Omega = 1$. These models have $M(200) = 3 \times 10^{12} M_\odot$. For small values of e , the $\Omega_0 = 1$ and $v_c(30) = 250 \text{ km s}^{-1}$ models can be rejected with greater than 90% confidence. By adopting $v_c(30) < 250 \text{ km s}^{-1}$, $\Omega = 1$ and $e = 0.5$ models are acceptable. However, then $M(200)$ is below $3 \times 10^{12} M_\odot$. Aside from this argument, there are other reasons¹⁷ to believe that the upper bound on Ω_0 is 1. Therefore, we conclude that our 90% confidence interval for $M(200)$ is given by $M(200) = (2 \pm 1) \times 10^{12} M_\odot$ if $0.5 \leq e < 0.9$. Of course, this conclusion depends slightly on the rejection of interlopers. As discussed previously, the lower bound appears firm. The upper bound depends on how well the preferred sample has constrained the upper envelope of the distribution in $r_p - |\Delta v|$ plane.

The acceptable model halos extend well beyond 200 kpc. Even for the rejected $\Omega_0 = 0.03$ model, only 80% of the mass within 500 kpc is also within 200 kpc. For the $\Omega = 1$ models 42% of the mass within 500 kpc is within 200 kpc. We see that $\Omega = 1$ models have $M \propto r$ out to at least 500 kpc, but are still consistent with the data.

¹⁷ $\Omega = 1$ models with $H_0 > 50 \text{ km s}^{-1} \text{ Mpc}^{-1}$ conflict with the observed ages of astronomical objects. Models with larger values of H_0 produce even worse discrepancies.

Comparison to EGH87

The only other mass analysis of a sample of satellite galaxies of spirals beyond the Local Group is that of EGH87¹⁸. Their sample criteria, with the exception of the isolation criteria, are only slightly different from ours. We would argue that because multiple companion systems are overrepresented (cf. §3.3.1) their sample is probably contaminated by background galaxies. However, it is still of interest to investigate whether our preferred models are consistent with their sample. It is especially interesting because they concluded from their analysis that the primaries had low M/L ratios (~ 20) and that a point-mass model was appropriate.

We examined the same set of (Ω_0, e) -case I models that we used with our sample of satellites and in the same manner as we did for our sample. We find that *all* combinations of Ω_0 and e for $0.01 < \Omega_0 < 1.0$ and $0.5 < e < 0.9$ are acceptable (*i.e.*, we cannot reject any of these models with 90% or greater confidence). We agree with their finding that their sample is consistent with low mass galaxy halos (*e.g.*, $\Omega_0 = 0.01$). However, we also find that it is consistent with very massive halos ($\Omega = 1$). Therefore, we conclude that their sample does not place interesting constraints on halo parameters. This illustrates the importance of large samples and of probing to large separations.

4.3.5 Additional Complications

In any interpretative analysis of a limited data sample there exists the possibility that the final conclusions are incorrect. The small sample size combined with statistical fluctuations can produce a final sample that is not representative of the parent distribution (cf. Chapter 2 for a discussion of this problem in the study of the mass of the Galaxy). We believe our relatively large sample and the agreement with the

¹⁸Their data are plotted in Figure 1.1.

independent Local Group analysis mitigates this concern. In addition, the models, which are always naive versions of reality, have excluded some possibly important physics. In this section, we present brief discussions of a few facets of the problem that were neglected.

The Effect of Dynamical Friction

Dynamical friction can alter the distribution of satellites in the $r_p - \Delta v$ plane. If giant galaxies have large halos, then dynamical friction may be an important process, especially for massive companions at small separation. Ostriker and Turner (1979) demonstrated that for certain original radial distributions of companions dynamical friction would produce a noticeable lack of massive, presumably bright, close companions. They concluded from an analysis of Turner's binary galaxy sample (Turner 1976a) that there was evidence for a depletion of bright companions near the primary. On the other hand, White and Valdes (1980), were able to fit to the same data a model with no dynamical evolution, although they needed to use a luminosity function that differed slightly from the field luminosity function. The issue is complex because there are many factors that can affect the observed distribution (cf. White and Valdes 1980). Nevertheless, following the analysis of Ostriker and Turner, we calculated the η_0 's for our sample. η_0 is a dimensionless parameter whose distribution is sensitive to the importance of dynamical friction and which is given by

$$\eta_0 = 0.35 \frac{10^{(-0.4m_s)}}{(r_p/D)^2}, \quad (4.59)$$

where m_s is the satellite's apparent magnitude and D is the system's distance. If dynamical friction is important, there will be a depletion of large values of η_0 relative to the expected distribution. Ostriker and Turner found a substantial depletion for values of $\eta_0 > 2$. All of our satellites have $\eta_0 < 2$. Therefore, our satellites appear

to be neither sufficiently luminous (massive) nor at small enough separation for dynamical friction to be important.

The lack of a deviation in the η_0 distribution of the T76 sample for $\eta_0 < 2$ is a reassuring sign that dynamical friction does not strongly affect that portion of the sample. However, as pointed out by Ostriker and Turner (1979) and Charlton and Salpeter (1991), for an initial number density profile of companions $\propto r^{-2}$, dynamical friction does not distort the distribution. As the orbit of one companion decays, another companion moves inward from a larger radius to take the first one's place. Therefore, we can only conclude that dynamical friction is unimportant if the initial profile is substantially different from r^{-2} and if no other effects compensate for the lack of large η_0 values. Unfortunately, estimates of the satellite number density radial profile are nearly $\propto r^{-2}$ (cf. Lorrimer *et al.* 1991). Additional effects, such as increased star formation for companions near the primary and peculiar initial distributions of companions, would severely complicate the interpretation (White and Valdes 1980).

An alternative way to conclude that dynamical friction is unlikely to be important is by considering the orbital decay times for satellites. Tremaine (1976) estimated the decay time of the LMC. He concluded that the orbit changes considerably in a few $\times 10^9$ years if the Galaxy has an isothermal halo that extends to at least the position of the LMC. Note that this assumption is consistent with our results (cf. Chapter 2). Since Tremaine's study the orbit of the LMC has been determined to be much larger than that which he had adopted (cf. Murai and Fujimoto (1980) and Mathewson *et al.* (1987)). Therefore, the decay time is underestimated by a factor of at least a few. In our sample, the majority of the satellites are less massive than the LMC (assuming equal M/L) and are also significantly farther away from the primary than the LMC is from the Galaxy (~ 50

kpc). Because the force from dynamical friction scales with the square of the mass of the companion and with the density of the background medium, which is roughly $\propto r^{-2}$, we are almost assured that the orbits of most companions in our survey are not dramatically altered by dynamical friction in 10^{10} years.

External Influences

We have assumed that the observed satellite velocities are due almost entirely to the combination of the Universal expansion and the gravitational influence of the primary galaxy. Despite our isolation criteria, it is clear that external gravitational fields have some effect on the satellites. In fact, we invoked external tides to generate angular momentum. Therefore, there is some concern that these external forces could also distort the resulting satellite velocity distribution. We have minimized this problem by adopting stringent isolation criteria. We crudely estimated the relative importance of a nearby perturber (cf. §3.2.1) and found the effect to be small. However, the definitive answer to this question will come from simulations of galaxy halo formation that include other nearby mass concentrations.

Most current models of the growth of structure in the Universe predict a substantial amount of direct interactions, such as merging, between discrete structures in the protogalactic environment. For example, in CDM models most high density peaks which are identified as galaxy halos, formed from the coalescence of at least two initial structures (Frenk *et al.* 1988). We have ignored this process in our study. However, of all galaxy types, we expect merging to be the least important in late-type spirals because their thin disks and small bulges imply a quiescent existence. These may be the only systems for which the model of isolated secondary infall is applicable. In any case, from the morphology of the primary galaxies in our sample — they are all late-type and none of our primaries have peculiar morphologies —

we argue that any merging that occurred did not significantly disturb the system and that the remnants of such a merger have apparently peacefully relaxed into the potential.

Mass and Number Density Profiles

We assumed an initially homogeneous universe and a particular power-law radial density distribution for the satellite galaxies. These are both certainly idealized descriptions. As discussed earlier, Hoffman and Shaham (1985) demonstrated that if there were initial perturbations of form $p(k) \propto k^n$, where $-1 \leq n \leq 0$, then one would obtain a halo of shallower density profile than in a uniform universe. The resulting power-law exponent of the density profile in the relaxed core in a model with initial perturbations is $-(9+3n)/(4+n)$. The exponent of the density profile will be between -2.25 and -2 . Therefore, even if there were initial perturbations of this form, we expect a quasi-isothermal core.

There exists the possibility of a cutoff in the satellite radial number density profile at some radius < 2 Mpc. This would reduce the number of relatively slow moving satellites at large r_p , and fast moving satellites at smaller r_p , if orbits are fairly radial in the simulated sample. Satellites at large separations have slower radial velocities than do the majority of the satellites at small separations. In effect, for large orbital eccentricities, the cutoff would increase the mean $|\Delta v|$ for a particular scaling velocity and thereby produce lower mass estimates. However, Lorrimer *et al.* (1991) demonstrated that the power-law density profile holds at least for radii < 0.75 Mpc, and from Figure 4.7 we know that over 70% of the simulated satellite sample lies at distances smaller than 0.75 Mpc. Therefore, the estimated mass for $r \leq 0.75$ Mpc, even if there is a break in the density profile, is unlikely to vary greatly.

4.4 Summary

In this chapter we attempted to determine the masses of late-type spiral galaxies using the data described in Chapter 3. Because previous results have depended strongly on the analysis technique and interpretation, we examined the data using two of the most popular existing techniques and our own technique. We believe that the standard and modified secondary infall models are much better suited for the study of our sample.

We began by using the simple point-mass projected-mass estimator developed first by Page (1952), and used widely by the community. First, we tested the accuracy of the projected mass estimator when selection effects, biases, and contamination are present in the sample. We concluded that if the model assumptions are not violated, the projected mass estimator is fairly accurate (a factor of two), except when there is contamination. Therefore, we developed a slightly different version of the estimator based on the median of the quantity $r_p|\Delta v|^2$ instead of the average. The median estimator is more robust (*i.e.*, less sensitive to outliers), and so is more accurate than the average estimator when there is contamination. We used both the average and the median estimators to estimate the mass of the typical primary in our sample. We concluded that $M \gtrsim 10^{12} M_\odot$. However, the point-mass models are invalidated because such a large point-mass (or nearly a point mass) is excluded by the observed disk rotation curves. So we then tried to fit models with different masses (assuming that the point-mass estimator results had been inaccurate) by comparing the observed and predicted distribution of data in the $r_p - |\Delta v|$ plane for various models. Again we inferred the presence of a mass of $10^{12} M_\odot$. Therefore, we proceeded to the extended mass models.

We continued our study with the most flexible and sophisticated models available in the literature (developed by White 1981). Again we examined the models under

various observational limitations and concluded that the models were accurate, even when interlopers were present¹⁹. We proceeded to examine models with $M(r) \propto r$ (i.e., isothermal sphere models) and with $M(r) \propto \sqrt{r}$. We concluded that neither model could be strongly rejected. The optimum models appeared to be between these two. The inferred masses within 200 kpc were again over $10^{12} M_{\odot}$. However, these models are not entirely satisfactory because they do not include the effects of the growth of the halo in a universe of finite lifetime. By examining the dynamics of halos that arise in universes with different but plausible values of Ω_0 , we believe that we might learn more both about the masses of halos and the value of Ω_0 . However, the primary reason for proceeding to the secondary infall models is that the orbits of satellites at large separations cannot be modeled accurately with random phase models. Satellites at separations > 100 kpc will at most have completed about 2 orbits. Therefore, we developed models that describe the growth of halos in a universe with chosen cosmology, and that do not depend on the assumption of random orbital phases.

The secondary infall models on which our simulations are based have been developed to study the formation and evolution of galactic halos. We described the standard models and our modification. The modification was employed to obtain a central mass profile that is more in accordance with observations. In any case, our modification was slight and conservative because it produces lower estimates for the value of Ω_0 . We also described other technical details of the code, including our *ad hoc* mechanism for the generation of angular momentum. Simulations of the modified secondary infall models were performed for $\Omega_0 = 0.01, 0.03, 0.1, 0.3$, and 1.0 , and for orbital eccentricities of $0.5, 0.7$, and 0.9 . The models were then compared to the data. We concluded that for the preferred sample $\Omega_0 > 0.03$. While this is not

¹⁹Accurate in the sense of the scaling of the Δv distribution. The correlations among various observables could still be strongly distorted by interlopers.

a strong constraint on Ω_0 , it implies larger halo masses than have been generally accepted previously ($> 10^{12} M_\odot$ within 200 kpc). This lower mass limit corresponds to $M/L_V > 80$ for the region within 200 kpc of the central galaxy. We have found consistent models for M/L_V as large as 240. We concluded that given our preferred sample, adopted constraints, $\Omega_0 \leq 1$, and $0.5 \leq e < 0.9$, our 90% confidence limit on the mass within 200 kpc is $(2 \pm 1) \times 10^{12} M_\odot$.

We argued that the models in the literature are not appropriate for a study of our data; however, a principal result from the modified secondary infall models — that halos have a mass of $\gtrsim 10^{12} M_\odot$ within the 200 kpc — was also roughly the result we obtained with the random phase models. The secondary infall models provide much more information: a mass profile, an estimate for Ω_0 , better detail on the structure of the orbits, and eventually with more sophisticated models even the ability to examine the effect of external influences. However, at a low level of precision, the answer (*i.e.*, $M(200 \text{ kpc}) \gtrsim 10^{12} M_\odot$) is apparent even from simple binding energy arguments and Figure 3.7. The mass required to bind gravitationally an object moving at $\sim 200 \text{ km s}^{-1}$ at 200 kpc is $1.8 \times 10^{12} M_\odot$. Our modified secondary infall models also imply that the halos have large extent. An $\Omega_0 = 0.03$ model has a current turnaround radius of $\sim 1 \text{ Mpc}$ and 20% of its mass beyond 200 kpc. Finally, we stress again that a lower bound on Ω_0 of 0.03 implies that halos have more than $10^{12} M_\odot$ within 200 kpc for $v_c = 250 \text{ kpc}$. If the v_c is significantly smaller than W because of the disk contribution to W , then the lower bound on Ω_0 will rise.

Chapter 5

Review and Preview. II

Interestingly, much of the previous work on companion galaxies is the result of a dissertation (*e.g.*, Page (1952), Turner (1976), Peterson (1979), van Moorsel (1982), and Schweizer (1987)). In that sense this work continues the tradition; in other ways this work is quite different from those. We believe that improvements in both sample selection and modeling allow us to claim that the results presented here provide a more robust estimate of the amount of dark matter in galaxy halos than presented before. Our fundamental conclusion is that isolated unbarred late-type spiral galaxies have halos that extend to at least 200 kpc and which contain at least $10^{12} M_{\odot}$ within 200 kpc. We believe that refinement is possible, both by expanding the satellite sample and by improving the models. However, we also believe that our result is robust. In this chapter, we review the results presented in this dissertation and discuss possible future avenues for research.

5.1 Summary of Results

5.1.1 Satellite Galaxies

We have identified a sample of satellite galaxies with $-20 < M_B < -13$ around isolated unbarred late-type spiral galaxies. Satellites were selected to have a projected separation from the primary of less than 500 kpc and a radial velocity that

differed by less than 500 km s^{-1} from that of the primary galaxy. Satellites were also defined to be at least a factor of eight fainter than the primary. While we primarily used the sample for a study of the dynamics of galaxy halos, it was also used to investigate the properties of satellite galaxies. The sample, 69 satellites of which about 10% are projected background galaxies, is rather small for conclusive studies of the properties of satellites. However, several interesting results were obtained:

- a) we confirmed the results of existing statistical studies (Holmberg 1969; Lorrimer *et al.* 1991) of between 1 and 2 satellite galaxies per primary within the survey parameters;
- b) we marginally detected (0.84 probability) a correlation between the mean number of satellites per primary and the primary's H I rotation width;
- c) we found that the radial density distribution of satellites is proportional to $r^{-2.0 \pm 0.2}$, which is in agreement with previous measurements of the galaxy-galaxy correlation function (Davis and Peebles 1983a) and the satellite-galaxy correlation function (Lorrimer *et al.* 1991);
- d) we found that there was very marginal, although supportive, evidence for the existence of the Holmberg effect within 50 kpc of the primary, but no evidence for it beyond 100 kpc;
- e) we identified a class of extended low surface brightness objects at large separations (mean separations were shown to be significantly larger than for the rest of the sample);
- f) we concluded that the satellite luminosity function is well-matched by the Schechter luminosity function;
- g) we found no evidence that early-type satellites are closer to the primary than late-type satellites (except for the low-surface brightness

class of satellite);

- h) we found an apparent lack of rapid satellites on retrograde orbits, although interestingly, the number of retrograde and prograde orbiting satellites is comparable; and
- i) we found that in a survey such as ours, interlopers will distort the Δv distribution and produce an apparent excess of satellites with positive Δv .

Results b and d certainly need more data before they are statistically reliable. Results c, e, f, g, and h could use refinement, but seem trustworthy. One should consider these results as the conclusions from a preliminary investigation of satellite galaxies. More specific and definitive conclusions await those who will endeavor to enlarge the sample.

5.1.2 Galactic Halos

We are especially satisfied that the mass estimates from independent analyses of three different samples (satellites of the Galaxy, Local Group timing arguments, and satellites of other late-type spiral galaxies) are in such good agreement. The results from the analyses are summarized below. It is inappropriate to quote a final result for the mass of late-type spiral galaxies because none except the point-mass model, which we have shown repeatedly to be inaccurate, is characterized by a single mass. For example, the isothermal sphere models developed by Little and Tremaine (1987) for application to the remote satellites of the Galaxy are characterized by a circular velocity and the secondary infall models discussed in Chapter 4 are characterized by a scaling circular velocity and Ω_0 . Because neither the isothermal sphere or secondary infall models provide a radius that can be identified as the edge of the halo, it is impossible to calculate a total mass. We have only hesitantly quoted total masses or M/L 's, and then only as lower limits.

The satellites of the Milky Way galaxy are currently the best tool for measuring the mass of the Galaxy to a Galactocentric distance of $\gtrsim 100$ kpc. We presented our measurements of radial velocities of satellites without reliable published velocities. We applied two different analysis techniques to the complete satellite sample to estimate the mass of the Galaxy. First, we used the point-mass and isothermal sphere models developed by Little and Tremaine (1987). We concluded from the point-mass models that the mass of the Galaxy is $\sim 10^{12} M_{\odot}$. However, such a large mass invalidates the point-mass assumption and the extreme effect of one object (Leo I) on the results was unsettling. The isothermal sphere model, which is more appropriate to extended mass distributions, was much more stable with respect to the presence or absence of Leo I in the sample. From it we concluded that the halo has a characteristic circular velocity of $\sim 170 \text{ km s}^{-1}$ if the satellites have isotropically distributed velocities. If the halo is isothermal and extends to 100 kpc, which is roughly the median value of the Galactocentric distances of the satellites, then the mass of the Galaxy is $6 \times 10^{11} M_{\odot}$. However, if it extends to the positions of Leo I and Leo II (~ 200 kpc) then the mass is over $10^{12} M_{\odot}$. Since the extent of the halo is unknown and because the assumption of random phases, which was used in the analysis, is not valid for this sample, we proceeded to use the timing arguments developed first by Kahn and Woltjer (1959). We applied the timing argument to Leo I and concluded from the results that the lower bound on the mass of the Galaxy had to be slightly larger than $10^{12} M_{\odot}$. We proceeded to compare this estimate to those derived using other galaxies in the Local Group.

Timing arguments are a classic technique for estimating the mass of the M 31-Milky Way pair. The appeal of such models is that they are so simple that the conclusions are difficult to ignore, especially since the result is a lower limit on the mass. The models have been extended to include the effects of torques from nearby systems (Einasto and Lynden-Bell 1982; Raychadhury and Lynden-Bell 1989), the

evolution of the Local Group as accretion onto seed masses (Peebles *et al.* 1989), and other members of the Local Group (Mishra 1985, and this work). All studies of the M31-Milky Way system conclude that the mass of the Local Group is between 3 and $7 \times 10^{12} M_{\odot}$, which implies a mass for the Milky Way of between 1 and $3 \times 10^{12} M_{\odot}$. The larger values are typically for models in which M31 and the Milky Way have greater orbital angular momentum, although age is important as well. We discussed timing arguments using other Local Group galaxies and obtained very similar results. We conclude that the large estimated mass cannot be the result of a single unbound interloping galaxy (*e.g.*, if M31 were unbound to the LG). If the MW has a mass of $> 10^{12} M_{\odot}$, a halo circular velocity of 170 km s^{-1} , and an isothermal halo, then the halo extends to at least 160 kpc. As we saw from the secondary infall models (reviewed below), we might expect that the mass actually increases at a rate slightly slower than r and so the extent of the halo corresponding to $10^{12} M_{\odot}$ is greater (the precise size depends on the density profile). Any inclusion of angular momentum in the system and any initial overlapping of the two galaxies only increases the estimates of the mass and extent of the halo.

To expand on the results from the study of Local Group galaxies, we collected a sample of satellites of other late-type spirals. The relatively large mass difference between satellites and primaries made the interpretation more straightforward than in binary galaxy studies. In addition, the large mean separation between satellites and primaries and the strict isolation criteria employed made this a unique sample with which to measure the mass of galactic halos of unbarred late-type spiral galaxies. However, because most satellites are at such large separations they have not had enough time to complete several orbits around the primary. Therefore, the assumption of random orbital phases cannot be adopted. We developed models based on the concept of secondary infall, which is a direct consequence of the big bang cosmological model and of the gravitational instability model for the growth

of structure in the Universe. We modified the standard secondary infall models slightly to produce flat rotation curves in the relaxed core of the halo. We began our simulations with a homogeneous universe and a seed mass at $z \sim 1000$, which were evolved under the influence of gravity and an *ad hoc* force added to generate angular momentum in the halos. The external force did no work on the particles. The models were “observed” in a manner that maintained all the properties of the real observations. The simulated observations were then carefully compared to the observed data. The $\Omega_0 - e - \gamma$ space was probed for acceptable models, where e is the eccentricity of the orbits of the halo particles, and γ is the negative power-law exponent of the radial number density profile of satellite galaxies. The results are not strongly sensitive to the value of γ . The observed H I rotation widths were used as an external constraint on the models. Acceptable models were found only for $\Omega_0 > 0.03$. The placement of the bound has a slight dependence on e . Models with $\Omega_0 = 0.01$ or 0.03 , which are the closest of our models to point-mass models, are rejected with greater than 90% confidence. Lower limits on the mass are provided by the $\Omega_0 = 0.03$ models. These models have $M(200 \text{ kpc}) = 1.1 \times 10^{12} M_\odot$ and $M/L \sim 80$. Galactic halos must have masses and mass-to-light ratios larger than these values. We have convincingly demonstrated that galaxies have mass distributions that extend well beyond the outermost measurement of observed H I rotation curves. Furthermore, this result is in perfect agreement with the results obtained from studying the Local Group and as such further confirms the growing body of evidence in support of very large dark matter halos.

In conclusion, we believe it is now evident that galaxies do have halos that extend to $\gtrsim 200 \text{ kpc}$ with enclosed masses at that radius greater than $10^{12} M_\odot$. Therefore, the region within 200 kpc has $M/L \gtrsim 80$. The bounds on Ω_0 will not surprise those who have worked in large scale structure where $\Omega_0 \sim 0.1$ is considered a lower limit, but it does constitute firm observational evidence for such large masses surrounding

isolated galaxies. We believe this is the most unambiguous and definitive study to date that constrains galaxy masses to radii of 200 kpc. We also stress that preferred models (60% confidence limits) have $\Omega_0 > 0.1$ and so imply even larger masses. Models with $\Omega = 1$ are also acceptable, although for some eccentricities require that $v_c(30)$ be smaller than $\langle W \rangle$. Based on the results for our galaxy and observations of the rotation curves of spirals (cf. Salucci and Frenk 1989), it is not unusual to have $v_c(30)$ be smaller than W . If $v_c(30) = 0.8 \langle W \rangle$, then our 90% confidence lower bound on Ω_0 is 0.3 and so $M(200) > 2.2 \times 10^{12}$ and $M/L > 160$. Recall the four types of models discussed in Chapter 1:

- 1) no dark halo, the entire mass of the galaxy is located within the optical component (Keplerian model: $M/L \sim \text{few}$);
- 2) the halo extent is a few tens of kpc, the entire mass is located within the region probed by H I observations (small halo model: $M/L \sim \text{few} \times 10$);
- 3) the halo extent is a few hundreds of kpc (medium halo model: $M/L \gtrsim 100$);
- 4) the halo is approximately an isothermal sphere whose extent is determined by its nearest neighbors (extent of order 1 Mpc; large halo model: $M/L \gtrsim 1000$).

We have concluded that models 1 and 2 can be confidently rejected and that model 3 constitutes a lower bound on the mass and extent of galactic halos. We have made progress in our attempt to determine the nature of galaxy halos.

The ultimate goal of any study of the distribution of dark matter is to constrain models of dark matter or non-Newtonian gravity. As discussed in Chapter 1, the mass distribution inferred from the dynamics could be used to reject candidates for dark matter or new theories of gravity. For example, the phase space density

in dwarf spheroidal galaxies can be used to constrain the mass of neutrinos that may constitute the dark matter (Tremaine and Gunn 1979). Although we have demonstrated the existence of large dark matter halos, the density and extent are not beyond what has been considered before. Therefore, besides providing observational evidence for massive quantities of dark matter in galactic halos, our results do not further constrain earlier arguments that assumed such halos existed. Our lower bound on Ω_0 does not imply the existence of exotic particles, even for homogeneous standard Big Bang nucleosynthesis models. However, our results certainly do not exclude $\Omega_0 = 1$ either. We achieved our more modest purpose of determining the mass distribution of dark matter halos around late-type unbarred spirals, but were unable to provide answers to greater questions.

5.2 The Future for Studies of Satellite Galaxies

We mentioned in §4.2.1, when considering the random phase point mass models, that there appeared to be no compelling reason to obtain samples of companion galaxies with more than 100 objects. This is actually incorrect for the following reasons. In that section, we considered models for which the eccentricity distribution was known. In reality, the eccentricity distribution is unknown, and larger samples allow one to constrain better the mean eccentricity and the mass scale. It is also true that for larger samples it will be easier to estimate the background contamination precisely and identify the locus of points of physical companions in the $r_p - |\Delta v|$ plane. If the entire sample were from the multiobject survey, then the contamination would only be 5%, instead of 10-15%. Therefore, it would be beneficial to increase the sample. Unfortunately, there are few isolated spirals in the appropriate redshift range. We believe that it would be impossible to more than double the size of current sample if the selection criteria remain the same; although, doubling the

sample would help. In Figure 5.1 we have plotted the constraints on Ω_0 and e that would be derived if the sample was doubled — that is if the exact same $r_p - |\Delta v|$ distribution was reproduced in the new sample (*i.e.*, we used sample 1 twice).

One way to increase the available number of primaries is to alter the selection criteria. For example, with larger telescopes one could extend the redshift criterion. Larger telescopes would also allow one to measure redshifts for intrinsically fainter satellites of nearby galaxies. On a more short term basis, it is also possible to relax the primary galaxy selection criteria. By obtaining an equivalent sample of earlier type galaxies, or barred galaxies, one could compare their halo properties to those of the late-type unbarred sample presented here. If the halo properties are similar, that is if one can conclude that all types of giant galaxies lie in equivalent halos, then the samples could be merged. In either case, such a sample would be useful and interesting. However, obtaining a large sample of isolated early type galaxies may be impossible since early-type galaxies are preferentially found in crowded environments.

On a more theoretical track, simulations that are coupled to the growth of structure on larger scales would help determine the effect of other galaxies on the dynamics of satellites. These simulations could provide an external constraint on the orbital eccentricities and would also allow one to estimate the effect of external perturbations on the distribution of observed satellite velocities. Further in the future, we envision galaxy formation simulations that produce not only the broad spectrum of observed galaxies, but their satellites as well. This could be helpful for the dynamical analysis, but would also shed light on some of the properties of satellite galaxies described in Chapter 3.

If the interest is shifted from the dynamics to the properties of satellites, then the isolation criteria could be relaxed. The properties of satellite galaxies and the

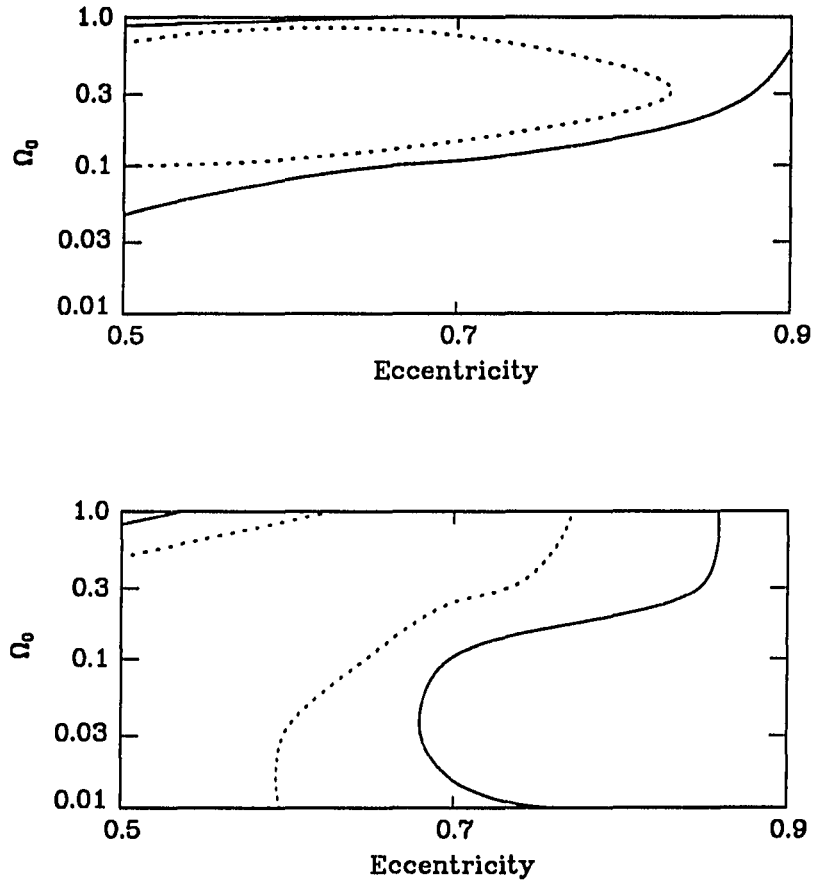


Figure 5.1: *Future Constraints on Ω_0 and e : The constraints placed on Ω_0 and e are shown when the sample is twice Sample 1. It is meant to illustrate the possible results when the size of the sample is doubled. In the upper panel, contours represent 60 and 90% confidence limits based on the distribution of ranks on acceptable models in the (Ω_0, e) subspace. In the lower panel, contours represent 60 and 90% confidence limits based on the correlation between r_p and R on acceptable models. These results are for case I and $\gamma = 1.8$.*

relationship with the primary, as discussed in §3.3, could be studied in greater detail. It should also be possible to choose a suitable subsample and study stellar population and chemical abundances in these systems.

Furthermore, the observational techniques for finding satellites might be expanded. For example, emission line systems, which comprise over half of the current subsample for which we have spectra, could be identified as satellites with the use of narrow-band imaging. A narrow-band filter, centered at the wavelength appropriate to a bright emission line at the redshift of the primary, could be used to identify satellites in the same fashion as H II regions are found. Although one would need to be wary of selection effects, this technique is potentially a powerful one for obtaining deep surveys of satellite galaxies (without precise redshifts) to determine such properties as the radial and angular distribution, and the luminosity function.

There are also possible improvements on the more "local" aspects of this work. Proper motions are being measured for some of the dSph satellites of our galaxy and for some remote globular clusters. In addition, surveys of distant halo stars are also being undertaken. Proper motion studies in particular would be especially informative. Space velocities of remote satellites would place much tighter constraints on the mass of the Galaxy than do the currently available radial velocities. Also more precise distances to the remote Local Group galaxies would be valuable, since the distance determinations are the largest source of uncertainty in the timing arguments. Finally, it is possible that more Galactic satellites will be found as surveys progress to fainter limits.

5.3 Conclusion

Evidence for dark matter in a variety of astronomical scales, from dwarf spheroidal galaxies (Aaronson 1983) to galaxy clusters (Zwicky 1933), has grown beyond the

original studies into a large volume of overwhelming evidence. So much so, that the paucity of knowledge regarding its constituents is particularly frustrating. Appropriately, there is a growing emphasis on direct detection and we hope that some positive detections are forthcoming. We have confirmed the existence of the dark matter problem in the halos of normal galaxies, shown that the discrepancy between the inferred and observed mass is larger than previously observed, and concluded that the observational constraints do not yet imply the existence of exotic particles. It is now clear that the dark halos of late-type unbarred galaxies are by far the principal mass component of these galaxies and that rotation curves provide only a glimpse into the true nature of this component.

REFERENCES

- Aaronson, M. 1983, *Astrophys. J. Lett.*, **266**, L11.
- Aaronson, M., and Mould, J. 1985, *Astrophys. J.*, **290**, 191.
- Aaronson, M., and Olszewski, E. W. 1988, in *IAU Symposium 190, Large Scale Structures in the Universe*, ed. J. Audouze, M.-C. Pelletan, and A. Szalay (Dordrecht: Kluwer Academic Publishers), p. 409.
- Aaronson, M., Schommer, R. A., and Olszewski, E. W. 1984, *Astrophys. J.*, **276**, 221.
- Aarseth, S. J., and Fall, S. M. 1980, *Astrophys. J.*, **236**, 43.
- Aguilar, L., Hut, P., and Ostriker, J. P. 1988, *Astrophys. J.*, **335**, 720.
- Allen, A. J., and Richstone, D. O. 1988, *Astrophys. J.*, **325**, 583.
- Applegate, J. H., Hogan, C. J., and Scherrer, R. J. 1988, *Astrophys. J.*, **329**, 572.
- Armandroff, T. E., and Da Costa, G. S. 1986, *Astron. J.*, **92**, 777.
- Arp, H., and Sulentic, J. W. 1985, *Astrophys. J.*, **291**, 88.
- Azzopardi, M., Lequeux, J., and Westerlund, B. E. 1985, *Astron. Astrophys.*, **144**, 388.
- Azzopardi, M., Lequeux, J., and Westerlund, B. E. 1986, *Astron. Astrophys.*, **161**, 232.
- Bahcall, J. N., Schmidt, M., and Soneira, R. M. 1982, *Astrophys. J. Lett.*, **258**, L23.
- Bahcall, J. N., and Tremaine, S. 1981, *Astrophys. J.*, **244**, 805.
- Barnes, J., and Efstathiou, G. 1987, *Astrophys. J.*, **319**, 575.
- Bertschinger, E. 1985, *Astrophys. J. Suppl.*, **58**, 39.

- Binney, J. 1976, *Mon. Not. R. Astron. Soc.*, **177**, 19.
- Binney, J., and Tremaine, S. 1987, *Galactic Dynamics*, (Princeton : Princeton Univ. Press).
- Blumethal, G. R., Faber, S. M., Flores, R., Primack, J. R. 1986, *Astrophys. J.*, **301**, 27.
- Bontekoe, Tj. R., and van Albada, T. S. 1987, *Mon. Not. R. Astron. Soc.*, **224**, 349.
- Bosma, A. 1978, Ph.D. Dissertation, Univ. of Groningen.
- Bosma, A., Goss, W. M., and Allen, R. J. 1981, *Astron. Astrophys.*, **93**, 106.
- Bothun, G. D., and Sullivan, W. T. III 1977, *Pub. Astron. Soc. Pac.*, **89**, 5.
- Bothun, G. D., Schombert, J. M., Impey, C. D., Schneider, S. E. 1990, *Astrophys. J.*, **360**, 427.
- Brück, H. A., Coyne, G. V., and Longair, M. S. (eds.) 1982, *Atrophyisical Cosmology, Proceedings of the Study Week on Cosomology and Fundamental Physics (Vatical City: Pontifical Academy of Sciences)*.
- Buonanno, R., Corsi, C. E., Fusi Pecci, F., Hardy, E., and Zinn, R. 1985, *Astron. Astrophys.*, **152**, 65.
- Carney, B. W., Latham, D. W., and Laird, J. B. 1988, *Astron. J.*, **96**, 560.
- Chandrasekhar, S. 1943, *Astrophys. J.*, **97**, 255.
- Charlton, J. C., and Salpeter, E. E. 1991, *Astrophys. J.*, **375**, 517.
- Christian, C. A., and Heasley, J. N. 1986, *Astrophys. J.*, **303**, 216.
- Clemens, D. P. 1985, *Astrophys. J.*, **295**, 422.
- Cohen, J. G., and Freeman, K. C. 1991, *Astron. J.*, **101**, 483.
- Cook, K. 1987, Ph.D. Dissertation, Univ. of Arizona.

- Cook, K., Schechter, P., and Aaronson, M. 1983, *B.A.A.S.*, **15**, 907.
- Da Costa, G. S. 1984, *Astrophys. J.*, **285**, 483.
- Da Costa, G. S. 1985, *Astrophys. J.*, **291**, 230.
- Da Costa, G. S., Hatzidimitriou, H., Irwin, M. J., and McMahon, R. G. 1991, *Mon. Not. R. Astron. Soc.*, **249**, 473.
- Da Costa, G. S., Ortolani, S., and Mould, J. 1982, *Astrophys. J.*, **257**, 633.
- Da Costa, G. S., and Seitzer, P. 1989, *Astron. J.*, **97**, 405.
- Davis, M., and Peebles, P. J. E. 1983a, *Astrophys. J.*, **267**, 465.
- Davis, M., and Peebles, P. J. E. 1983b, *Ann. Rev. Astron. Astrophys.*, **2**, 109.
- Dean, J. F., and Davies, R. D. 1975, *Mon. Not. R. Astron. Soc.*, **170**, 503.
- Dekel, A., Kowitt, M., and Shaham, J. 1981, *Astrophys. J.*, **250**, 561.
- Delhaye, J. 1965, in *Stars and Stellar Systems Vol. 4; Galactic Structure*, ed. A. Blaauw and M. Schmidt (Chicago: University of Chicago Press), p. 61.
- Demers, S., and Harris, W. E. 1983, *Astron. J.*, **88**, 329.
- de Vaucouleurs, G., de Vaucouleurs, A., and Corwin, H. G., Jr. 1976, *Second Reference Catalogue of Bright Galaxies* (Austin: University of Texas Press) (RC2).
- Doroshkevich, A. 1970, *Astrofizika*, **6**, 581.
- Dressler, A., Shecter, P. L., Rose, J. A. 1986, *Astron. J.*, **91**, 1058.
- Efstathiou, G., Ellis, R. S., and Peterson, B. A. 1988, *Mon. Not. R. Astron. Soc.*, **232**, 431.
- Efstathiou, G., and Jones, B. J. T. 1979, *Mon. Not. R. Astron. Soc.*, **186**, 133.
- Einasto, J., and Lynden-Bell, D. 1982, *Mon. Not. R. Astron. Soc.*, **199**, 67.
- Einasto, J., Saar, E., Kaasik, A., and Cherin, A. D. 1974, *Nature*, **252**, 111.

- Erickson, K., Gottesman, S. T., and Hunter, J. H., Jr. 1987, *Nature*, **325**, 779 (EGH87).
- Faber, S. M., and Gallagher, J. S. 1979, *Ann. Rev. Astron. Astrophys.*, **2**, 135.
- Fillmore, J.A., and Goldreich, P. 1984, *Astrophys. J.*, **281**, 1.
- Foltz, C. B., Chaffee, F. H., Jr., Ouellette, D. B., and Blanco, D. R. 1985, MMT Technical Memo 85-4.
- Fox, M. F., and Pritchett, C. J. 1987, *Astron. J.*, **93**, 1381.
- Freeman, K. 1970, *Astrophys. J.*, **160**, 811.
- Frenk, C. S., and White, S. D. M. 1982, *Mon. Not. R. Astron. Soc.*, **198**, 173.
- Frenk, C. S., White, S. D. M., Davis, M., and Efstathiou, G. 1988, *Astrophys. J.*, **327**, 507.
- Geller, M. J., and Huchra, J. P. 1983, *Astrophys. J. Suppl.*, **52**, 61.
- Godwin, J. G., Metcalf, N., Peach, J. V. 1983, *Mon. Not. R. Astron. Soc.*, **202**, 113.
- Goldstein, H. 1980, *Classical Mechanics*, (Reading: Addison-Wesley).
- Gott, J. R. III 1973, *Astrophys. J.*, **186**, 481.
- Gott, J. R. III 1975, *Astrophys. J.*, **201**, 296.
- Gott, J. R. III, and Turner, E. L. 1977, *Astrophys. J.*, **213**, 309.
- Gratton, R. G., and Ortolani, S. 1984, *Astron. Astrophys. Suppl.*, **57**, 177.
- Gunn, J. E. 1977, *Astrophys. J.*, **218**, 592.
- Gunn, J. E. 1980, *Phil. Tans. Royal Soc. London A*, **296**, 313.
- Gunn, J. E., and Gott, J. R. III 1972, *Astrophys. J.*, **176**, 1.
- Guth, A. H. 1981, *Phys. Rev.*, **D23**, 347.

- Harris, W. E. 1987, in *IAU Symposium No. 126 Globular Cluster Systems in Galaxies*, eds. J. E. Grindlay and A. G. D. Philip, (Dordrecht: Reidel), p. 237.
- Harris, W. E., and van den Bergh, S. 1984, *Astron. J.*, **89**, 1816.
- Hartwick, F. D. A., and Sargent, W. L. W. 1978, *Astrophys. J.*, **221**, 512.
- Heisler, J., Tremaine, S., and Bahcall, J. N. 1985, *Astrophys. J.*, **298**, 8.
- Hernandez, G. 1986, *Fabry-Perot Interferometers*, (Cambridge: Cambridge University Press)
- Hernquist, L., and Quinn, P. J. 1989, in *The Epoch of Galaxy Formation*, eds. C. S. Frenk *et al.* (Netherlands: Kluwer), p. 427.
- Hill, J. M. 1984, Ph.D. Dissertation, Univ. of Arizona.
- Hodge, P. W. 1971, *Ann. Rev. Astron. Astrophys.*, **2**, 35.
- Hoffman, Y., and Shaham, J. 1985, *Astrophys. J.*, **297**, 16.
- Hohl, F. 1971, *Astrophys. J.*, **168**, 343.
- Holmberg, E. 1937, *Lunds Ann.*, **6**.
- Holmberg, E. 1969, *Ark. Astr.*, **5**, 305.
- Hoyle, F. 1949, *Problems of Cosmological Aerodynamics* (International Union of Theoretical and Applied Mechanics and the International Astronomical Union), p. 195.
- Huchra, J. P. 1987, *The CfA Redshift Catalogue*.
- Huchra, J. P., and Geller, M. J. 1982, *Astrophys. J.*, **257**, 423.
- Huchtmeier, W. K., and Richter, O.-G. 1989, *HI Observations of Galaxies*, (New York: Springer-Verlag).
- Ingerson, T. E. 1987, in *Instrumentation for Ground-Based Optical Astronomy*, ed. L.B. Robinson (New York: Springer-Verlag), p. 222.

- Ingerson, T. E. 1988 in *A.S.P. Conference Series Vol. 9, Fiber Optics in Astronomy*, ed. S.C. Barden (Provo: Astronomical Society of the Pacific), p. 99.
- Ingerson, T. 1992, in preparation.
- Innanen, K. A., Harris, W. E., and Webbink, R. F. 1983, *Astron. J.*, **88**, 338.
- Impey, C., Bothun, G., Malin, D. 1988, *Astrophys. J.*, **330**, 634.
- Irwin, M. J., Bunclark, P. S., Bridgeland, M. T., and McMahon, R. G. 1990, *Mon. Not. R. Astron. Soc.*, **244**, 16P.
- Kahn, F. D., and Woltjer, L. 1959, *Astrophys. J.*, **130**, 705.
- Karachentsev, I. D. 1972, *Catalogue of Isolated Pairs of Galaxies in the Northern Hemisphere*, Soobsch. Special Astrophysics Obs., **7**, 3 (K72).
- Keel, W. C. 1991, *Astrophys. J. Lett.*, **375**, L5.
- Kendall, M. G. and Stuart, A. 1973, *Advanced Theory of Statistics*, vol. 2, (London: Griffin).
- Knapp, G. R., Tremaine, S. D., and Gunn, J. E. 1978, *Astron. J.*, **83**, 1585.
- Kolb, E. W., Turner, M. S., Lindley, D., Olive, K., and Seckel, D. (ed) 1986, *Inner Space/Outer Space: The Interface Between Cosmology and Particle Physics* (Chicago: University of Chicago Press).
- Kormendy, J., and Knapp, G. R. (ed) 1987, *IAU Symposium 117, Dark Matter in the Universe* (Dordrecht: Reidel).
- Kormendy, J. and Yu, G. 1988, *Origin, Structure, and Evolution of Galaxies*, (Singapore: World Scientific), p. 252.
- Lake, G., and Feinswog, L. 1989, *Astron. J.*, **98**, 166.
- Lake, G., and Tremaine, S. 1980, *Astrophys. J. Lett.*, **238**, L13.
- Lin, D. N. C., and Lynden-Bell, D. 1982, *Mon. Not. R. Astron. Soc.*, **198**, 707.

- Little, B., and Tremaine, S. 1987, *Astrophys. J.*, **320**, 493 (LT).
- Lorrimer, S. J., Frenk, C. S., Smith, R. M., White, S. D. M., and Zaritsky, D. 1991, in preparation.
- Lynden-Bell, D. 1967, *Mon. Not. R. Astron. Soc.*, **136**, 101.
- Lynden-Bell, D., Cannon, R. D., and Godwin, P. J. 1983, *Mon. Not. R. Astron. Soc.*, **204**, 87p (LCG).
- Lynden-Bell, D., and Lin, D. N. C. 1977, *Mon. Not. R. Astron. Soc.*, **181**, 37.
- Mateo, M., Nemec, J., Irwin, M., and McMahon, R. 1991, *Astron. J.*, **101**, 892.
- Mathewson, D. S., Wayte, S. R., Ford, V. L., Ruan, K. 1987, *Proc. Astr. Soc. Australia*, **7**, 19.
- Mathieu, R. D., Latham, D. W., Griffin, R. F., and Gunn, J.E. 1986, *Astron. J.*, **92**, 1100.
- McGlynn, T. A. 1984, *Astrophys. J.*, **281**, 13.
- Milgrom, M. 1983, *Astrophys. J.*, **270**, 365.
- Mishra, R. 1985, *Mon. Not. R. Astron. Soc.*, **212**, 163.
- Mould, J., and Aaronson, M. 1983, *Astrophys. J.*, **273**, 530.
- Murai, T., and Fujimoto, M. 1980, *Publ. Astr. Soc. Japan.*, **32**, 581.
- Olive, K. A., Schramm, D. N., and Steigman, G. 1990, *Phys. Lett. B*, **236**, 454.
- Olszewski, E. W., and Aaronson, M. 1985, *Astron. J.*, **90**, 2221.
- Olszewski, E. W., Peterson, R. C., and Aaronson, M. 1986, *Astrophys. J. Lett.*, **302**, L45 (OPA).
- Ostriker, J. P., and Peebles, P. J. E. 1973, *Astrophys. J.*, **186**, 467.
- Ostriker, J. P., and Turner, E. L. 1979, *Astrophys. J.*, **234**, 785.
- Page, T. 1952, *Astrophys. J.*, **116**, 63.

- Peebles, P. J. E., Melott, A. L., Holmes, M. R., and Jiang, L. R. 1989, *Astrophys. J.*, **345**, 108.
- Peterson, R. C. 1985, *Astrophys. J.*, **297**, 309.
- Peterson, R. C., and Foltz, C. B. 1986, *Astrophys. J.*, **307**, 143.
- Peterson, R. C., and Latham, D. W. 1989, *Astrophys. J.*, **336**, 178 (PL).
- Peterson, R. C., Olszewski, E. W., and Aaronson, M. 1986, *Astrophys. J.*, **307**, 139.
- Peterson, S. D. 1979a, *Astrophys. J. Suppl.*, **40**, 527 (P79).
- Peterson, S. D. 1979b, *Astrophys. J.*, **232**, 20 (P79).
- Pike, C. D. 1976, *Mon. Not. R. Astron. Soc.*, **177**, 257.
- Press, W. H., and Davis, M. 1982, *Astrophys. J.*, **259**, 449.
- Press, W. H., and Teukolsky, S. A. 1988, *Computers in Phys.*, **July/Aug**, 74.
- Pryor, C. P., Latham, D. W., and Hazen, M. L. 1988, *Astron. J.*, **96**, 123.
- Quinn, P. J., and Goodman, J. 1986, *Astrophys. J.*, **309**, 472.
- Quinn, P. J., and Zurek, W. H. 1988, *Astrophys. J.*, **331**, 1.
- Racine, R., and Harris, W. E. 1975, *Astrophys. J.*, **196**, 413.
- Raychadhury, S. 1990, Ph.D. Dissertation, Univ. of Cambridge.
- Raychadhury, S., and Lynden-Bell, D. 1989, *Mon. Not. R. Astron. Soc.*, **240**, 195.
- Reid, N., and Mould, J. 1991, *Astron. J.*, **101**, 1299.
- Rogstad, D. H., and Shostak, G. S. 1972, *Astrophys. J.*, **176**, 315.
- Rogstad, D. H., Wright, M. C. H., and Lockhart, I. A. 1976, *Astrophys. J.*, **204**, 703.
- Rubin, V. C., and Ford, W. K., Jr. 1970, *Astrophys. J.*, **159**, 379.
- Rubin, V. C., Ford, W. K., Jr., Thonnard, N. 1978, *Astrophys. J. Lett.*, **225**, L107.

- Salucci, P., and Frenk, C. S. 1989, *Mon. Not. R. Astron. Soc.*, **237**, 247.
- Sancisi, R., and Allen, R. J. 1979, *Astron. Astrophys.*, **74**, 73.
- Sandage, A. 1978, *Astron. J.*, **83**, 904.
- Sandage, A. 1986, *Astrophys. J.*, **307**, 1.
- Sandage, A., Katem, B., and Johnson, H. L. 1977, *Astron. J.*, **82**, 389.
- Sandage, A., and Tammann, G.A. 1981, *A Revised Shapley-Ames Catalogue of Bright Galaxies*, (Washington: Carnegie Institute of Washington).
- Schmidt, G., Weymann, R. J., and Foltz, C. B. 1989, *Pub. Astron. Soc. Pac.*, **101**, 713.
- Schommer, R. A., Olszewski, E. W., and Aaronson, M. 1984, *Astrophys. J. Lett.*, **285**, L53.
- Schweizer, F., Whitmore, B. C., and Rubin, V. C. 1983, *Astron. J.*, **88**, 909.
- Schweizer, L. Y. 1987a, *Astrophys. J. Suppl.*, **64**, 411 (S87).
- Schweizer, L. Y. 1987b, *Astrophys. J. Suppl.*, **64**, 417 (S87).
- Schweizer, L. Y. 1987c, *Astrophys. J. Suppl.*, **64**, 427 (S87).
- Seitzer, P., and Carney, B. W. 1990, *Astron. J.*, **99**, 229.
- Seldner, M., Siebers, B., Groth, E. J., and Peebles, P. J. E. 1977, *Astron. J.*, **82**, 249.
- Sellwood, J. A. 1982, in *I.A.U. Proc. 100: Internal Kinematics and Dynamics of Galaxies*, ed. E. Athenassoula (Dordrecht: Reidel), p. 197.
- Setti, G., and Van Hove, L. (eds.) 1984, *Large Scale Structure of the Universe and Fundamental Physics* (Geneva: ESO and CERN).
- Shipman, H. L. and Strom, S. E. 1970, *Astrophys. J.*, **159**, 183.
- Simkin, S. M. 1974, *Astron. Astrophys.*, **31**, 129.

- Smith, S. 1936, *Astrophys. J.*, **83**, 23.
- Soneira, R. M., and Peebles, P. J. E. 1977, *Astrophys. J.*, **211**, 1.
- Sparke, L. S., and Casertano, S. 1988, *Mon. Not. R. Astron. Soc.*, **234**, 873.
- Staveley-Smith, L., and Davies, R. D. 1987, *Mon. Not. R. Astron. Soc.*, **224**, 953.
- Steiman-Cameron, T. Y., Kormendy, J., and Durisen, R. H. 1991, *Astron. J.*, submitted.
- Stetson, P. B. 1979, *Astron. J.*, **84**, 1149.
- Suntzeff, N. B., Aaronson, M., Olszewski, E. W., and Cook, K. H. 1986, *Astron. J.*, **91**, 1091.
- Suntzeff, N., Olszewski, E., and Stetson, P. B. 1985, *Astron. J.*, **90**, 1481.
- Thuan, T.-X., and Gott, J. R. III 1977, *Astrophys. J.*, **216**, 194.
- Tonry, J., and Davis, M. 1979, *Astron. J.*, **84**, 1511.
- Toomre, A. 1982, in *I.A.U. Proc. 100: Internal Kinematics and Dynamics of Galaxies*, ed. E. Athenassoula, E. (Dordrecht: Reidel), p. 177.
- Tremaine, S. D. 1976, *Astrophys. J.*, **203**, 72.
- Tremaine, S., and Gunn, J. E. 1979, *Phys. Rev. Lett.*, **42**, 407.
- Trimble, V. 1987, *Ann. Rev. Astron. Astrophys.*, **2**, 425.
- Tully, R. B., and Fisher, J. R. 1977, *Astron. Astrophys.*, **54**, 661.
- Turner, E. L. 1976a, *Astrophys. J.*, **208**, 20 (T76).
- Turner, E. L. 1976b, *Astrophys. J.*, **208**, 304 (T76).
- van Albada, T. S. 1982, *Mon. Not. R. Astron. Soc.*, **201**, 939.
- van den Bergh, S. 1980, in NATO ASI *The Structure and Evolution of Normal Galaxies*, ed. S.M. Fall and D. Lynden-Bell (Cambridge: Cambridge University Press), p. 201.

- van Moorsel, G. A. 1982, Ph.D. Dissertation, Univ. of Groningen.
- van Moorsel, G. A. 1987, *Astron. Astrophys.*, **176**, 13 (vM87).
- Webbink, R. F. 1985, *IAU Colloquium No. 113, Dynamics of Star Clusters*, ed. J. Goodman and P. Hut (Dordrecht: Reidel), p. 541.
- Weinberg, M. D. 1989, *Mon. Not. R. Astron. Soc.*, **239**, 549.
- Weinberg, S. 1972, *Gravitation and Cosmology*, (New York: Wiley and Sons).
- Welch, D. L., McAlary, C. W., McLaren, R. A., and Madore, B. F. 1986, *Astrophys. J.*, **305**, 583.
- White, S. D. M. 1981, *Mon. Not. R. Astron. Soc.*, **195**, 1037.
- White, S. D. M. 1983, *Astrophys. J.*, **274**, 53.
- White, S. D. M. 1984, *Astrophys. J.*, **286**, 38.
- White, S. D. M., Huchra, J., Latham, D., and Davis, M. 1983, *Mon. Not. R. Astron. Soc.*, **203**, 701 (WHL83).
- White, S. D. M., and Valdes, F. 1980, *Mon. Not. R. Astron. Soc.*, **190**, 55.
- Whitmore, B. C., McElroy, D. B., and Schweizer, F. 1987, *Astrophys. J.*, **314**, 439.
- Yahil, A., Tammann, G. A., and Sandage, A. 1977, *Astrophys. J.*, **217**, 903.
- Zaritsky, D., and White, S. D. M. 1988, *Mon. Not. R. Astron. Soc.*, **235**, 289.
- Zaritsky, D., Olszewski, E. W., Schommer, R. A., Peterson, R., and Aaronson, M. 1989, *Astrophys. J.*, **345**, 759.
- Zwicky, F. 1933, *Helv. Phys. Acta*, **6**, 110.